



University  
of Glasgow

Jebur, Qusai Hatem (2013) *Characterisation and modelling of transversely isotropic flexible viscoelastic foam.*

PhD thesis

<http://theses.gla.ac.uk/4497/>

Copyright and moral rights for this thesis are retained by the author

A copy can be downloaded for personal non-commercial research or study, without prior permission or charge

This thesis cannot be reproduced or quoted extensively from without first obtaining permission in writing from the Author

The content must not be changed in any way or sold commercially in any format or medium without the formal permission of the Author

When referring to this work, full bibliographic details including the author, title, awarding institution and date of the thesis must be given

# **Characterisation and Modelling of Transversely Isotropic Flexible Viscoelastic Foam**

**Qusai Hatem Jebur**

**A thesis for the degree of Doctor of Philosophy (PhD)  
Submitted to the School of Engineering,  
College of Science and Engineering,**

**University of Glasgow**

**June 2013**

## **DECLARATION**

I declare that this thesis is a record of the original work carried out by myself under the supervision of Dr. Philip Harrison in the School of Engineering at the University of Glasgow, United Kingdom. The copyright of this thesis therefore belongs to the author under the terms of the United Kingdom Copyright acts. Due acknowledgement must always be made of the use of any material contained in, or derived from, this thesis. The thesis has not been presented elsewhere in consideration for a higher degree.

Signature \_\_\_\_\_

Printed name: Mr Qusai Hatem Jebur

Signature \_\_\_\_\_

Printed name: Dr. Philip Harrison

## I. Abstract

Polymer foams have unique properties covering a wide range of mechanical and physical behaviours. This makes them important engineering materials that can be used in numerous applications including packaging, impact energy absorption, cushioning and spacers in sandwich construction. In general, the mechanical response of foam materials is not isotropic, though for most design purposes they are treated as such. The validity of this assumption depends on the degree of anisotropy of the foam and in some cases may be questionable. Most polymeric foams tend to display at least some degree of anisotropy that can usually be related back to their manufacture process. The aim of this investigation is to look at the extent of mechanical anisotropy in commonly used polymer foams and explore options currently available in modelling such materials, using established analytical theories and constitutive models implemented in a commercially available finite element code as a starting point. Attempts are made to relate the transversely anisotropic macro-scale response to the microstructure within the material.

A melt-extruded closed-cell Low-Density Polyethylene (LDPE) foam has been chosen as a representative foam material with which to explore the topic. Uniaxial compression, simple shear and relaxation tests have been used to characterise the material's response. Two techniques have been used to determine the Poisson's ratio of foam under uniaxial compression. As expected, results reveal the LDPE foam to be a strongly transversely isotropic material that is both viscoelastic and highly compressible. The stiffness and strength of the foam are almost three times higher in the extrusion (or principle) direction used to manufacture the foam, when compared with the properties in the transverse directions. It is also noted that the foam's mechanical behaviour depends on the specimen size. For larger specimens measuring  $80 \times 80 \times 80 \text{mm}^3$ , the modulus at small strain and the yield stress, are approximately twice that of smaller specimens measuring  $10 \times 10 \times 10 \text{mm}^3$ . The compressive behaviour of the LDPE foam is also rate dependent. The yield stress of foam increases approximately linearly with the natural logarithm of the compression strain rate. The Poisson's ratio values decreases with increasing compression strain rates. While the energy absorption efficiency of foam increases with strain rate. Micro-CT and optical microscopy has been performed to determine the average microstructural cell shape and dimensions within the LDPE foam. Results indicate an average cell geometry that is

elongated in the foaming direction by about 20% compared to the transverse direction. A combined analytical and numerical modelling strategy has been employed to provide a better understanding of the relationship between microstructure and macroscopic behaviour. Combined use of analytical and numerical modelling shows that it is possible to give a good prediction of the foam's macroscopic response based on an understanding of the inherent anisotropy within the foam's microstructure.

## **II. Acknowledgment**

First I would I would like to express my many thanks to Allah (God) for providing me the blessing to finish this work. Then, I am truly thankful to the following colleagues, family and friends who contributed their advice and support towards the development of this research.

I would like to express my great and special thanks of gratitude to my supervisor, Dr Philip Harrison for his supervision, advice, guidance. He continuously encouraged and challenged me through my research programme and never accepted less than my best efforts that enabled me to know more and more about so many things.

I would like to give great thanks and truly much appreciated to my previous supervisor Dr Zaoyang Guo for his guidance and assistance to start this work.

The Iraqi Ministry of Higher Education and Scientific Research, for funding this research.

The technical staffs, in particular Mr Brian Robb and Mr John Davidson for their expertise, extensive help and assistance in the material lab and preparations of specimens.

Staff at the School of Engineering, University of Glasgow, for their assistance, help and accommodating my demanding needs on resources throughout my studies.

Most especially to my uncle Professor Muhsen Jebur, big family, my lovely mother and brothers, and to my small family, my wonderful wife Hadeel Mousa and my sons, Hasan, Husain and Ibrahim for their understanding and support. Words alone cannot express what I owe them for their encouragement and patient love that inspired me to complete this work.

### III. Table of Contents

I. Abstract .....	I
II. Acknowledgment .....	III
III. Table of Contents .....	IV
IV. List of Table Captions .....	IX
V. List of Figure Captions .....	IX
VI. List of Symbols .....	XVII
VII. Abbreviations .....	XXI
Chapter 1. Introduction .....	1
1.1. Properties of Foams and their Applications .....	2
1.2. Manufacture of Foams .....	3
1.2.1. Extrusion Process .....	6
1.2.2. Effects of Manufacture Method on Microstructure of Foams .....	7
1.3. Influence of Foam Microstructure on Mechanical Properties .....	7
1.3.1. Cell Structure: Open- or Closed-cell .....	7
1.3.2. Relative Density .....	8
1.3.3. Cell Size and Distribution .....	8
1.4. Mechanical Response of Foams under Compressive Loading .....	9
1.4.1. Linear Elastic and Isotropic Foam .....	11
1.4.2. Non-linear Elastic and Isotropic Foam .....	11
1.4.3. Linear Elastic and Transversely Isotropic Foam .....	11
1.4.4. Non-linear Elastic and Transversely Isotropic Foam .....	11
1.4.5. Elastic-Plastic Foam .....	12
1.4.6. Elastic-Brittle Foam .....	12
1.4.7. Visco-Elastic Foam .....	12
1.5. Objectives .....	14
1.6. Outline .....	15
Chapter 2. Literature review .....	17
2.1 Modelling of Foam Behaviour .....	17
2.1.1 Linear or Small Strain Models .....	17

2.1.1.1 Linear Elastic Isotropic Compressible Model .....	18
2.1.1.2 Linear Elastic, Transversely Isotropic Compressible Model .....	18
2.1.1.3 Linear Viscoelastic Model.....	20
2.1.2 Large Strain Models .....	21
2.1.2.1 Isotropic Hyperelastic Behaviour .....	21
2.1.2.2 Hypoelasticity .....	24
2.1.2.3 Transversely Isotropic Hyperelastic Incompressible Behaviour .....	24
2.1.2.4 Elastic-Plastic Transversely Isotropic Model.....	25
2.1.2.5 Hyper-Viscoelasticity .....	25
2.2 Micro-scale Modelling .....	26
2.2.1 Small Strain Modelling .....	29
2.2.1.1. Analytical Models for Small Strains .....	29
2.2.1.2. Numerical Model for Small Strains.....	36
2.2.2 Large Strain Modelling .....	38
2.2.2.1 Analytical Models .....	38
2.2.2.2 Gas Diffusion Model .....	40
2.2.2.3 Analytical Modelling (Kelvin Model).....	41
2.2.2.4 Numerical Modelling (Kelvin model) .....	42
2.2.2.5 Numerical Modelling (Voronoi Model) .....	42
2.3 Experimental Investigations .....	45
2.3.1 Macro-scale Experimental Investigations .....	45
2.3.1.1 Digital Image Correlation Technique for Strain Measurements in Foams.....	45
2.3.1.2 Uniaxial compression test .....	46
2.3.1.3 Multi-Axial Tests .....	47
2.3.1.4 Shear Test .....	48
2.3.1.5 Uniaxial Tensile Test.....	49
2.3.1.6 Hydrostatic Compression Test .....	50
2.3.1.7 Creep and Relaxation Test .....	52
2.3.2 Factors Affecting Mechanical Response .....	54
2.3.2.1 Influence of Strain Rate.....	54
2.3.3 Influence of Specimen Size .....	55
2.3.4 Influence of Relative Density .....	55
2.3.5 Determination of Strain Regime.....	57
2.3.5.1 Onset Strain of Densification .....	57

2.3.5.2 Energy Absorption Efficiency .....	58
2.3.6 Micro-scale Experimental Investigations .....	59
Chapter 3. Experimental Characterisation of a Transversely Isotropic Polymer Foam.....	62
Introduction .....	62
3.1. Macromechanical Characterisation .....	63
3.1.1. Uniaxial Compression Tests .....	64
3.1.1.1. Procedure to Determine Stress and Strain (under Uniaxial Compression) .....	64
3.1.1.2. Procedure to Determine the Modulus (under Uniaxial Compression) .....	68
3.1.1.3. Procedure to Determine the Yield Stress (under Uniaxial Compression).....	69
3.1.1.4. Procedure to Determine Energy Absorption Efficiency and Onset Strain of Densification (under Uniaxial Compression).....	69
3.1.1.5. Procedure to Determine Poisson's ratio (under Uniaxial Compression) .....	71
3.1.1.6. Procedure to determine Poisson's ratio by Manual Image Analysis.....	72
3.1.1.7. Procedure to determine Poisson's ratio by Digital Image Correlation.....	73
3.1.2. Stress Relaxation (under Uniaxial Compression).....	74
3.1.2.1. Procedure to Measure Stress Relaxation (under Uniaxial Compression) .....	74
3.1.3. Simple Shear Test.....	75
3.1.3.1. Procedure to Determine the Shear Modulus.....	77
3.2. Results: .....	78
3.2.1. Influence of Specimen Size and Material Orientation under Uniaxial Quasi-Static Compression on Mechanical Response: .....	78
3.2.2. Influence of Compressive Strain and Time on Recovery.....	83
3.2.3. Influence of Compressive Strain on Poisson's ratio.....	85
3.2.4. Influence of Compressive Strain Rate on Stress versus Strain Response .....	88
3.2.5. Influence of Rate of Compressive Strain on Energy Efficiency .....	90
3.2.6. Influence of Strain Rate on Poisson's ratio .....	91
3.2.7. Influence of Stress Relaxation on Relaxation Modulus .....	95
3.2.8. Influence of Shear Strain on Shear Modulus.....	96
3.2.9. Influence of Material Direction on the Off Principal Axis Compressive Stress- Strain Response .....	98
3.2.10. Influence of Material Direction on the Off Principal Axis Compressive Modulus and Yield stress at Small Strains .....	100

3.2.11. Influence of Material Direction on the Off Principal Axis Energy Absorption Efficiency at Large Strains .....	100
3.2.12. Influence of Material Direction on the Off Principal Axis Poisson's ratio .....	101
3.3. Micromechanical Characterisation .....	104
3.3.1. Experimental Setup and Procedure for Micro CT Imaging .....	104
3.3.2. Experimental Setup and Procedure for Optical Microscopy .....	105
3.3.3. Quantitative Analysis of 2D Images .....	107
3.3.3.1. Cell shape Characterisation .....	107
3.3.3.2. Measurement of Cell Dimensions .....	109
3.4. Summary .....	111
Chapter 4. : Macro-Mechanical Modelling of Foam .....	112
4.1. Introduction .....	112
4.2. Interpolating the Off-axis Stress-strain Curves .....	113
4.3. Combined Empirical Rate Law and Gas Model.....	116
4.4. Prediction of Size Effect on Mechanical Properties.....	123
4.5. Evaluation of Constitutive Models Currently Implemented in a Commercial FEA Software.....	127
4.5.1. Influence of Material Direction on the Off Principal Axis Large Strain Kinematics .....	129
4.5.1.1. Hyperfoam Evaluation .....	133
4.6. Summary .....	137
Chapter 5. Modelling of Transversely Isotropic Closed-cell Foam Using a Micro to Macromechanics Approach.....	138
5.1. Introduction .....	138
5.1.1. Gibson and Ashby Analytical Model .....	139
5.1.1.1. Determination of Small-strain Elastic Moduli for the Isotropic Case.....	140
5.1.1.2. Determination of Yield Stress and Strain for Isotropic Case .....	144
5.1.1.3. Determination of Small-strain Elastic Moduli for the Transversely Isotropic case .....	146
5.1.1.4. Determination of Yield Stress for Transversely Isotropic Case.....	150
5.1.2. Kevin Numerical Model .....	152
5.1.2.1. Analysis Procedure.....	154
5.1.2.2. Finite Element Model.....	155

5.1.2.3. Periodic Boundary Conditions .....	156
5.1.2.3.1. Boundary Conditions during Compression and Simple Shear Simulations...	156
5.1.2.4. Dimensions of Isotropic Kelvin Representative Unit Cell .....	158
5.1.2.5. Dimensions of Elongated Kelvin Repeat Unit Cell Model .....	159
5.1.2.6. Mesh Convergence of RUC .....	160
5.1.2.7. Influence of Detailed RUC Microstructure and Boundary Condition.....	161
5.1.2.8. Methods to Artificially Soften the Kelvin RUC Response .....	163
5.1.2.9. Fitting the Edge and Face Thicknesses Using Uniaxial Compression Tests.....	165
5.1.2.10. Simulations of Uniaxial Compression Test.....	166
5.1.2.11. Shear Test Results .....	168
5.2. Large strain Modelling .....	170
5.2.1. Predicting the Off-axis Stress-strain Curves .....	170
5.2.2. Comparison between Model and Actual Foam .....	170
5.3. Summary .....	173
Chapter 6. Conclusions and Recommendations for Future Work.....	175
6.1. Future Work .....	178
Appendix I: Publications .....	179
Appendix II: References.....	180

## IV. List of Table Captions

Table 1.1. The manufacture process of foam, $r$ cells shape anisotropy, $E_p$ , $E_t$ elastic parameters in the principal and transverse directions respectively . The subscript $p$ and $t$ refer to principal and transverse directions respectively.....	5
Table 2.1. Young's modulus for the Kelvin foams with difrent strut cross-section, $A$ is area of sreut, $I$ is second moment of area of the strut, $J_p$ is polar second moment of area of the strut, $E_s$ is elastic modulus of solid constituent material, $E$ is elastic modulus of foam and $R$ is relative density of foam[4, 75]. Where $r_c$ is radius of cucle, $b_s$ is side of the square, Equilateral triangle and Plateau border .....	36
Table 3.1 Elastic modulus in principal and transverse directions with versus specimen sizes .....	80
Table 3.2. Yield stress in principal and transverse directions with versus specimen sizes.	80
Table 3.3. Energy absorption efficiency in principal and transverse directions, with versus specimen sizes.....	81
Table 3.4. The average difference between the two methods of measuring the Poisson's ratio. ....	94
Table 4.1. Parameters for the hyperfoam model, $N=2$ and zero Poisson's ratio: Uniaxial compression test.....	134
Table 4.2. Parameters for the hyperfoam model, $N= 5$ or $6$ : Uniaxial compression test...	135
Table 5.1. Experimental and predicted results obtained using G&A model for the properties of LDPE foam .....	149
Table 5.2. Experimental and predicted yield stress and elastic yield strain obtained using G&A model for LDPE foam.....	152
Table 5.3. Dimensions of Kelvin model closed-cell RUC predicted by G&A model [1] and measured using microscopy. ....	159
Table 5.4. Experimental and predicted results obtained for the properties of extruded LDPE foams.....	169

## V. List of Figure Captions

Figure 1-1. Applications of foam.....	3
Figure 1-2. Simple schematic of the extrusion process [2].....	6

Figure 1-3. SEM photographs of polyurethane foam from [4].	8
Figure 1-4. Compressive stress-strain curves.	10
Figure 1-5. Compressive stress-strain curves at varies strain rates.	14
Figure 2-1. Orthotropic material with plane of transverse isotropy [36].	19
Figure 2-2. Two basic phenomenological models (a) Maxwell Model and (b) Voigt Model [50].	21
Figure 2-3. Prony model (a spring and dashpot in series) [49].	21
Figure 2-4. (a) A cubic cell model for isotropic open-cell foam showing the edge length $l$ , the edge thickness, $t_e$ , (b) cuboid model for anisotropic open-cell foam showing the edge lengths $l$ and $h$ [1].	27
Figure 2-5. Body centred cubic (BCC) packing of 14-sided cells in the Kelvin foam (a) regular Kelvin model, and (b) elongated Kelvin model.	28
Figure 2-6. Irregular microstructure models (a) 2-D Voronoi construction for cells inside a square box and (b) 3-D Voronoi model of a closed-cell dry foam with 512 cells [4].	29
Figure 2-7. (a) Data for relative Young's modulus of foams plotted against relative density. The solid line represents the theory for open-cell foams. The two dashed lines represent the theory for close-cell foams, (b) data for the elastic collapse stress for foams, normalized by the solid modulus, the solid line represent the theory for open-cell foams, the dashed line that for closed-cells, (c) data for the relative shear modulus foams, plotted against relative density, the solid data represent the theory for open-cell foams [1].	31
Figure 2-8. Schematic representation of (a) Kelvin cell foam model (b) a Plateau border/cell face section [83].	33
Figure 2-9. (a) Anisotropic and (b) Isotropic open-cell Kelvin foam models.	35
Figure 2-10. Effects of cell regularity on the (a) reduced Young's modulus of random Voronoi foams having a constant relative density, (b) reduced shear modulus of random Voronoi foams having a constant relative density $R=0.01$ , (c) reduced bulk modulus of random Voronoi foams having a constant relative density $R =0.01$ and (d) Poisson's ratio of random Voronoi foams having a constant relative density $R =0.01$ [78].	38
Figure 2-11. Phase volume in foam of zero Poisson's ratio and relative density $R$ , before and after uniaxial compression [4].	39
Figure 2-12. Cubic cell foam with a pressure gradient in x-direction.	41

Figure 2-13. (a) An undeformed random Voronoi cell and (b) The reduced stresses against the compressive strains of foams having a regularity parameter  $\alpha=0.7$ , compared with the predicted results [96].....43

Figure 2-14. (a) The dimensionless stress-strain curves of models with different relative density, (b) the Poisson’s ratio-strain curves of models with different relative density, (c) the dimensionless stress-strain curves of models with different strut cross-section shapes, and (d) the Poisson’s ratio-strain curves of models with different strut cross-section shapes [97]. .....44

Figure 2-15. Uniaxial compression test. ....47

Figure 2-16 Sketch of the loading rig for the biaxial and hydrostatic tension tests[66]. .....48

Figure 2-17. Shear test procedure. ....49

Figure 2-18. Tensile test setup [116]. .....50

Figure 2-19. Schematic of the hydrostatic compression test rig [2]. .....52

Figure 2-20. (a) Stress relaxation tests (constant strain) and (b) Creep test (constant stress) [46]. .....53

Figure 2-21. (a) The peak stress generated in foams of three densities in absorbing the same energy  $W$  are given by  $\sigma_1, \sigma_2$ , and  $\sigma_3$ . The lowest-density foam ‘bottoms out’ before absorbing the energy  $W$ , generating a high peak stress. The highest-density foam also generates a high peak stress before absorbing the energy  $W$ . (b) stress-strain curves for elastic foam, showing the energy absorbed per unit volume .....59

Figure 2-22. ( a) The closed-cell aluminum foams specimen between two loading platens and (b) its finite element model [40]. .....61

Figure 3-1. Stress-strain diagram showing typical mechanical properties of interest. ....65

Figure 3-2. Compression testing configuration (a) Zwick/Roell Z250 and, (b) Zwick/Roell Z2. ....66

Figure 3-3. Schematic of the uniaxial compression test setup. ....67

Figure 3-4. Example of the slope versus strain curve; points above the red line are selected for determining Young’s modulus. ....68

Figure 3-5. Uniaxial compression tests for determining stress-strain curves in the linear elastic region and yield point .....69

Figure 3-6. Stress-strain curves resulting from a uniaxial compression test. ....70

Figure 3-7. Compression tests for determining Poisson’s ratio: (a) before compression and (b) after compression.....72

Figure. 3-8. The digital image correlation setup. ....	74
Figure 3-9. Compression test to determine stress relaxation. ....	75
Figure 3-10. Schematic of shear test set-up. ....	76
Figure 3-11. Typical force versus shear strain curve. ....	77
Figure 3-12. Photograph of test specimens, cubes with side lengths of: 10, 20, 50 and 80mm. ....	78
Figure 3-13. Stress-strain curves in the principal direction for four different cube sizes. ....	79
Figure 3-14. Stress-strain curves in the transverse direction for four different cube sizes. ....	79
Figure 3-15. Effect of specimen size on elastic modulus. ....	80
Figure 3-16. Effect of specimen size on yield stress. ....	81
Figure 3-17. Efficiency-strain curves with various specimen sizes. ....	82
Figure 3-18. Compression loading and unloading stress–strain curves for 50x50x50 mm cube 90% strain loading/unloading in the principal and the transverse directions. The error bars indicate the standard deviation (SD) from five repeats. ....	83
Figure 3-19. Compression loading and unloading stress–strain curves in the principal direction conducted several days apart for 50x50x50 mm <sup>3</sup> (a) 25% compression and (b) 50% compression. ....	84
Figure 3-20. Compression loading and unloading stress–strain curves in the transverse direction conducted several days apart for 50x50x50 mm <sup>3</sup> (a) 25% compression and (b) 50% compression. ....	84
Figure 3-21. Compression tests for determination of the Poisson’s ratio: (a) before compression; (b) after compression; (c), (d) measured lateral strains versus compressive strain; and (e) measured Poisson’s ratios versus compressive strain, error bars indicate the standard deviation of 3 repeat tests. ....	86
Figure 3-22. Compression tests for determining Poisson’s ratio: (a) before compression; (b) after compression and the colours are indicate the displacement in x-direction of specimen test. ....	87
Figure 3-23. Comparison between Poisson’s ratio calculated by manual <i>image-J</i> method and DIC: (a) comparison of Poisson’s ratio $\nu_{12}$ and (b) comparison of Poisson’s ratio $\nu_{21}$ . ....	88
Figure 3-24. Experimental uniaxial compression curves according to data at different strain rates in the principal direction. ....	89
Figure 3-25. Experimental uniaxial compression curves according to data at different strain rates in the transverse direction. ....	89

Figure 3-26. Efficiency-strain curves with various strain rates, specimen size 50x50x50 mm <sup>3</sup> .....	90
Figure 3-27. Effects of strain rate on the energy absorption efficiency in the principal and transverse directions.....	91
Figure 3-28. Compression tests for determining Poisson's ratio: (a), (b), (c), (d), (e) and (f), measuring lateral strains versus compressive strain rates; error bars indicate the standard deviation of three repeated tests.....	93
Figure 3-29. Compression tests for determining Poisson's ratio, measuring lateral strains versus compressive strain rates. ....	94
Figure 3-30. Comparison of the compression relaxation stress of LDPE (a) in the principal and (b) transverse directions. ....	95
Figure 3-31. Comparison of the compression secant modulus of LDPE (a) in the principal and (b) transverse directions. ....	95
Figure 3-32. Shear test results: (a), (b) and (c) measured nominal shear stress- nominal shear strain curve and the computed tangent shear modulus, the error bars indicate the standard deviation of 3 repeat tests .....	97
Figure 3-33. Specimen cutting with rotation at angles. ....	98
Figure 3-34. Uniaxial compression for a cube sized 50x50x50mm <sup>3</sup> with different degrees of rotation of the foam's (a) principal axis; and (b) transverse axis, error bars indicate the standard deviation of 5 repeat tests. ....	99
Figure 3-35. Stiffness varies with angle of rotation.....	100
Figure 3-36. Yield stress varies with angle of rotation.....	100
Figure 3-37. Efficiency-strain curves with various angle of rotation. ....	101
Figure 3-38. Comparison of Poisson's ratio determined for large strain using two methods with different degrees of rotation: (a) cube rotation at 22.5°, (b) cube rotation at 45° and (c) cube rotation at 67.5° .....	103
Figure3-39. Poisson's ratio in the elastic region versus rotation angle (value taken at a strain less 0.05). ....	103
Figure 3-40. Micro-CT scan image.....	104
Figure 3-41. (a) multiple slices are recorded in three mutually orthogonal planes and (b) reconstruction of 3D image.....	105
Figure 3-42. A BRESSER Biolux optical microscope.....	106
Figure 3-43. Optical micrographs of LDPE foam the white rectangle was used to obtain the basic dimensions of the cells diameter.....	107

Figure 3-44. Optical micrographs of LDPE foam (a) the extrusion is in x-direction and (b) the extrusion is in z-direction. ....	108
Figure 3-45. Histogram showing the cell shape anisotropy ratio distribution for (a) principal directions and (b) transverse direction. ....	108
Figure 3-46. Histogram distributions and average values showing (a) cell edge length, (b) cell edge thickness, (c) width of cells in transverse direction, (d) cell width in principal direction and (e) cell wall thickness. ....	110
Figure 4-1. Principal and transverse uniaxial compression curves with secant modulus shown at 0.2 strain. ....	113
Figure 4-2. Curves for polynomial fit equation of experimental measurement and predicted shear modulus for LDPE. ....	115
Figure 4-3. Experimental uniaxial compression curves (continuous lines) with different degrees of rotation of principal axis together with predicted uniaxial compression curves (dashed lines) using Equation (4-1), for $\theta = 22.5^\circ$ , $45^\circ$ and $67.5^\circ$ . ....	115
Figure 4-4. Experimental uniaxial compression curves in the principal direction (continuous lines) with fitted uniaxial compression and curves using Equation (4-4) (dotted line). ....	117
Figure 4-5. Experimental uniaxial compression curves in the transverse direction (continuous lines) with fitted uniaxial compression and curves using Equation (4-5) (dotted line). ....	117
Figure 4-6. Effects of strain rate on yield stress in the principal and transverse directions. ....	118
Figure 4-7. (a), (b) and (c) Experimental uniaxial compression curves (continuous lines) with different strain rates in the principal direction, together with predicted uniaxial compression curves (dotted lines) using Equations (4-4) and (4-6). ....	120
Figure 4-8. (a), (b) and (c) Experimental uniaxial compression curves (continuous lines) with different strain rates in the transverse direction, together with predicted uniaxial compression curves (dotted lines) using Equations (4-5) and (4-7). ....	121
Figure 4-9. (a), (b), (c), (d), and (e) Experimental uniaxial compression curves (continuous lines) with different strain rates in the transverse direction, together with predicted uniaxial compression curves (dotted lines) using Equation (4-8). ....	122
Figure 4-10. Experimental uniaxial compression curves in the transverse (continuous lines) with predicted (dotted lines) uniaxial compression curves using Equation (4-8) for specimen sizes (a) $80 \times 80 \times 80 \text{ mm}^3$ , (b) $50 \times 50 \times 50 \text{ mm}^3$ , (c) $20 \times 20 \times 20 \text{ mm}^3$ and (d) $10 \times 10 \times 10 \text{ mm}^3$ . ....	123

Figure. 4-11. Typical stress and gas volumetric strain curves for four cubes in the principal direction.....	124
Figure. 4-12. Typical stress and gas volumetric strain curves for four cubes in the transverse direction. ....	125
Figure 4-13. Curves for pressure decreases inside cells in the principal direction. ....	125
Figure 4-14. Curves for pressure decreases inside cells in the transverse direction. ....	126
Figure 4-15. Experimental uniaxial compression curves in the transverse (continuous lines) with predicted (dotted lines) uniaxial compression curves for specimen sizes (a) 80x80x80 mm <sup>3</sup> , (b) 50x50x50 mm <sup>3</sup> , (c) 20x20x20 mm <sup>3</sup> and (d) 10x10x10 mm <sup>3</sup> .....	127
Figure 4-16. Off-axis uniaxial compression of foam to 26% engineering strain. (a): experimental observation showing principal direction. (b): Displacement predictions of linear compressible transversely isotropic model. ....	130
Figure 4-17. Off-axis uniaxial compression of foam to 26% engineering strain. (a): DIC observation showing principal direction. (b): Displacement predictions of linear compressible transversely isotropic model. ....	132
Figure 4-18. (a) Experimental uniaxial compression curves (continuous lines) predicted by compressible isotropic hyperfoam model fitted to the predicted curves with positive shear moduli ( $N = 2$ ); and (b) Experimental uniaxial compression curves (continuous lines) predicted by compressible isotropic hyperfoam model fitted to the predicted curves with negative shear moduli ( $N = 5$ or 6). ....	136
Figure 5-1. (a) A cubic representative unit-cell model for closed cell foam, showing face thickness $t_f$ , and the cell edge thickness $t_e$ ; (b) An elongated cuboid representative unit cell with, shape anisotropy ratio $r = 1.5$ where $r = h/l$ [1].....	140
Figure 5-2. Stretching of the face of closed-cell foam during compression. ....	143
Figure 5-3. Elastic buckling in the cell walls of a closed cell.....	145
Figure 5-4. Variation of modulus of elasticity with relative density for a cubic and an elongated cuboid unit cell (curves predicted with $r=1.2$ ). ....	149
Figure 5-5. Variation of shear modulus with relative density for a cubic and an elongated cuboid unit cell (curves predicted with $r=1.2$ ). ....	149
Figure 5-6. Variation of yield stress with relative density for a cubic and an elongated cuboid unit cell (curves predicted with $r=1.2$ ). ....	151
Figure 5-7. Stress-strain curves show the predicted yield strain in the principal and transverse directions using Gibson and Ashby model. ....	152

Figure 5-8. (a) Isotropic closed-cell Kelvin model (b) Anisotropic closed-cell Kelvin model.....	154
Figure 5-9. FEM models of (a) Isotropic and (b) Anisotropic Kelvin closed-cell foam. ..	156
Figure 5-10. Side numbering of (a) Isotropic and (b) Anisotropic closed-cell Kelvin model. ....	158
Figure 5-11. Number of elements to achieve convergence of response of isotropic unit cell model.....	161
Figure 5-12. The Young's modulus-relative density with different edges cross sections. ....	162
Figure 5-13. The shear modulus-relative density with different edge cross sections. ....	162
Figure 5-14. The $E_t$ elastic modulus of LDPE foam in transverse direction versus $E_s$ the elastic modulus of polyethylene at a constant relative density 0.043 of Polyethylene foam (for edges of Circular ross-section).....	163
Figure 5-15. The $E_t$ elastic modulus of foam in transverse direction- $t_{ek}$ edge thickness (for edges of circular cross-section).....	164
Figure 5-16. The $E_t$ elastic modulus of transverse direction versus $t_{fk}$ face thickness (for edges of circular cross-section).....	164
Figure 5-17. Uniaxial compression tests for (a) isotropic and (b) anisotropic Kelvin model. ....	166
Figure 5-18. Young's modulus concentration versus relative density.....	167
Figure 5-19. Shear test for (a) isotropic and (b) anisotropic Kelvin model unit cell. ....	168
Figure 5-20. Shear modules with verses relative density for principal $G_{12}$ transverse $G_{23}$ ....	169
Figure 5-21. Experimental uniaxial compression curves (continuous lines) with different degree of rotation of principal axis together with predicted uniaxial compression curves (dashed lines) using equations (5-58), (2-33) and (5-59), (a) for $\theta = 0^0$ , (b) for $\theta = 22.5^0$ , (c) for $\theta = 45^0$ , (d) for $\theta = 67.5^0$ and (e) for $\theta = 90^0$ .....	171
Figure 5-22. Comparison between modulus of elasticity predicted by analytical and numerical with experimental data. ....	172
Figure 5-23. Comparison between Poisson's ratio predicted by analytical model and experimental data. ....	172

## VI. List of Symbols

$A$	Edges or strut cross-section area
$a_{el}$	Slope of the force-displacement curve in shear test
$A_o$	Original cross-section area of the specimen
$a, \beta$	Empirically determined constants
$a_i$	Material constant
$b$	Material parameters
$b_s$	Side of the square, Equilateral triangle and Plateau border
$C_1$	Constant of proportionality of foam material
$C_2$	Constant
$C_m$	Constant characterise the shear modulus of the material
$C_p$	Fit parameter in principal direction
$C_t$	Fit parameter in transverse direction
$d$	displacement
$D$	Stretching tensor
$D_1$	Constant characterise the inverse of the bulk modulus of the material
$D_f$	Gas diffusion coefficient of foam
$dp/d\varepsilon$	change of the internal gas pressure with respect to the volumetric strain
$d_{mm}$	Measured cell dimensions (mm)
$D_p$	Gas diffusion coefficient of polymer
$d_{se}$	Shear displacement
$E_{(100)}$	Kelvin foam model for the (001) compression direction
$E_e$	Elastic modulus of foam
$E_f$	The contribution from bending of the cell edges
$E_g$	The influence of the compression of gas inside the close-cells foam
$E_p$	Elastic modulus of foam in principal direction
$E_s$	Elastic modulus of solid constituent material
$E_t$	Elastic modulus of foam in transverse direction
$E(t)$	Secant modulus
$E_{(\theta)}$	Elastic modulus as function of angle rotation
$e_v$	Engineering volumetric strain
$F$	Applied force

$F_b$	The bending force of edges
$F_{\text{crit}}$	Edge buckling force
$F_{\text{el}}$	Shear force
$F_s$	Force due to stretching of the faces
$G$	Shear modulus of foam
$G_{12}$	Shear modulus in the principal direction
$G_{13}$	Shear modulus in the transverse direction
$G_{23}$	Shear modulus in the transverse direction
$G_s$	Shear modulus of the edge material
$H^*$	The hypo-elastic tensor
$h$	Edge length cubed model for anisotropic foam
$h_k$	Edge length Kelvin model for anisotropic foam
$h_o$	The original height of specimen
$I$	Second moment of area of the edge
$I_s$	Strain invariants
$I_{\text{mm}}$	Image dimensions (mm)
$J$	Volumetric strain
$J_p$	Polar second moment of area of the edge
$K$	Bulk modulus
$l$	Edge length Gibson and Ashby model
$l_{\text{ek}}$	Edge length Kelvin foam model
$l_k$	Edge length Kelvin foam model
$L_m$	Average distance between membranes
$l_v$	Length of Irregular microstructure model
$m$ and $\beta_m$	Constants
$n$	Characterises the degree of freedom at the end of the column
$N_{\text{pixel}}$	Number of pixels in the image
$P$	Hydrostatic loading
$P_{\text{at}}$	Atmospheric pressure
$P_c$	Initial yield stress in hydrostatic compression
$P_{\text{cell}}$	The effective absolute gas pressure in the foam cells
$P_{\text{co}}$	Initial cells pressure value
$P_t$	Initial yield stress in hydrostatic tension

$R$	Relative density of foam
$r$	Cells shape anisotropy ratio
$R^*$	Relative root mean square error
$S$	Stiffness of the cell edge
$S_g$	Solubility of the gas
$t_e$	Edge thickness Gibson and Ashby model
$t_{ek}$	Edge thickness Kelvin foam model
$t_f$	Cell-edge thickness Kelvin foam model
$t_{fk}$	Cell-face thickness G&A model
$t_s$	Cell-face thickness Kelvin foam model
$U_s$	Strain energy
$V_g$	Volume of gas inside closed-cell foam
$V_g^o$	Initial volume of gas inside closed-cell foam
$W$	Energy absorbed per unit volume
$w_k$	Edge length Kelvin model for isotropic foam
$\sigma$	Stress
$\sigma_c$	Cauchy stress tensor
$\sigma_e$	Von Mises stress
$\sigma_{el}$	Elastic yield stress
$\sigma_o$	Yield stress of foam
$\sigma^{O*}$	Objective stress rate
$\sigma_{pl}$	Plastic yield stress
$\sigma_{pr}$	Stress in principal direction
$\sigma_t$	Elastic yield stress in the transverse direction
$\sigma(t)$	Stress relaxation
$\sigma_{tr}$	Stress in transverse direction
$\sigma_{ys}$	Yield stress of the solid constituent material
$\sigma_{(\theta)}$	Yield stress as function of angle rotation
$\rho$	Foam density
$\rho_s$	Density of the solid constituent material

$\varepsilon$	Strain
$\varepsilon^{\bullet}$	Strain rates
$\varepsilon_D$	Onset strain of densification
$\varepsilon_{el}$	Elastic strain
$\varepsilon_o$	Initial constant strain
$\varepsilon_{de}$	Densification strain of foam
$\nu$	Poisson's ratio of foam
$\nu_{12}$	Poisson's ratio of foam in the principal direction
$\nu_{21}$	Poisson's ratio of foam in the transverse direction
$\nu_{23}$	Poisson's ratio of foam in the transverse direction
$\nu_{fit}$	Fit Poisson's ratio
$\lambda$	Principal extensions of the deformation
$\mu$	Constant related to the current shear modulus
$\mu_i$	Constant related to the initial shear modulus
$\beta_i$	Content related to a nominal Poisson's ratio
$\phi$	The edges in the foam's microstructure consisted of a volume fraction,
$\eta$	Energy absorption efficiency
$\gamma$	Shear strain
$\delta$	Cell faces deformation

## VII. Abbreviations

BCC	Body centroid cubic
BS	British Standard
CAE	Computer Aided Engineering
DIC	Digital image correlation
EPSRC	Engineering and Physical Science Research Council
EXP	Experimental
FEM	Finite element method
G&A	Gibson and Ashby
LDPE	Low density polyethylene
PBC	Periodic Boundary Conditions
PP	Polypropylene
RUS	Representative Unit Cell
RVE	Representative volumetric element
SD	Standard deviation
VIC	Video image correlation

## Chapter 1. Introduction

Most cellular materials show some level of anisotropy in their microstructure. This anisotropic nature can have a significant impact on the material's mechanical behaviour. This research focuses on determining the effects of anisotropy in the material's microstructure on the mechanical response of foams.

In this work, a review of existing anisotropic micro and macro-scale analytical and numerical models is conducted. The work in this thesis aims to use and, in some instances, enhance these models in order to characterise, fit and predict the mechanical response of anisotropic foams. Cellular materials can be broadly defined as a porous material comprised of an interconnected network of solid edges and faces which form individual cells [1].

They can be found in nature, for example, wood, cancellous bone and coral, or they can be man-made, for example, honeycomb, lattice structures and random foams. Man-made foams can be manufactured from a variety of materials such as metals, ceramics and polymers.

Cellular materials generally can be found in many forms. The simplest form of a cellular structure is honeycomb which essentially possesses a two-dimensional shape. In regular cases, the cells appear as groups of squares, triangles or hexagons [1].

Foams are an important subcategory of cellular materials and can be defined as materials consisting of random microstructures with either a liquid or a solid phase, constituting the structure of the foam and either a gas or a liquid phase permeating the structure. Foams consist of a large number of cells. Each cell has struts at its edges. Depending on the type of foam, these struts may act as the frames for cell faces, the occurrence of faces creates a closed cellular structure, and the absence of faces creates an open cellular structure. An extensive body of literature has been published on the mechanical properties of foams and several excellent texts reviewing the topic are available [1-3] . In this chapter a brief overview of themes relevant to the detailed investigations performed in subsequent chapters is provided.

## 1.1. Properties of Foams and their Applications

In general, foams possess unique mechanical properties, making them attractive for many engineering applications [1, 4]. Some of these properties, and how they facilitate applications, are:

- **High compressibility at constant stress:** Many types of foam can be compressed to high strain under an approximately constant stress (typical forms of stress-strain curves for random foams are discussed in Section 1.4). Consequently, a large amount of energy can be absorbed without generating a large amount of stress. Hence they are used in packaging of electronic and fragile products etc., see Figure 1-1a.
- **Relatively low strength and high specific properties:** Low-strength foams made from elastomeric polymer are important in cushioning applications, for example in helmets as presented in Figure 1-1b, also in seating, automotive interiors, furniture, training shoes, etc. their flexibility and elastomeric nature is useful in distributing loads across wider areas.
- **Thermal insulation:** Low thermal conductivity of non-metallic forms is beneficial for thermal insulation applications, for example in insulating frozen food, modern buildings and pipes as shown in Figure 1-1c.
- **Buoyancy:** One of the important physical behaviours of closed-cell foams is their high resistance to water absorption. Combined with their low density this behaviour makes closed-cell foams attractive for floating applications such as life jackets, boats, toys, etc., see Figure 1-1d.
- **High porosity of open-cell foams:** The microstructure of open-cell foams offers many applications such as filters for air, gas, water as presented in Figure 1-1e.
- **Rough surface:** This property gives foams a high-coefficient of friction; thus, they can be applied in non-slip surfaces for floors, furniture, etc. see Figure 1-1f.
- **Modifiable mechanical properties and density:** The mechanical properties of foams depend on their density and microstructure both of which are determined by the manufacturing process, which can vary. So, the strength of foams can be controlled, making them ideal in many applications, such as composite structures used in aircraft structures. Hence, the mechanical response of foams under different rates of loading, as

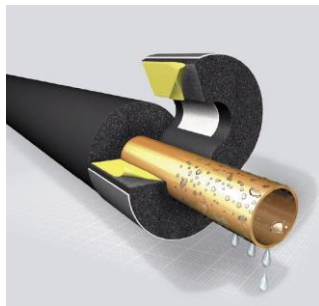
well as their bulk properties and type of manufacturing process, must be considered in designing products based on foams.



(a) packaging [5]



(b) cushioning (helmet cross section)[6]



(c) thermal insulation [7]



(d) buoyancy [8]



(e) water filter [9]



(f) non-slip surface [10]

Figure 1-1. Applications of foam.

## 1.2. Manufacture of Foams

Synthetic foam can be made out of plastics, metals, glasses, ceramics, composites, etc. The different constituent material is one of the determining factors in choosing which manufacturing methods can be used to produce the foam. Some gas-expanded foams are made by mixing in a chemical foaming agent which reacts to form a gas. Here the mixture

is injected into a cavity during the foaming process, allowing the mixture to inflate in-situ as bubbles expand internally. Others are made by injecting gas into hot molten fluids, bubbles expand and are trapped when the material cools and solidifies [1]. Consequently, foams can be made by direct injection of gas into hot polymer or liquid metal, which are then solidified by cooling. Also, various indirect methods involve casting or the use of powder compacts which contain blowing agents [11]. In practice, it is found that the mechanical properties of foams are sensitive to their processing method. Hence, the choice of method also depends on the target properties of the foam.

Various methods are used for foaming polymers. These may be classified by several, such as direct and indirect foaming methods [12, 13]. The most general classification is based on the method by which cells are produced. There are two types of foaming agents [1]:

- 1- Physical blowing agents include those agents that produce cells as a result of a physical technique.
- 2- Chemical blowing agents include a mixture or individual compounds that liberate gas as a result of a chemical reaction.

There are many processes to produce polymer and metal foams, most of these methods result in some degree of anisotropy in the final material. Most of the time the manufacturing processes causes anisotropy in the cellular microstructure. The cells are often elongated in the direction of greatest expansion of the foam, referred to here as the principal direction. The stiffness in the principal and transverse directions are defined here as  $E_p$  and  $E_t$  respectively.  $\sigma_p$  and  $\sigma_t$  are the uniaxial yield stress in the principal and transverse directions. Examples of some the manufacture processes, and where possible, examples of the anisotropy ratio induced in the microstructure, the ratio between the  $E_p / E_t$  and  $\sigma_p / \sigma_t$  are shown in Table 1.1

Table 1.1. The manufacture process of foam,  $r$  cells shape anisotropy,  $E_p$ ,  $E_t$  elastic parameters in the principal and transverse directions respectively. The subscript  $p$  and  $t$  refer to principal and transverse directions respectively.

Process type	Material	$r$	$E_p / E_t$	$\sigma_p / \sigma_t$
Extrusion [14-16]	Low-density polyethylene foam	1.2	2.7	2.41
Slabstock [4, 17]	polyurethane foam	1.29	-	-
Pouring the polymer plus hardener and foaming agent into a mould [1, 3]	Flexible polyurethane foam	1.3	$\approx 1.8$	$\approx 1.09$
Melt foaming [18-20]	Al-Si alloy foams	1.4	$\approx 1.75$	$\approx 1.55$

where  $r$  is the cells anisotropy ratio, measured as the ratio between the largest and smallest cell dimension. Though the cells may even be temporarily significantly elongated during the manufacture process, i.e. during high, fast expansion in one direction, the cells speedily return to a more equalized shape to reduce some of their the anisotropy though some of the elongation in the microstructure remains [4, 21].

An important manufacturing route for closed-cell foams is direct gas-injection melt extrusion. This process is suitable for the manufacture of low-density foams e.g. 20 to 60 kg/m<sup>3</sup>. The extrusion and foaming process can have a significant effect on the microstructure and consequently on the mechanical response of the foam. This is because the flow field through the extruder, the gas expansion during the foaming process and the subsequent post-extrusion drawing of the foam can produce elongated cells along the direction of extrusion, and potentially, molecular orientation within the skeletal polymeric foam structure itself. The degree of anisotropy can be manipulated by controlling the process conditions. The large degree of anisotropy inherent in this particular manufacture process makes extruded foams an interesting candidate for the study of the relationship between micro-structural and macro-scale anisotropy.

### 1.2.1. Extrusion Process

In the extrusion method, foams are made by combining physical or chemical blowing agents, liquids or gases into a polymer melt. As shown in Figure 1-2, the gas is injected in the polymer melt in a screw extruder section, here the pressure from the extrusion process keeps the gas compressed in the melt. The die is designed to have a high pressure gradient to keep the gas compressed inside the die, preventing foaming. As the molten polymer exits the die, the decreasing melt pressure permits the gas to expand, creating a porous foam structure in the desired extruded shape. The density of extruded foam depends on the type and amount of blowing agent used and the melt temperature. Gas and liquid blowing agents added downstream within an extruder can reduce the final part density by about 90% or more. In LDPE the part density can be reduced from  $926 \text{ kg/m}^3$  to  $40 \text{ kg/m}^3$  [15, 16]. In practice, any thermoplastic polymer can be used to produce extruded foam. Harold et al. [22] showed the most common thermoplastic materials used include:

- Polystyrene
- Polyethylene
- Polypropylene
- Polyvinyl chloride

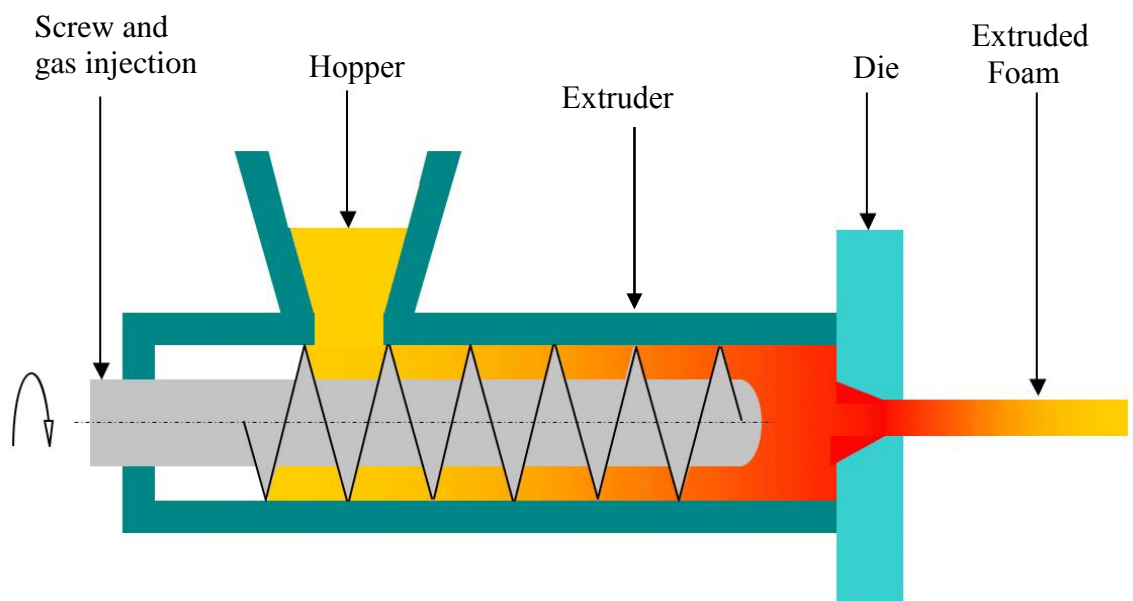


Figure 1-2. Simple schematic of the extrusion process [2].

## **1.2.2. Effects of Manufacture Method on Microstructure of Foams**

Many previous investigations have considered the link between manufacturing process and final microstructure of open- and closed-cell foams [1, 3, 4, 14, 18, 19, 23-25].

The microstructure is a key factor in determining the mechanical and physical properties of foams. Their bulk properties are dependent on both the shape and the dimensions of the cells within the foam microstructure. Numerous investigations [1, 3, 4, 14, 18, 19, 23-25] have noted the correlation between macro-scale structural anisotropy and the average cell shape inside the foams. In the next section an overview of the relationship between manufacturing process, the microstructure and the bulk properties of solid foams is given.

## **1.3. Influence of Foam Microstructure on Mechanical Properties**

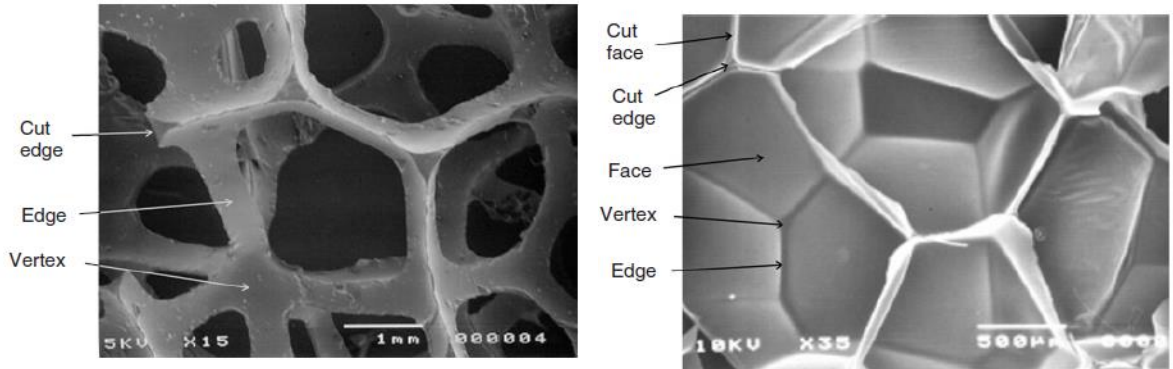
In order to identify the relationship between the microstructural morphology and mechanical properties of foams, it is first necessary to characterise the internal microstructure. In reviewing the extensive body of literature on this topic, the books of both Gibson and Ashby [1] and Mills [4] discuss how various micro-structural parameters influence the relationship between microstructure and macro-scale mechanical behaviour. In the following section, these parameters are listed and their influence is briefly outlined.

- Open or closed-cell structure
- Relative density
- Cell size

### **1.3.1. Cell Structure: Open- or Closed-cell**

According to the foam's internal microstructural morphology, foams be classified as open- or closed-cell foams. The important difference between these two types of foam is the lack of membranes in open-cell foam [4] (see Figure 1-3). Open- and closed-cell foams have very different mechanical behaviours. Open-cell foams do not trap gas within the cells, so the gas pressure does not significantly affect their mechanical response. The importance of

this effect depends on the composition of the foam. The influence of internal gas pressure on strong, rigid materials is relatively much less important than on more compliant flexible foams.



(a) open-cell foam with a density of  $28\text{kg/m}^3$ .

(b) Closed-cell LDPE foam with a density of  $24\text{kg/m}^3$ .

Figure 1-3. SEM photographs of polyurethane foam from [4].

### 1.3.2. Relative Density

One of the most important properties for a given type of foam is its relative density,  $R$ , defined as the foam density,  $\rho$ , divided by the density of the solid constituent material,  $\rho_s$ . Based on the volumetric fraction of the solid phase, foams are usually classed as either high or low-density foams. Mills [4] considered foams with a relative density of less than 0.1 to be low-density foams. Increasing relative density increases both cell wall and edge thickness and consequently leads to an increase in the foam's stiffness and a reduction in the porosity of the foam.

### 1.3.3. Cell Size and Distribution

The average cell size and the distribution of cell sizes are other significant factors affecting the mechanical response of foams. Many investigations draw different conclusions about this issue. For instance, Morgan et al. [26] and Cao et al. [27] observed that smaller cell sizes produced stronger foams, with strength changing as a function of the inverse square root of the cell diameter in a closed-cell glass foam. However, Hagi et al. [28] found that increasing the cell size makes open-cell alumina foams stiffer. Recently, Mills [4] and

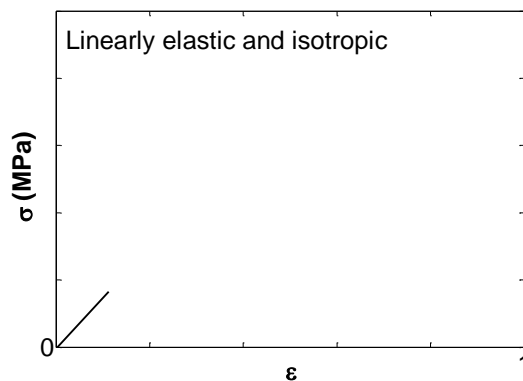
Mills and Gilchrist [29] concluded that cell size affects the gas diffusion coefficient in closed-cell foams and increasing cell size increases gas diffusion, thus affecting the shape of the creep-time curve during high strain creep. Consequently, cell size affects the air flow resistance of open-cell foams; this affects the form of the stress-strain curve.

## 1.4. Mechanical Response of Foams under Compressive Loading

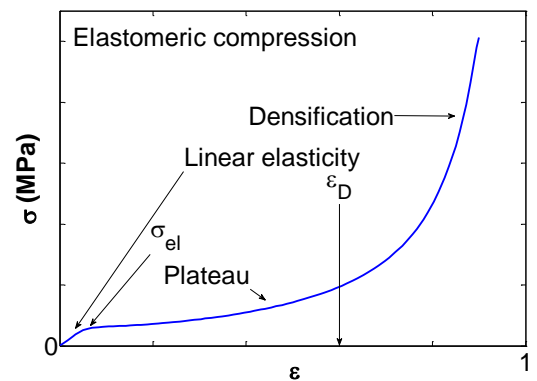
As touched upon previously, foams have a wide range of mechanical applications, and are often used under conditions involving compressive loading. For this reason, the response of foams under compression is often used to classify the generic response of the foam. The mechanical response of most foam can be described as compressible and one of:

- Linear elastic and isotropic
- Non-linear elastic and isotropic
- Linear elastic and transversely isotropic
- Non-linear elastic and transversely isotropic
- Elastic-plastic
- Elastic-brittle
- Visco-elastic

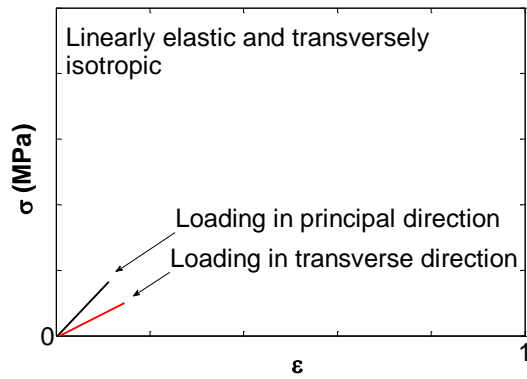
Typical loading curves corresponding to these generic behaviours are shown in Figure 1-4



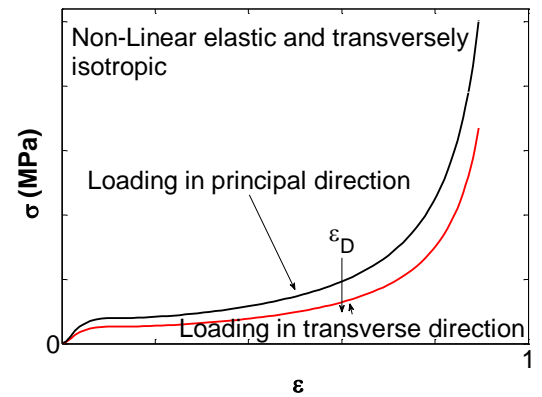
(a) Linearly elastic and isotropic response.



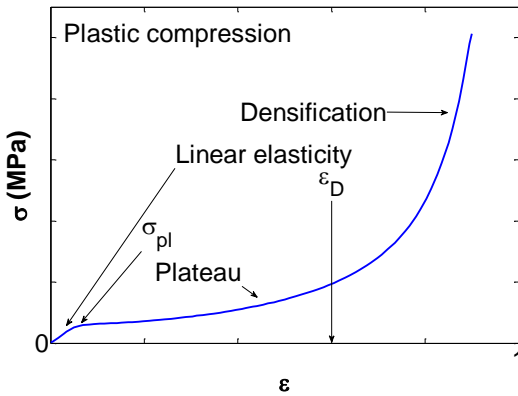
(b) Elastic and non-linearly isotropic response.



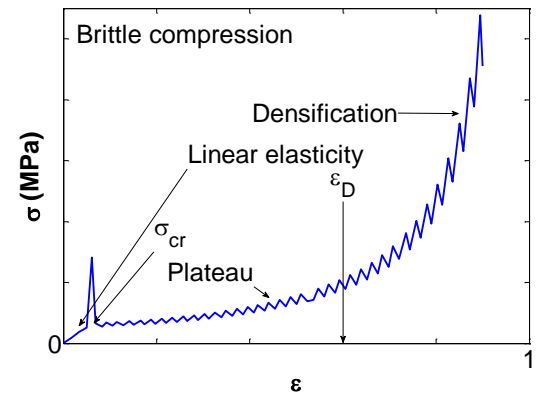
(c) Linearly elastic and transversely isotropic response.



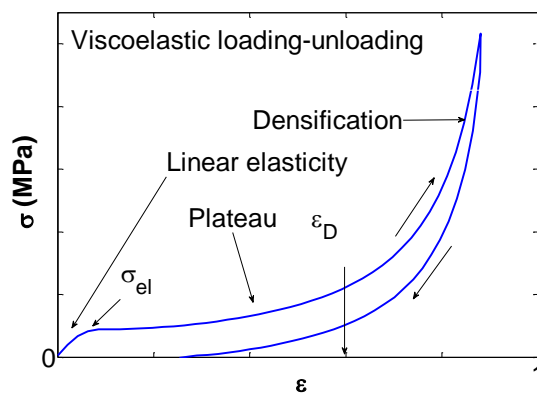
(d) Non-linear elastic and transversely isotropic response.



(e) Isotropic and elastic-plastic response.



(f) Elastic-brittle response.



(g) Visco-elastic response.

Figure 1-4. Compressive stress-strain curves.

### **1.4.1. Linear Elastic and Isotropic Foam**

The linear elastic response shown in Figure 1-4a can be characterised using two elastic parameters: the modulus of elasticity and Poisson's ratio [30, 31]. At low strains foams typically follow a linear elastic behaviour. At high compressive strains, a different deformation response can occur in different types of foam materials, leading to different stress-strain curves. For isotropic foams the mechanical response is the same in all directions though as discussed, the mechanical properties of most foam materials do have at least some degree of directional dependence.

### **1.4.2. Non-linear Elastic and Isotropic Foam**

The non-linear elastic behaviour of most foam materials is partially due to deformation of the microstructural geometry at high compressive strains. These foams are classified into non-linear elastic materials with flexible and recoverable behaviour, as shown in Figure 1-4b. They can be modelled using hyperelasticity theory, which means the stress-strain response can be predicted from a strain energy function [32-35].

### **1.4.3. Linear Elastic and Transversely Isotropic Foam**

As discussed previously, most foaming processes cause some elongation of cells. Hence, the stress-strain behaviour is a function of the direction of the applied stress (e.g. parallel, normal or oblique to the direction of extrusion) (see Figure 1-4c). Such materials require more elastic parameters to describe their mechanical response than do isotropic materials. Materials with a transversely isotropic response have five independent engineering elastic constants: two Poisson's ratios, two modulus of elasticity and a shear modulus. For example, the linear transversely isotropic model has been used by Isaac and Ori [36] and Tagarielli et al. [37] to model the behaviour of composite materials and balsa wood respectively.

### **1.4.4. Non-linear Elastic and Transversely Isotropic Foam**

In recent years, there has been increasing interest in the study of non-linear elastic transversely isotropic materials. This class of material can be analysed by considering

more advanced non-linear theory. The investigation of non-linear elastic transversely isotropic foams is rather new. Weiss et al. [38] presented a model for incompressible transversely isotropic material and Tagarielli et al. [37] proposed a model for plastic transversely isotropic material. Jebur et al. [15, 16] proposed a simple method of calculating the uniaxial compressive stress in foams subjected to a compression load at an specified angle to the material's principal direction, see for example, Figure 1-4d. [16].

### **1.4.5. Elastic-Plastic Foam**

If plastic foams are subjected to stresses higher than the yield stress, further deformation is permanent and does not recover when the compressive stress is removed because of plastic deformation or fracture of the constituent material. Plastic foams are often made out of rigid polymers or metals such as closed-cell aluminium foams [1, 39, 40]. Figure 1-4e shows the stress-strain curve for plastic foam under uniaxial compression.

### **1.4.6. Elastic-Brittle Foam**

The typical stress-strain curve for elastic-brittle foam is shown in Figure 1-4f. At low strain, brittle foam shows a steep increase in compressive stress due to the high strength of the material in the elastic region. The material then yields at the end of the elastic region and then the stress-strain curve dramatically decreases with a non-linear behaviour. This class of foam includes glass foams, ceramic foams and foams made out of brittle polymer or other brittle materials. Experimental data for the crushing of these kinds of foams have been measured and analysed by, for example, Rusch [41] and Gibson and Ashby [1].

### **1.4.7. Visco-Elastic Foam**

Most polymer foams show some degree of viscoelastic behaviour [4, 34, 42]. For example, flexible foams exhibit a hysteresis response upon unloading, as shown in Figure 1-4g. The stress-strain data of unloading is lower than during loading, indicating absorbed energy in the loading-unloading cycle. The term viscoelastic means a combination of both viscous and elastic response under loading. The viscoelastic response can be classified into linear and non-linear behaviour. Linear viscoelastic response can be modelled using linear

equations, with mechanical analysis based on linear springs and Newtonian viscous dampers. Non-linear viscoelastic behaviour can be modelled using constitutive equations containing a higher order power of the engineering variables.

As mentioned above, several factors affect the mechanical properties of foam including the type of solid material in the foam and microstructure of the foam (see Section 2.2). Strain rate can have an important effect on stress-strain response for various reasons, though for polymer foam this is mostly attributable to the viscoelastic nature of the constituent material. Song et al. [43] noted that as the strain rate is increased the yield stress increases linearly with the natural logarithm of strain rate in uniaxial compression tests. Figure 1-5 illustrates the effects of strain rates on the stress-strain curve. Figure 1-4 (b, d, e, f and g) and Figure 1-5 show the schematic compressive stress-strain curves for foams. They share some similar mechanical characteristics, i.e. linear elasticity in the small strain region (<5% strain), followed by a long plateau region ending in a densification region, where the stress rises dramatically. These mechanical characteristics are different from those of common solid materials such as metals, which normally do not have a long relatively low stress plateau region under compression. The plateau region allows foams to exert a nearly constant reaction stress under compression, up to very high strains. This characteristic is important for the design of both protective and cushioning applications. In crash events, the plateau region provides protection by absorbing kinetic energy without transmitting high stresses and accelerations. For cushioning applications for example a car seat, foams provide good vibration damping and this contributes to ride comfort.

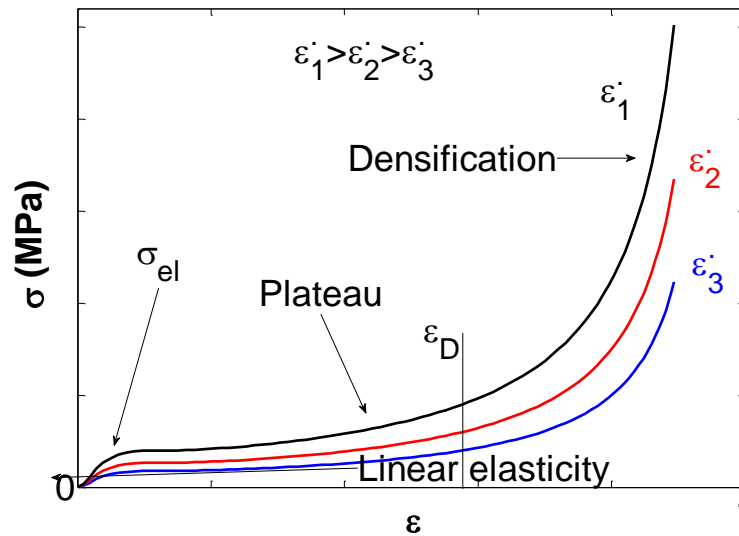


Figure 1-5. Compressive stress-strain curves at varies strain rates.

## 1.5. Objectives

The main goal of this work is to examine the current state of the art in terms of characterising and modelling the mechanical behaviour of polymeric foams. Particular attention is paid to transversely isotropic foams subject to large compressive strains. Possible approaches to enhance existing models are explored. Sub tasks of this work are to:

- Characterise the mechanical properties of transversely isotropic foam. This detailed experimental dataset will provide a benchmark with which to explore the utility of the various different modelling approaches.
- Examine the current state of the art in terms of macro-scale modelling of foams. This work does not aim to develop a new constitutive model but rather the goal is to examine the accuracy of existing macro-scale constitutive relations in modelling these materials.
- Analyse the microstructure of the chosen benchmark foam and relate this microstructure to macroscopic mechanical behaviour, using existing analytical and numerical microstructural elastic models. This work evaluates the utility of these models and routes for further enhancement are suggested the microstructural work will

demonstrate the degree of anisotropy that can be expected from a typical extrusion-based foaming process.

- Examine the use of a simple viscoelastic gas-based constitutive model to introduce the effects of strain rate on the mechanical behaviour of the benchmark foam. Here it will be shown how the relationship between specimen size and mechanical response can be predicted by determining the gas diffusion coefficient of closed-cell foams subject to compressive loading.

## 1.6. Outline

The remainder of this thesis is structured as follows:

**Chapter 2: Literature Review.** This chapter is a detailed survey of relevant literature, covering background theories and examining the context of the research in relation to the mechanical response of foams and the various methods of mechanical characterisation.

**Chapter 3: Experimental Characterisation of a Transversely Isotropic Polymer Foam.** This chapter presents experimental testing and macro-scale modelling of a representative benchmark foam; a melt-extruded Low Density Polyethylene (LDPE) foam. The experimental setup is presented in Section 3.1. Material characterization and macro-scale modelling and the effects of strain rate on the elastic yield stress are proposed in Section 3.3 and are presented in Section 3.2. The methods available for geometric characterisation of the microstructure are described in Section 3.3.

**Chapter 4: Macro-Mechanical Modelling of Foam.** This chapter shows methods of interpolating between measured data from a smaller dataset and of calculating the data using simple analytical models are explored. A modified method for modelling transversely isotropic material is presented in Section 4.2. The effects of strain rate on the elastic yield stress are proposed in Section 4.3. The specimen size effect on mechanical properties of closed-cell foams is presented in Section 4.4. The aim of this research is to predict the stress-strain curves as a function of specimen size and thereby account for the influence of test specimen dimensions when estimating the true bulk response of the foam. The constitutive models currently implemented in a Commercial FEA Software are presented in Section 4.5.

**Chapter 5: Modelling of Transversely Isotropic Closed-cell Foam using a Micro to Macromechanics Approach.** This chapter explains the relationship between the foam's microstructure and its mechanical response. A closed-cell foam model is created in Section 5.2. Analytical and numerical analyses are performed to calculate the linear elastic and elastic yield stress for isotropic and transversely isotropic foam. In Section 5.3 analytical analysis is used to calculate the non-linear elastic response during compression. Stress-strain curves for isotropic and transversely isotropic foams are predicted from the microstructure and Section 5.4 compares experimental and predicted data.

**Chapter 6: Conclusions and Recommendations for Future Work** of this thesis are summarised.

## **Chapter 2. Literature review**

Polymeric foams are widely used in various areas due to their unique mechanical behaviour, such as for packaging, impact energy absorption and cushioning [1, 4]. Mechanical modelling and experimental testing approaches have been developed to model both isotropic and transversely isotropic foams. In this chapter, the relevant literature is reviewed. The main goal of this Chapter is to describe current experimental testing techniques and give an overview of both macro and micro-scale modelling approaches for foam materials. In particular, a goal is to highlight how previous studies have aimed to use the foam's properties such as relative density, microstructure and the nature of the foam's solid constituent material in order to predict the mechanical response of the foam

The content of this chapter is structured into the following sections in this order: modelling of foam behaviour and experimental investigations, macro-scale and then micro-scale modelling.

### **2.1 Modelling of Foam Behaviour**

The content of this section is organised into linear (small strain) and non-linear (large strain) models. Both of these strain regimes are important when considering the mechanical behaviour of foams. Work relating to elastic, viscous and plastic behaviours are considered, together with various combinations of these behaviours (e.g. visco-elastic or elastic-plastic), in the small and large strain sections. In order to limit the scope of this review, attention is focused primarily on research relevant to the understanding of polymer foams.

#### **2.1.1 Linear or Small Strain Models**

The linear elastic model is the simplest model of elasticity. It can be used to describe the isotropic, transversely isotropic and orthotropic response of materials and it is valid for small elastic strains only.

### 2.1.1.1 Linear Elastic Isotropic Compressible Model

A material is isotropic when its mechanical properties are the same in all directions [44]. The simplest case of linear elasticity is the isotropic case. The mechanical response is fully characterised by the Young's modulus,  $E$ , the Poisson's ratio,  $\nu$  and the shear modulus,  $G$ . The constitutive relation for a linear elastic material can be described as:

$$\begin{bmatrix} \varepsilon_1 \\ \varepsilon_2 \\ \gamma_3 \end{bmatrix} = \begin{bmatrix} \frac{1}{E} & -\frac{\nu}{E} & 0 \\ -\frac{\nu}{E} & \frac{1}{E} & 0 \\ 0 & 0 & \frac{1}{G} \end{bmatrix} \begin{bmatrix} \sigma_1 \\ \sigma_2 \\ \tau_3 \end{bmatrix} \quad (2-1)$$

here  $G$  can be determined from these two independent constants using

$$G = \frac{E}{2(1+\nu)} \quad (2-2)$$

### 2.1.1.2 Linear Elastic, Transversely Isotropic Compressible Model

An orthotropic material is transversely isotropic when one of the principal planes is isotropic, i.e. at every point there is a plane in which the mechanical parameters are the same in any direction in that plane [36, 45]. Many unidirectional materials, such as unidirectional composites materials with aligned fibres can be assumed to be transversely isotropic, with the 2-3 plane (normal to the fibres direction) as the plane of uniformity as shown in Figure 2-1. The constitutive relationship of linear elastic transversely isotropic materials can be written as:

## CHAPTER 2 LITERATURE REVIEW

$$\begin{bmatrix} \varepsilon_{11} \\ \varepsilon_{22} \\ \varepsilon_{33} \\ \gamma_{12} \\ \gamma_{13} \\ \gamma_{23} \end{bmatrix} = \begin{bmatrix} \frac{1}{E_1} & -\frac{\nu_{21}}{E_2} & -\frac{\nu_{31}}{E_3} & 0 & 0 & 0 \\ -\frac{\nu_{12}}{E_1} & \frac{1}{E_2} & -\frac{\nu_{32}}{E_3} & 0 & 0 & 0 \\ -\frac{\nu_{13}}{E_1} & -\frac{\nu_{23}}{E_2} & \frac{1}{E_3} & 0 & 0 & 0 \\ 0 & 0 & 0 & \frac{1}{G_{12}} & 0 & 0 \\ 0 & 0 & 0 & 0 & \frac{1}{G_{13}} & 0 \\ 0 & 0 & 0 & 0 & 0 & \frac{1}{G_{23}} \end{bmatrix} \begin{bmatrix} \sigma_{11} \\ \sigma_{22} \\ \sigma_{33} \\ \sigma_{12} \\ \sigma_{13} \\ \sigma_{23} \end{bmatrix} \quad (2-3)$$

Here, five elastic constants are required for transversely isotropic materials, two moduli of elasticity corresponding to the stiffness in the principal and transverse directions,  $E_1$ ,  $E_2 = E_3$ , two Poisson's ratios defined as  $\nu_{12} = -\frac{\varepsilon_{22}}{\varepsilon_{11}}$  and  $\nu_{21} = -\frac{\varepsilon_{11}}{\varepsilon_{22}}$  for uniaxial compression in the principal and transverse directions and the shear modulus,  $G_{12}$ , in the principal direction, is as given in Equation (2-3),  $\nu_{12} = \nu_{13}$  are the Poisson's ratios when loaded in the principal direction,  $\nu_{21} = \nu_{31}$ , and  $\nu_{23}$  are the Poisson's ratios when loaded in the transverse direction and  $G_{12} = G_{13} \neq G_{23}$  are the shear moduli.

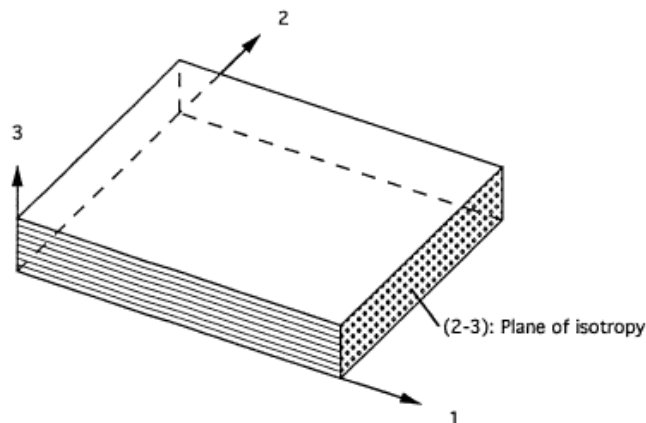


Figure 2-1. Orthotropic material with plane of transverse isotropy [36].

### 2.1.1.3 Linear Viscoelastic Model

Viscoelastic materials display both viscous and elastic behaviours. Most viscoelastic materials show linear or nearly linear response under small strains. Linear visco-elastic models composed of linear elements (springs and dashpots), are linearly elastic at small strains, but can also be used to model large strain behaviour, making them very useful. Sabah [46] developed a linear model of viscoelastic behaviour capable of providing a representation of the stress-strain response as a function of time this model has been applied in many subsequent viscoelastic analyses. One of the characteristic features of viscoelastic materials is the stress relaxation response, in which the material shows a time-dependent stress in response to an imposed constant strain.

The simplest viscoelastic models are the Maxwell and Voigt models, shown in Figure 2-2a and Figure 2-2b. Johnson et al. [47] used the Maxwell model to characterise the stress relaxation of rubber and Kim [48] used the Voigt model to describe the creep strain for polymer pipeline flows. However, the behaviour of most elastomeric and polymeric materials is too complicated to be accurately modelled with either of these simple models. Other combinations of linear viscoelastic models can also be used to approximate the response of polymer foams, such as the so-called Prony model (a number of Maxwell models in parallel to a single spring, see Figure 2-3. Mills [49] used a Prony series to model more complex behaviours of elastomeric foams. The Prony model is appropriate for modelling the macroscopic response of viscoelastic materials to a reasonable degree of accuracy, provided that enough Maxwell elements are used. Also, one feature of this model is that it is suitable for inter-conversion of the modulus and creep compliance function from the time-domain to the frequency-domain using Laplace transformation [46].

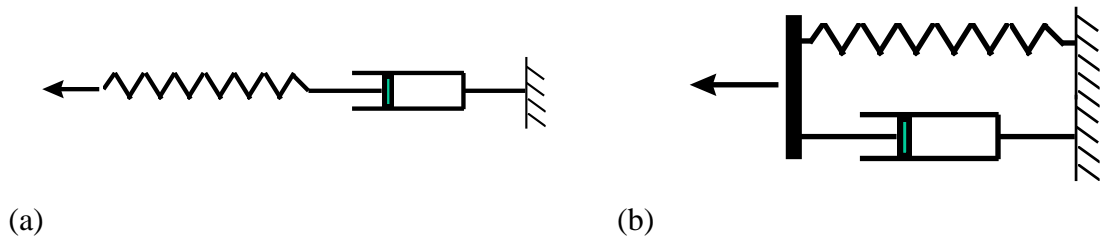


Figure 2-2. Two basic phenomenological models (a) Maxwell Model and (b) Voigt Model [50].

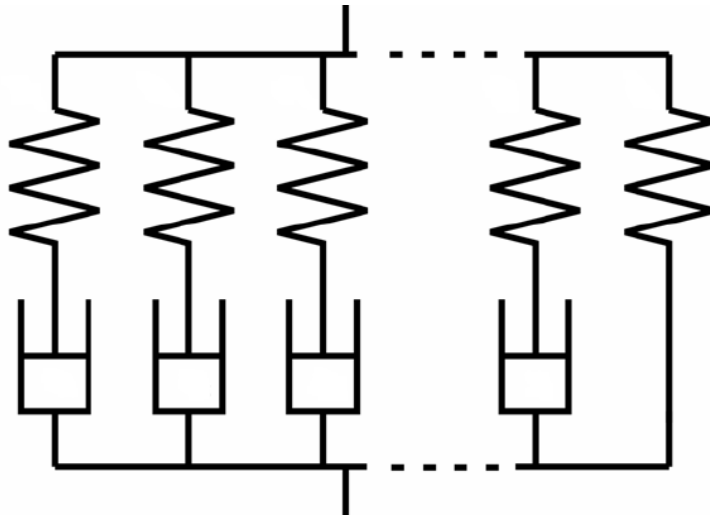


Figure 2-3. Prony model (a spring and dashpot in series) [49].

## 2.1.2 Large Strain Models

### 2.1.2.1 Isotropic Hyperelastic Behaviour

Hyperelastic models can be used to calculate the mechanical response for rubber-like elastomeric substances subjected to large deformations. Ogden [32] and Holzapfel [51] discuss how the most important assumption of a hyperelastic model is the existence of a strain energy density function, which is dependent only on the current state of strain. In hyperelasticity the energy density function is normally expressed in terms of the invariants of the finite strain tensor. The hyperelastic model is path independent, since the stored elastic energy at any point in the material is determined only by its current state of strain. A hyperelastic material is isotropic if the strain energy function can be represented as:

$$U_s = U_s(I_1, I_2, I_3) \quad (2-4)$$

## CHAPTER 2 LITERATURE REVIEW

where  $I_1, I_2$  and  $I_3$  are the principal strain invariants [51]. In terms of the principal extensions of the deformation  $\lambda_1, \lambda_2$  and  $\lambda_3$ , the principal strain invariants can be written as:

$$I_1 = \lambda_1^2 + \lambda_2^2 + \lambda_3^2 \quad (2-5)$$

$$I_2 = \lambda_1^2 \lambda_2^2 + \lambda_2^2 \lambda_3^2 + \lambda_1^2 \lambda_3^2 \quad (2-6)$$

$$I_3 = \lambda_1^2 \lambda_2^2 \lambda_3^2 \quad (2-7)$$

Many isotropic materials (such as rubber) can be deformed without a change in volume. Such materials are said to be incompressible. The incompressibility of this class of materials is characterized by  $J = 1$ , where

$$J = \lambda_1 \lambda_2 \lambda_3 \text{ is the volume change ratio } \lambda_i \text{ (} i = 1, 2, 3 \text{)} \quad (2-8)$$

Foam materials that can be subjected to compressive strains are called compressible materials. For this class of material, the volume ratio is  $J \neq 1$ . Several hyperelastic material models have been published [4, 32, 51]. Below is a brief review of some hyperelastic models used to describe isotropic compressible materials.

- **Neo-Hookean**

The Neo-Hookean model is the simplest hyperelastic model, the model was first suggested by Rivlin [52]. In this model the strain energy density is calculated from the integration of stress and strain in cases where the tangent moduli remain constant and isotropic. The equation below is a first order general equation which has been implemented in several commercial FEM software programs.

$$U_s = C_{m1}(I_s - 3) + \frac{1}{D_1}(J - 1)^2 \quad (2-9)$$

This model is ideal for isotropic compressible material under low strains. The constant  $C_{m1}$  characterises the initial shear modulus of the material and the constant,  $D_1$ , characterises the inverse of the initial bulk modulus.

- **Moony-Rivlin**

In order to improve the fitting to data, Rivlin [53] suggested a dependence of the strain energy function on both the first and second invariants. This model is more general than the neo-Hookean model. In this model the strain energy can be calculated using

## CHAPTER 2 LITERATURE REVIEW

$$U_s = C_{m1}(I_1 - 3) + \frac{1}{D_1}(J - 1)^2 + C_{m2}(I_2 - 3) \quad (2-10)$$

Clearly the Neo-Hookean model is a reduced form of the first-order Mooney Rivlin equation with  $C_{m2} = 0$ .

- **Ogden Model**

The Ogden model, as presented here, is suitable for highly compressible materials and defines the deformation of the hyperelastic material in terms of the principal stretches rather than the invariants of the deformation tensor. Therefore, implementation of the Ogden model requires the use of the eigenvectors in addition to the eigenvalues. Anisotropic response can develop along the principle directions; however, the model is still “isotropic” in the sense that the elastic response can be derived from the deformation tensor without regard to the reference state [32, 51]. Also, the non-integer exponential coefficients provide greater flexibility than polynomial forms in describing the nonlinear deviatoric response when  $N$  (the number of terms) is low. The implementation of higher order expansions permits comprehensive descriptions of polymeric response at high strains. A hyperfoam Ogden model can be expressed as:

$$U_s = \sum_{i=1}^N \frac{2\mu_i}{a_i^2} \left[ (\lambda_1^{a_i} + \lambda_2^{a_i} + \lambda_3^{a_i} - 3) + \frac{1}{\beta_i} (J^{-a_i\beta_i} - 1) \right] \quad (2-11)$$

where the coefficients  $\mu_i, a_i$  and  $\beta_i$  are material constants. The coefficients,  $\mu_i$ , are related to the initial shear modulus,  $\mu$ , in the reference configuration as

$$\mu = \sum_{i=1}^N \mu_i \quad (2-12)$$

The initial bulk modulus can also be computed as:

$$K = \sum_{i=1}^N 2\mu_i \left[ \frac{1}{3} + \beta_i \right] \quad (2-13)$$

In this algorithm, the coefficient,  $\beta_i$ , is related to a nominal Poisson’s ratio,  $\nu$ , by

$$\beta_i = \frac{\nu}{1 - 2\nu} \quad (2-14)$$

Numerous investigations have shown that isotropic elastic compressible foams can be modelled using a range of models of gradually increasing complexity, such as the Neo-

## CHAPTER 2 LITERATURE REVIEW

Hookean model used by Bardenhagen [54] and the Mooney-Rivlin model or Ogden's model for isotropic compressible rubber used by Ogden et al. [33, 55] and Widdle et al. [34, 56].

### 2.1.2.2 Hypoelasticity

Hypoelasticity generally refers to constitutive equations in rate form e.g. Zhou et al. [57] and Xiao et al. [58]. This differs from the hyperelastic method in that a unique governing strain energy potential is not recognised, and often, does not exist. Hence, unlike the hyperelastic model, the hypoelastic model can be path dependent and can violate the laws of thermodynamics. Consequently, the hypoelastic form, as shown below, is a more general description of a constitutive response

$$\sigma^{O*} = H^* : D, \quad (2-15)$$

where  $\sigma_c$  and  $D$  are the Cauchy stress tensor and the stretching tensor respectively,  $\sigma^{O*}$  is an objective stress rate, and  $H^* = H^*(\sigma)$ , is the hypo-elastic tensor, a fourth order tensor depending on the stress,  $\sigma$ .

### 2.1.2.3 Transversely Isotropic Hyperelastic Incompressible

#### Behaviour

Transversely isotropic incompressible hyperelastic models have been proposed for aligned fibre reinforced elastomers and biological materials[38, 59-61]; the high water content of which means the incompressibility condition advocated by Jemiolo et al. [62] is appropriate. Zhurov et al. [63, 64] developed a transversely isotropic compressible visco-hyperelastic model in order to predict the behaviour of the periodontal ligament under large deformations. However, Guo et al. [61] showed that the predictions of this model are valid only for weakly compressible or weakly anisotropic behaviour. The model is not appropriate when considering a highly compressible and anisotropic material such as certain polymer foams. This is because of the decomposition of the strain energy into decoupled volumetric and isochoric contributions see Equation (2-16). In this case, the volumetric contribution depends solely on the determinant of the deformation gradient tensor with no dependence on the anisotropy of the material, which means that a

## CHAPTER 2 LITERATURE REVIEW

hydrostatic stress state is predicted during the application of a hydrostatic strain [63], see below Equation (2-16)

$$W_h = W_{Vol} + W_{Iso}^e + W_{Iso}^V \quad (2-16)$$

The subscripts ‘*Vol*’, ‘*Iso*’, ‘*e*’ and ‘*V*’ denote the volumetric, isotropic, elastic and viscoelastic terms, respectively.

### 2.1.2.4 Elastic-Plastic Transversely Isotropic Model

Most authors use elastic properties and the initial yield surface to calculate transversely isotropic behaviour for plastic materials. Thus to create a model for transversely isotropic compressible materials under large strain, a linear elastic/plastic approach has been developed by Tagarielli et al. [37] for balsa wood. Beyond small strains, the deformation was modelled as irreversible which is appropriate for balsa wood. Also, the aluminium alloy foams used by Deshpande and Fleck [65] and the square-honeycomb [66] show transversely isotropic responses.

Moreu et al. [2], Mills et al. [67] and Gilchrist et al. [68] have used the crushable foam model, see Equation (2-17), and have compared its mechanical behaviour with that of low density polystyrene (PS) foam. However, elastic-plastic models are not suitable for describing the recovery of predominantly viscoelastic materials and are therefore not suitable for many types of polymeric foam. The von Mises stress depends on the hydrostatic loading as

$$\left( p - 0.5(p_c - p_t)^2 \right) + \left( \frac{a\sigma_e}{b} \right)^2 = a^2 \quad (2-17)$$

The terms  $\sigma_e$ ,  $p$ ,  $p_c$ ,  $p_t$  are the von Mises stress, hydrostatic loading, initial yield stress in hydrostatic compression and yield stress in hydrostatic tension respectively. Also,  $a$  and  $b$  are material parameters.

### 2.1.2.5 Hyper-Viscoelasticity

In recent years, there has been a considerable amount of development in hyper-viscoelastic models. Lubliner [69] presented the general approach of incorporating viscoelasticity within a hyperelastic framework. Here the free energy function is additively separated into

## CHAPTER 2 LITERATURE REVIEW

equilibrium and non-equilibrium parts. Both a Voigt model and a Maxwell model (see Section 2.1.1.3 ) were used to model relaxation and the author's concluded that the Maxwell model is better since it is readily expanded for multiple relaxations. After Lubliner [69], Holzapfel [51] and other researchers developed specific viscoelastic models using this approach. Such a model is available in Abaqus<sup>TM</sup>, a commercial finite elements software package. The technique of the FEM has been used by Li et al. [70] to describe the nonlinear behaviour of foam used in indentation tests. Similarly, Mills et al. [49, 71] used this method to analyse the mechanical response of foam used as protective cushioning.

### **2.2 Micro-scale Modelling**

In previous investigations [1, 4, 72-78], both analytical and numerical micro-scale models for polymer foams have been devised in order to develop constitutive models to describe the relationship between the mechanical properties of flexible and rigid foams and their micro-structure, including information such as cell size and shape, relative density and the mechanical response of the constituent polymer. This method is useful in relating the compression experienced by cell walls and edges to the general bulk deformation of polymer foams. In so doing, such micro-models can predict stiffness and can also describe how failure occurs within the microstructure by buckling, elastic deformation and yielding. When regular models, such as the Kelvin foam model, see Section 2.2.1.1, are used to analyse a specific type of loading, a representative unit cell (RUC) is required. The deformation mechanisms of these models are repeated periodically at the boundaries. Also, the RUC technique is very useful for predicting small and large deformation mechanisms and can be applied in both analytical and numerical analyses. In contrast, when irregular stochastic models such as the Voronoi model (see Section 2.2.2.5) are used in calculating the mechanical properties of foam, it is necessary to use the concept of a representative volume element (RVE) and again a periodic boundary condition has to be applied.

The simple cubic and cuboid open-cell models shown in Figure 2-4a and Figure 2-4b were suggested by Gibson and Ashby [1]. The elastic behaviour of the unit cell during uniaxial compression is governed by bending of the edges and the yielding behaviour is governed by buckling of the edges. The cross-section of the edges is usually considered as a square to simplify the subsequent analysis. The advantage of the Gibson and Ashby model is that

## CHAPTER 2 LITERATURE REVIEW

it is reliable and simple. While this model geometry is quite different from the actual random cellular geometry of random foams, which is irregular, it can nevertheless produce useful predictions in the small strain regime. The limitation of the cubic and cuboid models is that they cannot produce accurate predictions beyond the yield stress of the foam.

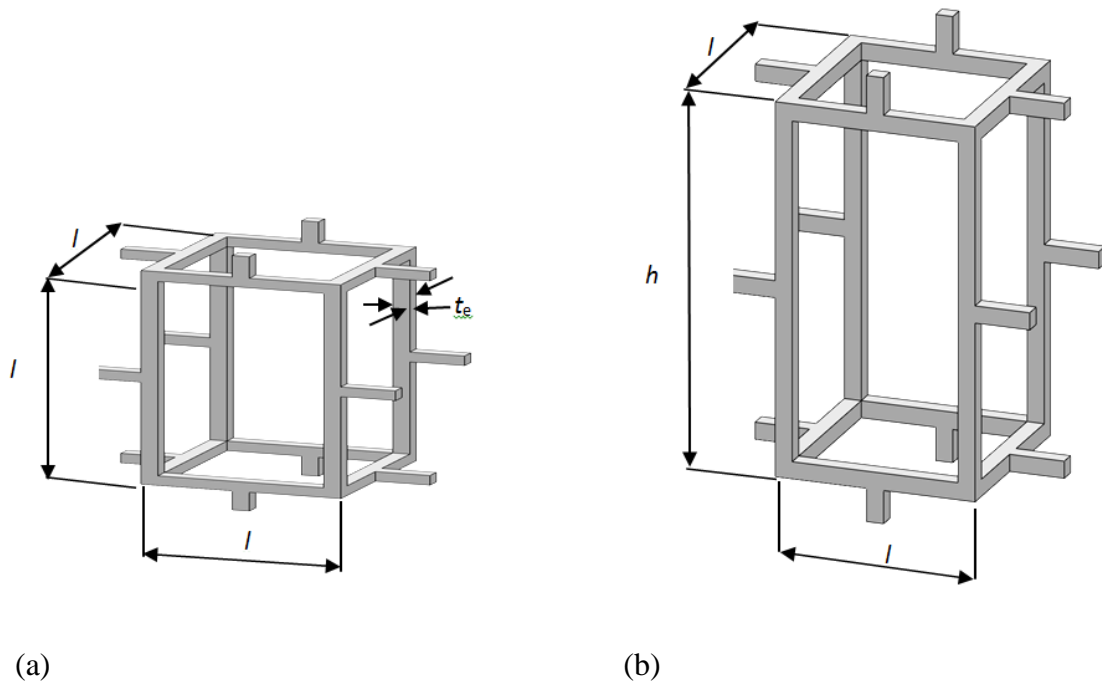
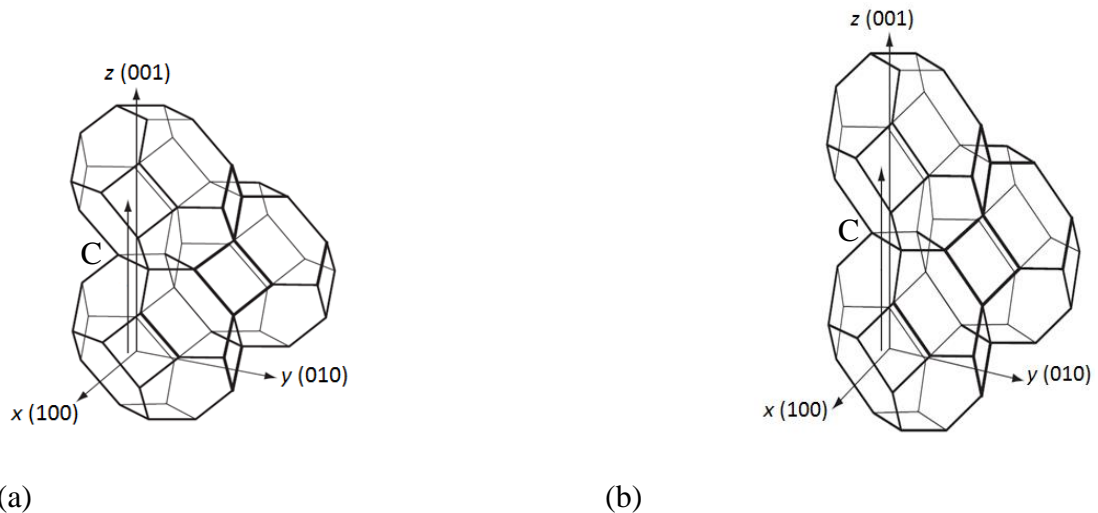


Figure 2-4. (a) A cubic cell model for isotropic open-cell foam showing the edge length  $l$ , the edge thickness,  $t_e$ , (b) cuboid model for anisotropic open-cell foam showing the edge lengths  $l$  and  $h$  [1].

Prior to the development of the cubic repeat unit cell model, Thomas [4] (Lord Kelvin, 1887) suggested the ‘Kelvin’ model consisting of a lattice of tetrakaidecahedra used to represent the foam (see Figure 2-5). It consists of 8 non-planar hexagonal surfaces and 6 planar quadrilateral surfaces, all with bowed edges, while the interface angles between edges at the vertices is  $109.5^\circ$ . Mills [4] presented the use of a modified form of Lord Kelvin’s tetrakaidecahedra cells. The modified model as shown in Figure 2-5a has uniform inter-edges and the interface angles are either  $90^\circ$  or  $120^\circ$ . The edges lengths,  $l$ , are jointed with two hexagonal faces to a square face. Further, an elongated modified Kelvin model as shown in Figure 2-5b was proposed by Dement’ev and Tarakanov [79] to predict the mechanical response of anisotropic foams. The relative density of the closed-cell Kelvin

## CHAPTER 2 LITERATURE REVIEW

model can be calculated from the edges and face dimensions. The shape of this model conforms more closely to the shape of actual foam cells than does the Gibson and Ashby model.



(a) (b)  
Figure 2-5. Body centred cubic (BCC) packing of 14-sided cells in the Kelvin foam (a) regular Kelvin model, and (b) elongated Kelvin model.

Stochastic microstructural RVE models can be generated using a variety of techniques, such as Voronoi tessellation which can be useful for understanding and characterising the mechanical properties of cellular structures. The Voronoi technique provides a better representation of the microstructure of real foams than either the Kelvin or cubic models. However, the analysis of these models can be computationally expensive and complicated. Figure 2-6a, and Figure 2-6b show examples of 2-D and 3-D Voronoi cell models.

Model microstructures describing various types of microstructural models that have been used, include: cubic, cuboid, Kelvin, modified Kelvin, Voronoi and annealed Voronoi, etc.

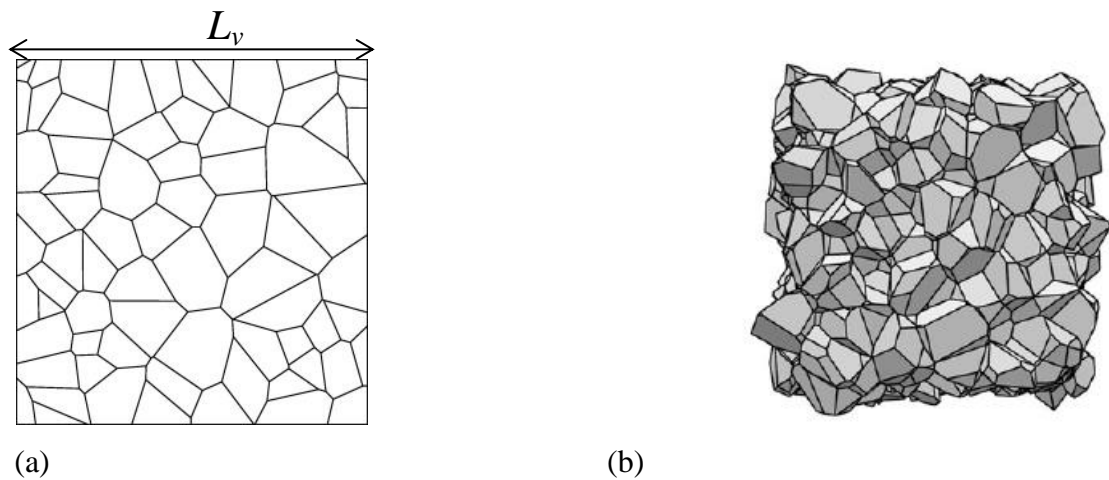


Figure 2-6. Irregular microstructure models (a) 2-D Voronoi construction for cells inside a square box and (b) 3-D Voronoi model of a closed-cell dry foam with 512 cells [4].

## 2.2.1 Small Strain Modelling

### 2.2.1.1. Analytical Models for Small Strains

Over the last 40 years many researchers have attempted to develop analytical models. Examples include those developed by Dement'ev and Tarakanov [79], Kraynik and Warren [72] and Zhu et al. [73, 80]. Gibson and Ashby [1] employed analytical models such as the cube, cuboid and Kelvin model. In general, the analysis of micro-scale models is performed by considering the unit-cell response. The mechanics of deformation of the regular unit cell leads to a set of equations for calculating the modulus of elasticity, yield stress and shear modulus of the foam and for determining the non-linearity of the stress-strain relationship. The variation of these properties can be related to microstructural geometry, the relative density, and the stiffness of the solid material.

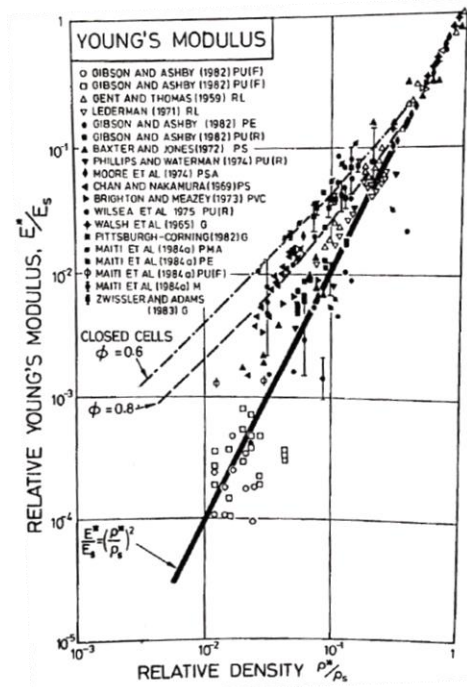
Simplified unit cell models (see Figure 2-4) based on open cubic cells have been investigated by Gibson et al. [74], Triantafillou [81] and Maiti et al. [82] in order to characterise the mechanical response of open-cell foams. Using such models Gibson and Ashby [1] concluded that the bending of cell edges provides the main resistance to deformation at small compressive strains. Also, Gibson and Ashby's analytical model can be used to accurately estimate the elastic moduli and yield stress for isotropic foams (see Figure 2-4). Further, the cubic model was enhanced [1] into a cuboid model (stretched along one of the principle axis) in order to characterise the relationship between the anisotropy of the foam's microstructure and the macro-mechanical response such as its

## CHAPTER 2 LITERATURE REVIEW

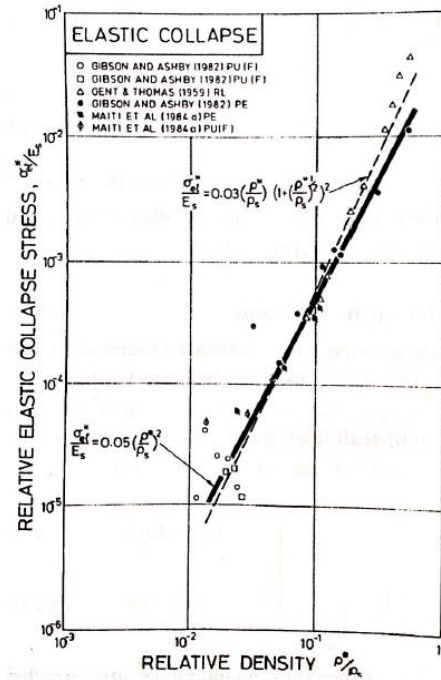
Young's modulus. The cubic model can be analysed for both elastic and plastic behaviours [1] Gibson and Ashby found this model was more sensitive to the anisotropy ratio (the ratio between the major and minor axis of the unit cell) for plastic foams than for elastic foams. Mu and Yao [18] used the Gibson and Ashby model to investigate the effects of various cell anisotropy ratios on the compressive response of closed-cell Al-Si alloy foams and found that the modulus of elasticity is more sensitive to cell shape than is the yield stress. The cuboid model has also been used to predict Young's modulus, fracture toughness, yield stress and plastic collapse of anisotropic flexible and rigid polyurethane foams by Huber and Gibson [3] who compared experimental against predicted results and observed that the cuboid model describes anisotropy well.

Mu et al. [18] used the Gibson and Ashby model to calculate the energy absorption and plastic collapse stress for anisotropic closed-cell Al-Si foam. Results showed that the energy absorption and plastic collapse stress in the principal direction were higher than in the transverse direction over a range of foam densities. Mu et al. [18] also developed a mathematical power law equation relating the plastic collapse stress and energy absorption property with the foam's relative density. Most of the cubic models suggested for open- or closed-cell foams are capable of relating the small strain mechanical properties to relative density and the properties of the solid constituent material.

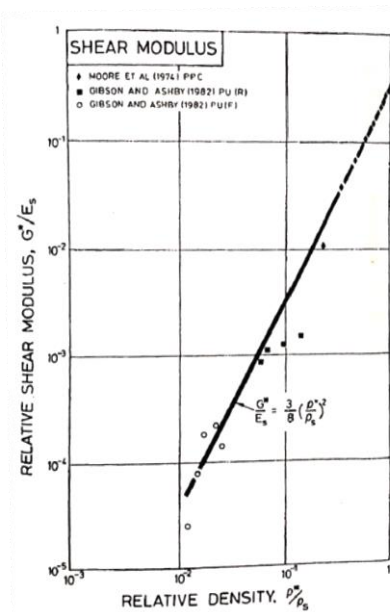
CHAPTER 2 LITERATURE REVIEW



(a)



(b)



(c)

Figure 2-7. (a) Data for relative Young's modulus of foams plotted against relative density. The solid line represents the theory for open-cell foams. The two dashed lines represent the theory for close-cell foams, (b) data for the elastic collapse stress for foams, normalized by the solid modulus, the solid line represent the theory for open-cell foams, the dashed line that for closed-cells, (c) data for the relative shear modulus foams, plotted against relative density, the solid data represent the theory for open-cell foams [1].

## CHAPTER 2 LITERATURE REVIEW

Analytical solutions of the Kelvin foam model with 14 faces, as presented in Figure 2-5a and Figure 2-5b, have been used by many investigators such as Dement'ev and Tarakanov [79], Zhu and Mills [80] and Kraynik and Warren [72] who developed analytical equations to define the elastic mechanical behaviour of isotropic, anisotropic, open- and closed-cell foams. Dement'ev and Tarakanov [79] were the first to predict the  $E_{100}$  modulus of elasticity of a Kelvin foam model for the (001) compression direction, where a square cross-section of the edges was assumed, using the below equation

$$\frac{E_{100}}{E_s} = \sqrt{2} \frac{(t_{ek}/l_k)^4}{2 + t_{ek}/l_k} \quad (2-18)$$

where  $E_s$  is the Young's modulus of the solid material,  $l_k$  is the edge length, and  $t_e$  is the edge thickness. The relative density,  $R$ , of a Kelvin foam is related to the edge cross-section area and length by the expression,

$$R = \frac{3A}{2\sqrt{2}l_k^2} \quad (2-19)$$

where  $A$  is the edge cross-section area. Zhu et al. [73, 80] analysed the elastic deformation of open-cell foams using a body centred cubic (BCC) lattice of cells, each of which is a Kelvin foam model. Edge deformation (torsion) was illustrated when the lattice was compressed in the (111) direction. Consequently, Zhu et al. [80] predicted the modulus of elasticity, using a Kelvin open-cell model with struts having a uniform triangular cross-section, to be

$$\frac{E_{100}}{E_s} = \frac{8\sqrt{6}R}{27 + 12\sqrt{6}R} \quad (2-20)$$

This is more practical than the corresponding equation by Dement'ev and Tarakanov [79], see Equation (2-18), because the analysis does not depend on the geometrical dimensions of the foams, making the analysis easier and more accurate. In addition, Zhu et al. [73] presented a model with so-called Plateau border cross-section struts (see Figure 2-8).

## CHAPTER 2 LITERATURE REVIEW

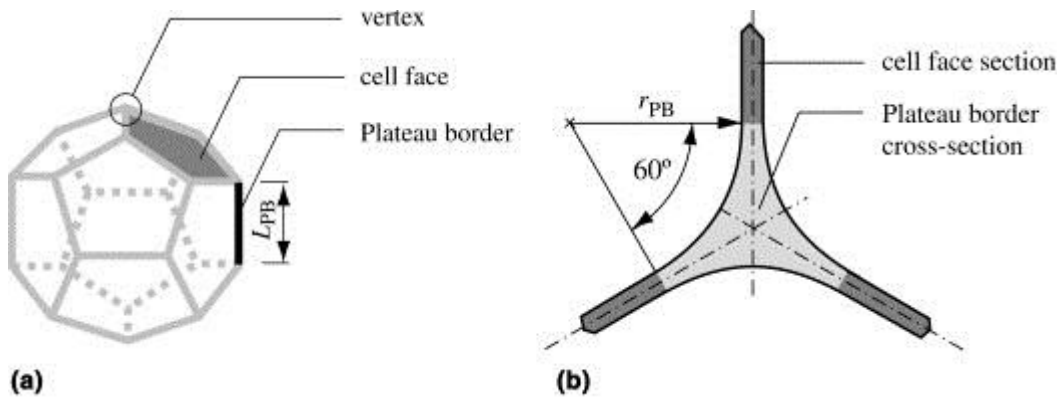


Figure 2-8. Schematic representation of (a) Kelvin cell foam model (b) a Plateau border/cell face section [83].

The modulus of elasticity is calculated as:

$$\frac{E}{E_s} = \frac{1.009R^2}{1+1.1514R} \quad (2-21)$$

and Poisson's ratio,  $\nu_{12}$ , is calculated by:

$$\nu_{12} = 0.5 \frac{1-1.514R}{1+1.514R} \quad (2-22)$$

Subsequently, Zhu et al. [73] showed that the modulus of elasticity is about 38% higher for the same relative density for the case where the edge cross sections are Plateau borders rather than equilateral triangles, and the Poisson's ratio of the Plateau border cross-section is higher than the ratio of the triangular cross-section. Moreover, the shear modulus for isotropic and anisotropic foam was predicted based on the mechanical properties of the edge material, see Equations (2-23) and (2-24).

$$G = \frac{0.2333ER^2}{1+0.7R} \quad \text{for isotropic material} \quad (2-23)$$

$$G_{12} = \frac{6EI}{\sqrt{2}l_k^4} \left( \frac{5E_s I + G_s J_p}{8E_s I + G_s J_p} \right) \quad \text{for anisotropic material} \quad (2-24)$$

where  $G_{12}$  is the shear modulus of the foam in the lattice axes,  $G_s$  is shear modulus of the edge material,  $I$  is the second moment of area of the edge and  $J_p$  is the polar second moment of area of the edge.

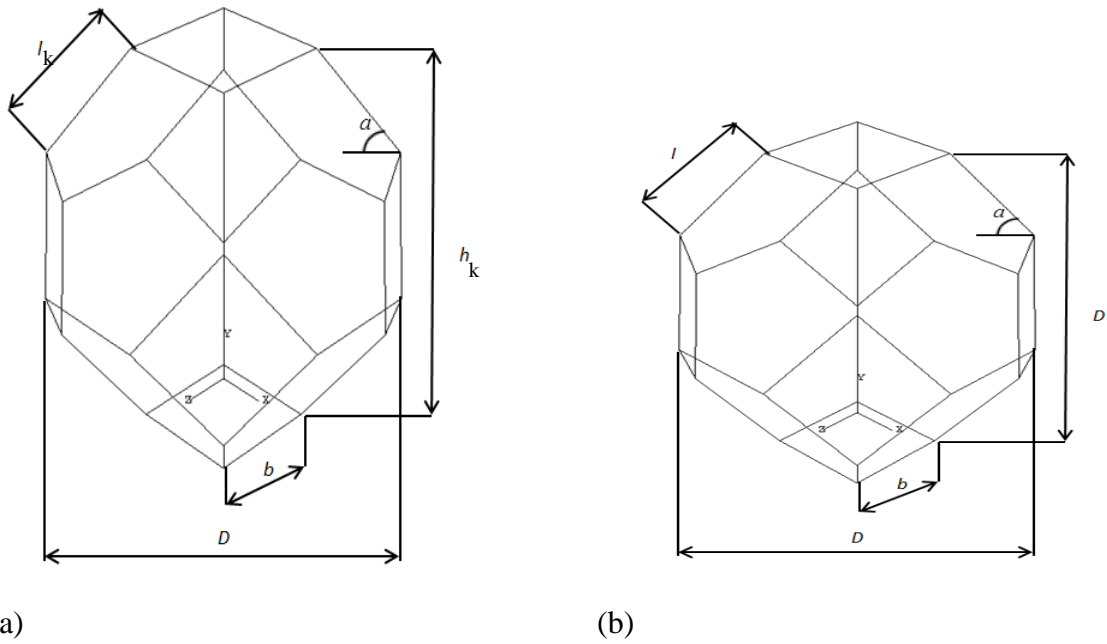
Mills et al. [84] investigated the compression loading of anisotropic closed-cell foam, using a Kelvin model to predict the mechanical response. The influences of edge bending

## CHAPTER 2 LITERATURE REVIEW

and cell face tensions were studied, assuming that the cell faces act as membranes for both small and large strain. They assumed that the resistance of the face to wrinkling should be ignored during foam compression, and that if the edges in the foam's microstructure consisted of a volume fraction,  $\phi$ , greater than 0.6 then the edges act as the main structural members in the microstructure with negligible contribution provided by the tension in the cell faces. This assumption was found to improve the predictions of the mechanical parameters of the foam. The predicted yield stress values for polyethylene foams were close to experimental values. The modulus of elasticity predicted for a polystyrene foam using a volume fraction,  $\phi$ , of 0.6 is given as a function of the foam's relative density,  $R$ , and the polystyrene's modulus of elasticity,  $E_s$ , was found to be

$$E = 0.0598E_s R^{1.066} \quad (2-25)$$

A micro-scale model for anisotropic foam was developed by elongating the tetrakaidecahedron (Kevin cell foam model) in the single principal direction, as shown in Figure 2-5b. Assuming that the cell edges and faces of the elongated model undergo axial and rotational deformations, a set of equations for calculating the linear and non-linear mechanical behaviour can be obtained. These equations were developed and written in terms of the anisotropic ratio, cell edge length, cell edge thickness and cell face thickness for closed-cell foam and the buckling torsional stiffness of the edges and the stiffness of the constituent material by [85-87]. The influence of this elongated shape on the non-isotropic stiffness and strength behaviour was demonstrated and the advantages of this more general micro-mechanical model were applied by Dement'ev and Tarakanov [85] to predict the elastic mechanical properties of open-cell plastic foams in the direction of foaming  $E_1$  and in the perpendicular direction  $E_2$  (see Equations (2-26), (2-27) and Figure 2-9).



(a) Anisotropic and (b) Isotropic open-cell Kelvin foam models.

$$E_1 = \frac{E\beta_m^4 \sin a}{(2/k + \beta_m)^2 \sin a} \quad (2-26)$$

$$E_2 = \frac{E\beta_m^4 \sin a}{(2/k + \beta_m) \cos(\pi/4) \cos a ((1/2k^3) + \cos^2 a)} \quad (2-27)$$

where  $\beta_m = t_e / l$ , and  $k = l / b$

Similarly, this model was implemented by Vladimir [86] to predict  $E_1$  and  $E_2$  the Young's moduli of anisotropic and isotropic closed-cell foams, respectively, see Equations (2-28) and (2-29).

$$E_1 = E_s \left[ m \left( \frac{r}{r+2} \right)^2 \phi^2 R^2 + \beta_m \left( \frac{r}{2r+1} \right) \left( \frac{2}{3} r^2 + \frac{r}{3} \right) (1-\phi) R \right] \quad (2-28)$$

$$E_2 = E_s \left[ \frac{m}{2} \left( \frac{r}{r+2} \right)^2 \left( \frac{1}{r} + \frac{1}{r^4} \right) \phi^2 R^2 + \frac{\beta_m}{3} \left( \frac{r}{2r+1} \right) \left( \frac{1}{r^2} + \frac{1}{r} + 1 \right) (1-\phi) R \right] \quad (2-29)$$

where the coefficients  $m$  and  $\beta_m$  are taken to be 9 and 3,  $r$  is the anisotropy ratio equal to  $h_k / D$  and  $\phi$  is the volume fraction of the solid material. More recently, the elongated Kelvin model was used by Sullivan et al. [87] to calculate the shear modulus of anisotropic open-cell foams, they derived equations for the shear properties as a function of the three

## CHAPTER 2 LITERATURE REVIEW

unit cell dimensions. In general, the predictions for anisotropic closed-cell foams are less accurate than those for anisotropic open-cell foams due to the more complex microstructure of closed-cell foams.

### 2.2.1.2. Numerical Model for Small Strains

Numerical computation, such as use of FEM, allows an alternative more detailed strategy for investigating the relationship between microstructure and macro-scale response. Clearly the effort in generating and running a numerical simulation is greater than use of simple equations resulting from analytical models, though potentially results are more accurate and a greater range of parameters can be explored. One of the simplest but most useful numerical approaches has been to use the Kelvin cell as a representative unit cell (RUC) in order to explore the mechanical properties of the foam. When the foam is subjected to compressive strain of 1% or less, there is insufficient deformation in the foam microstructure to generate a non-linear mechanical response in the constituent material. Thus, the linear moduli of elasticity are enough to describe the foam's compressive behaviour. Warren and Kraynik [75] computed the elastic compressive modulus using periodic boundary conditions. They analysed the effects of edge cross-sectional shape on the predicted Young's modulus of a Kelvin model by changing the edge cross-section from circular, square, or equal triangular to a Plateau border configuration (see Table 2.1)

Table 2.1. Young's modulus for the Kelvin foams with difrent strut cross-section,  $A$  is area of sreut,  $I$  is second moment of area of the strut,  $J_p$  is polar second moment of area of the strut,  $E_s$  is elastic modulus of solid constituent material,  $E$  is elastic modulus of foam and  $R$  is relative density of foam[4, 75]. Where  $r_c$  is radius of cucle,  $b_s$  is side of the square, Equilateral triangle and Plateau border

Strut cross section	Area $A$	$I/A^2$	$J_p/A^2$	$E_s/ER^2$
Circle	$\pi r_c^2$	0.0796	0.1592	0.593
Square	$b_s^2$	0.0833	0.1406	0.619
Equilateral triangle	$\sqrt{3} b_s^2 / 4$	0.0923	0.1155	0.710
Plateau border	$b_s^2 (\sqrt{3} - \pi / 2)$	0.1338	0.0808	0.979

## CHAPTER 2 LITERATURE REVIEW

For anisotropic open-cell foams, Gong et al. [88] investigated compression under large strain using the Kelvin cell as the RUC, with an anisotropy ratio of 1.3 and cell edges with variable cross-sections. Compression stress-strain curves were predicted in the principal and transverse directions. The predicted modulus of elasticity in the principal direction for a relative density of 0.025 was twice that in the transverse direction. Thiyagasundaram et al. [89] recently applied an elongated Kelvin model to predict the modulus of elasticity and shear modulus of anisotropic open-cell foams. The predicted elastic data from the FEM models agree with those predicted from analytical methods. The edges were modelled using both Timoshenko and Euler-Bernoulli beam elements. Also, they analysed the effects of a variable edge cross-section on the elastic terms. For the same relative density, they observed that foams with varying cross-section edges had a lower stiffness than foams with constant cross-section edges.

In practice, all foam microstructures are random. In order to calculate  $E$  for irregular foams, Roberts and Garboczi [90] used FEM to calculate the Young's modulus and Poisson's ratio of various isotropic irregular closed-cell foams based on simple Voronoi tessellation models. The predicted results showed reasonable agreement with the experimental data. Similarly, Zhu et al. [78] used FEM and random periodic Voronoi based RVE models to study the influence of cell regularity on the elastic properties of open-cell foams. The predicted results showed that low-density foams with high irregularity have higher modulus of elasticity, shear modulus and lower values of bulk modulus than perfect foams. The results also indicate that Poisson's ratio values are insensitive to cell regularity (see Figure 2-10).

## CHAPTER 2 LITERATURE REVIEW

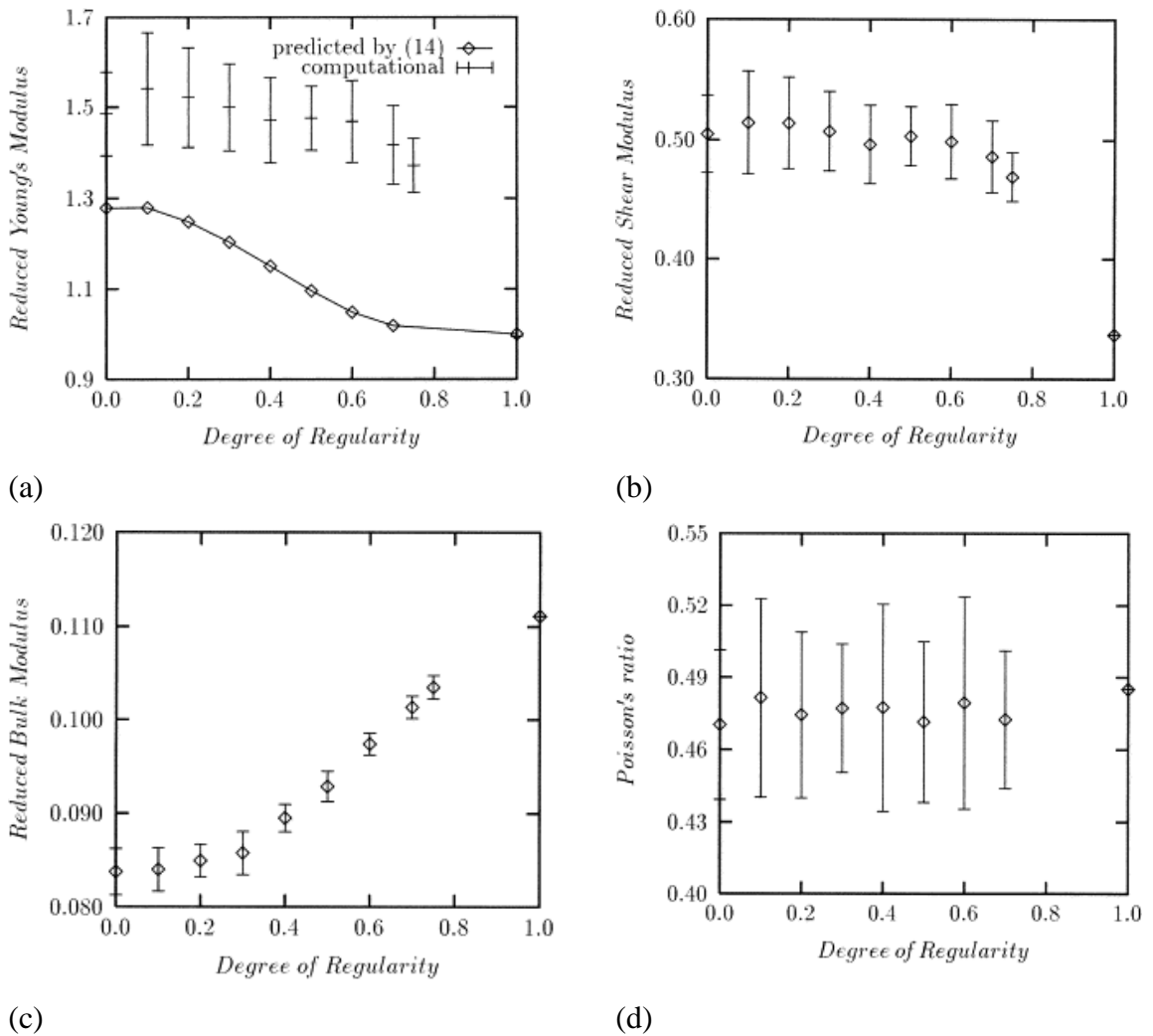


Figure 2-10. Effects of cell regularity on the (a) reduced Young's modulus of random Voronoi foams having a constant relative density, (b) reduced shear modulus of random Voronoi foams having a constant relative density  $R=0.01$ , (c) reduced bulk modulus of random Voronoi foams having a constant relative density  $R=0.01$  and (d) Poisson's ratio of random Voronoi foams having a constant relative density  $R=0.01$ [78].

## 2.2.2 Large Strain Modelling

### 2.2.2.1 Analytical Models

Simple analytical models have been proposed to predict the large strain response of flexible closed-cell foams. For this class of material, the gas pressure inside the foam can provide the most significant contribution to the foam's compressive resistance and can be easily calculated by considering the change in the gas volume inside the foam as a function of compressive strain. By combining results from small-strain analytical models with

CHAPTER 2 LITERATURE REVIEW

large-strain gas models, it is possible to make first-order micro to macro predictions over a large range of strains and consequently estimate model parameters of large-strain non-linear constitutive models suitable for implementation in finite element software.

The influence of gas compressed inside closed-cell foams on the mechanical behaviour has considered in many investigations, such as, Rusch [41], Mills [4], Gibson and Ashby [1], Clutton et al. [91] and Ostrogorsky et al. [92]. Rusch [41] assumed isothermal compression of the gas inside closed-cell foams, with no lateral deformation, i.e. Poisson’s ratio of the foams is zero, and that the variation of the bulk stress in the foam,  $\sigma$ , with atmospheric pressure can be expressed as:

$$\sigma = \frac{p_a \varepsilon \phi}{1 - \varepsilon - R} \tag{2-30}$$

where  $p_a$  is the atmospheric pressure,  $\varepsilon$  is the applied compressive strain, and  $\phi$  is volume fraction of solid material in the closed-cell foam.

In order to understand the effects of gas and polymer on the response of materials, Mills [4] characterised the phase volumes for closed-cell foams. A foam cube of  $1\text{m}^3$  contains both gas and polymer. It was assumed that the pressure inside the cell before loading is  $P_0$ , a zero Poisson’s ratio after loading, the compression strain  $\varepsilon$  is the same as the volumetric strain, and the polymer is incompressible. Therefore, the expression  $(1 - \varepsilon - R)$  represents the changes in the volume of the gas under the compression stages, as illustrated in Figure 2-11.

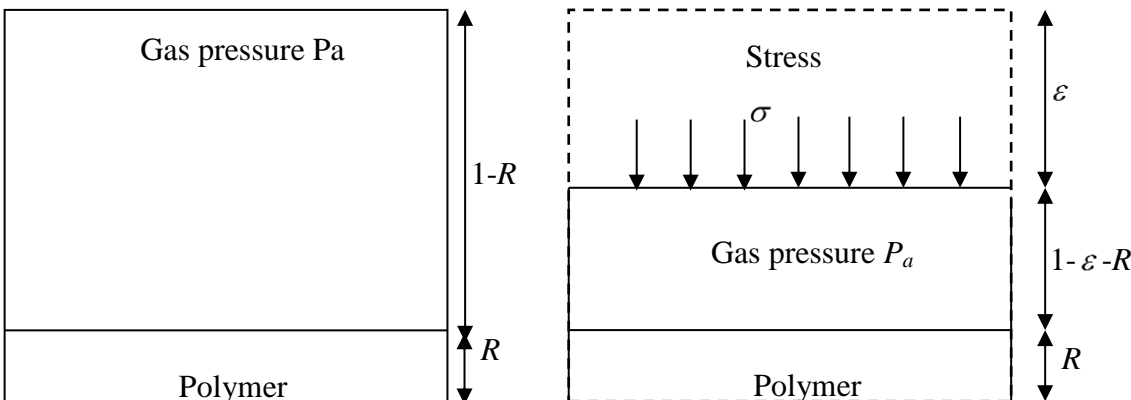


Figure 2-11. Phase volume in foam of zero Poisson’s ratio and relative density R, before and after uniaxial compression [4].

## CHAPTER 2 LITERATURE REVIEW

The absolute pressure of an isothermal gas in compressed foam can consequently be expressed as:

$$p_o(1-R) = p_a(1-\varepsilon-R) \quad (2-31)$$

and the compressive stress can be expressed as:

$$\sigma = p_o - p_a = p_a \frac{\varepsilon}{(1-\varepsilon-R)} \quad (2-32)$$

Gibson and Ashby [1] simplified Equation

(2-29) by assuming  $\phi = 1$  and added the influence of the polymer on the response of the foam. Clutton and Rice [91] modified Gibson and Ashby's assumption by fitting the compressive stress-strain curves of a compressible polyolefin foam. Furthermore, by considering the effects of Poisson's ratio, they found that the pressure inside cells is not equal to atmospheric pressure, so do the predictions compare well to experiments.

$$\sigma = \sigma_{el} + P_a \left( \frac{1-R}{(1-\varepsilon)(1+\nu \varepsilon)^2 - R} - 1 \right) \quad (2-33)$$

### 2.2.2.2 Gas Diffusion Model

Most polymer foams are two-phase materials consisting of gas and solid polymer. In order to describe the mechanical properties of these materials, the important parameters considered for flexible foams are usually the relative density, the properties of the gas inside the cells, the geometric description of the cellular microstructure such as anisotropy of the cells, the average cell size, the cell wall thickness and cell shape and the properties of the constituent material. Ostrogorsky et al. [92] showed the relationship between the cell shape, the  $D_f$  gas diffusion coefficient of foam. It was used a unit cell model (see Figure 2-12) to determine the gas diffusion as show in Equation (2-34)

$$D_f = 2 \frac{L_m}{\delta} D_p S_g \quad (2-34)$$

where,  $D_p$  is gas diffusion coefficient of polymer,  $S_g$  solubility of the gas,  $t_f$  is the face thickness,  $L_m$  is the average distance between membranes, and  $S_g$  is the solubility of the gas in the foam. Normally, when closed-cell foam is subjected to small compressive strains

## CHAPTER 2 LITERATURE REVIEW

(in the elastic region) its creep behaviour can be calculated from the constituent polymer's viscoelastic properties alone. Beyond this region, gas compression results in an increasingly higher amount of stress and outward diffusion of the gas contained in the cells takes place. Pilon et al. [93] modified the diffusion equations in closed-cell polymeric foams to produce a good result.

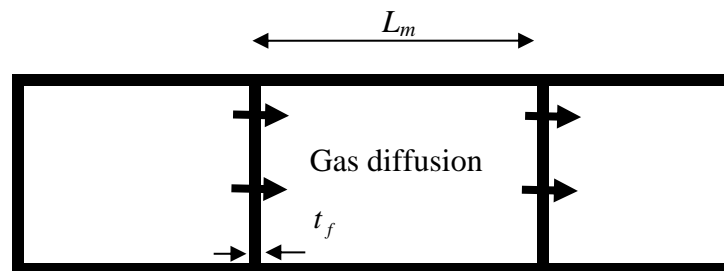


Figure 2-12. Cubic cell foam with a pressure gradient in x-direction.

### 2.2.2.3 Analytical Modelling (Kelvin Model)

The Kelvin cell is a useful model when investigating the linear small strain behaviour of foam (see Section 2.2.1.1) but can also be used to study nonlinear behaviour at larger strains. The large strain hydrostatic compression of a Kelvin foam with uniform edges was investigated by Dement'ev and Tarakanov [79]. The predicted stress-strain curves were shown to be reasonably close to experimental data on plastic polyurethane foam. Zhu and Mills [80] described an approach for the high strain compression of open-cell foams using a lattice with tetrakaidecahedral cells. The stress-strain curves and Poisson's ratio were calculated for large deformations. The study by Kraynik and Warren [72] suggested that it is more difficult to analyse the deformation of closed-cell foams than open-cell foams using this approach. If the walls of closed-cell foams do not tear during compression, then the pressure of gas trapped inside the cells increases, inducing tension in the cell walls. For this reason, predicting the modulus of elasticity and the yield stress is difficult. Mills and Zhu [84] proposed that the contribution of cell faces and gas to the modulus of elasticity for low density foams is important. A maximum of 40% strain in the cell faces was predicted. Also, the compressive foam yield stress was predicted based on tensile yielding of the cell faces. The predicted data were close to experimental results for polyethylene foam.

#### **2.2.2.4 Numerical Modelling (Kelvin model)**

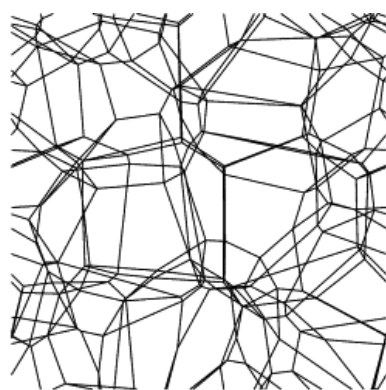
It is generally accepted that representative unit cell models based on the Kelvin cell are useful in investigating foam's nonlinear behaviour under large strains. McKown [94] used FEM for a Kelvin closed-cell foam model simulating faces using shell elements for uniaxial compression at a strain rate of  $10\text{s}^{-1}$ . In this model, the air pressure inside the cells was ignored. Similarly, Mills et al. [95] attempted to predict the compressive impact behaviour of low density closed-cell polyethylene and polystyrene foams using a FE analysis of a Kelvin RUC model. In this case, cell air compression was considered. The predicted stress-strain behaviours were close to the experimental data for a wide range of foam densities.

#### **2.2.2.5 Numerical Modelling (Voronoi Model)**

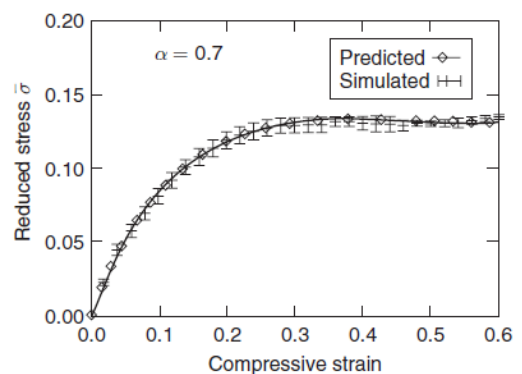
Models incorporating a random foam microstructure as their Representative Volume Element (RVE) have also been used extensively to investigate the large strain response of foams. Various methods have been used to generate such microstructures, including use of Voronoi mesh generation algorithms such as those used by, Zhu and Windle [96] who predicted the large compressive stress-strain curves of low-density open-cell polymer foams using FEM (see Figure 2-13). Also, they used a Voronoi model under periodic boundary conditions and cell shapes and sizes of various degrees of regularity. It was found that even if the reduced compressive stress-strain relationship and the Poisson's ratio changed in different directions for the same samples, the models were, on average, isotropic. Furthermore, they showed that highly irregular foam has greater tangent modulus at small strains and less of an influence on stress at large compressive strain rates when compared with regular foam. This stochastic RVE approach is very promising for structural foams and various researchers have used the method to predict the stress-strain relationship of foams under large deformations with various degree of regularity of cell shapes and sizes. Similarly, Zhang and Lu [97] calculated the large compressive mechanism of low-density polymer foam, which was analysed using a random foam model. The influence of relative density, edge cross-section, and cell shape irregularity on the compressive mechanical response of the foam was studied. The results showed that the

## CHAPTER 2 LITERATURE REVIEW

relative density has significant influence on the compressive stress strain-curves and the values of the Poisson's ratio, see Figure 2-14a and Figure 2-14b. Also, the edge cross section shape have significant effect on compressive stress-strain curves but not on the value of the Poisson's ratio - see Figure 2-14c and Figure 2-14d. Recently, 3D FE models based on Voronoi tessellation were developed by Song et al. [98] to analyse the dynamic crushing response of closed-cell foams. The effects of the cell shape irregularity, relative density, impact loading and strain hardening on the energy absorption capacity of foams were investigated. The numerical results showed that an increase in the cell shape irregularity increased the plateau stress and the densification strain energy for all cellular foams considered.



(a)



(b)

Figure 2-13. (a) An undeformed random Voronoi cell and (b) The reduced stresses against the compressive strains of foams having a regularity parameter  $\alpha=0.7$ , compared with the predicted results [96].

CHAPTER 2 LITERATURE REVIEW

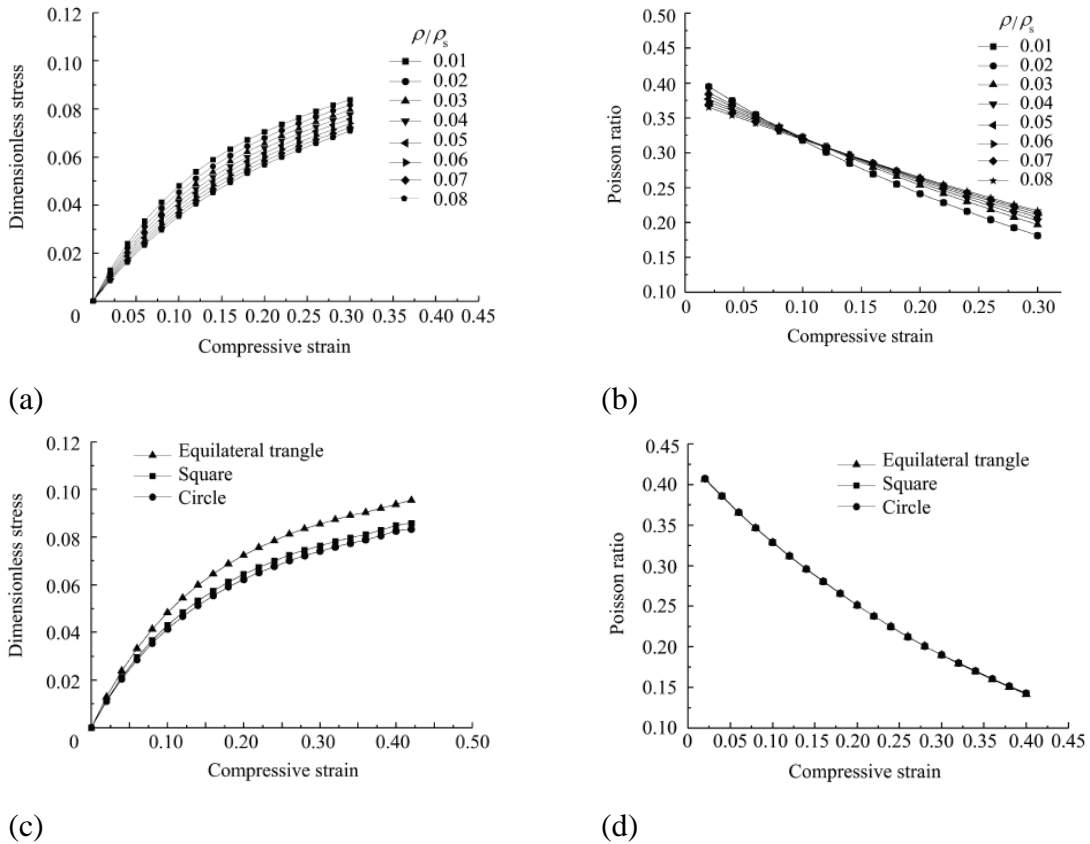


Figure 2-14. (a) The dimensionless stress-strain curves of models with different relative density, (b) the Poisson's ratio-strain curves of models with different relative density, (c) the dimensionless stress-strain curves of models with different strut cross-section shapes, and (d) the Poisson's ratio-strain curves of models with different strut cross-section shapes [97].

Nevertheless, the method is computationally expensive and requires considerable user expertise. Currently, no convenient commercial software package is available to perform the required mesh generation, making it relatively difficult for engineers looking for a fast, efficient and accurate approach to perform multi-scale modelling of foams. Also, under large strains, gas pressure is often the main contributor to the compressive resistance of flexible closed-cell foam. Consequently, the choice of using a random RVE computational approach to modelling such materials is not always the most appropriate. Also, use of structural elements based on this technique leads to tractable computation times but restricts the analysis to very low foam densities. The analysis of large strain compression of foams is complex due to self-contact within the foam microstructure. This introduces a great deal of computational resource requirement for the numerical simulations.

## **2.3 Experimental Investigations**

### **2.3.1 Macro-scale Experimental Investigations**

A range of experimental test methods have been used to characterise the mechanical properties of foams. The response is generally highly non-linear under large strains (see Section 1.4), and foams are often used under complex loading conditions and under different ranges of strain. Thus, mechanical testing of foams and the determination of their linear and non-linear properties and their degree of anisotropy is necessary for complete characterisation of their mechanical behaviour. Test data can be used to determine the parameters of suitable constitutive models implemented in computer-aided engineering numerical simulations for the purposes of product design and virtual testing. The characterisation techniques used for foams are the same as those used for other materials. Most experimental studies on the mechanical testing of foams include the use of uniaxial compression, tensile, shear, hydrostatic or biaxial tests [1, 4, 56, 99-104]. These tests require the definition of strain rates, specimen size, specimen shape and all boundary conditions of the test. Some of these tests are discussed below.

#### **2.3.1.1 Digital Image Correlation Technique for Strain**

##### **Measurements in Foams**

Strain measurement is important for all accurate mechanical characterisation. Strain measurement in the loading direction is required to produce the stress versus strain response of the material. The foam's Poisson's ratio can be characterised by simultaneously measuring the strain in the transverse direction using image analysis techniques such as Digital Image Correlation (DIC). DIC is able to accurately capture the full-field large deformation of strains in any direction across the surface of a sample. For this reason, the DIC technique is very useful for strain measurement of foams. DIC is a contactless measurement method, based on mathematical comparison of a subset of digital images captured from a deformed surface. Researchers at the University of South Carolina including Sutton et al. [105] and Bruck et al. [106] were amongst the first to established this technique. Examples of the use of DIC in characterising the deformation of foams include Wang et al. [107] who determined the deformation distribution for an ultra-light

## CHAPTER 2 LITERATURE REVIEW

open-cell foam during compression and Jin et al. [108] who used DIC to calculate the heterogeneous deformation of closed-cell polyurethane foam under uniaxial compression. Similarly, Widdle et al. [56] used digital images taken at different compression levels, and the deformation of the material was computed using digital image processing tools in MATLAB<sup>TM</sup>.

### **2.3.1.2 Uniaxial compression test**

The uniaxial compression test is a popular experimental method for testing mechanical properties of foam (see Figure 2-15). This is because, as presented in Section 1.1, most mechanical applications of foams tend to involve compressive loading. A typical test involves strain rates effects, influences of specimen size, influences relative density on mechanical response and determination the strain regions. Specific issues in testing foams involve influences of the friction at the metal/foam specimen contact, their effects on mechanical response. This class of problem can be arising for metals and rubbers it possible to lubricate the surface, it cannot do this for foams, though because they have a low Poisson's ratio, is not such a big problem. Also, other issues testing foams such specimen size effects and strain rates influences, will be studied in this work.

The uniaxial compressive response of most types of foam can be classified according to the categories listed in Section 1.4. Polymer foams cover a broad range of behaviours in compression. They can be either rigid polyurethane (PU) or flexible (low density polyethylene foam (LDPE), they can be plastic polystyrene (PS). In general most polymer foams show strong strain-rate dependence under compression polystyrene foam (PS).

Previous investigations have shown that the compressive deformation stress-strain response is dependent on the anisotropy ratio (see Section 1.2), specimen test size and relative density [1, 3, 4, 26, 109-111].

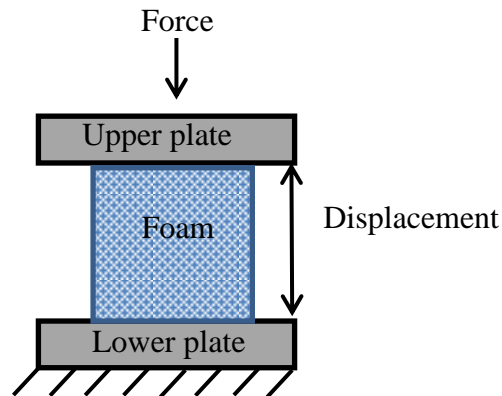


Figure 2-15. Uniaxial compression test.

### 2.3.1.3 Multi-Axial Tests

In many applications foam is subjected to multi-axial compressive loads, here the experimentalist needs to determine a set criterion to measure the combination of these multiaxial loads which can cause failure (see Figure 2-16).

Polymer foams cover a broad range of behaviours when tested under multi-axial loads though the volume of literature in this area is more limited, for example, Deshpande and Fleck [66] performed multiaxial mechanical tests on two densities of PVC foam under tensile and compressive axisymmetric loadings (see Figure 2-16). The shapes of the yield surfaces were examined. These experimental results showed that the yield surfaces are adequately defined by the Deshpande-Fleck yield surface, capped by a maximum compressive principal stress criterion. The uniaxial tensile strength of these foams was found to be similar to their hydrostatic tensile strength. The compressive deformation of these foams is described by the elastic buckling of the cell walls. Similarly, Andrews et al. [112] studied the uniaxial compressive and tensile elastic modulus of open and closed cell aluminium foams. The open cell foam can be adequately defined by the models for cellular solids. The closed cell foams have moduli and strengths that were found to be lower than the predicted values. This is mainly due to the defects in the cellular microstructure which causes bending rather than stretching of the cell walls.

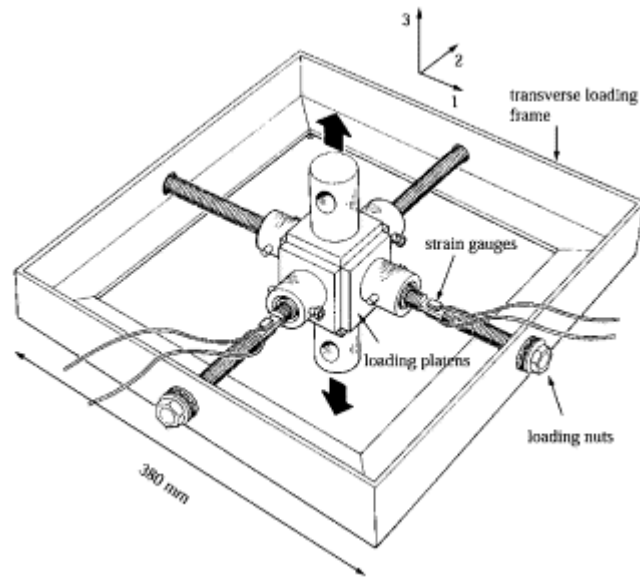


Figure 2-16 Sketch of the loading rig for the biaxial and hydrostatic tension tests[66].

### 2.3.1.4 Shear Test

Another common mechanical test is the shear test (see Figure 2-17). Shear testing is necessary for all three dimensional constitutive model parameter fitting and evaluation. The significance of shear testing for foam depends on the type of foam and its application. For example, Mills [4] showed that the shear modulus of foam used in a motorbike helmet can be related to the resulting rotational acceleration of the head during impact. This rotational acceleration can cause serious brain injuries and should be reduced as much as possible.

As discussed, the response of anisotropic foams depends on the relative properties in the principal (foaming) and transverse directions (see Section 1.2.1). Similarly, shear properties in the foaming direction can be quite different to those in the transverse direction. Therefore it is important to study the shear modulus of transversely isotropic materials.

Several researchers have determined experimentally the shear properties of compressible transversely isotropic cellular materials. For instance, Tagarielli et al. [37] determined the shear modulus of balsa wood in its principal and transverse directions. Similar studies have been carried out by Jebur et al. [15] for extruded LDPE foams (see Section 4.5.1). Both

## CHAPTER 2 LITERATURE REVIEW

groups of researchers found that the shear modulus in the principal direction is higher than that in the transverse direction by a factor of two times.

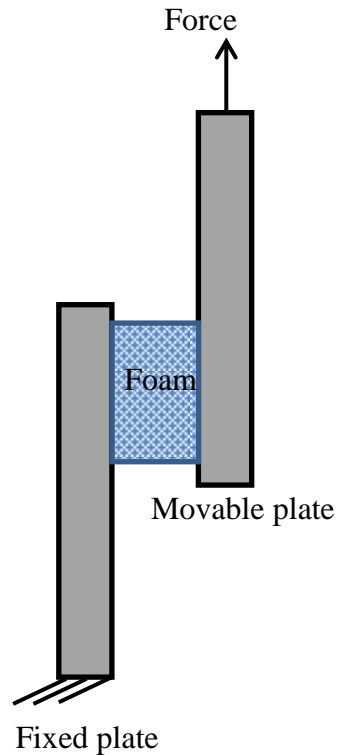


Figure 2-17. Shear test procedure.

### 2.3.1.5 Uniaxial Tensile Test

The tensile test is an important experimental test as foam structures may be subjected to bending loading, resulting in ductile or brittle tensile behaviour (see Figure 2-18).

An improved technique for tensile testing Figure 2-18 of ceramic foams was suggested by Rehorek et al. [113]. This technique involved embedding the specimen test in alumina pots with a carefully chosen gripping adhesive, the tensile load was then transferred from the test machine fixtures to the specimen.

Aly [114] investigated the effects of pore size on the tensile behaviour of open-cell Ti foams, having an average pore size of 50 and 150  $\mu\text{m}$ . The mechanical properties of foams

## CHAPTER 2 LITERATURE REVIEW

were measured by a camera which recorded the resulting deformation during the tensile loading. The experimental data showed that the Ti foam samples of smaller pores were found to show higher tensile strength and elongation than those with larger ones.

Kabir [115] performed tension tests for polymer foams under quasi-static and dynamic fractures, with various densities. The experimental results showed that the tensile and quasi-static fracture behaviours are linear up to the failure load, both the tensile strength and the modulus are found to be significantly dependent on the foam density. Also, mathematical relationships of the tensile strength, modulus and fracture toughness with the foam density are measured from the best fitting of the experimental data. The mathematical relationships are found to provide a good prediction of the of the foam elastic and fracture properties.



Figure 2-18. Tensile test setup [116].

### 2.3.1.6 Hydrostatic Compression Test

The hydrostatic compression test is a significant test as the yielding point of foams. The hydrostatic compression test requires relatively complex samples for preparation, especially for foam; this is due to the difficulty involved in covering the foam material with an impermeable but flexible membrane preventing liquid ingress and instrumentation inside a fluid-filled pressure chamber. Many of physical phenomena make the experimental data less than ideal for use in modelling foam. One important phenomenon is the influence of air diffusion in foam at low and high strain rates, this influence significantly on mechanical behaviour of material. Viot [117] tested polypropylene (PP)

## CHAPTER 2 LITERATURE REVIEW

foams under hydrostatic compression, both quasi statically and high strain rates. The stress–volumetric strain behaviours of the foam were determined for specimens of foam of density from 35 to 120 kg/m<sup>3</sup>. A Photron APX RS3000 high speed camera was used to determine the volumetric strain of the sample as a function of testing time, using image processing techniques. Hydrostatic test performed by using water or alcohol after coating the specimens with thin layers of silicone gel.

PP foam behaviour under hydrostatic compression was found to show a non-linear elastic response, followed by a plastic plateau and densification. The plastic plateau was non-linear, with a slope increasing with strain, probably due to the increasing gas pressure inside the foam cells and the progression of the damage to the more rigid cells (at the beginning of the plastic plateau, the weaker cell walls buckle before the stronger). The polypropylene (PP) foam response under hydrostatic compression indicates a transversely isotropic response under hydrostatic compression.

Kim and Kang [118] described the pressure dependent yield point for polymeric foams using a test rig consisting of a hydraulic pressure chamber for applying hydrostatic oil pressure on polyurethane (PU) foam samples. The pressure and volumetric strain were indirectly measured from the piston of the hydraulic press by using a load cell and a wire potentiometer connected to the piston.

Moreu and Mills and Mills [2] improved a test rig to determine the rapid hydrostatic compression of low density foams without using a piston to apply the hydrostatic pressure, see Figure 2-19.

The foam volume vs pressure behaviour was modelled with an equation reflecting the influence of air-compression and experimental data used for implementing crushable foam model in FEM. The stress-volumetric strain curve (under hydrostatic compression) of Polypropylene foam of density 43kg/m<sup>3</sup> was fitted according to the Equations (2-35) and (2-36)

$$p_c = p_{co} + \frac{P_{cell} e_v}{1 - e_v - R} \quad (2-35)$$

where  $p_c$  is the yield stress in hydrostatic compression,  $p_{co}$  the initial value,  $p_{cell}$  the effective absolute gas pressure in the foam cells,  $R$  the relative density of PP foam,  $e_v$  the

## CHAPTER 2 LITERATURE REVIEW

engineering volume strain described from the initial foam volume  $V_o$  and the current volume,  $V$  using

$$e_v = \frac{(V_o - V)}{V_o} \quad (2-36)$$

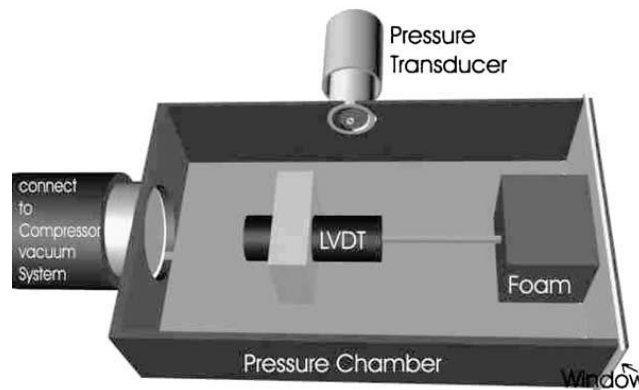


Figure 2-19. Schematic of the hydrostatic compression test rig [2].

### 2.3.1.7 Creep and Relaxation Test

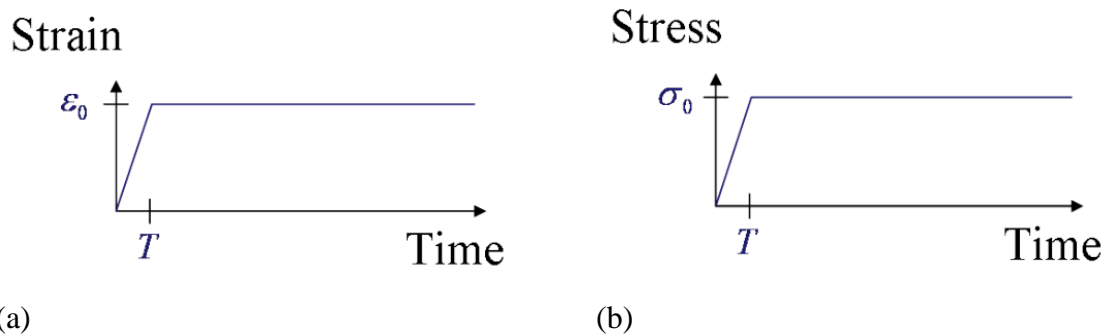
As discussed in Section 1.4.7, most polymer foams display viscoelastic behaviour. This behaviour can be measured by two common tests namely: the stress relaxation test and the creep test. When a foam specimen is subjected to constant strain, the force required to keep that strain is not constant but decreases with time, this behaviour is called stress relaxation (see Figure 2-20a) [42]. Also, when a constant stress is applied to a foam specimen, there is an increase in the strain with time, this behaviour is called creep (see Figure 2-20b). In practice, relaxation and creep are terms normally associated with time related to stress-strain variables.

Investigations involving the stress relaxation and compressive creep response of foams should be conducted over a long time, but this can be costly. In order to reduce the time of viscoelastic tests, Briody et al. [104] used the time-stress superposition technique in creep tests over a wide range of temperatures on flexible polyurethane foam. They found that viscoelastic behaviour is highly temperature dependent. The time-stress superposition technique has been used to investigate viscoelastic stress relaxation and viscoelastic creep in rigid polymers [119-121]. In these studies, the creep was determined using various

## CHAPTER 2 LITERATURE REVIEW

methods. For example, Bozorg et al. [119] used an accelerated test technique for predicting the compressive creep of recycled High Density Polyethylene (HDPE). This technique is based on the equivalence of strain energy density between conventional constant-stress creep tests and stress-strain tests conducted at various strain rates. Good agreement was observed between the creep rates obtained from a conventional test and strain energy density (SED) calculations when two stress-strain experiments with strain rates varying by two or more orders of magnitude were used. Yeo and Hsuan [121] determined the tensile creep response of neat polyethylene-terephthalate (PET) and high density neat polyethylene (HDPE) using several test techniques; for instance, the short- and long-term stepped isothermal method, the short- and long-term time-temperature superposition method

The next section of this review of experimental methods is addresses: (i) the parameters influencing the mechanical response of foams and (ii) the methods of determining the strain regime i.e. methods of determining the start and end of the linear small strain regime, the plateau stress regime and the densification regime (as discussed in Section 1.4).



(a) (b)  
Figure 2-20. (a) Stress relaxation tests (constant strain) and (b) Creep test (constant stress) [46].

## 2.3.2 Factors Affecting Mechanical Response

### 2.3.2.1 Influence of Strain Rate

Various investigators [43, 109, 110, 122-126] have showed that the behaviours of both polymeric and metallic foams are sensitive to strain rate. For example, Bo Song et al. [43] found the yield stress and Young's modulus of polystyrene foam to be nearly linear with the natural logarithm of the strain rate. Similarly, Luong et al. [127] showed that the compressive strength of closed-cell polyvinyl chloride foam (PVC) increased with strain rate by as much as 200%. Cao et al. [27] studied the strength of open-cell aluminium foams over a range of strain rates from  $0.001\text{s}^{-1}$  to  $10^3\text{s}^{-1}$ , and found this class of foams to be very sensitive to strain rates; the strength at high strain rates can more than twice as high than that at low strain rates.

Yu et al. [128] studied the compressive response of both open and closed-cell aluminium foams under various strain rates, with uniaxial compression and two types of lateral constrained tests. The experimental data showed that in both quasi-static and dynamic tests the yield stress of the open-cell aluminum foam under lateral constraints tests is significantly higher than that under uniaxial compression tests. Also, the experimental results showed a significant increase in the yield stress of the closed-cell aluminum foam in quasi-static test when lateral constraints were applied. At the same time, it is not expected that dynamic yield stress tests under lateral constraints be less than those in the quasi-static tests.

The Poisson's ratio of auxetic open-cell foam at low and high compressive strain rates have been studied using image data processing by Pastorino et al. [129], who observed that Poisson's ratio values increased by as much as 50% with increasing compressive strain rate. Recently, Wang et al. [130] stated that the Poisson's ratio decreases during high-rate dynamic compression of closed-cell aluminium foam. They explained the decrease of Poisson's ratio as follows: under low strain rates and uniaxial compression, lateral deformation takes place because of the influence of Poisson's ratio. If impact velocity is low, the foam has enough time to deform in the lateral directions. However, at high impact velocity, the lateral deformation is low due to the inertia effect. Consequently, the value of the Poisson's ratio decreases with increasing impact velocity.

When polymeric foams are used for energy absorption, it is important to understand their mechanical properties under high strain rates. For example, Paul and Ramamurty [124] found that the energy absorbed during plastic deformation of a closed-cell aluminum foam increased with increasing strain rates. This is important for impact energy absorption applications. Also, it demonstrates that metallic foam can absorb more energy at higher strain rates. Similarly, Yi et al. [131] found that the energy absorption of aluminium alloy foams increased by 14-40% when the strain rate increased from  $10^{-3}$  to  $2600\text{s}^{-1}$ . Wang et al. [132] also found that strain rate has a significant effect on the energy absorption efficiency and energy absorption curves of foams, noting that absorption efficiency at strain rates of  $450\text{s}^{-1}$  can be up to 20% higher than at strain rates of  $10^{-3}\text{s}^{-1}$ . They also found that the onset strain of densification (see Section 1.4) is not dependent on the strain rate.

### **2.3.3 Influence of Specimen Size**

Many publications show that the mechanical properties of foams depend significantly on the ratio of the specimen size to the cell size. Mills [4] found that size effects arise whenever the specimen dimensions are not more than 20 times the cell size. Andrews et al. [133] reported that the modulus of elasticity and plastic yield strength of both closed-cell and open-cell aluminium foams increased to a plateau level as the ratio of specimen size to cell size increased. Also, they noted that the strength and the Young's modulus of open-cell foams are reduced more significantly with decreasing specimen size than for closed-cell foams. Size affects are also apparent in the physical properties of foams. Ruiz et al. [134] reported that the diffusion coefficient [92] of an LDPE foam was found to increase when the specimen size decreases. The occurrence of size effects in foams has therefore to be considered when conducting any characterisation of their mechanical properties.

### **2.3.4 Influence of Relative Density**

The mechanical properties of all foams are strongly dependent on their relative densities, which is defined as the foam density, divided by the density of the solid constituent material. Previous researchers [1, 25, 135, 136] have modelled the mechanical behaviour of foams in terms of their relative density. Gibson and Ashby [1] showed that the results of their model (see Equations (2-37) - (2-40)) compared well with experimental

## CHAPTER 2 LITERATURE REVIEW

measurements for rigid and flexible foams over a range of foam densities. The data for open-cell foams of different densities was well-fitted by the expressions:

$$\frac{E}{E_s} \approx R^2 \quad (2-37)$$

$$\frac{G}{E_s} \approx \frac{3}{8} R^2 \quad (2-38)$$

$$\frac{\sigma_{pl}}{\sigma_{ys}} \approx 0.3R^{3/2} \quad (2-39)$$

or

$$\frac{\sigma_{pl}}{\sigma_{ys}} \approx 0.23R^{3/2}(1 + R^{0.5}) \quad (2-40)$$

where  $R$  is relative density,  $E_s$  is the Young's modulus of the polymer,  $E$  is the Young's modulus of the foam,  $G$  is the shear modulus of the foam,  $\sigma_{pl}$  is plastic collapse strength of rigid foam and  $\sigma_{ys}$  is the yield strength of the solid constituent material.

It is clear from above equations that an increase in the relative density generally leads to an increase in the foam's mechanical properties, including Young's modulus, shear modulus, and plastic yield stress, though the Poisson's ratio is generally much less sensitive to a foam's relative density. The influences of relative density on the onset strain of densification and energy absorption have been comprehensively investigated in the literature [1, 25, 137]. The onset strain of densification decreases with increasing relative density, while energy absorption increases. Malekjafarian and Sadrnezhad [136] experimentally studied closed-cell aluminium alloy foams with densities ranging from 0.4 to 0.7  $\text{gcm}^{-3}$  manufactured by a melt-foaming process. They noted that bending stress and compressive strength increase linearly with increasing foam densities in agreement with the Gibson and Ashby model. Moreover, they observed that the energy absorption increases linearly with increasing foam densities.

### 2.3.5 Determination of Strain Regime

In order to describe the mechanical behaviour of foam under large uniaxial compression, it is very useful to determine the onset strain of densification and the efficiency of energy absorption. The values of these terms are useful for effective design of packaging and crush-padding using foam materials and can be measured directly from compression stress-strain curves.

#### 2.3.5.1 Onset Strain of Densification

In general the compressive stress versus strain curves of polymeric foam can be divided into three regions namely: the linear elastic region, the plateau region and the densification region (see Section 1.4). The plateau region starts from the yield stress. The end of the plateau region represents the onset strain of densification. Several publications [1, 124, 138-141] have attempted to determine the onset strain of densification in an objective manner. The works published in [124, 138, 139] all advocate the measurement of the onset strain of densification using the intersection of tangent lines fitted to both the stress plateau region and the densification region. Vural and Ravichandran [140] characterised the onset strain of densification as the last point on the plateau region before the stress rapidly increases. Chan and Xie [138] suggested another means of determining the onset strain of densification and suggested it be identified as the point where the slope is approximately equal to the slope in the elastic region. Li et al. [141] proposed yet another method for estimating the onset strain of densification by determining the maximum value of the energy absorption efficiency versus strain curve and. This method is objective and simple. The energy absorption efficiency will be discussed in next section.

Tuncer and Arslan [142] used the concept of the onset strain of densification for designing and optimising titanium foams.

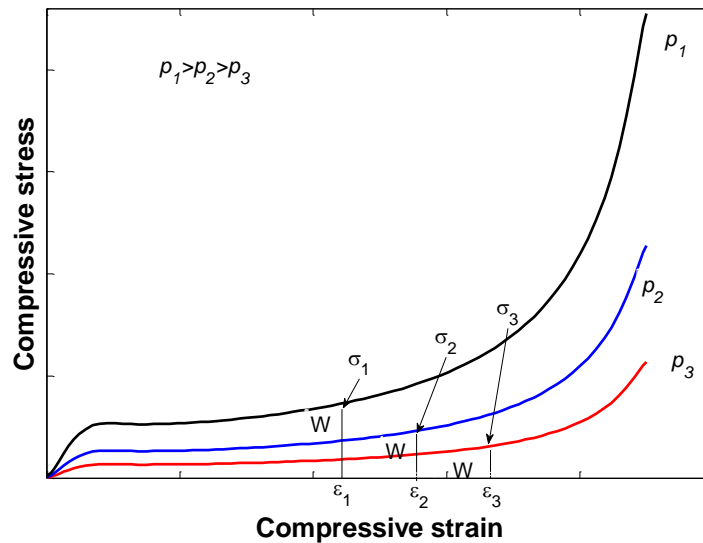
Gibson and Ashby [1] showed that experimental data for densification strain of cellular solids can be modelled accurately over a range of densities using

$$\varepsilon_{de} = 1 - 1.4R \quad (2-41)$$

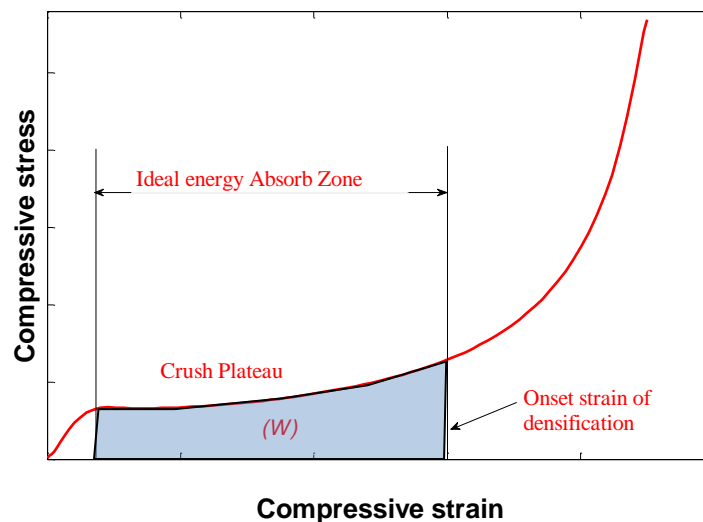
### 2.3.5.2 Energy Absorption Efficiency

For a given application, foam with optimum density can be selected using these techniques. For example, if the foam density is too low, the densification region is reached and a very high loading is achieved before the absorption of the all dynamic energy, whereas if the foam density is too high, the plateau loading can exceed the critical stress magnitude before the dissipation of sufficient energy (see Figure 2-21a). In order to explain this idea, it is important to define energy-absorption.

Energy-absorption represents the area under the compressive stress-strain diagram, see Figure 2-21b. Miltz and Ramon [143] described the energy-absorption efficiency as the ratio between the energy absorbed by the foam compressed to a maximum strain. As previously discussed (see Section 1.1), one goal of using foams is to absorb dynamic energy and keep the maximum load experienced behind the protective foam below some limit. Several publications have attempted to characterise the impact response of polymeric foam, for example, experimental data have been reported for foams made from PE by Miltz and Ramon [143] and PU by Brezny and Green [144]. Avalle et al. [137] developed the characterisation and determination of the energy absorption by the efficiency diagram method and this approach was further enhanced by Li et al. [141].



(a)



(b)

Figure 2-21. (a) The peak stress generated in foams of three densities in absorbing the same energy  $W$  are given by  $\sigma_1, \sigma_2$ , and  $\sigma_3$ . The lowest-density foam ‘bottoms out’ before absorbing the energy  $W$ , generating a high peak stress. The highest-density foam also generates a high peak stress before absorbing the energy  $W$ . (b) stress-strain curves for elastic foam, showing the energy absorbed per unit volume

### 2.3.6 Micro-scale Experimental Investigations

The macro-mechanical behaviour of foams results from their microstructure and the nature of the constituent material. Hence, characterisation of microstructure is important for

## CHAPTER 2 LITERATURE REVIEW

understanding and predicting the mechanical behaviours of foam. As discussed in Chapter 1, microstructure investigations have shown that details of the foam morphology, like variations in the cell wall thickness, cell shape irregularity and anisotropy, can strongly affect the mechanical response of these structures. Consequently, it can be concluded that modelling from a microstructural perspective can only be achieved accurately by using realistic micro-structural information. Over the last 40 years, several methods have been used to characterise the microstructure of foams, such as optical microscopy, scanning electronic microscopy (SEM), X-ray and a microtomography scanner (commonly known as industrial micro-CT scanner). Several researchers have used these techniques to characterise foam microstructure; for example, Rhodes [145] used optical microscopy techniques to measure many details of foam microstructure, including cell walls thickness, cell diameters, cell edges thickness and cell edge lengths. However, due to the complicated random microstructure of foams, characterising the latter manually using optical microscopy techniques is time-consuming, and often damages the specimen, in contrast micro-CT is a non-destructive technique. In addition, some distinguishing features of foams, such as cell volume, are extremely difficult to measure using optical microscopy. Digital image processing can help resolve these issues. Previous studies using 2-D and 3-D image processing have been used to automate foam measurement data in a fraction of the time required for manual inspection. In most of these investigations [17, 40, 146] automated image analysis is used to extract micro-structural information. Eric et al. [147] used X-ray CT in their studies. This technique can directly provide a 3-D description of the foam's microstructure. An advantage of this technique is that it can be used in different directions and consists of voxel data, including grayscale values, corresponding to the solid material of the microstructure. This technique can be used to determine the final 3-D geometry. The latter can be used as a starting point for FEM analysis. For example, Knackstedt et al. [148] used this method to analyse rigid PU foams with relative densities ranging from 0.28 to 0.52. Using the subsequent computational models the transport properties (fluid permeability, diffusivity and thermal conductivity), Young's modulus, Poisson's ratio and bulk modulus were calculated as a function of the foam's relative density. Their calculation of Young's modulus was close to the relationship given by Equation (2-37). Also, the best correlation for Poisson's ratio was obtained by assuming

## CHAPTER 2 LITERATURE REVIEW

that the Poisson's ratio is a linear function of the porosity. Consequently, Jeon et al. [40] used a similar approach to calculate the plastic collapse stress and the magnitude of the plateau stress of closed-cell aluminum foams subjected to uniaxial compressive loading. Their study was carried out using FEM combined with experimental measurements (see Figure 2-22). It was founded that an increase in the 0.2% offset yield stress of the aluminium constituent material significantly raises the magnitude of the plateau stress; while a reduction in the power-law hardening exponent not only increases the magnitude of the plateau stress, but also modifies the shape of the plateau stage. Subsequently, Youssef et al. [149] applied X-ray micro-tomography in a 3D FEA model for a rigid PU foam of relative density 0.33. The predicted compressive stress-strain curve, Young's modulus, Poisson's ratio, yield stress and hardening coefficient were close to the experimental data. Eventually, Maire et al. [147] compared some of the methods using very simple meshes in two and three dimensions.

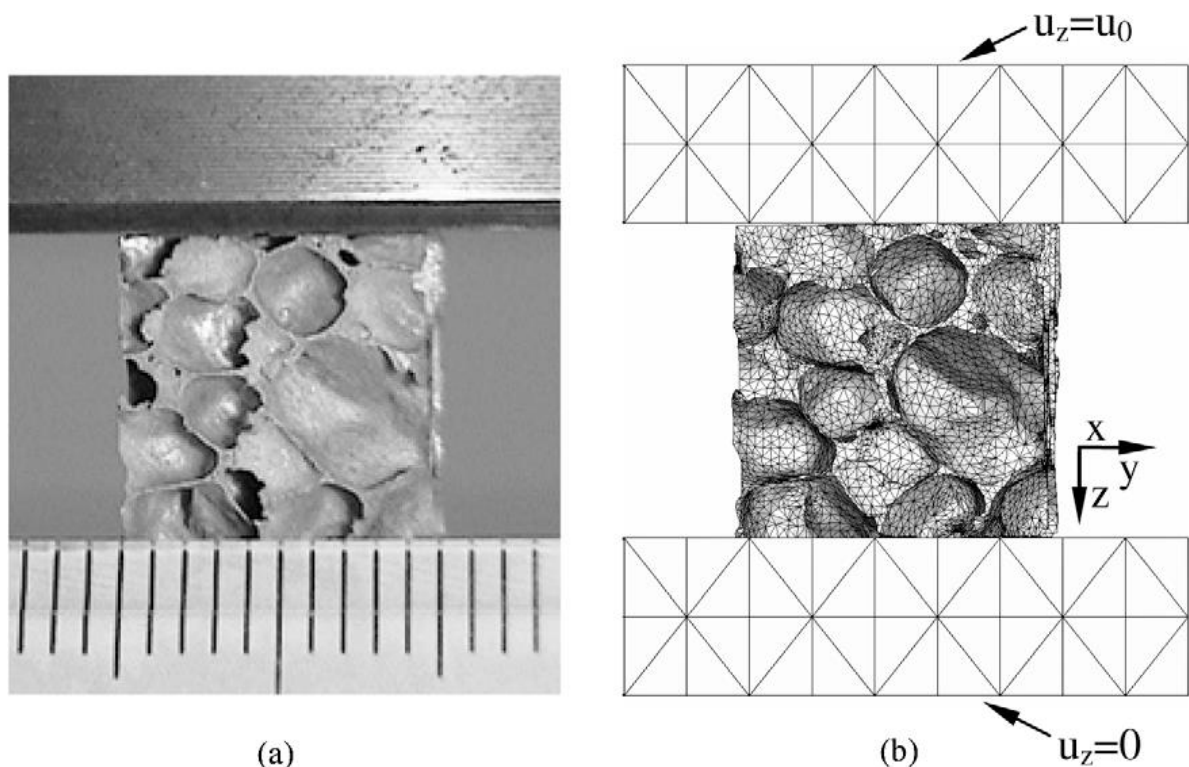


Figure 2-22. ( a) The closed-cell aluminum foams specimen between two loading platens and (b) its finite element model [40].

## **Chapter 3. Experimental Characterisation of a Transversely Isotropic Polymer Foam**

### **Introduction**

There is increasing interest in characterising viscoelastic compressible anisotropic foams such as PUR, PP, PVC and extruded LDPE foams, constitutive models for such foams are not widely available and modelling of anisotropic foams is often only approximate (see Chapter 2). Several published studies have been performed to characterise the mechanical properties for such materials [4, 86, 150]. Experimental data are required in order to evaluate and develop more accurate constitutive models for transversely isotropic foam. Such models can eventually be implemented in finite element software and used in the Computer Aided Engineering (CAE) design process. Factors to consider in model development include the influence of viscoelastic effects such as the dependence of stress on, strain, strain rate and time; other factors include plasticity due to plastic flow of the constituent material and also due to damage of the microstructure.

This chapter focuses on the mechanical and microstructural experimental characterisation of extruded LDPE made by SABIC company (manufacturer's code 2601TX17) closed-cell foam, relative density is 0.0432. This particular material is considered to be a good example of a transversely isotropic viscoelastic compressible material and is consequently chosen for the study. A thorough knowledge of the behaviour of the extruded LDPE foam is vital in understanding the mechanical behaviour of anisotropic flexible polymer foams. Usually, characterisation tests involve well-defined stress or strain fields that allow fitting of the model parameters. When characterising the mechanical behaviour of a given material, the choice of characterisation test can be determined either by the model to which the material response is to be fitted, or by the particular deformation that the material is likely to experience. Material parameters in many constitutive models for compressible foams can be determined using just uniaxial compression without lubrication specimens test and simple shear tests. Other test methods (such as tensile and multi-axial tests are also of interest and can improve the accuracy of fitted material parameters, see Section 2.3), though due to time constraints, attention is limited here to these two primary test methods.

The structure of this chapter is split into two broad sections on experimental characterisation. The first, longer section deals with the macro-scale mechanical characterisation of the foam while a second, shorter section focuses on characterising the foam's microstructure using image analysis techniques. Experimental test setup and procedures for the macro-scale mechanical characterisation tests are first defined. Results from compression and simple shear tests are then presented and discussed. The influence of specimen size, material orientation and rate dependence on mechanical properties including, compressive modulus, yield stress, energy absorption efficiency and onset strain of densification and stress relaxation are evaluated using uniaxial compression tests along the principal material directions. Simple shear tests are used to investigate the shear modulus as a function of the shear strain. Following these tests, compression tests are performed off the material's principal axis, these tests are intended for model evaluation purposes. In the second broad section on experimental characterisation, the cell morphology of the LDPE transversely isotropic closed-cell foam has been examined using optical microscopy and micro-CT. Information on microstructural parameters are quantified and fitted with statistical distributions. This information is used later in Chapter 5 in which both analytical and numerical microstructural models are employed to analyse the foam's macro-mechanical response using computational homogenisation methods.

### **3.1. Macromechanical Characterisation**

Melt-extruded closed-cell LDPE foam specimens were tested under uniaxial compression and simple shear loading. Force versus displacement was measured in each test and in some cases full-field strain measurements were recorded. Ideally further tests on the foam's tensile, hydrostatic and biaxial response would have been performed over a range of temperatures, though the time consuming nature of the tests meant the investigation had to be restricted to practical test matrix. Despite this constraint, the uniaxial and shear tests serve to provide a good understanding of the foam's generic response and provide enough information for basic fitting of constitutive parameters in models already implemented in a commercial FEA code (see Section 4.5).

### 3.1.1. Uniaxial Compression Tests

This test provides important data about the behaviour of foam under compression loads. The uniaxial compression test is often chosen to characterise foams because of the simplicity of the testing configuration and the specimen test shape. Compression data is obtained and from the load-displacement curve it is possible to determine the compressive stress versus strain curves and from there obtain mechanical properties such as the Young's modulus, the yield stress and the Poisson's ratio. Energy absorption efficiency and the onset strain of densification are other well defined properties for foams and because of their importance in the design of foam products have also been used in evaluating the foam mechanical response in this investigation. The uniaxial compression test has been used in this work to investigate various factors including: (i) influence of specimen size on the quasi-static and rate dependent response, (ii) recovery following compression (hysteresis) and (iii) rate dependence and (iv) the foam's off-axis response.

#### 3.1.1.1. Procedure to Determine Stress and Strain (under Uniaxial Compression)

During a uniaxial test, the applied force required to compress the specimen and the displacement of the crosshead are recorded. The nominal stress,  $\sigma$ , is calculated by using Equation (3-1). Here  $A_0$  is the original cross-section area of the specimen and  $F$  is the compression force.

$$\sigma = F / A_0 \quad (3-1)$$

Elastic mechanical properties, such as Young's modulus,  $E$ , and elastic yield stress  $\sigma_{el}$ , are shown in Figure 3-1, which represents the elastic response of the material. Young's modulus,  $E$ , is defined as the gradient of the linear elastic region of the nominal stress-strain curve.

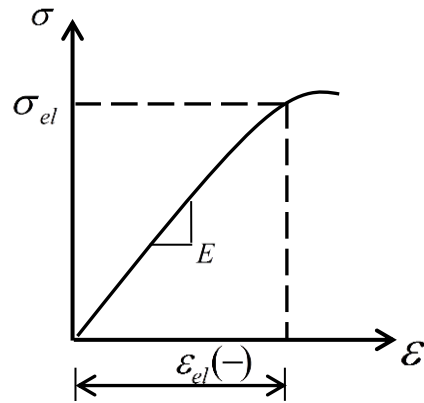


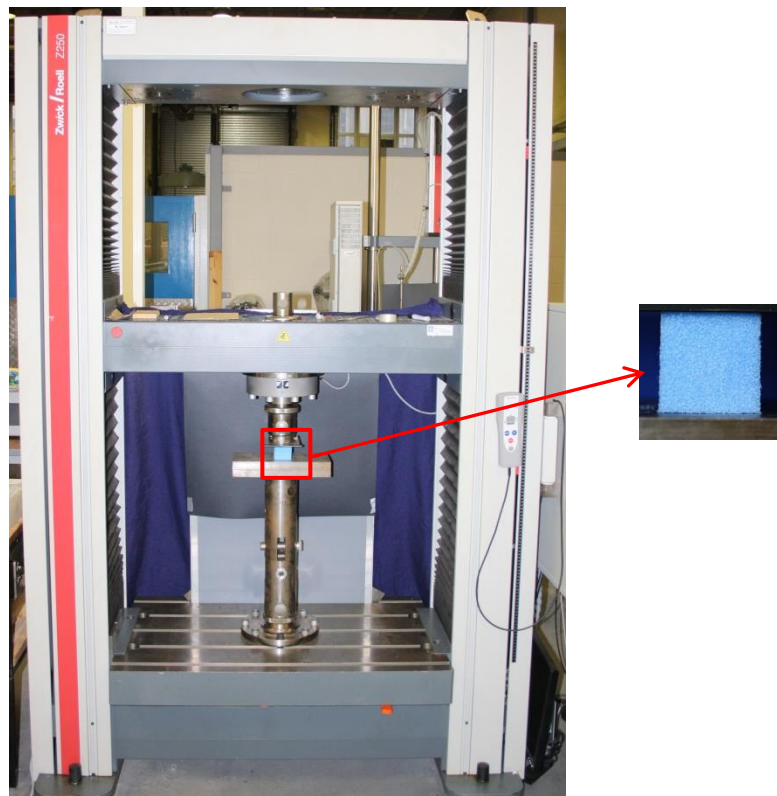
Figure 3-1. Stress-strain diagram showing typical mechanical properties of interest.

The nominal strain,  $\varepsilon$ , is calculated by dividing the specimen compression deformation by the initial height of the specimen (see Figure 3-3), i.e.

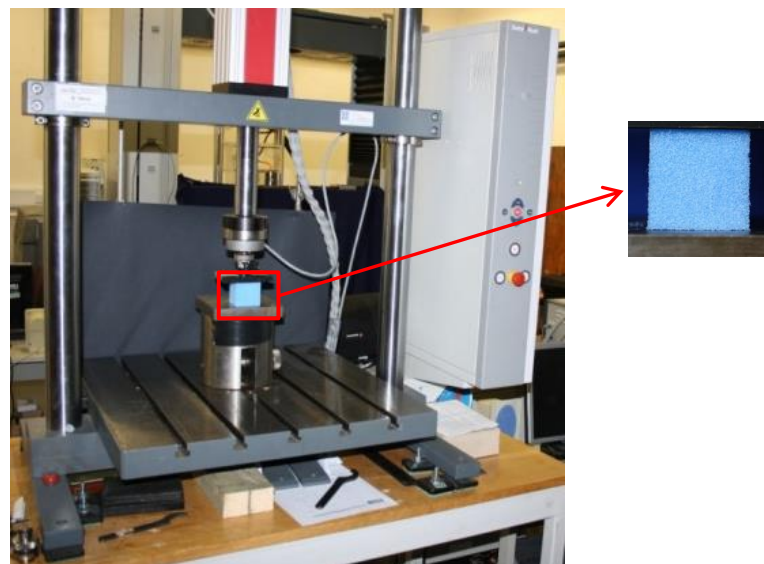
$$\varepsilon = \Delta h / h_0 \tag{3-2}$$

where  $\Delta h$  represents the change in height and  $h_0$  represents the original height of specimen before loading.

All experimental tests were performed using two calibrated compression machines: the first one is a Zwick/Roell Z250 machine with a maximum load of 250 kN, a load cell with 0.01% full-scale accuracy and a maximum compression speed of 600mm/min. The second compression machine is a Zwick/Roell Z2 machine with a maximum load of 2 kN, a load cell with 0.01% full-scale accuracy and a maximum compression speed of 15000mm/min. Photographs of both Zwick/Roell machines are shown in Figure 3-2a and Figure 3-2b. The compression machine consists of a stationary bed and movable crosshead with a driver system for controlling velocity and displacement. These two flat plates are larger than the test specimen and guarantee that compression loading is uniformly distributed over the test specimen.



(a)



(b)

Figure 3-2. Compression testing configuration (a) Zwick/Roell Z250 and, (b) Zwick/Roell Z2.

The set-up of the uniaxial compression test is illustrated in Figure 3-3. Following the relevant test standard, ASTM D1621 [151], all uniaxial compression experiments designed to measure the quasi-static response were carried out at a strain rate of  $0.0016\text{s}^{-1}$ . The specimen dimensions used in this preliminary investigation are cubes measuring:  $10\times 10\times 10\text{ mm}^3$ ,  $20\times 20\times 20\text{ mm}^3$ ,  $50\times 50\times 50\text{ mm}^3$  and  $80\times 80\times 80\text{ mm}^3$ . These were cut using a band saw from an original rectangular extruded section, supplied directly from the manufacturer, which measured approximately  $2000\times 100\times 100\text{ mm}$ . 50 mm and 80 mm side-length cube specimens were compressed using the Zwick/Roell Z250 and Zwick/Roell Z2 machines. The foam specimens were compressed by the upper metal plate. The specimen was placed between the compression plates, ensuring that the specimen centre line passed through the centre line of the two compression plates and the compression loading was distributed as homogeneously as possible on the specimen surface. The parameter  $d$  represents the displacement of the upper plate and  $h_o$  is the original height of specimen. Before compression the specimen is set upon the bottom plate, visual checking of the specimen during the test is required to ensure there is no slippage between the specimen and both metal plates before beginning the test. During the test, the cross-head moves down. The maximum displacement of the top plate was set as  $d = -0.9h_o$  after which the material was completely unloaded at the same rate of strain.

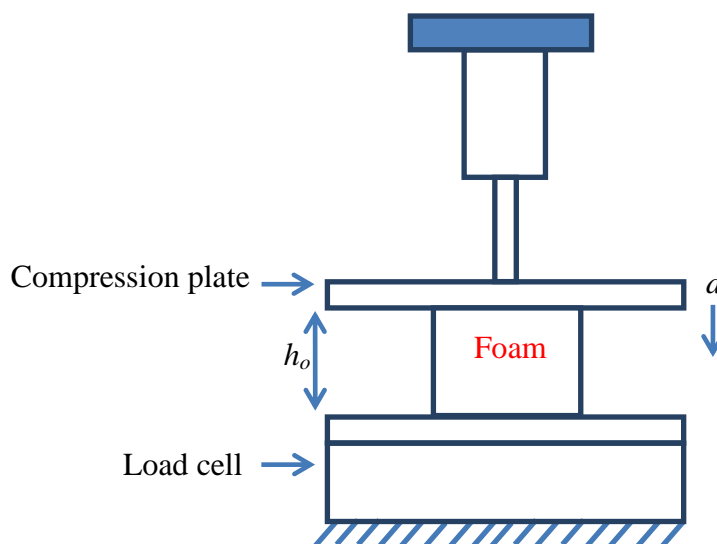


Figure 3-3. Schematic of the uniaxial compression test setup.

### 3.1.1.2. Procedure to Determine the Modulus (under Uniaxial Compression)

The Young's modulus is an important mechanical property. Several techniques have been proposed to determine the Young's modulus from a uniaxial compression test [151]. Here, a modified offset technique is used to compute Young's modulus. This method is used as the initial slope of the compressive stress-strain curves was found to be non-linear, gradually changing with strain (see Figure 3-4). The non-linearity at the start of the curve is thought to be partly due to slight imperfections in the shape of the initial specimen. An objective procedure to determine the Young's modulus was followed: (1) the tangent modulus was determined as a function of strain up to 5%; (2) the maximum modulus in this region was found; (3) data for the tangent modulus lying above 0.7 of this maximum value were used to determine the Young's modulus of the initial 'linear' region; and (4) the average value from the 5% tests was determined, as shown in Figure 3-4 and Figure 3-5.

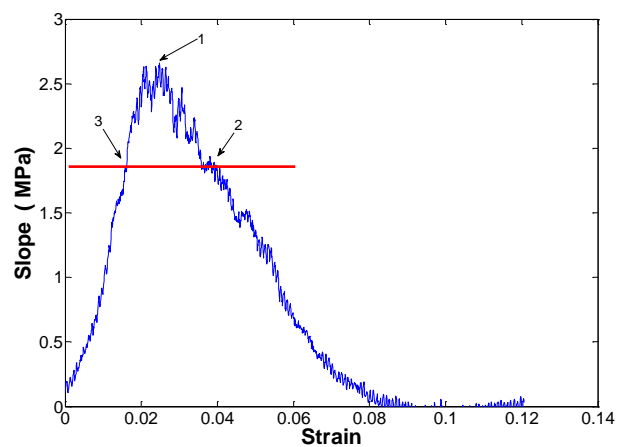


Figure 3-4. Example of the slope versus strain curve; points above the red line are selected for determining Young's modulus.

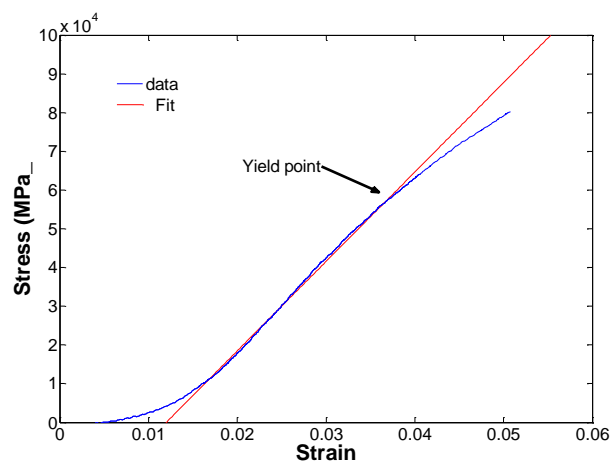


Figure 3-5. Uniaxial compression tests for determining stress-strain curves in the linear elastic region and yield point

### 3.1.1.3. Procedure to Determine the Yield Stress (under Uniaxial Compression)

The yield stress is the location where, as strain increases, there is no increase in the material's stress. However, in a number of soft materials, including many types of foam, the yield point in compression stress-strain curves is difficult to locate accurately. In this investigation the yield stress was taken at the point that the fitted linear line (red line in Figure 3-5) and the actual experimental stress-strain curve diverged by 3%.

### 3.1.1.4. Procedure to Determine Energy Absorption Efficiency and Onset Strain of Densification (under Uniaxial Compression)

The energy absorption efficiency and onset strain of densification are important properties in the design of foam products in protective applications; the maximum force transmitted by the foam must remain below the limit which will cause damage due to excessive accelerations [1]. These well-defined properties are convenient for evaluation of factors such as the influence of size, specimen orientation and strain rate on the mechanical response of foam.

To help explain these properties in more detail, Figure 3-6 shows the three regions typically identified for flexible foams undergoing large compressive deformation, namely the linear elastic, plateau and densification regions. From a microstructural perspective, as the compression stress increases, the foam's cell edges start to collapse through elastic

buckling, elastic yielding or plastic flow and crushing. Yielding of cells tends to progress at a nearly constant load, causing a stress plateau. When foam is subjected to large compressive strain, this eventually results in significant self-contact within the microstructure as the cells collapse. This is the start of the densification region or the ‘onset strain of densification’ and is the cause of the dramatic rise in the stress-strain curve. The stiffness in this region tends towards that of the solid constituent material,  $E_s$ . In the unloading stage, the stress-strain curve also shows a non-linear behaviour.

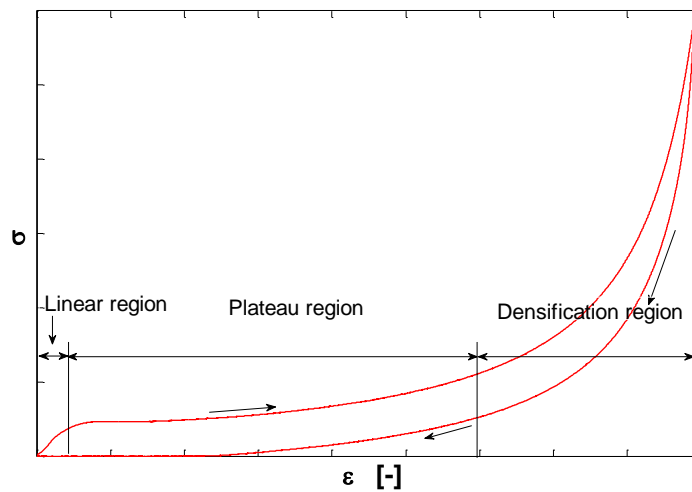


Figure 3-6. Stress-strain curves resulting from a uniaxial compression test.

Understanding energy absorption during impact is one of the most important motivations for characterising the mechanical behaviour of foam, including transversely isotropic foam. The energy input per unit volume in compressing a foam to a specified strain,  $\varepsilon$ , is simply the area under the stress-strain curve, up to the strain  $\varepsilon$ . Relatively little energy is absorbed in the elastic region; in contrast a high plateau stress permits large energy absorption at a near constant stress. The range of the plateau region depends on the mechanical properties, the density of foam and the strain rate.

The most practical method for calculating energy absorption efficiency is by recording the absorbed energy,  $W$ , as a function of stress. The total energy absorption (the area under compression stress-strain curve) is

$$w = \int_0^{\varepsilon} \sigma(\varepsilon) d\varepsilon \quad (3-3)$$

the energy absorption efficiency, is then defined as the ratio of the work done (energy

absorption),  $W$ , to the value of nominal stress

$$\eta(\varepsilon) = \frac{1}{\sigma(\varepsilon)} \int_0^{\varepsilon} \sigma(\varepsilon) d\varepsilon \quad (3-4)$$

The energy absorption efficiency gives a good indication of the efficient application of the foam until a maximum applied stress  $\sigma$ . According, to Li [141], the energy absorption efficiency  $\eta(\varepsilon)$  can be used to objectively identify the onset strain of densification by locating the maximum in the energy efficiency, i.e.

$$\left. \frac{d\eta(\varepsilon)}{d\varepsilon} \right|_{\varepsilon=\varepsilon_{cd}} = 0 \quad (3-5)$$

The ‘onset strain of densification’ and the ‘maximum energy absorption efficiency’ have been used in this investigation to evaluate the influence of specimen size, specimen orientation and strain rate (see Section 3.2.1 ).

### 3.1.1.5. Procedure to Determine Poisson’s ratio (under Uniaxial Compression)

The Poisson’s ratio is another important mechanical property. Determining the Poisson’s ratio versus the compressive strain is necessary because a changing Poisson’s ratio can make an important difference to stress prediction and incorrect values of Poisson’s ratio can reduce accuracy. There are several methods to measure the transverse strain in stiff materials, including, for example, use of an extensometer or an electric gauge. However, for flexible materials such as foam, it is difficult to obtain results using these techniques because they are unsuitable for large strain measurements. Characterisation using image analysis is a more accurate technique. In this work, two optical methods have been used. The first method involves manual analysis of digital images taken at regular intervals during the course of tests and the second method is digital image correlation (DIC). For both methods, specimen dimensions of  $50 \times 50 \times 50 \text{ mm}^3$  were used and compression tests were conducted both along the transverse and principal directions, and at off-axis angles, under different strain rates, in order to characterise the strain and strain rate dependence of the Poisson’s ratios.

### 3.1.1.6. Procedure to determine Poisson's ratio by Manual Image Analysis

The experimental setup consists of a digital camera, camera tripod, and a laptop to record the experimental data, image analysis software and the compression machine. This method is contact-less, and involves only one high-resolution digital camera. The analysis procedure is based on a specimen subject to the uniaxial compression setup described in Section 3.1.1.1. The change in width of the compressed cube is determined by the difference in the number of pixels in the digital images taken at regular intervals using a digital camera and measured using simple image analysis software. The vertical and horizontal dimensions of the specimen were measured according to the change in pixel numbers for each image. According to the description of Poisson's ratio, it is calculated for cube specimens using the following equation

$$\nu = -\frac{\Delta w}{\Delta h} \quad (3-6)$$

where  $\Delta w$  represents the change in width and  $\Delta h$  represents the change in height. The Poisson's ratios of the foam were characterised, as shown in Figure 3-7. Images were taken at regular intervals using a Canon EOS 1000D digital camera and measured using simple image analysis software *ImageJ* [152]. Vertical and horizontal dimensions of the specimen were measured from each image. Specimen dimensions were  $50 \times 50 \times 50 \text{ mm}^3$ , for high strain rates a digital video camera was used. The video was recorded and then converted to images using simple software to determine the Poisson's ratios.

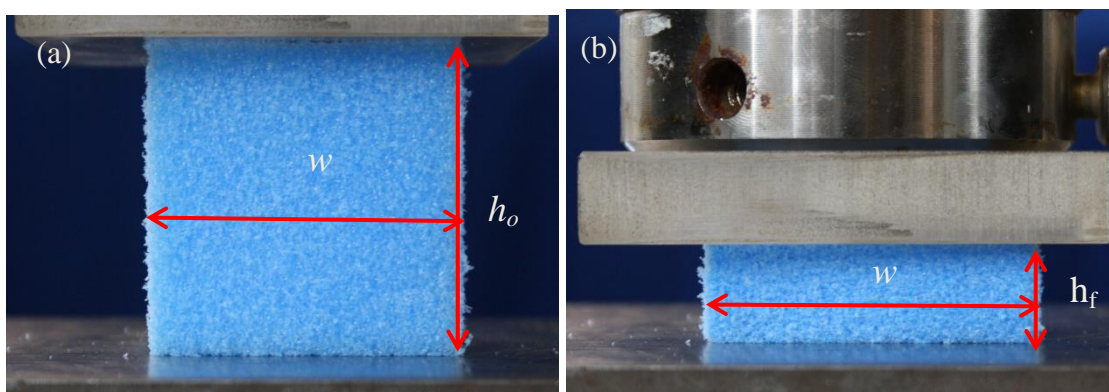


Figure 3-7. Compression tests for determining Poisson's ratio: (a) before compression and (b) after compression.

### **3.1.1.7. Procedure to determine Poisson's ratio by Digital Image Correlation**

The VIC-3D 2010 system has borrowed from EPSRC equipment pool. The VIC-3D system is based on another non-contact optical technique of deformation measurement. This system consists of two video cameras fixed on a tripod by means of a connecting rod (see Figure. 3-8). All analyses were carried out following the relevant Vic-3D testing guide [153]. The specimen was first dotted with spots using a black marker. The spots show high contrast, necessary for accurate deformation measurements. The VIC-3D system was calibrated using a special calibration plate. After the calibration process, the cameras carry out the image acquisition. Images taken using two cameras are analysed sequentially. Eventually, after finishing the image analysis, the software determines the strain data. These data will include a required number of points along which the software calculates the deformation and strain in 3D [153].

In this work the experimental set up for DIC consists of two digital cameras, two light sources, a computer used to record the experimental data and a compression machine. AVT Pike high-resolution 2048x2048 pixel advanced digital cameras were used to obtain the 3D images of the specimen test. These two cameras are capable of shooting 15 frames per second. Gray scale images were used in tests. The size of the tested specimen was (50x50x50mm<sup>3</sup>). The image of the specimen was taken both before and during deformation to facilitate the image analysis. Experimental tests were run for low and high strain rates, so the images were taken at different times and different loading values; these deformed images show the loading distribution in the specimen test. The Poisson's ratio for high strain rates were measured using two methods. The first was based on videos taken using a Sony Cyber-shot DSC-W230 digital camera; the videos were converted to images using a 'video to image converter' software [154]. The second method for measuring Poisson's ratio is performed using the VIC-3D system.

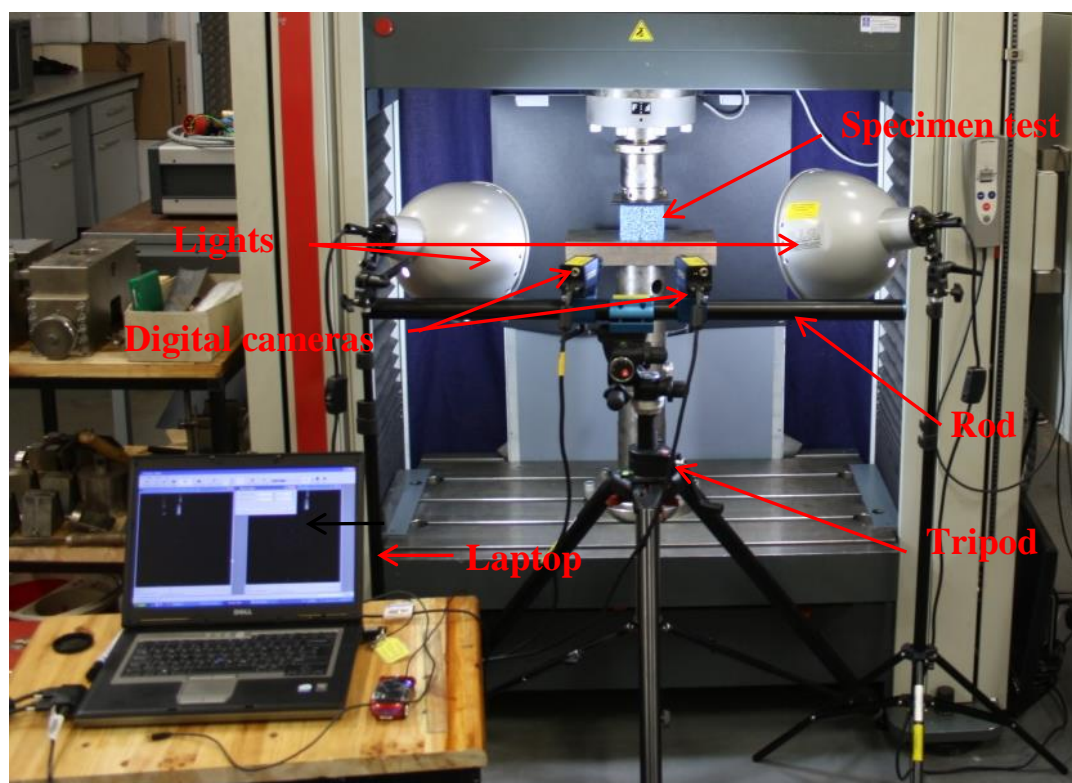


Figure. 3-8. The digital image correlation setup.

### 3.1.2. Stress Relaxation (under Uniaxial Compression)

Viscoelasticity of material can be characterised using a stress-relaxation test. The setup for this test used a Zwick/Roell Z2 machine. A constant strain was applied and the force was measured as a function of time. Cylindrical specimens of dimensions 72 mm diameter and 36mm height were tested as shown in Figure 3-9. The specimens dimensions and experimental setup follow that of BS ISO 3384-2005 [155] .

#### 3.1.2.1. Procedure to Measure Stress Relaxation (under Uniaxial Compression)

Viscoelastic materials show a time-dependent stress in response to the application of constant strain  $\varepsilon_0$ . During the test, the stress relaxation  $\sigma(t)$  is calculated using Equation (3-7)

$$\sigma(t) = F(t) / A_0 \quad (3-7)$$

where  $t$  is time,  $A_0$  is the original cross-section area of the specimen and  $F(t)$  is the compression force as a function of time.

According to time-dependent stress data, the relaxation modulus can be determined from the Equation (3-8)

$$E(t) = \overline{\sigma(t)} / \varepsilon_o \quad (3-8)$$

where  $E(t)$  is the relaxation modulus,  $\sigma(t)$  is the stress both of which are functions of time and  $\varepsilon_o$  is a constant strain.

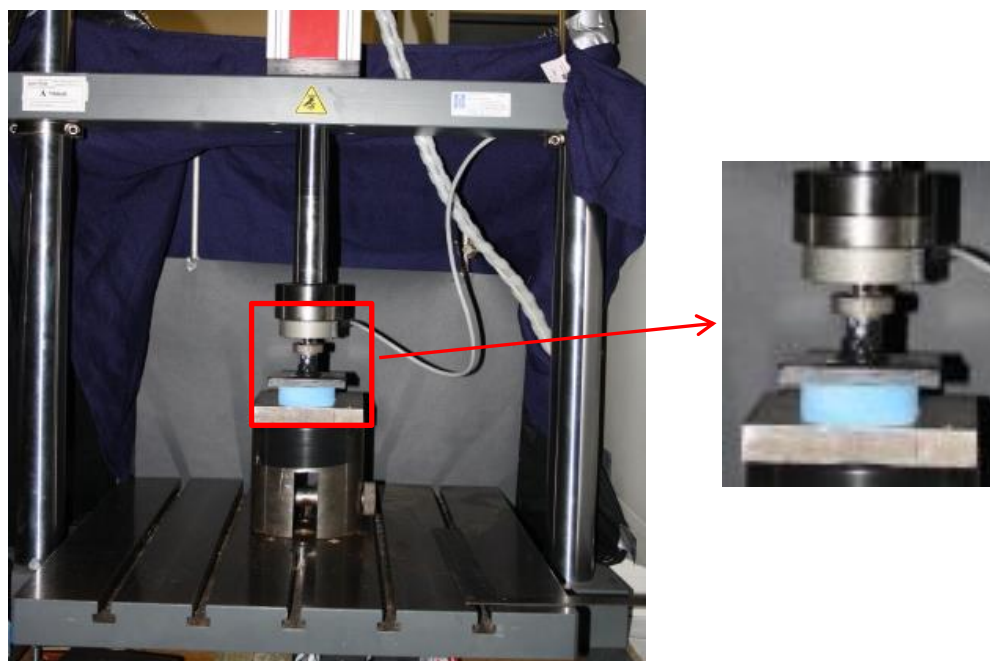


Figure 3-9. Compression test to determine stress relaxation.

### 3.1.3. Simple Shear Test

The experiment set-up for the simple shear test is performed according to BS ISO 1922-2001 [156]. A Zwick/Roell Z250 machine was used for the shear test, with constant speed of movement of the crosshead of 3 mm/min, in a direction parallel to the longitudinal axis of the shear. The test machine exerts a shear force,  $F_e$ , on the specimen (the subscript is refer to elastic region) and creates shear displacement during the test,  $\gamma_e$ . The set-up creates a longitudinal shear loading through two parallel flat rigid plates supports, with plate dimensions 50 mm width, 25 mm thickness and 330 mm length. The plates are fixed to the grips of the test machine as shown in Figure 3-10. In this test epoxy was used to glue the samples to the plates of the test specimen. The adhesive was required to be both stiffer and stronger than that of foam specimen in order to minimise its influence on the test

results. The specimen size (25x50x250 mm) was mounted in the shear test fixture to ensure that the specimen was uncompressed before and during the simple shear test. It was necessary to ensure that the specimen centre line passed through the centre line of the machine to prevent any specimen bending during the shear test, the distance between the metal support plates remains constant and simple shear deformation is applied to the foam sample. Each shear test was repeated five times.

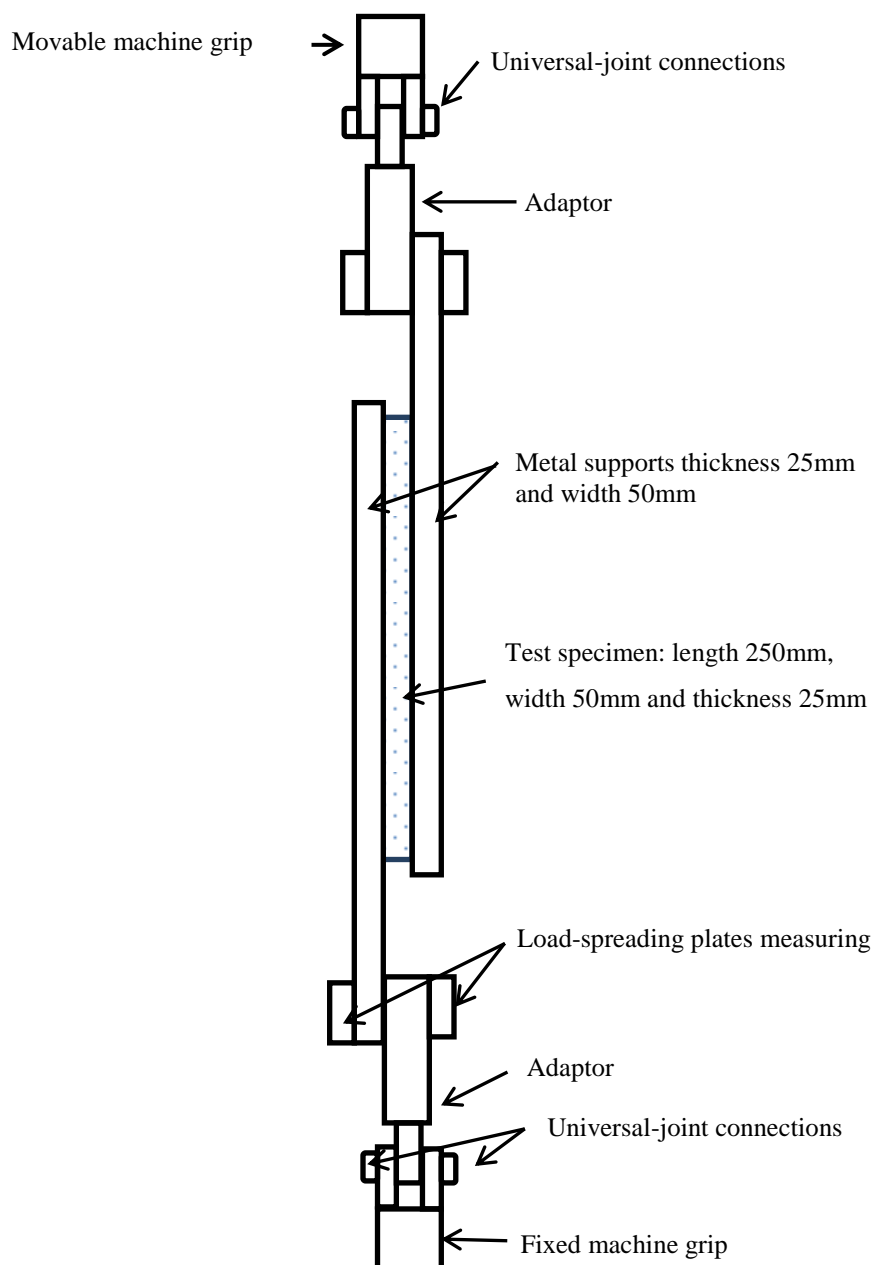


Figure 3-10. Schematic of shear test set-up.

### 3.1.3.1. Procedure to Determine the Shear Modulus

The target of this test is to calculate shear modulus,  $G$ . It is calculated using Equation (3-9)

$$G = \frac{t_s \times \tan a_{el}}{A_o} \quad (3-9)$$

where

$$\tan a_{el} = \frac{F_{el}}{d_{se}} \quad (3-10)$$

and  $A_o$  is the original cross-section area of the specimen,  $t_s$  is the thickness of the specimen and  $a_{el}$  is the slope of the force-displacement curve,  $F_{el}$  is shear force and  $d_{se}$  is shear displacement (Figure 3-11). Here the nominal shear strain (i.e., the engineering shear strain, or the tangent of the shear angle) are used.

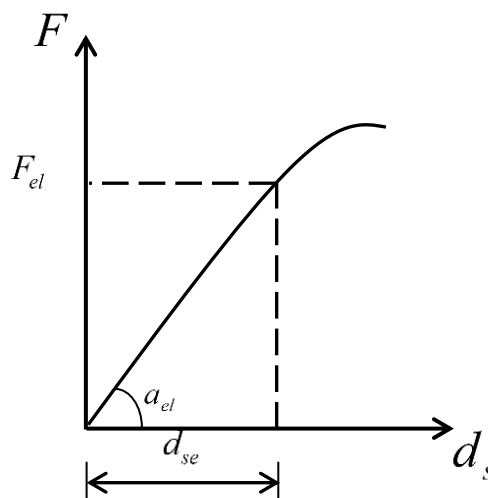


Figure 3-11. Typical force versus shear strain curve.

## 3.2. Results:

### 3.2.1. Influence of Specimen Size and Material Orientation under Uniaxial Quasi-Static Compression on Mechanical Response:

Exploring the specimen size effect on mechanical properties is of interest for both fundamental and practical reasons. One reason is to ensure that the specimen size used in the experimental investigation is a good representation of the foam's actual bulk behaviour. Another reason is to explore the influence of gas diffusion through the specimen. Over time gas diffusion can lead to significant creep in a foam product under load and it is useful to understand the significance of this effect when designing a foam-based product [134]. An initial investigation to explore the effect of specimen size was performed and is described in this section. According to Mills [4] the specimen size should be at least 20 times the cell size to obtain reasonable results. The average cell size was measured to be about  $0.62 \pm 0.3$  mm in the LDPE foam chosen for this investigation (see Section 3.3.2) for a detailed analysis of the foam microstructure), suggesting a minimum sample size of  $10 \times 10 \times 10$  mm<sup>3</sup> side length. The specimen dimensions used in this preliminary investigation are cubes measuring:  $10 \times 10 \times 10$  mm<sup>3</sup>,  $20 \times 20 \times 20$  mm<sup>3</sup>,  $50 \times 50 \times 50$  mm<sup>3</sup> and  $80 \times 80 \times 80$  mm<sup>3</sup> (see Figure 3-12). Specimens were compressed using a Zwick/Roell Z250 machine. All uniaxial compression tests followed the test standard ASTM D1621 [151]. For each specimen size, the tests were repeated at least five times.

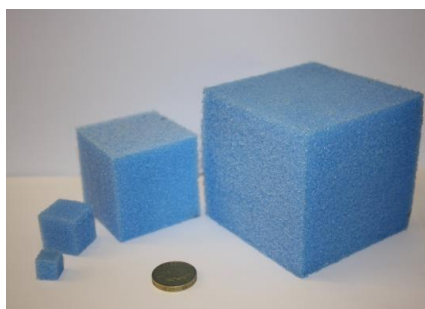


Figure 3-12. Photograph of test specimens, cubes with side lengths of: 10, 20, 50 and 80mm.

All four different sizes were tested under the same strain rate ( $0.0016\text{s}^{-1}$ ). The specimens were cut such that the cubes had one face orthogonal to the direction of extrusion (the principal and transverse directions). Nominal strains and nominal stress definitions are used though large deformation is considered (see Section 3.1.1.1). The mechanical

responses of the principal and the transverse directions for the cube are shown in Figure 3-18. Each test was repeated five times, error bars in Figure 3-18 correspond to the standard deviation (SD). The average compressive stress-strain curves of principal and transverse directions are shown in Figure 3-13 and Figure 3-14. Compressive curves of Figure 3-13 show a significant increase in both the compressive stiffness and strength with specimen size, in both the principal and transverse directions.

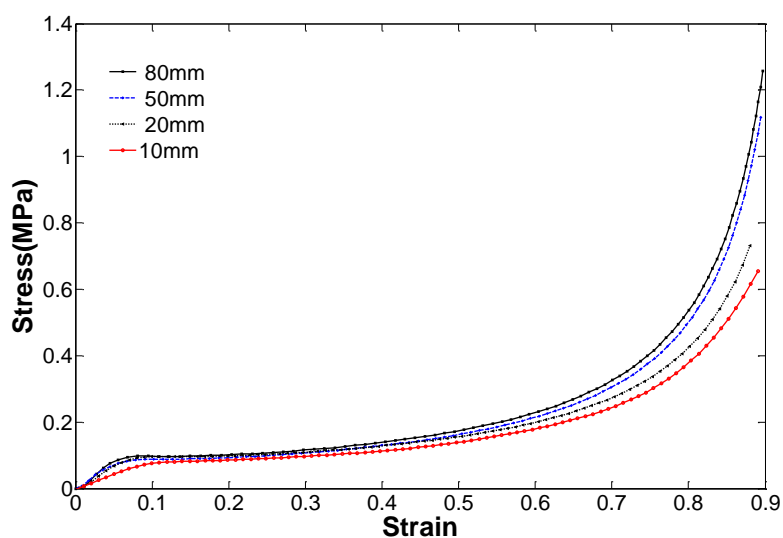


Figure 3-13. Stress-strain curves in the principal direction for four different cube sizes.

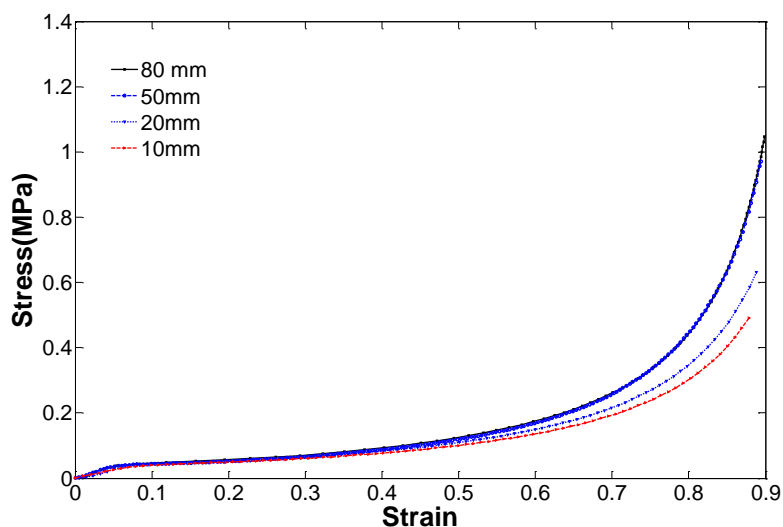


Figure 3-14. Stress-strain curves in the transverse direction for four different cube sizes.

Table 3.1 and Figure 3-15 summarises the measured  $E_p$  (elastic modulus in the principal direction) and  $E_t$  (elastic modulus in the transverse direction) against the specimen sizes.

Table 3.1 Elastic modulus in principal and transverse directions with versus specimen sizes

Specimen size(mm <sup>3</sup> )	10x10x10	20x20x20	50x50x50	80x80x80
$E_p$ (MPa)	0.933±0.562	1.720±0.124	2.039±0.363	2.420±0.124
$E_t$ (MPa)	0.338±0.169	0.750±0.100	0.741±0.157	1.089±0.221

Table 3.1 and Figure 3-15 summarises the measured  $E_p$  (elastic modulus in the principal direction) and  $E_t$  (elastic modulus in the transverse direction) plotted against the specimen size

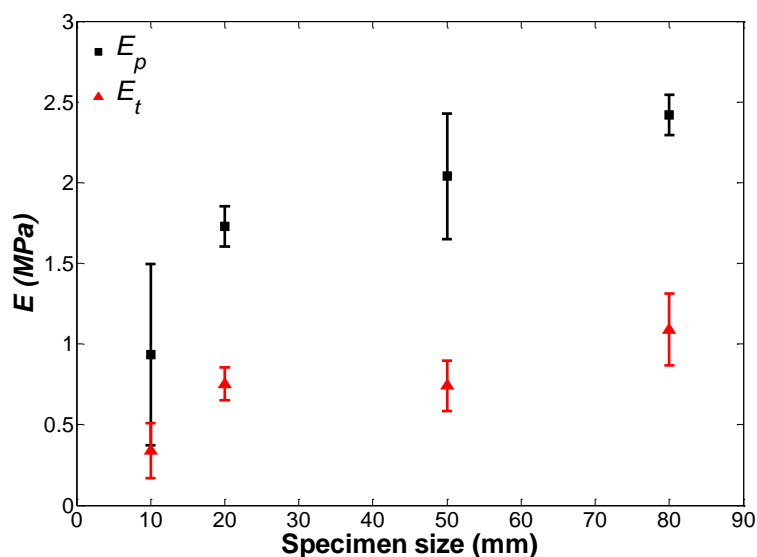


Figure 3-15. Effect of specimen size on elastic modulus.

Similarly, Table 3.2 and Figure 3-16 and summarises the measured  $\sigma_p$  (elastic yield stress in the principal direction) and  $\sigma_t$  (elastic yield stress in the transverse direction) against specimen sizes.

Table 3.2. Yield stress in principal and transverse directions with versus specimen sizes

Specimen size(mm <sup>3</sup> )	10x10x10	20x20x20	50x50x50	80x80x80
$\sigma_p$ (MPa)	0.0410±0.028	0.059±0.004	0.061±0.014	0.073±0.003
$\sigma_t$ (MPa)	0.030±0.001	0.027±0.001	0.026±0.016	0.025±0.002

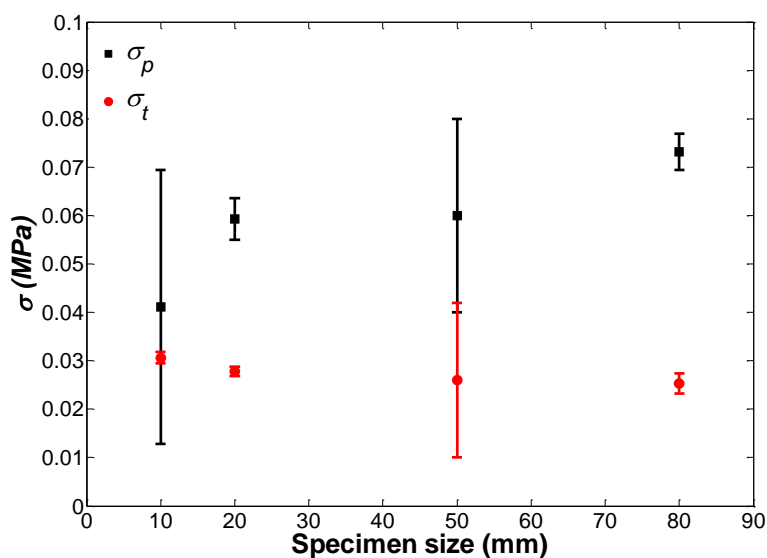


Figure 3-16. Effect of specimen size on yield stress.

The maximum efficiency versus specimen sizes is presented in Table 3.3. The onset strain of densification is approximately constant for different specimen sizes for both directions; it occurs at  $0.61 \pm 0.01$  strain. Efficiency-strain curves are plotted in Figure 3-17. Experimental data show that energy absorption efficiency is much more influenced by the direction of loading than by the size effect.

Table 3.3. Energy absorption efficiency in principal and transverse directions, with versus specimen sizes.

Specimen sizes ( $\text{mm}^3$ )	10x10x10	20x20x20	50x50x50	80x80x80
Efficiency in principal direction%	34.06	35.28	32.45	32.93
Efficiency in transverse direction%	27.96	28.55	27.01	27.56

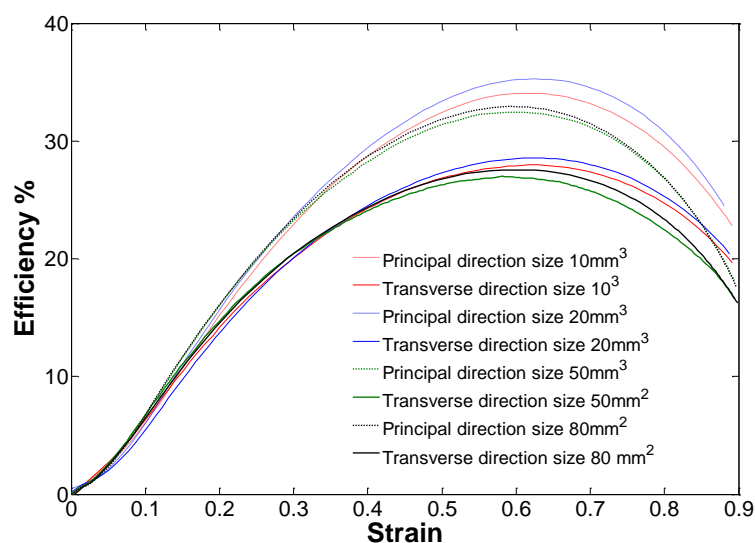


Figure 3-17. Efficiency-strain curves with various specimen sizes

The method to calculate onset strain of densification based on an energy absorption efficiency diagram appears to provide reliable and accurate results. The experimental data showed that energy absorption efficiency is higher in specimens of 10x10x10 mm<sup>3</sup> and 20x20x20 mm<sup>3</sup>, and lower in specimens of 50x50x50 mm<sup>3</sup> and 80x80x80 mm<sup>3</sup> size. The onset strain of densification is approximately constant with different specimen sizes. Following these tests on specimen size, it was concluded that the 50mm cubes were sufficiently accurate for use in further experimental testing and due to their recommendation in the test standard [151] were chosen over the 80mm cubes for the remainder of the tests. In Section 4.4 an explanation for this strong size dependency in terms of gas diffusion is proposed.

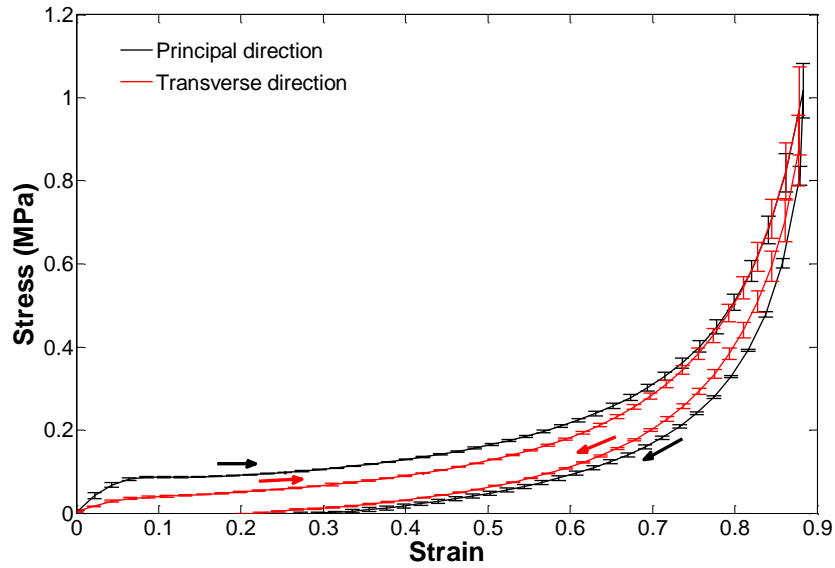


Figure 3-18. Compression loading and unloading stress–strain curves for 50x50x50 mm cube 90% strain loading/unloading in the principal and the transverse directions. The error bars indicate the standard deviation (SD) from five repeats.

Because the compressive responses along the transverse directions are very close to each other (especially when the strain is less than 0.6, as indicated by the small standard deviation in Figure 3-18, the LDPE foam can be considered to be well described as a transversely isotropic material. The modulus along the principal direction,  $E_p = 2.039 \pm 0.363$  MPa (error is given by the standard deviation), where the subscript  $p$  indicates the principal direction (and axis  $x_1$  is always used for the principal direction), and the transverse directions are indicated by subscript  $t$  (or axes  $x_2$  and  $x_3$ ). This is much larger than the average modulus along the transverse direction,  $E_t = 0.741 \pm 0.157$  MPa. Thus, in the small-strain regime, the foam is almost three times as stiff in the principal direction than in the transverse directions and therefore shows significant transverse isotropy [45]. Also, using the procedure described in Section 3.1.1.3, the average yield stress in the principal direction,  $\sigma_p$ , is found to be  $0.061 \pm 0.014$  MPa, this is more than twice as high as the average yield stress in the transverse direction,  $\sigma_t$ , which is  $0.026 \pm 0.016$  MPa.

### 3.2.2. Influence of Compressive Strain and Time on Recovery

Looking now at the time dependent loading/unloading response of the foam Figure 3-19a - b, and Figure 3-20a-b and show hysteresis in the curves suggesting viscoelasticity and at least some degree of semi-permanent deformation. However, given enough time the

specimen almost completely recovers its Figure 3-20 original shape. Still, repeat tests after several days indicate permanent changes in the loading curve, suggesting damage to the foam's internal structure. As the maximum applied strain is increased the degree of permanent change to the loading curve (damage) also increases. Thus, the general behaviour of this material is complex and results from a combination of viscoelastic and plastic deformation in the skeletal framework of the polymer foam coupled with compression and diffusion of the gas within and between the closed cell microstructure.

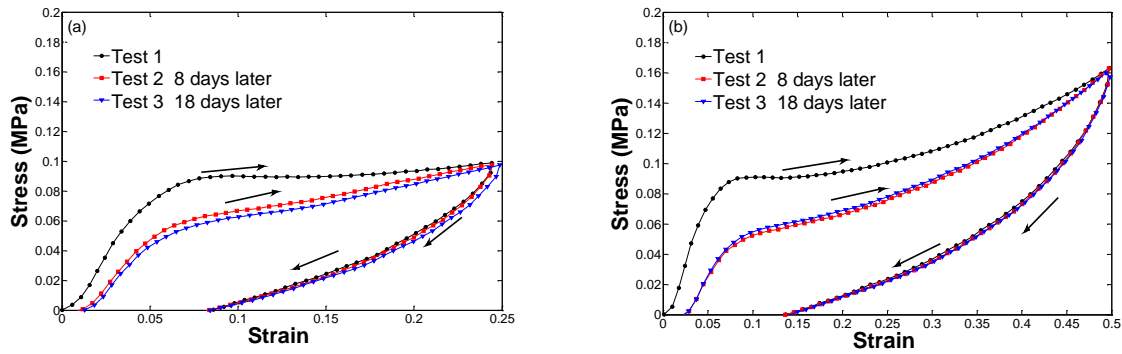


Figure 3-19. Compression loading and unloading stress–strain curves in the principal direction conducted several days apart for 50x50x50 mm<sup>3</sup> (a) 25% compression and (b) 50% compression.

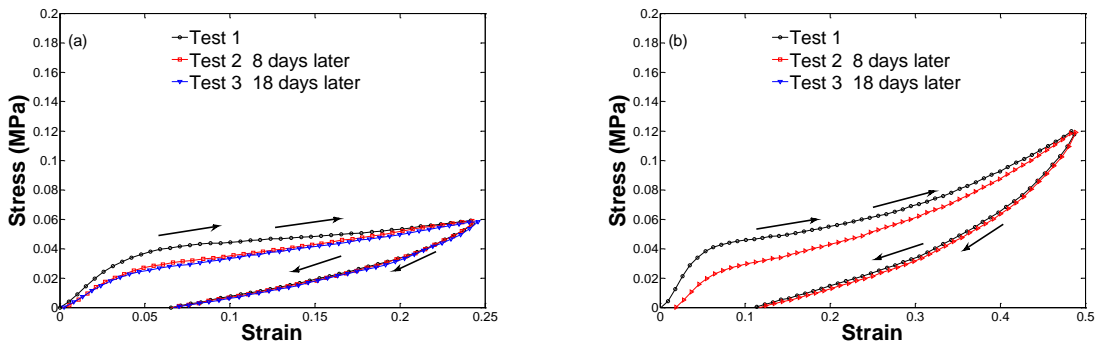


Figure 3-20. Compression loading and unloading stress–strain curves in the transverse direction conducted several days apart for 50x50x50 mm<sup>3</sup> (a) 25% compression and (b) 50% compression.

### 3.2.3. Influence of Compressive Strain on Poisson's ratio

Compression tests were conducted both along and orthogonal to the principal direction in order to calculate the Poisson's ratios in these different directions (see sections 3.1.1.5 and 3.1.1.6 for set-up and procedure). Initially the manual method was employed before using the DIC method to complement and compare the data. When compression is along the principal direction, the nominal strains can be determined as shown in Figure 3-21a and Figure 3-21b

$$\varepsilon_{11} = \varepsilon_p = \frac{|kr| - |KR|}{|KR|}, \quad \varepsilon_{22} = \varepsilon_t = \frac{|mn| - |MN|}{|MN|} \quad (3-11)$$

where  $|KR|$  represents the distance between points  $K$  and  $R$ . The lateral strain  $\varepsilon_{22}$  is plotted against the compression strain  $\varepsilon_{11}$  in Figure 3-21c. The Poisson's ratio  $\nu_{pt}$  is defined as

$$\nu_{pt} = -\frac{\varepsilon_t}{\varepsilon_p} = \nu_{12} \quad (3-12)$$

Here the first subscript  $p$  indicates the compressive loading direction ( $\mathbf{x}_1$ ), while the second subscript  $t$  indicates that the lateral direction of the measured strain is a transverse direction ( $\mathbf{x}_2$ ). Similarly, when the compressive loading is applied along a transverse direction,  $\mathbf{x}_2$ , the lateral strains  $\varepsilon_{11}$  and  $\varepsilon_{33}$  are measured (see Figure 3-21d) and the related Poisson's ratios are defined as

$$\nu_{tp} = -\frac{\varepsilon_{11}}{\varepsilon_{22}} = \nu_{21}, \quad \nu_{tt} = -\frac{\varepsilon_{33}}{\varepsilon_{22}} = \nu_{23} \quad (3-13)$$

Because of the nonlinear nature of the material's response, the three Poisson's ratios are not constants and are plotted against the compressive strain in the loading direction (Figure 3-21e).

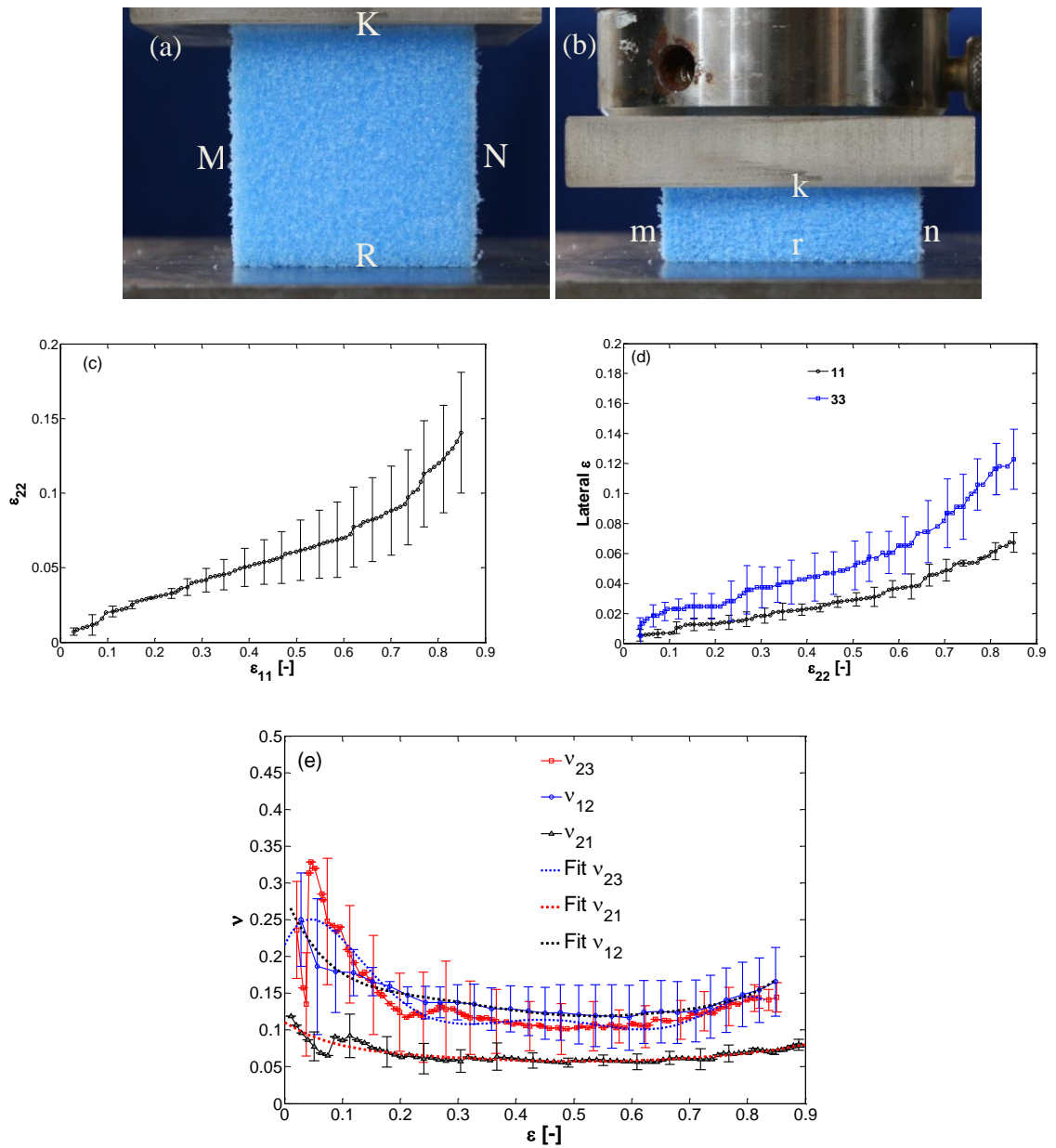


Figure 3-21. Compression tests for determination of the Poisson's ratio: (a) before compression; (b) after compression; (c), (d) measured lateral strains versus compressive strain; and (e) measured Poisson's ratios versus compressive strain, error bars indicate the standard deviation of 3 repeat tests.

The strain-dependence shown in Figure 3-21e can be fitted by the following sixth order polynomials:

$$\nu_{pt} = 0.265 - 1.503\epsilon_p + 8.493\epsilon_p^2 - 26.931\epsilon_p^3 + 45.890\epsilon_p^4 - 39.413\epsilon_p^5 + 13.562\epsilon_p^6 \quad (3-14)$$

$$\nu_{tp} = 0.110 - 0.501\epsilon_t + 2.482\epsilon_t^2 - 7.167\epsilon_t^3 + 11.425\epsilon_t^4 - 9.215\epsilon_t^5 + 2.975\epsilon_t^6 \quad (3-15)$$

$$\nu_{tt} = 0.215 + 1.750\epsilon_t - 26.535\epsilon_t^2 + 120.470\epsilon_t^3 - 249.9\epsilon_t^4 + 244.490\epsilon_t^5 - 91.264\epsilon_t^6 \quad (3-16)$$

The Poisson's ratio was also measured using a DIC system (see sections 3.1.1.5, 3.1.1.6 and 3.1.1.7 for set-up and procedure). Figure 3-22 shows the images of the undeformed and deformed specimens; both images are correlated using DIC software. The Poisson's ratio of the test specimen was defined for specific positions, as shown in Figure 3-22. This position is correlated using DIC software to calculate average strains in the horizontal and normal directions for these selected positions. Poisson's ratio is determined as

$$\nu = -\frac{\varepsilon_x}{\varepsilon_y} \quad (3-17)$$

Figure 3-23a shows the comparative data of Poisson's ratio measured using DIC with data measured using the manual image analysis method. The same position has been selected on the specimen for comparison though because of the DIC software limitations, it is not possible to cover all the edges of the specimen during the test see Figure 3-22a and Figure 3-22b. Figure 3-23a shows the data obtained using the two techniques. The Poisson's ratio values  $\nu_{12}$  using the manual method gives results that are 100% higher than DIC method. This is thought to be due to the limitation of the DIC to cover the high strain changes at the edges of the specimen during the test. Figure 3-23b shows the results for the Poisson's ratio  $\nu_{21}$  are in better agreement with an average discrepancy of about 25% between the two methods.

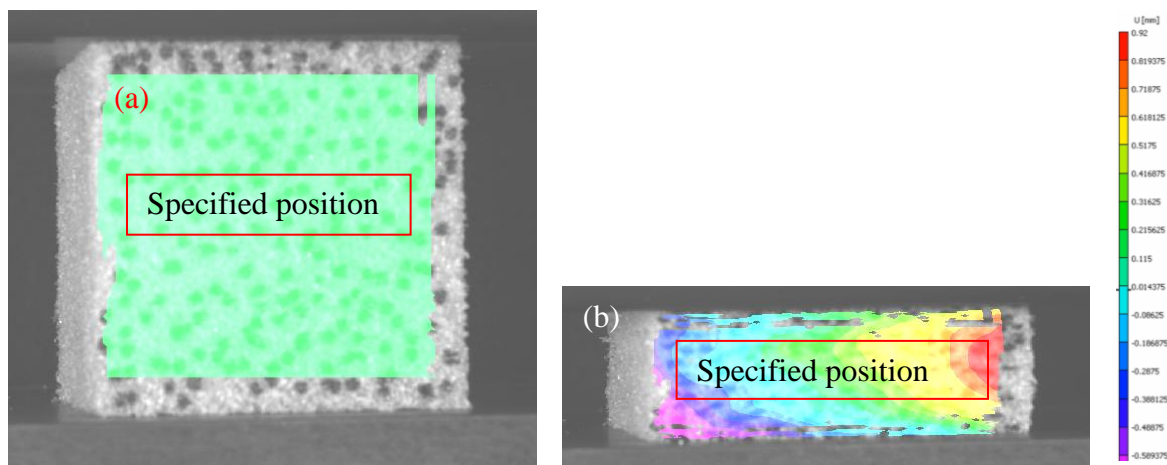


Figure 3-22. Compression tests for determining Poisson's ratio: (a) before compression; (b) after compression and the colours are indicate the displacement in x-direction of specimen test. .

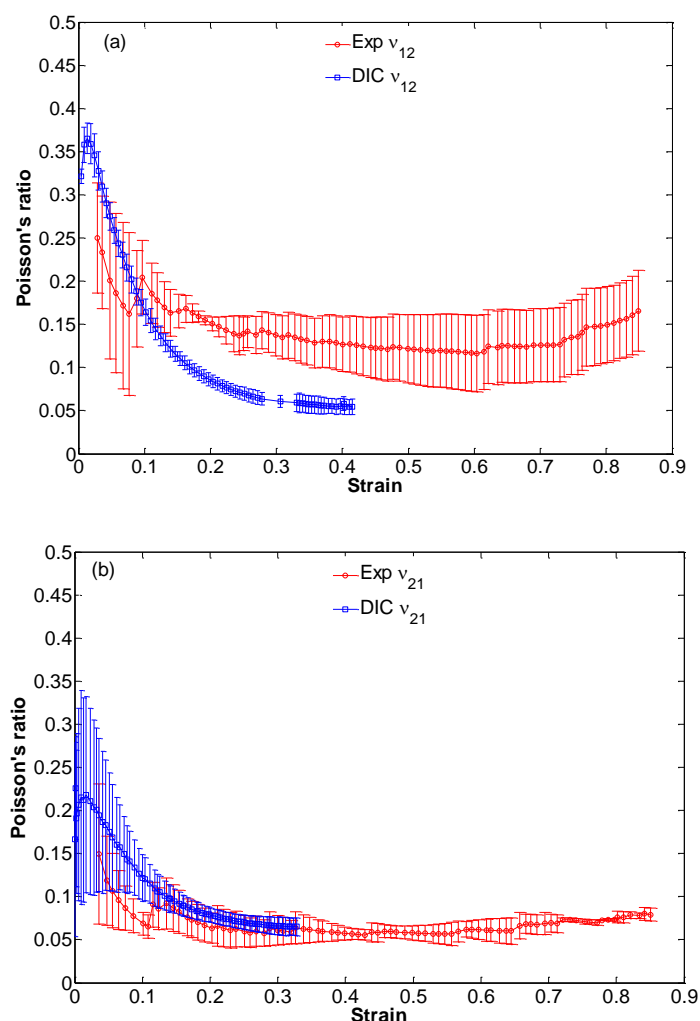


Figure 3-23. Comparison between Poisson's ratio calculated by manual *image-J* method and DIC: (a) comparison of Poisson's ratio  $v_{12}$  and (b) comparison of Poisson's ratio  $v_{21}$

### 3.2.4. Influence of Compressive Strain Rate on Stress versus Strain Response

Polymeric foam is extensively used for impact energy absorption applications under various strain rates; thus it is important that the mechanical response is known at different strain rates. In order to examine the rate dependent behaviour of the foam, uniaxial tests were conducted over a range of strain rates. The same set-up as that described in section 3.1.1.1 was used though here the test procedure involved the compressive response from the lowest strain rate of  $0.0016\text{s}^{-1}$  to highest strain rate of  $5\text{s}^{-1}$ . Two compression machines were used for uniaxial compression tests. The first machine was a Zwick/Roell Z250, used for compression speeds of 5mm/min, 50mm/min and 500 mm/min and the

second machine was a Zwick/Roell Z2, used for compression speeds of 5000 mm/min and 15000 mm/min. The mechanical behaviour of the principal and transverse directions for a  $50 \times 50 \times 50 \text{ mm}^3$  cube under different strain rates were investigated (this specimen size was chosen following the size effect investigation). An average of three repeats was used to determine the stress-strain curves at a specified strain. The error bars in Figure 3-24 and Figure 3-25 correspond to the standard deviation of the three tests.

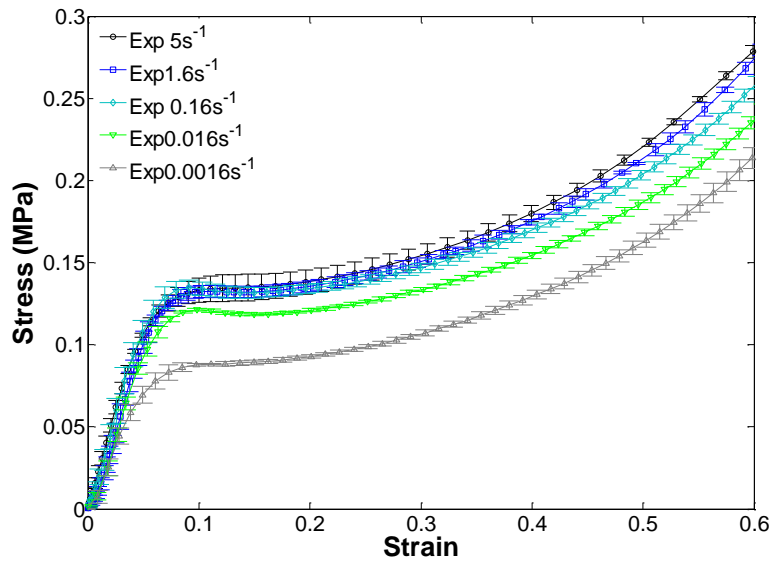


Figure 3-24. Experimental uniaxial compression curves according to data at different strain rates in the principal direction

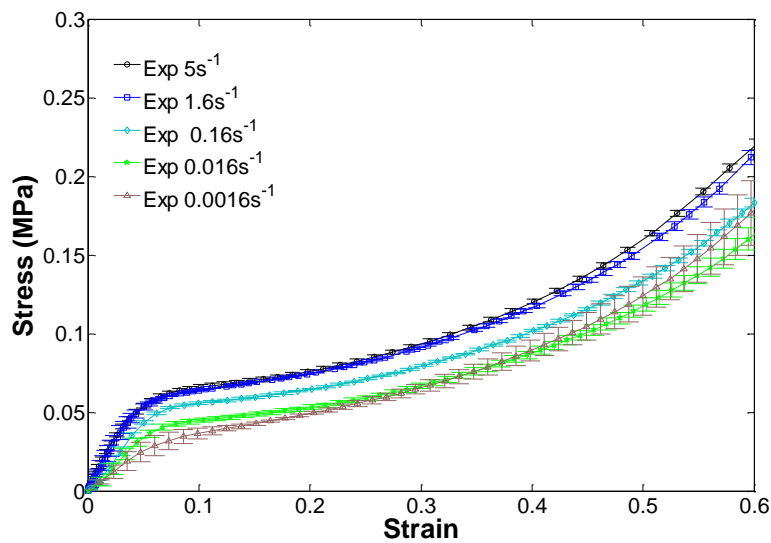


Figure 3-25. Experimental uniaxial compression curves according to data at different strain rates in the transverse direction

The results of various strain rate tests are shown in Figure 3-24 for compression in the principal direction and in Figure 3-25 for the transverse direction. As expected, the stiffness of the material in the principal direction is larger than in the transverse direction. It is clear from Figure 3-24 and Figure 3-25 that the yield stress is sensitive to strain rate.

### 3.2.5. Influence of Rate of Compressive Strain on Energy

#### Efficiency

Figure 3-26 shows the energy absorption efficiency versus strain curves under three different strain rates. It is clear from Figure 3-26 that energy absorption efficiency in the transverse direction is less than in the principal direction. The results show a maximum efficiency of about 36% in the principal direction at a strain rate of  $0.16\text{s}^{-1}$  and a minimum efficiency of about 27% in the transverse direction at strain rate  $0.0016\text{s}^{-1}$ . Under larger strain rates, the maximum efficiency increases slightly. It can also be observed that maximum efficiency for both directions increases nearly linearly with the natural logarithm of compression strain rate (see Figure 3-27), while the onset strains of densification is approximately constant for various strain rates for both directions and it occurs at  $0.59 \pm 0.012968$  strain.

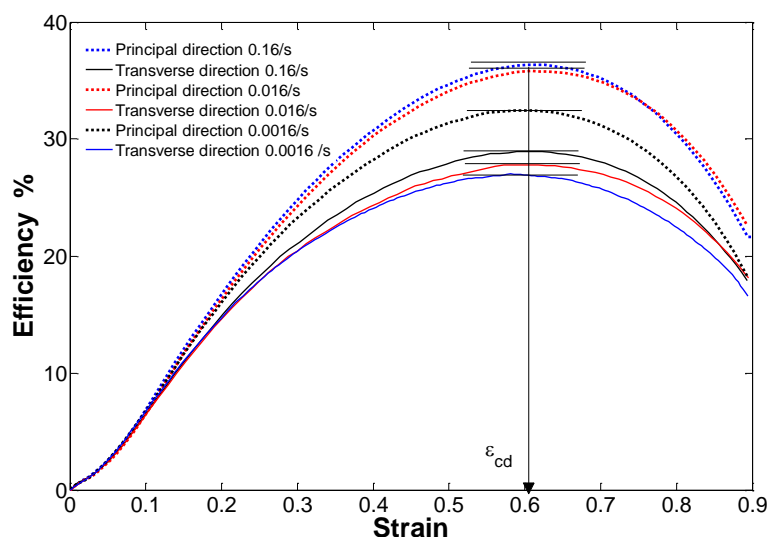


Figure 3-26. Efficiency-strain curves with various strain rates, specimen size  $50 \times 50 \times 50 \text{ mm}^3$ .

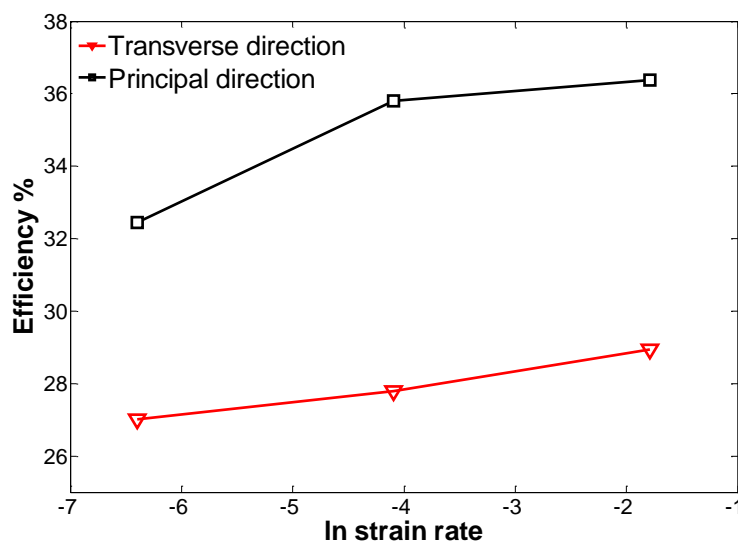


Figure 3-27. Effects of strain rate on the energy absorption efficiency in the principal and transverse directions.

Experimental results showed that the energy absorption efficiency of foam increases nearly linearly with the natural logarithm of strain rate in the transverse direction whereas the behaviour in the principal direction is slightly non-linear. Also, the experimental data show that the energy absorption efficiency in the principal direction is larger than in the transverse direction, while the onset strain of densification is approximately constant with different strain rates.

### 3.2.6. Influence of Strain Rate on Poisson's ratio

The non-linear nature of Poisson's ratio of LDPE foam is highlighted by characterising its dependence on strain rates in the principal and transverse directions (see Section 3.2.3). The aim of this section is to characterise strain rate effects on Poisson's ratio for transversely isotropic foam.

Again, specimens dimensions were (50x50x50 mm<sup>3</sup>), and compression tests were conducted both along and orthogonal to the principal direction in order to calculate different Poisson's ratios. Figure 3-28 (a, b, c, e and f) show the Poisson's ratio versus compressive strain diagrams of the LDPE foams at three strain rates in the principal and transverse directions. Also, Figure 3-28a-f show the determined Poisson's ratio using the manual image-J method compared with the DIC under the same conditions.

Figure 3-28a-f shows the Poisson's ratios,  $\nu_{12}$  and  $\nu_{21}$  versus strain, under various strain

rates. Figure 3-28a shows  $\nu_{12}$  versus strain when compressed at a rate of  $0.016\text{s}^{-1}$ , here the results show poor agreement between the two measurement methods though there is better agreement in Figure 3-28b-f. In order to more easily compare the Poisson's ratio data against strain at different strain rates, Figure 3-29a and Figure 3-29b are plotted using the same data. The Poisson's ratio shows a non-linear response and tends to decrease with strain. In most tests the magnitude of the Poisson's ratio at low strain rates is higher than those at equivalent strains, but at higher strain rates.

The average discrepancies of two measurement methods are shown in Table 3.4.

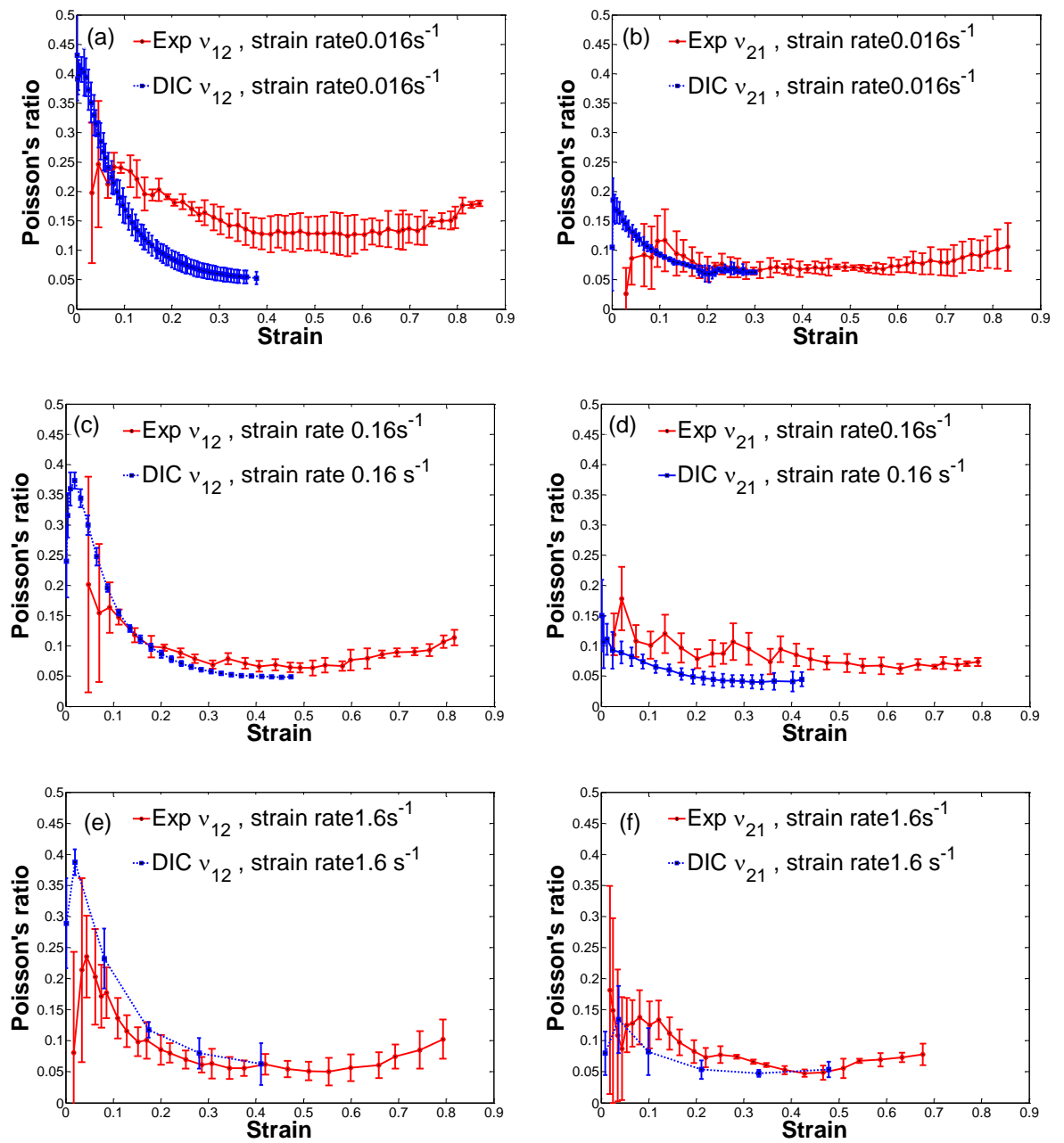


Figure 3-28. Compression tests for determining Poisson's ratio: (a), (b), (c), (d), (e) and (f), measuring lateral strains versus compressive strain rates; error bars indicate the standard deviation of three repeated tests.

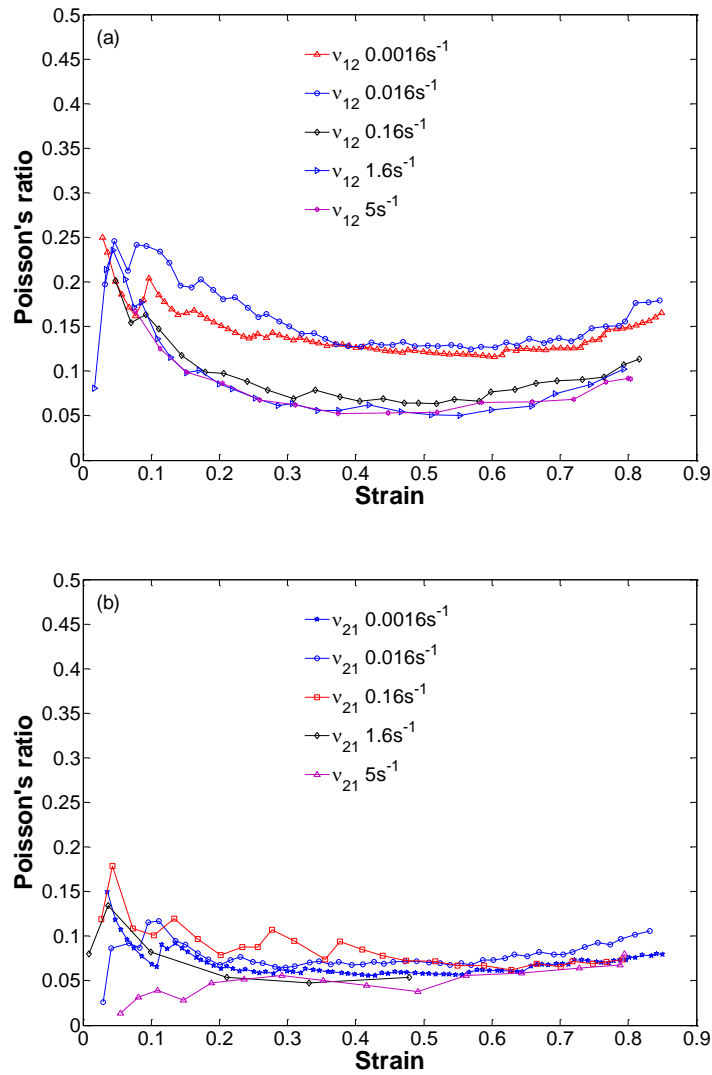


Figure 3-29. Compression tests for determining Poisson's ratio, measuring lateral strains versus compressive strain rates.

Table 3.4. The average difference between the two methods of measuring the Poisson's ratio.

Strain rate	0.016s <sup>-1</sup>	0.16s <sup>-1</sup>	1.6s <sup>-1</sup>
Discrepancy ( $v_{12}$ )	100%	24.03%	19.26%
Discrepancy ( $v_{21}$ )	27.37%	50%	25%

Figure 3-29a shows that the Poisson's ratio  $v_{12}$  is very sensitive to strain rates 0.16s<sup>-1</sup>, 1.6s<sup>-1</sup> and 5s<sup>-1</sup>, the Poisson's ratio  $v_{12}$  values are 0.094 at strain rate 0.16s<sup>-1</sup>, 0.096 at strain rate 1.6s<sup>-1</sup> and 0.082 at strain rate 5s<sup>-1</sup>. Figure 3-29b shows that Poisson's ratio  $v_{21}$  is sensitive to the highest strain rate, 5s<sup>-1</sup>; the average  $v_{21}$  is 0.048.

### 3.2.7. Influence of Stress Relaxation on Relaxation Modulus

Figure 3-30a-b show the stress relaxation values as function of time  $\sigma(t)$ , at two strains in the principal and transverse directions. The material tested under 0.05 compressive strain for a period of 4 hours and tested under 0.2 compressive strain for a period of 0.5 hours. The mechanical behaviour of LDPE show higher stress relaxation in the principal direction than transverse direction by a factor about two times.

Figure 3-31a-b compares the secant moduli of LDPE foam under 0.05, 0.2 strain respectively, in principal and transverse directions. It can be observed that secant modulus in the principal direction is higher than the transverse direction. It can be also noted that the value of  $E(t)$  at 0.05 strain is higher than 0.2 strain by a factor of more than two times.

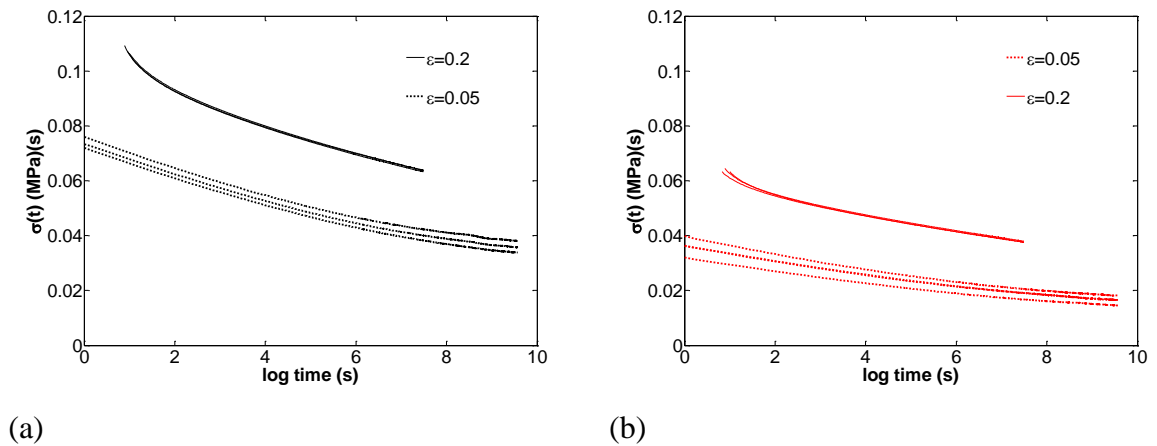


Figure 3-30. Comparison of the compression relaxation stress of LDPE (a) in the principal and (b) transverse directions.

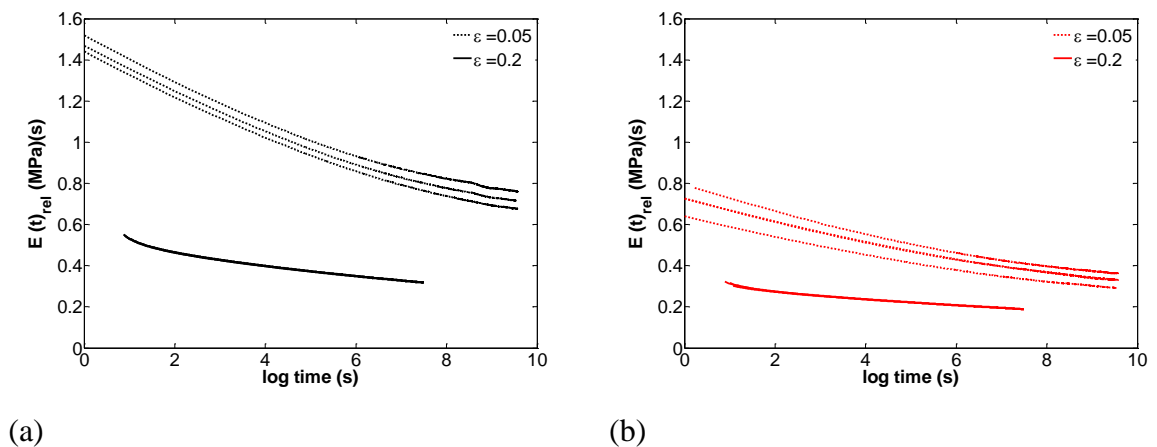


Figure 3-31. Comparison of the compression secant modulus of LDPE (a) in the principal and (b) transverse directions.

### 3.2.8. Influence of Shear Strain on Shear Modulus

The shear moduli of the foam in three different orientations was determined, results in Figure 3-32a show the nominal shear stress versus nominal shear strain,  $\gamma$ , in the principal direction. The curve can be well fitted by the following polynomial function (up to a shear strain of 0.3):

$$\tau(\gamma) = 7.707 \times 10^{-4} + 1.115\gamma - 11.249\gamma^2 + 88.490\gamma^3 - 481.510\gamma^4 + 16.462 \times 10^2 \gamma^5 - 30.925 \times 10^2 \gamma^6 + 2.391 \times 10^3 \gamma^7 \quad (3-18)$$

The tangent shear modulus in this region of strain can then be derived as

$$G_{pt}(\gamma) = \frac{d\tau}{d\gamma} = 1.115 - 22.498\gamma + 265.470 \times \gamma^2 - 1.926 \times 10^3 \gamma^3 + 8.231 \times 10^3 \gamma^4 - 18.555 \times 10^3 \gamma^5 + 16.738 \times 10^3 \gamma^6 \quad (3-19)$$

The tangent shear modulus,  $G_{pt}$  (or  $G_{12}$ ), in the principal direction is plotted against the shear strain in Figure 3-32a. Clearly  $G_{pt}$  decreases dramatically with increasing shear strain. Similarly, the shear modulus,  $G_{tp}$  (or  $G_{21}$ ), in the principal direction versus shear strain is shown in Figure 3-32b. The results in Figure 3-32a and Figure 3-32b show there is reasonable agreement between the two shear modulus,  $G_{pt}$  and  $G_{tp}$ , in the elastic region with a maximum difference of about 20%. Figure 3-32c shows the tangent shear modulus in the transverse direction,  $G_{tt}$ , against shear strain. The results in Figure 3-32b shows that  $G_{tt}$  is the lowest value among three directions. Also, it can be observed, that the shear modulus,  $G_{tt}$ , decreases with shear strain, but at a lower rate of decrease compared to  $G_{pt}$  and  $G_{tp}$ . Note that ideally, both specimen size and rate effects would also have been investigated using the shear test set-up. However due to time constraints only the specimen size and strain rate recommended in BS ISO 1922-2001 [156] were used in the simple shear test investigation.

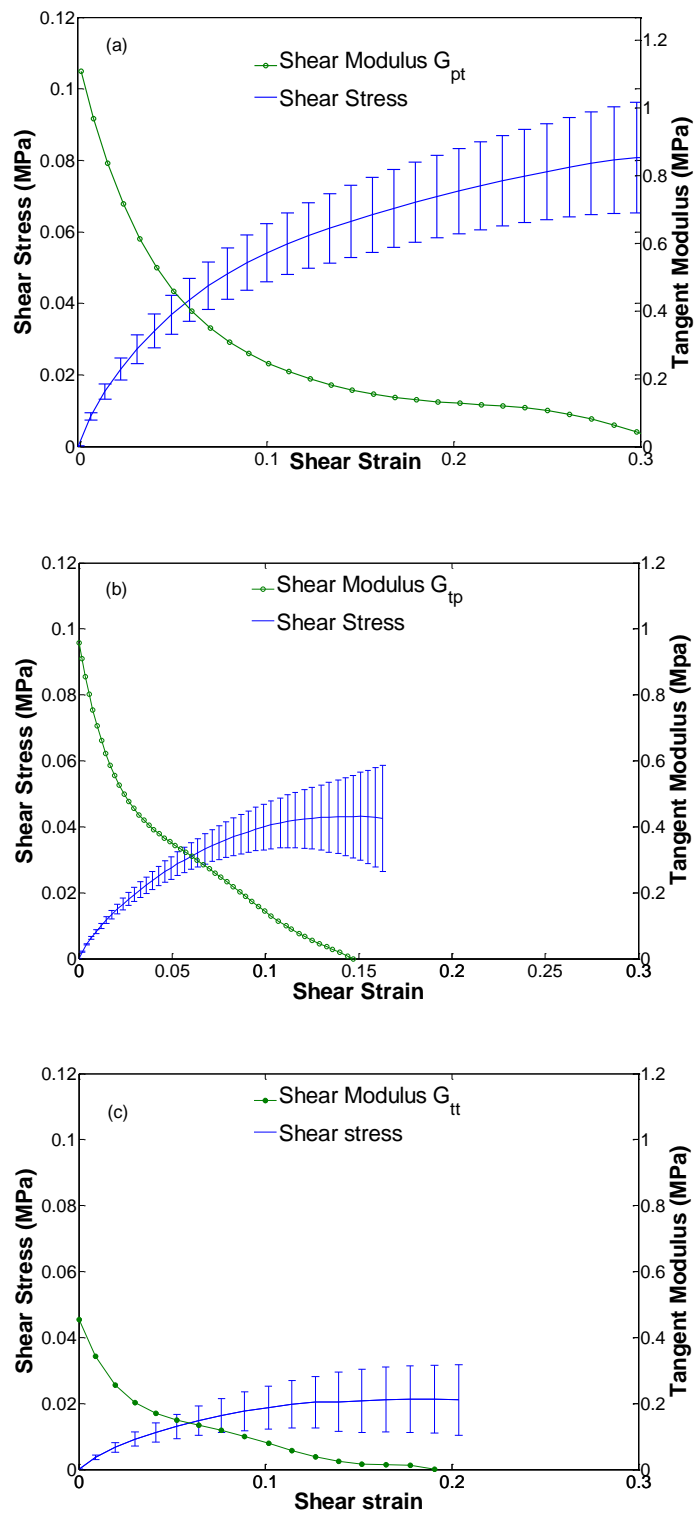


Figure 3-32. Shear test results: (a), (b) and (c) measured nominal shear stress- nominal shear strain curve and the computed tangent shear modulus, the error bars indicate the standard deviation of 3 repeat tests

### 3.2.9. Influence of Material Direction on the Off Principal Axis Compressive Stress-Strain Response

The experimental data measured in off-axis tests are useful in evaluating the predictions of models and numerical simulations (see Section 4.5.1). In order to investigate the ‘off axis’ response of the transversely isotropic LDPE foam, samples were cut off-axis to measure the mechanical response of the foam at specified angles (see Figure 3-33). The principal direction was assumed to be  $0^\circ$  and the transverse direction was assumed to be  $90^\circ$ . The procedure used the 50 mm side-length cubic specimen size, rotating the specimen at  $22.5^\circ$ ,  $45^\circ$  and  $67.5^\circ$  degrees relative to the principal direction prior to cutting.

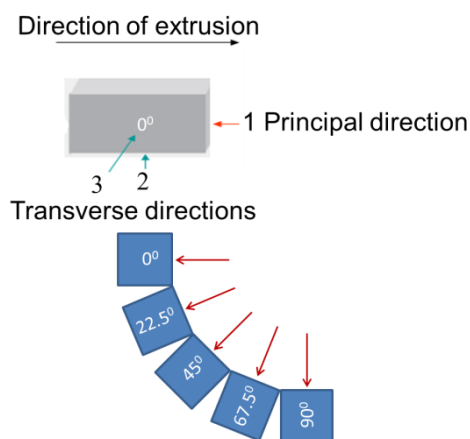
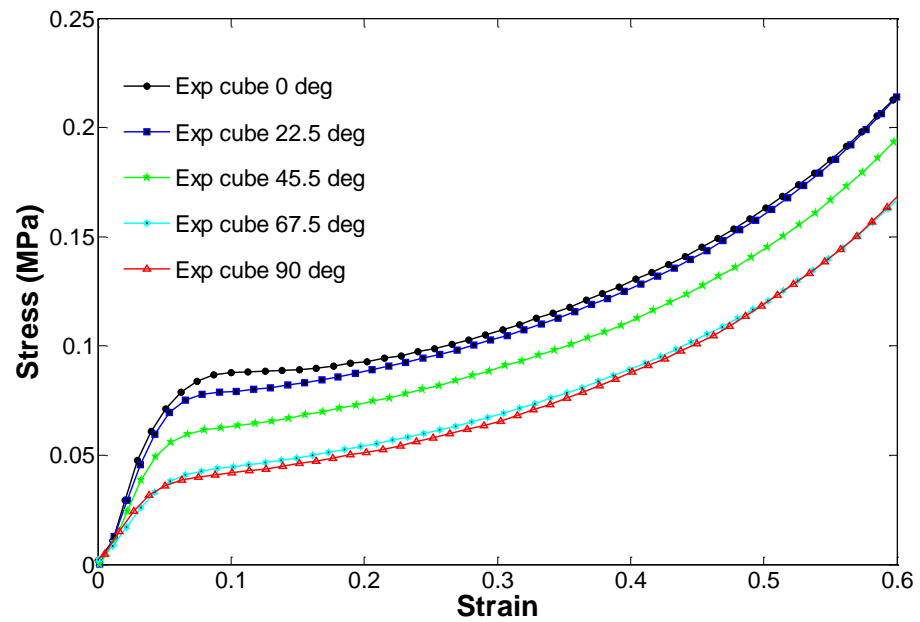


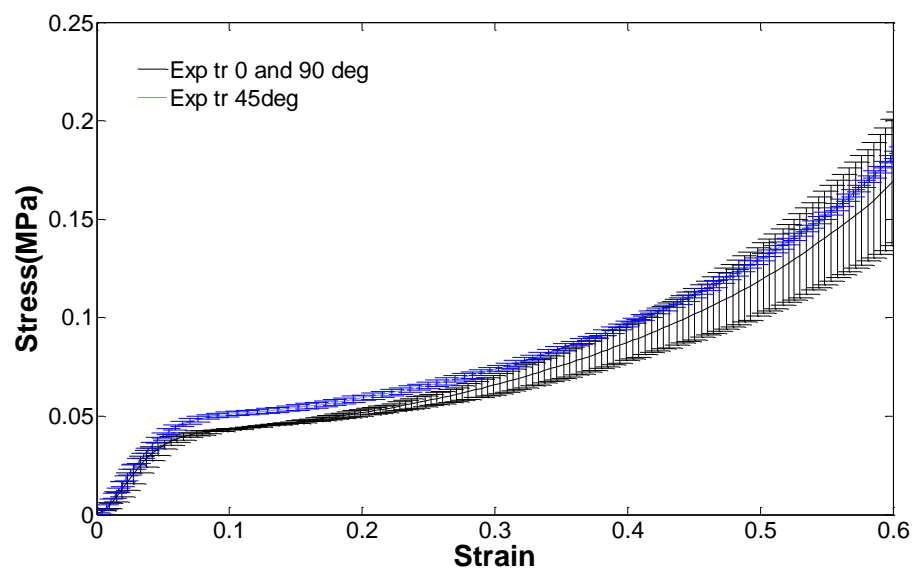
Figure 3-33. Specimen cutting with rotation at angles.

Again, test specimens were cut as cubes of size  $50 \times 50 \times 50 \text{ mm}^3$  and following the test standard ASTM D1621, all uniaxial compression experiments were carried out at a strain rate of  $1.6 \times 10^{-3} \text{ s}^{-1}$ . Foam specimens were compressed using the uniaxial compression experimental setup. Stress-strain results from the off-axis uniaxial compression tests are shown in Figure 3-34a. Each test was repeated five times. As expected, the stress-strain curves of the specimen, orientated at  $45^\circ$ , lie approximately mid-way between the  $0^\circ$  and  $90^\circ$  curves. However, the equivalent curves for the specimens orientated at  $22.5^\circ$  and  $67.5^\circ$  are clearly shifted in a non-linear manner. In order to examine effects of the off axis of LDPE foam at transverse direction. Rotated specimens at  $0^\circ$ ,  $45^\circ$  and  $90^\circ$  were compressed at transverse direction. Figure 3-34b shows that the compressive behaviours of rotated cubes of  $0^\circ$ ,  $45^\circ$  and  $90^\circ$  are similar. Results indicate that the mechanical response of extruded

LDPE foam is not sensitive to the specimen's rotation when specimen compressed at transverse direction.



(a)



(b)

Figure 3-34. Uniaxial compression for a cube sized  $50 \times 50 \times 50 \text{ mm}^3$  with different degrees of rotation of the foam's (a) principal axis; and (b) transverse axis, error bars indicate the standard deviation of 5 repeat tests.

### 3.2.10. Influence of Material Direction on the Off Principal Axis Compressive Modulus and Yield stress at Small Strains

The compressive stress-strain curves can be used to determine the elastic stiffness data. Elastic mechanical properties in the small strain region were determined using the procedure described in Section 3.2.9. Figure 3-35 shows the Young's modulus as a function of the rotation angle. Figure 3-36 shows the Yield stress as a function of the rotation angle.

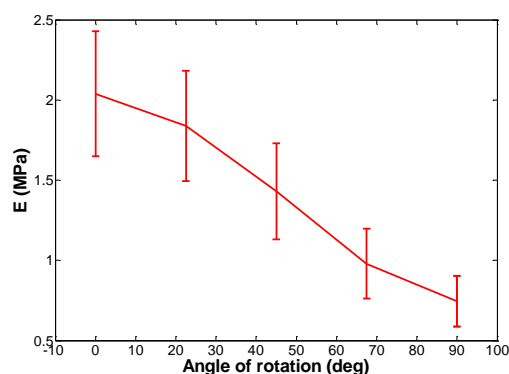


Figure 3-35. Stiffness varies with angle of rotation.

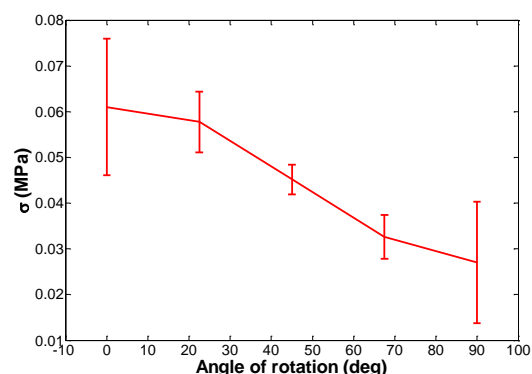


Figure 3-36. Yield stress varies with angle of rotation.

### 3.2.11. Influence of Material Direction on the Off Principal Axis Energy Absorption Efficiency at Large Strains

The compressive stress-strain curves can be used to determine the energy absorption efficiency data. Non-linear mechanical properties in large deformation were performed using the method described in section 3.2.9. Figure 3-37 shows the energy absorption efficiency as a function of the rotation angle.

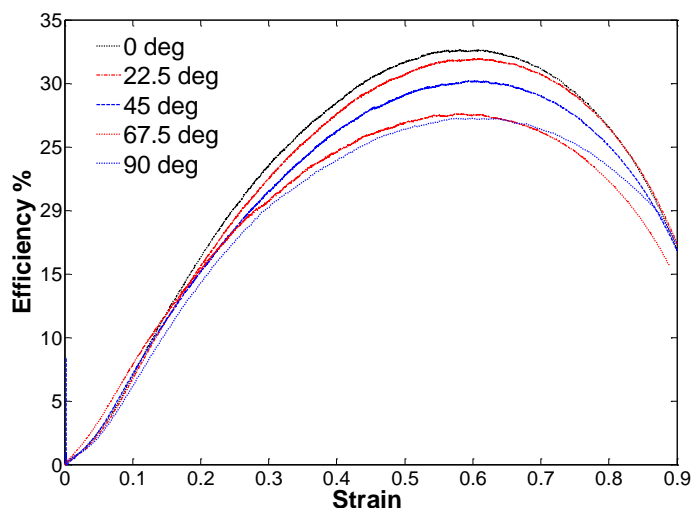
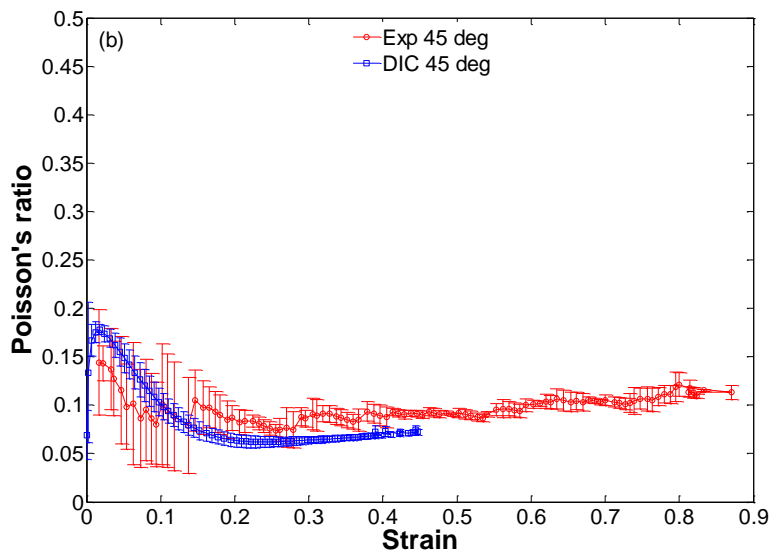
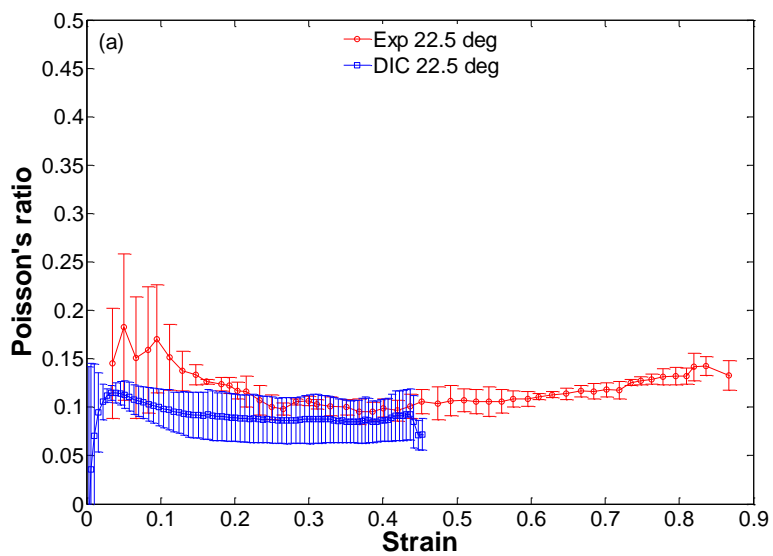


Figure 3-37. Efficiency-strain curves with various angle of rotation.

### 3.2.12. Influence of Material Direction on the Off Principal Axis Poisson's ratio

Poisson's ratio-strain results from the off-axis compression tests are shown in Figure 3-38. Two methods were used to determine Poisson's ratio at specified off-axis angles. The results show that the highest average Poisson's ratio is in the cube rotated at 22.5°; this value reduces with the angle in the principal direction. The lowest average Poisson's ratio is in the cube rotated at 67.5°. In all cases there is good agreement between values measured using manual *image-J* analysis and DIC. In Figure3-39 the Poisson's ratio in the small strain elastic region is plotted using test data from both on-axis (see Section 3.2.3) and off-axis tests from this section.



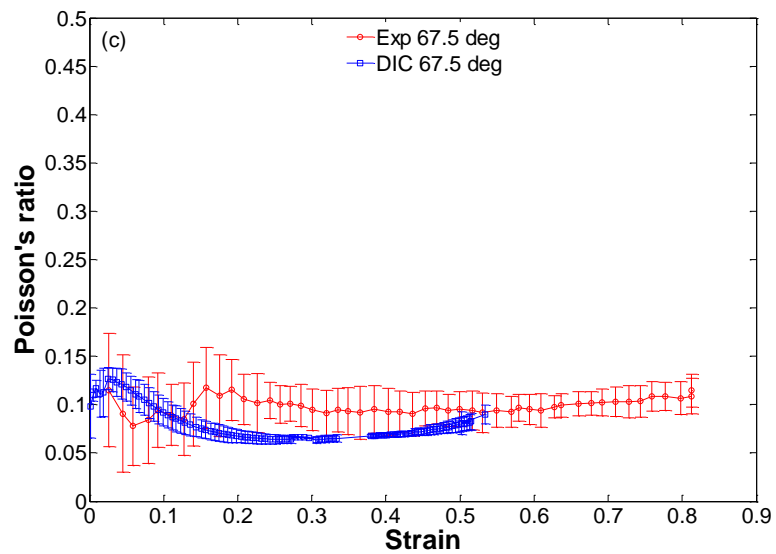


Figure 3-38. Comparison of Poisson's ratio determined for large strain using two methods with different degrees of rotation: (a) cube rotation at  $22.5^\circ$ , (b) cube rotation at  $45^\circ$  and (c) cube rotation at  $67.5^\circ$ .

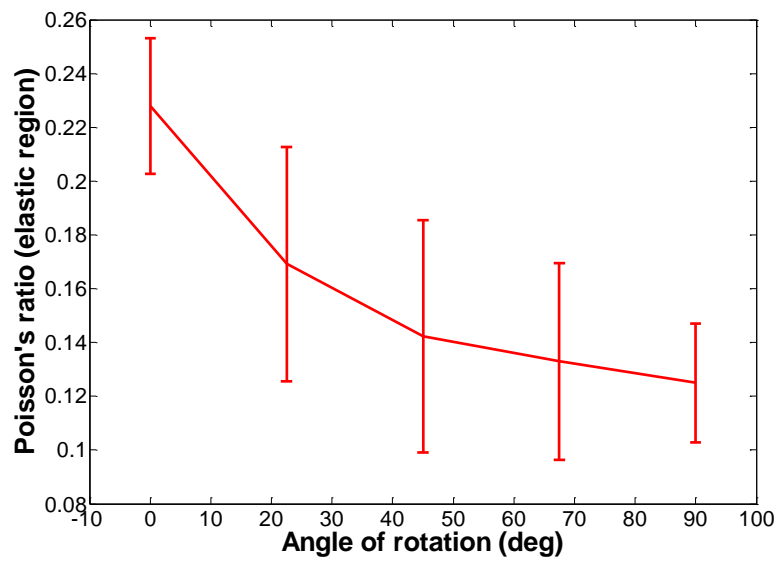


Figure3-39. Poisson's ratio in the elastic region versus rotation angle (value taken at a strain less 0.05).

### 3.3. Micromechanical Characterisation

In this section the cell morphology of the LDPE transversely isotropic closed-cell foam has been examined using both micro-CT and optical microscopy. Geometric properties such as the length of cell edges, thickness of cell walls and cell diameter have been determined. Comprehensive characterisation of the geometric properties of foam assists in formulating 2D or 3D computer models of the foam microstructure. Many microstructural measurements, including cell diameter, face thickness, cell edge length as well as the general cell geometry can be incorporated into such models, as will be shown in Chapter 5.

#### 3.3.1. Experimental Setup and Procedure for Micro CT Imaging

Micro-CT scanning using a SkyScan<sup>TM</sup>-1172 machine with a resolution of 9 microns pixel size was used to investigate the foam microstructure, cell edges thickness and average cell geometry of the flexible LDPE foam specimen, mechanically characterised in Chapter 3. This resulted in 2D images of the specimen cross-section (see Figure 3-40), which could be converted to 3D images using the commercial image analysis software, Simpleware<sup>TM</sup>. Figure 3-41a shows the images of cells obtained from the micro-CT scan into Simpleware<sup>TM</sup>. Figure 3-41a shows cells elongated in the direction of extrusion. Figure 3-41b shows the final 3D reconstruction.

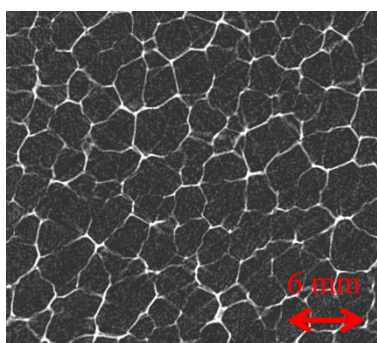
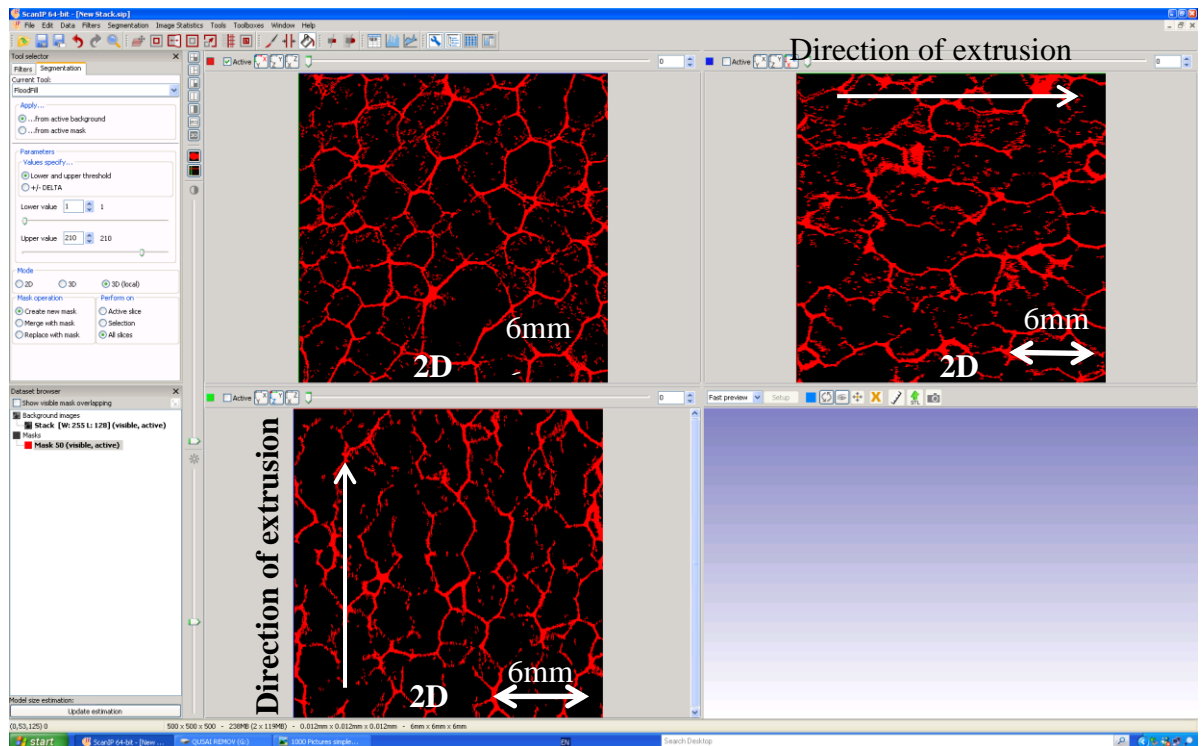
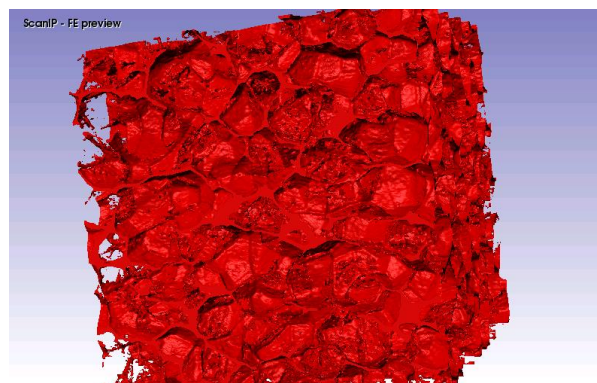


Figure 3-40. Micro-CT scan image



(a)



(b)

Figure 3-41. (a) multiple slices are recorded in three mutually orthogonal planes and (b) reconstruction of 3D image.

Data from the microCT scans were used primarily in measuring the thickness of the cell edges, see Section 3.3.3.

### 3.3.2. Experimental Setup and Procedure for Optical Microscopy

A BRESSER Biolux optical microscope [157] (see Figure 3-42), with magnifications of 4X, 20X and 40X was used to examine foam microstructure (see Section 1.3). Quantities to

be characterised included the cell size, cell edge length and wall thickness. Specimens were carefully cut in thin slices using a sharp razor blade. A typical sliced cross-section is shown in the micrograph of Figure 3-43. Optical micrographs of LDPE foam the white rectangle was used to obtain the basic dimensions of the cells diameter Figure 3-43. The specimens were mounted on the microscope to facilitate easy handling with a minimum amount of damage. As there is no set scale in the microscope viewer, a ruler is used to determine the scale for each lens magnification. Finally, the dimensions of microscope image are converted from pixel to mm using the expression below:

$$d_{mm} = I_{mm} / N_{pixels} \quad (3-20)$$

where  $d_{mm}$ ,  $I_{mm}$  and  $N_{pixels}$  represent the measured cell dimensions in mm, the image dimensions in mm and the number of pixels in the image respectively. In order to explain statistical measurements made from the images, Figure 3-43 shows some of the measurements marked. The cells shapes are clearly irregular and the wall edges vary considerably in length, even within a single cell.



Figure 3-42. A BRESSER Biolux optical microscope.

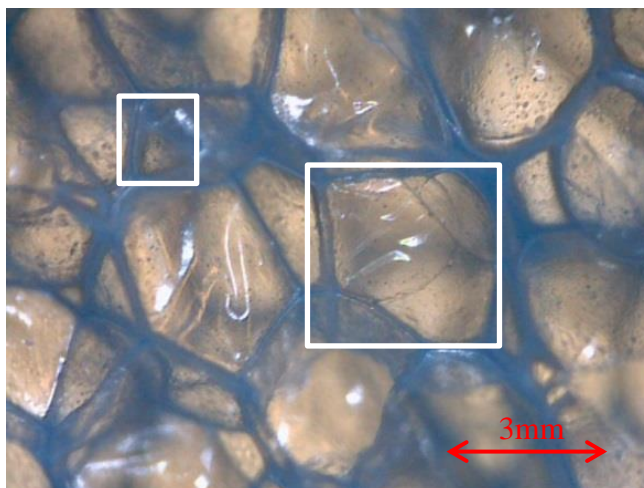


Figure 3-43. Optical micrographs of LDPE foam the white rectangle was used to obtain the basic dimensions of the cells diameter.

### 3.3.3. Quantitative Analysis of 2D Images

For extruded LDPE foam, statistical measurement is the basic and dominate factor influencing the foam mechanical properties. Consequently, in order to complete the characterization of cell geometry and provide statistical morphological data, a microscopic classification of cells is presented in this work. In the following sections the statistical measurements are presented.

#### 3.3.3.1. Cell shape Characterisation

Figure 3-44a shows an example of the cell geometry. Anisotropy in the microstructure is not obvious from a single image, though by collecting enough data from numerous images the anisotropy in the microstructure becomes evident and its statistical significance can be examined.

It can be observed that the cell diameter varies widely throughout the foam. Optical measurements are taken on cut surfaces, the longest dimension of cells is primarily in the extrusion direction (or  $x$ -direction in these images). 300 measurements were taken in both the principal and transverse directions. The cell shape anisotropy ratio,  $r$ , is defined by the cell dimensions in the extrusion or  $x$  direction divided by that in the normal or  $y$  direction, see Figure 3-44a and Figure 3-44b. The data for  $r$  is plotted in Figure 3-45a-b.

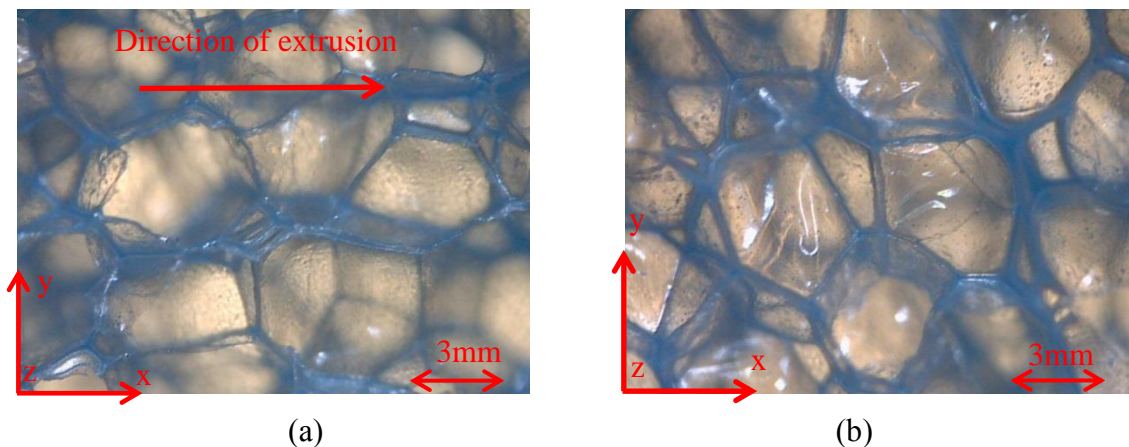


Figure 3-44. Optical micrographs of LDPE foam (a) the extrusion is in x-direction and (b) the extrusion is in z-direction.

The histograms represent individual measurements of the cell anisotropy ratio,  $r$ , and the red lines represent the fitted distribution. Fitting of the data was performed using MatLab software. If the maximum in the fitted distribution is equal to the mean value, then the distribution is said to be well represented by a normal distribution.

Figure 3-45a shows the distributions are skewed. The location of the maximum of the fit in the principal direction (direction of extrusion) is  $1.201 \pm 0.386$ , indicating the average cell geometry is elongated in the extrusion direction. In Figure 3-45b location of the maximum of the fit in the transverse direction is  $1.018 \pm 0.298$ , indicating the average cell geometry has no preferred direction of elongation in the plane normal to the extrusion direction.

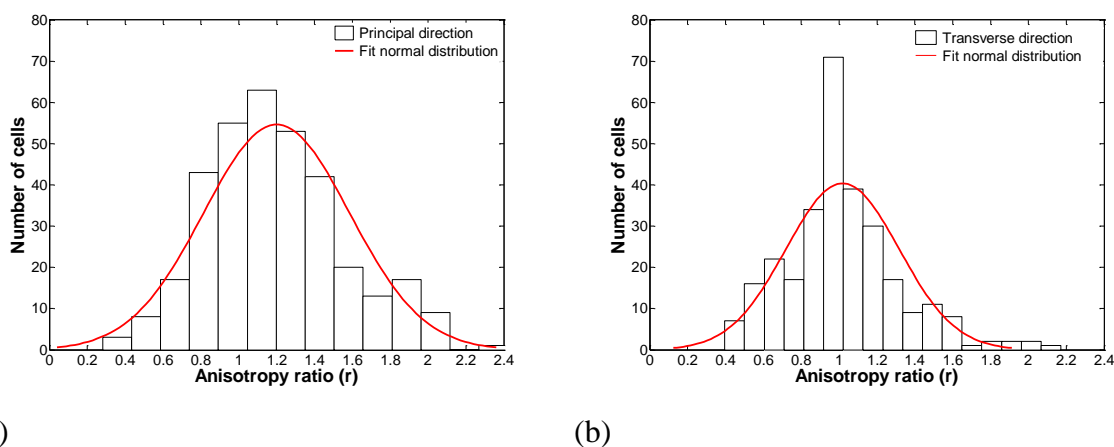


Figure 3-45. Histogram showing the cell shape anisotropy ratio distribution for (a) principal directions and (b) transverse direction.

### 3.3.3.2. Measurement of Cell Dimensions

In this section, other aspects of the cell microstructure are characterised. At least 100 measurements were taken for cell wall thickness, cell edge length and thickness from randomly selected areas microCT and optical measurements. Figure 3-46a shows that the average edges length of cells is  $0.430 \pm 0.150$  mm, Figure 3-46b reveals that the average cell edge thickness is  $0.056 \pm 0.011$  mm.

Moreover, Figure 3-46c and Figure 3-46d show that the average cell widths in the transverse and principal directions are  $0.615 \pm 0.319$  mm and  $0.622 \pm 0.317$  mm respectively. The average cell diameter represents the cell size while the variation of histograms describes the degree of difference in cell sizes. It is clear that the cells in Figure 3-46d are more regular than those in Figure 3-46c, and this variation in the cell size and cell size distribution comes from the manufacturing process. Subsequently, in the same process the cell wall thickness are measured and shown in Figure 3-46e, which reveals that the average cell wall thickness is  $0.003 \pm 0.001$  mm. From the results in Figure 3-46a-e, it can be observed that the histograms of cell dimensions are significantly skewed. This indicates that geometry of this class of foam is highly irregular and complex.

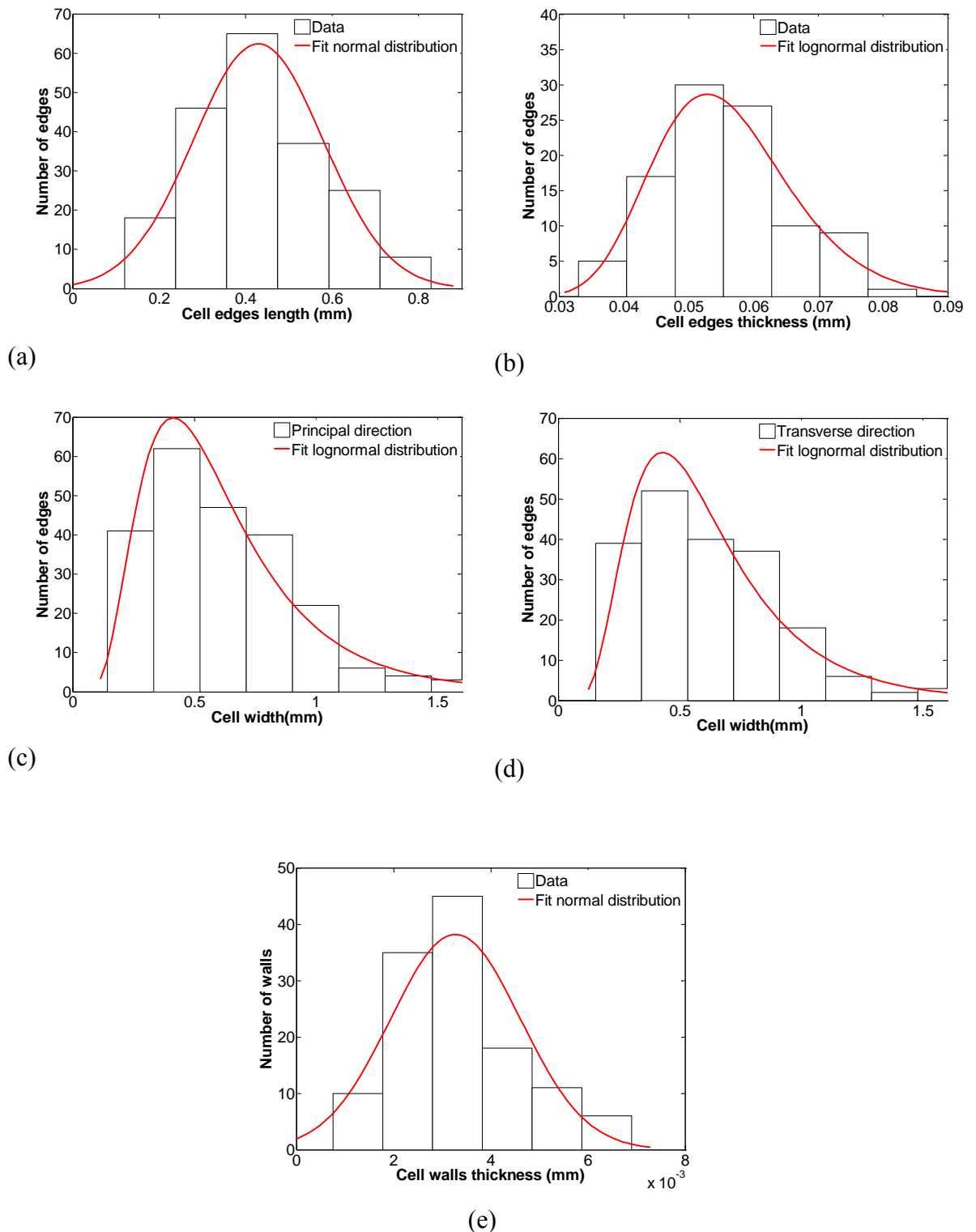


Figure 3-46. Histogram distributions and average values showing (a) cell edge length, (b) cell edge thickness, (c) width of cells in transverse direction, (d) cell width in principal direction and (e) cell wall thickness.

### 3.4. Summary

The mechanical response of LDPE foam at strain rates from  $0.0016$  to  $5\text{s}^{-1}$  were experimentally investigated, using Zwick/Roell Z250 and Zwick/Roell Z2 testing machines and a uniaxial compression setup. The results show that specimen size has a large influence on the test results and so a minimum specimen size of  $50\times 50\times 50\text{ mm}^3$  was used for the remainder of the investigation. Section 3.2 describes the mechanical characterisation of the LDPE melt-extruded foam and reveal a strongly non-linear transversely isotropic and highly compressible behaviour, with strain rate dependence. Recovery after unloading is time dependent and given sufficient time is almost 100%, though a permanent change in the form of the foam's subsequent stress-strain curve suggests permanent damage occurs despite the recovery in strain. Clearly this behaviour is very complex and collecting such data is a relatively slow and costly process. It is therefore of value if methods of interpolating measured data from a smaller dataset or better still, of predicting the data using analytical models can be devised; this possibility is explored in Chapters 4 and 5. Microstructural characterisation using image analysis method reveals statistically significant anisotropy in the cell morphology. In Chapter 5, this information, along with the detailed characterisation of information on cell structure is incorporated in microstructural models and used to examine whether this microstructural anisotropy can explain the transversely isotropic mechanical response measured in this chapter.

## **Chapter 4. : Macro-Mechanical Modelling of Foam**

### **4.1. Introduction**

Chapter 3 demonstrated a strongly transversely isotropic mechanical response in the extruded LDPE polymer foam chosen for this investigation and also revealed significant anisotropy in the foam's microstructure. In this chapter methods of interpolating between measured data from a smaller dataset and of predicting the data using simple analytical models are explored. The idea here is that if stress-strain data can be interpolated and predicted using simple transformations and shifting, involving the use of empirical models based on simple underlying assumptions, then this: (i) would go some way to explaining the real physical mechanisms behind the foam's otherwise complex orientation- and rate-dependent response and (ii) could be used as a means to predict rather than to measure data using time consuming and expensive experiments. The predicted dataset could then be used to determine the parameters of constitutive models implemented in FEA software.

To this end, first a simple method of predicting the off-axis compression data from the on-axis compression response, using a matrix rotation method is proposed. Next, a combined model involving a fitted rate-dependent empirical law and a simple gas compression model is used to interpolate the full set of compression data using just a limited number of experimental input curves. These predicted results are compared with the experimental data from Chapter 3. Finally, experimental results from Chapter 3 are used to fit the parameters of two different constitutive models currently implemented in a commercial finite element code, Abaqus<sup>TM</sup>. These models include (i) a compressible transversely isotropic linear elastic model and (ii) a compressible isotropic hyper-elastic model. The success of these models in capturing the complex behaviour of the LDPE benchmark foam selected for this investigation is assessed.

## 4.2. Interpolating the Off-axis Stress-strain Curves

In this section a method of interpolating the approximate uniaxial compression stress versus strain curves for defined off-axis specimen orientations is explored. The method uses just the principal and transverse uniaxial compression data, together with the simple shear test measurement of  $G_{pt}$  and involves the use of a matrix rotation operating on ‘apparent’ elastic properties. The purpose of this work is to: (i) determine if the off-axis stress-strain curves can be predicted from the principal and transverse uniaxial compression data at small strain using a simple rotation matrix; if so this suggests that the response at small strain can be modelled using a simple linear transversely isotropic model and (ii) to enable faster preliminary evaluation of non-linear constitutive models; if the rotation method works also at large strains then this could reduce the amount of experimental characterisation tests required to produce off-axis data for model evaluation. To do this, the same rotational transformation used to determine the stiffness of a linear compressible transversely isotropic material, when loaded off-axis has been used in the analysis [36], i.e.

$$\begin{aligned} \frac{1}{E_{\theta}(\varepsilon)} = & \frac{\cos^2(\theta)}{E_p(\varepsilon)} \left[ \cos^2(\theta) - \sin^2(\theta)v_{pt}(\varepsilon) \right] \\ & + \frac{\sin^2(\theta)}{E_t(\varepsilon)} \left[ \sin^2(\theta) - \cos^2(\theta)v_{tp}(\varepsilon) \right] + \frac{\cos^2(\theta)\sin^2(\theta)}{G_{pt}(\varepsilon)} \end{aligned} \quad (4-1)$$

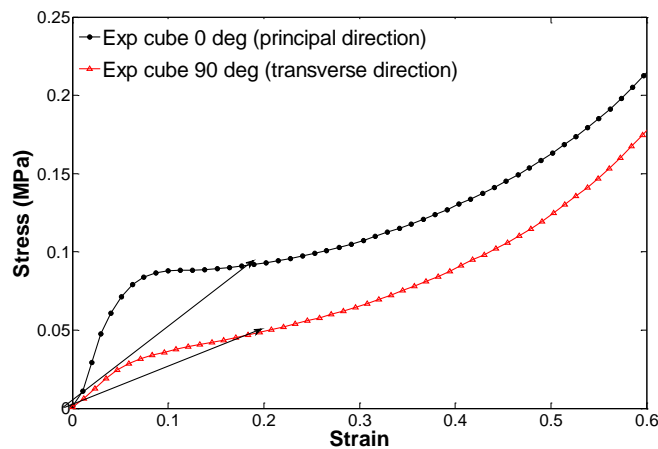


Figure 4-1. Principal and transverse uniaxial compression curves with secant modulus shown at 0.2 strain.

The equation is adapted for large strains using an ‘apparent’ stiffness for  $E_p$  and  $E_t$ , the modulus in the principal and transverse directions, as indicated for a strain of 0.2 in Figure 4-1. These apparent moduli are therefore functions of the strain, i.e.  $E_p(\varepsilon)$  and  $E_t(\varepsilon)$ . Also  $G_{pt}(\varepsilon)$  is taken to mean the small strain shear modulus measured as a function of the finite uniaxial compressive strain,  $\varepsilon$ . To actually measure this function would require many simple shear tests at incrementally increasing levels of compression using specialised apparatus; a difficult and time consuming task that would defeat the purpose of this investigation. Instead, a suitable empirical function for  $G_{pt}(\varepsilon)$  has been found that meets the three criteria: (i)  $G_{pt}(\varepsilon) = G_{pt}(\gamma)$  as  $\gamma$  and  $\varepsilon$  approach 0 strain; (ii) the function is based on data measurable from the three characterisation tests performed in this investigation (compression in principal & transverse directions plus simple shear); and (iii) the resulting function provides good shifting results when used in Equation (4-1). Thus, at small strain the approximation  $G_{pt}(\gamma) = G_{pt}(\varepsilon)$  is made, and Equation (3-19) becomes

$$G_{pt}(\varepsilon) = 1.115 - 22.498\gamma + 265.47\gamma^2 - 1.9260 \times 10^3 \gamma^3 + 8.231 \times 10^3 \gamma^4 - 18.555 \times 10^3 \gamma^5 + 16.738 \times 10^3 \gamma^6 \quad (4-2)$$

For larger strains, after a process of trial and error, an equation of similar form to the theoretical shear modulus prediction for an isotropic compressible elastic material under small strains has been found to provide good results

$$G_{pt}(\varepsilon) = \frac{E_p(\varepsilon)}{2[1 + \nu_{pt}(\varepsilon)]} \quad (4-3)$$

(see Equation (4-3) where the Poisson’s ratio,  $\nu_{pt}(\varepsilon)$ , is given by Equation (3-14). It is noted that Equation (4-3) is a purely an empirical function. Thus, the final function used to estimate  $G_{pt}(\varepsilon)$  is a combination of Equations (4-2) and (4-3) as shown in Figure 4-2 Equation (4-3) is used in place of Equation (4-2) for strains where the prediction Equation (4-3) is greater than that of Equation (4-2).

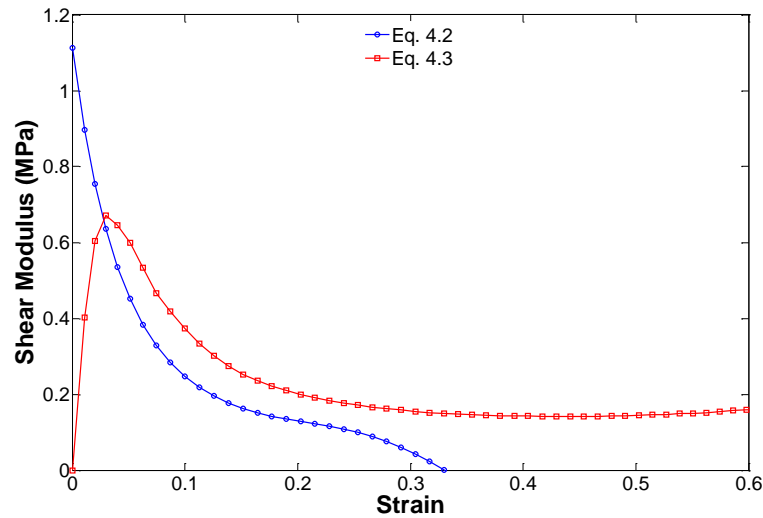


Figure 4-2. Curves for polynomial fit equation of experimental measurement and predicted shear modulus for LDPE.

The empirical method described above predicts the compressive stress behaviour of the foam when rotated at defined angles to the direction of compression very well (see Figure 4-3). This is a pragmatic approach that can dramatically reduce the amount of experimentation involved in determining the off-axis response of the foam. Its applicability to other transversely isotropic foams is not certain and remains something to be tested in the future. The off-axis predictions could then be used to evaluate numerical simulations.

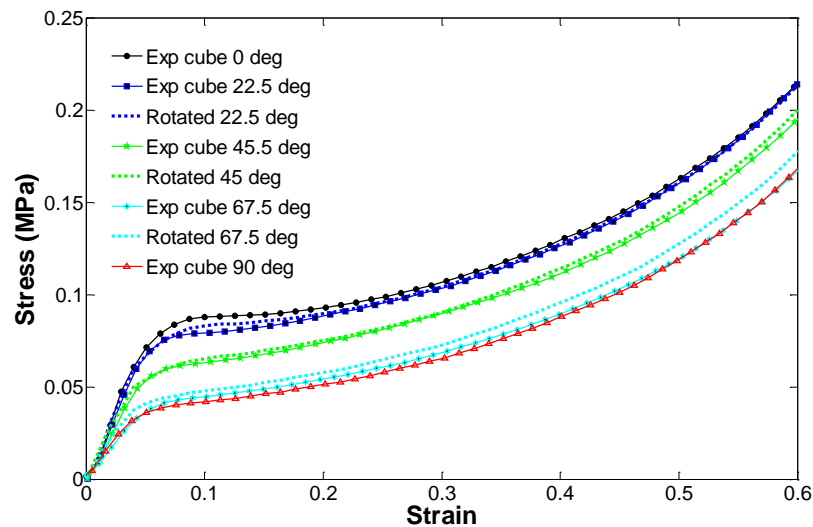


Figure 4-3. Experimental uniaxial compression curves (continuous lines) with different degrees of rotation of principal axis together with predicted uniaxial compression curves (dashed lines) using Equation (4-1), for  $\theta = 22.5^\circ$ ,  $45^\circ$  and  $67.5^\circ$ .

### 4.3. Combined Empirical Rate Law and Gas Model

The rotation method described in the previous section, Section 4.2, can be used to interpolate between the principal and transverse stress curves determined at a given strain rate. In this section, a gas model is used to predict the large strain response of the foam from just four stress-strain curves, namely using the data obtained at the lowest and highest rates in the principal and transverse directions. The interest here is in generating large-strain datasets across a range of strain rates from a more limited dataset.

To do this, a gas model proposed previously for closed-cell flexible foam Clutton and Rice [91], given here in Equations (4-4) and (4-5), has been used to fit the compression data in the principal and transverse directions when compressed at the minimum and maximum strain rates.

$$\sigma_{pr} = \sigma_p + P_a \left( \frac{1-R}{(1-\varepsilon)(1+v_{fit}\varepsilon)^2 - R} - 1 \right) \quad (4-4)$$

and

$$\sigma_{tr} = \sigma_t + P_a \left( \frac{1-R}{(1-\varepsilon)(1+v_{fit}\varepsilon)^2 - R} - 1 \right) \quad (4-5)$$

where  $\sigma_{pr}$  and  $\sigma_{tr}$  represent the stress in the principal and transverse directions  $\sigma_p$ ,  $\sigma_t$  represent the values of yield stress in the principal and transverse directions respectively. The latter are found simply by extrapolating the fitted equations back to zero strain. Similarly,  $v_{fit}$  represents the value of the fitted Poisson's ratio. Figure 4-4 and Figure 4-5 show the curves fitted in the principal and transverse directions and at the lowest and highest rates. The experimental data is also shown in the figures.

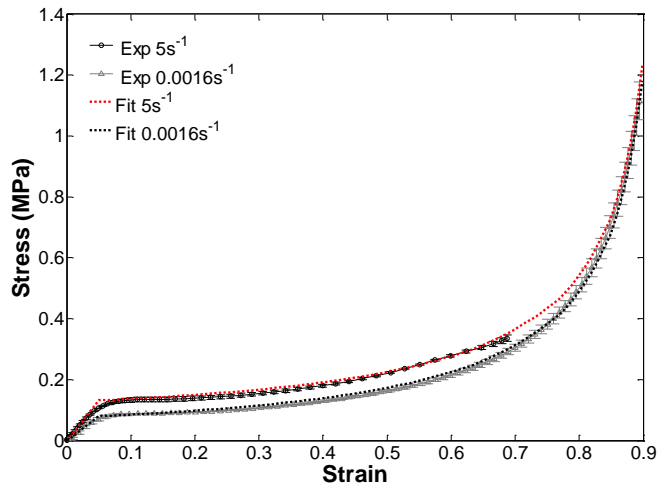


Figure 4-4. Experimental uniaxial compression curves in the principal direction (continuous lines) with fitted uniaxial compression and curves using Equation (4-4) (dotted line).

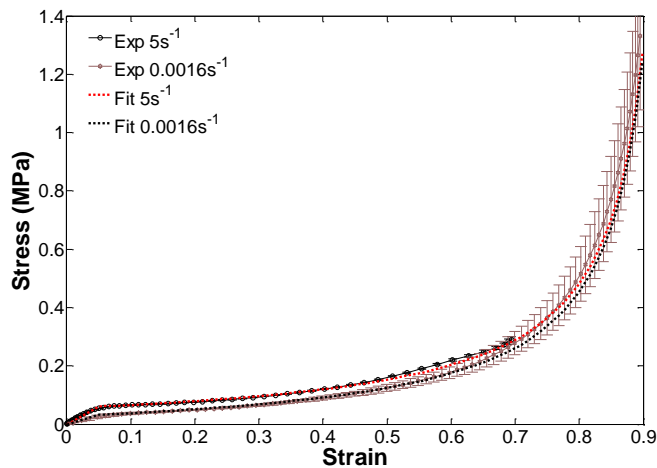


Figure 4-5. Experimental uniaxial compression curves in the transverse direction (continuous lines) with fitted uniaxial compression and curves using Equation (4-5) (dotted line).

Figure 4-4 and Figure 4-5 show that the yield stress depends on the strain rate. An equation relating the yield stress to the natural logarithm of the strain rate  $\dot{\epsilon}$  was proposed previously by Song et al. [43] and is fitted to the yields stress values found by extrapolating the fitted stress-strain curves back to zero strain. The relation can then be used to predict the yield stress for the intermediate strain rates of  $0.016\text{s}^{-1}$ ,  $0.16\text{s}^{-1}$  and  $1.6\text{s}^{-1}$ .

$$\sigma_p = \sigma_{op} + C_p * \ln\left(\frac{\dot{\epsilon}}{\dot{\epsilon}_0}\right) \quad (4-6)$$

$$\sigma_t = \sigma_{ot} + C_t * \ln\left(\frac{\dot{\epsilon}}{\dot{\epsilon}_0}\right) \quad (4-7)$$

where  $\dot{\epsilon}_0 = 0.0016\text{s}^{-1}$  is the reference strain rate and  $\dot{\epsilon}$  is a strain rate. The fitted yield stress in the principal direction is  $\sigma_{op} = 0.078$  MPa and fitting parameter  $C_p = 0.0065$  MPa are fitted from experimental results, the fitted yield stress in the transverse direction is  $\sigma_{ot} = 0.028$  MPa and fitting parameter  $C_t = 0.0035$  MPa are fitted from the experimental data. Equations (4-6) and (4-7) characterise the phenomenological equations that define the strain rate effects on the elastic yield stress of the foam in the principal and transverse directions. The fitted and predicted data are shown in Figure 4-6 shows that the yield stress response of the LDPE foam, over a range of compression strain rate, is found to follow a natural log-linear relationship with the compression strain rate for both the principal and transverse directions. This relation is useful for calculating the stress-strain curves at any arbitrary compression speed (or strain rate).

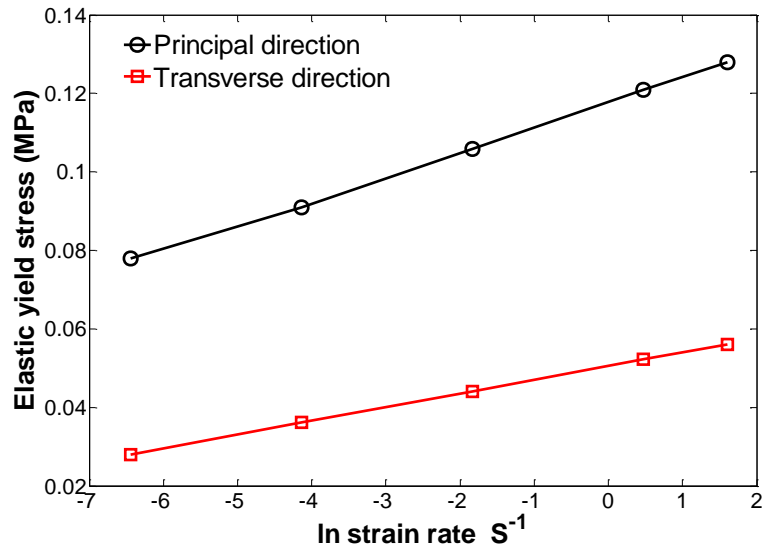
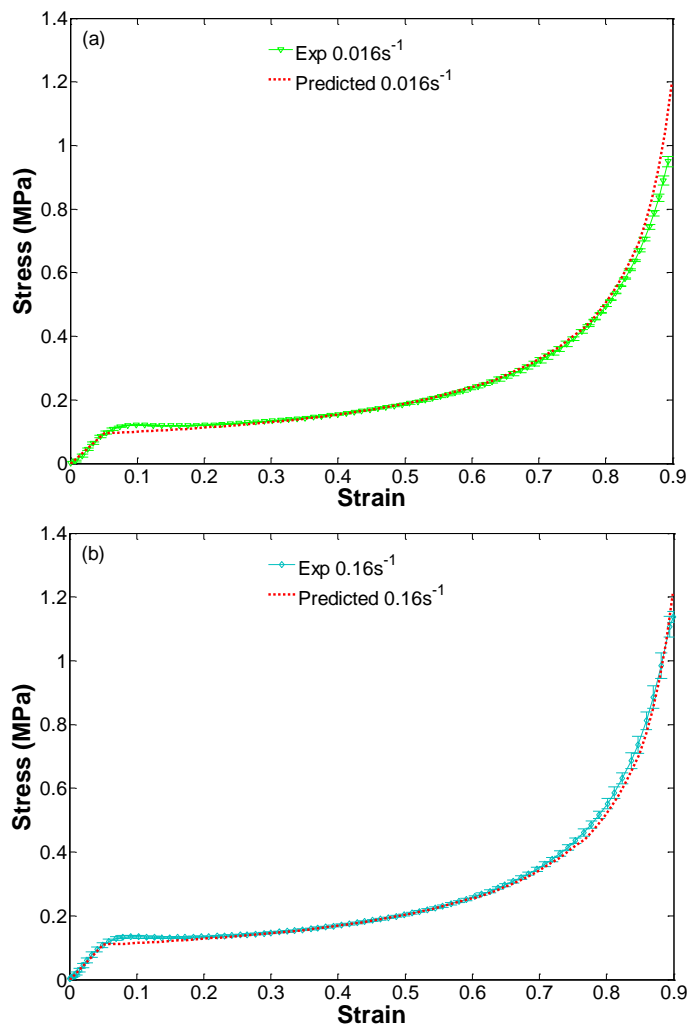


Figure 4-6. Effects of strain rate on yield stress in the principal and transverse directions.

Equations (4-4) and (4-5) were fitted at the maximum and minimum strain rates of  $0.0016\text{s}^{-1}$  with  $5\text{s}^{-1}$ . The combined phenomenological equations, Equations (4-6), (4-7) and gas model, Equation (4-4) and (4-5) can be used to accurately predict the compressive

stress-strain behaviours of the foam in the principal and transverse directions when subjected to arbitrary strain rates. Figure 4-7a-c shows the experimental and predicted stress-strain behaviour under compression loading in the principal direction, at strain rates of  $0.016\text{s}^{-1}$ ,  $0.16\text{s}^{-1}$  and  $1.6\text{s}^{-1}$ . The results show good agreement between the predicted response and experimental data. Figure 4-8a-c shows the predicted and experimental stress versus strain behaviour under compression loading in the transverse direction, at strain rates of  $0.016\text{s}^{-1}$ ,  $0.16\text{s}^{-1}$  and  $1.6\text{s}^{-1}$  respectively, the results again show good agreement between predictions and experimental data.



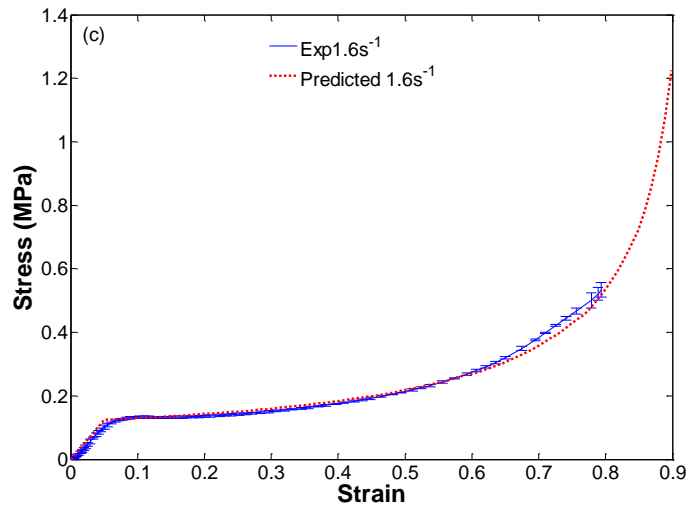
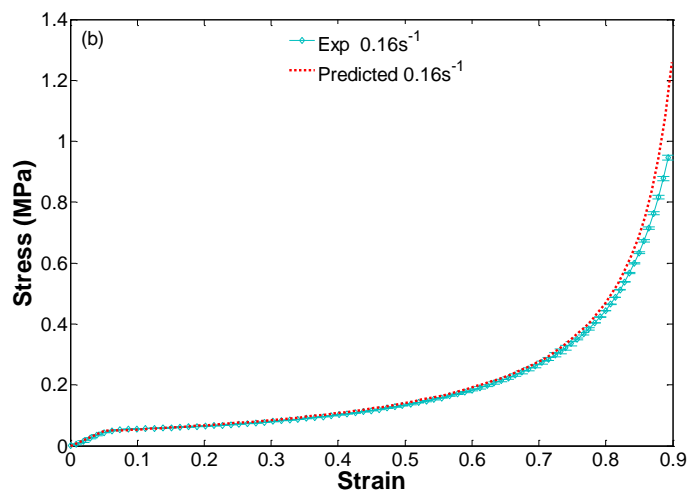
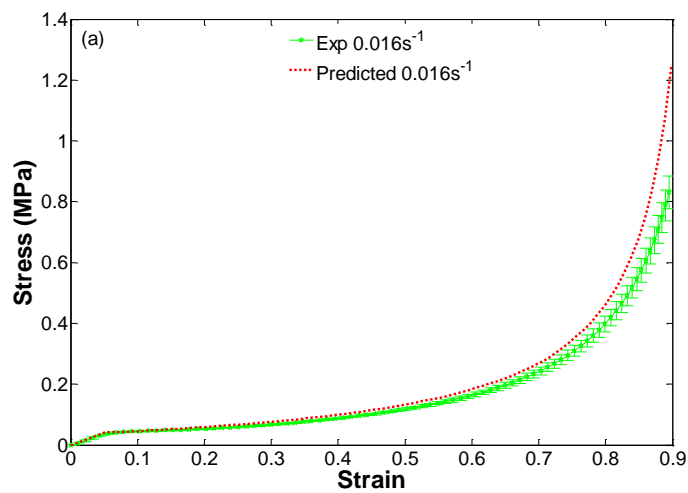


Figure 4-7. (a), (b) and (c) Experimental uniaxial compression curves (continuous lines) with different strain rates in the principal direction, together with predicted uniaxial compression curves (dotted lines) using Equations (4-4) and (4-6).



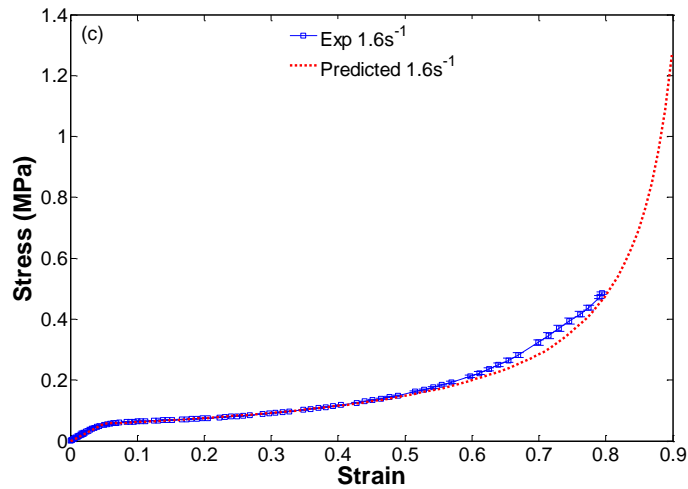


Figure 4-8. (a), (b) and (c) Experimental uniaxial compression curves (continuous lines) with different strain rates in the transverse direction, together with predicted uniaxial compression curves (dotted lines) using Equations (4-5) and (4-7).

Taking this approach a step further, it is interesting to see if a simple method of predicting the stress-strain response in the principal direction from that in the transverse direction, or versa, can be achieved by using the microstructural anisotropy ratio,  $r$ . In this case  $r = 1.2$ , multiplying the yield stress in the principal direction by a factor of  $1/cr^2$  where  $c = 2$  is a constant, this factor is fitted with Gibson and Ashby model see Equation (5-1). The predicted curves using Equation (4-8) compared against the experimentally determined stress-strain response in the transverse direction (at the various rates (see Figure 4-9 and also for the various different specimen sizes at a constant rate see Figure 4-10.

$$\sigma_{tr} = \sigma_p / (cr^2) + P_a \left( \frac{1-R}{(1-\varepsilon)(1+\nu_{12}\varepsilon)^2 - R} - 1 \right) \quad (4-8)$$

Figure 4-9 show a comparison between uniaxial compressions for various strain rates in transverse direction and those predicted a factor of  $1/cr^2$  in the principal direction and gas model (see Equations (4-8) ) and a good agreement in the results is can be observed. The method is reasonably successful, in Chapter 5 micromechanical models are used to explore this relationship in greater detail. At this point, given the stress-strain response of the foam in once direction at two different rates (i.e. the principal or transverse directions) and also the microstructural anisotropy ratio,  $r$ , a reasonable approximation of a full rate dependent data set can be made.

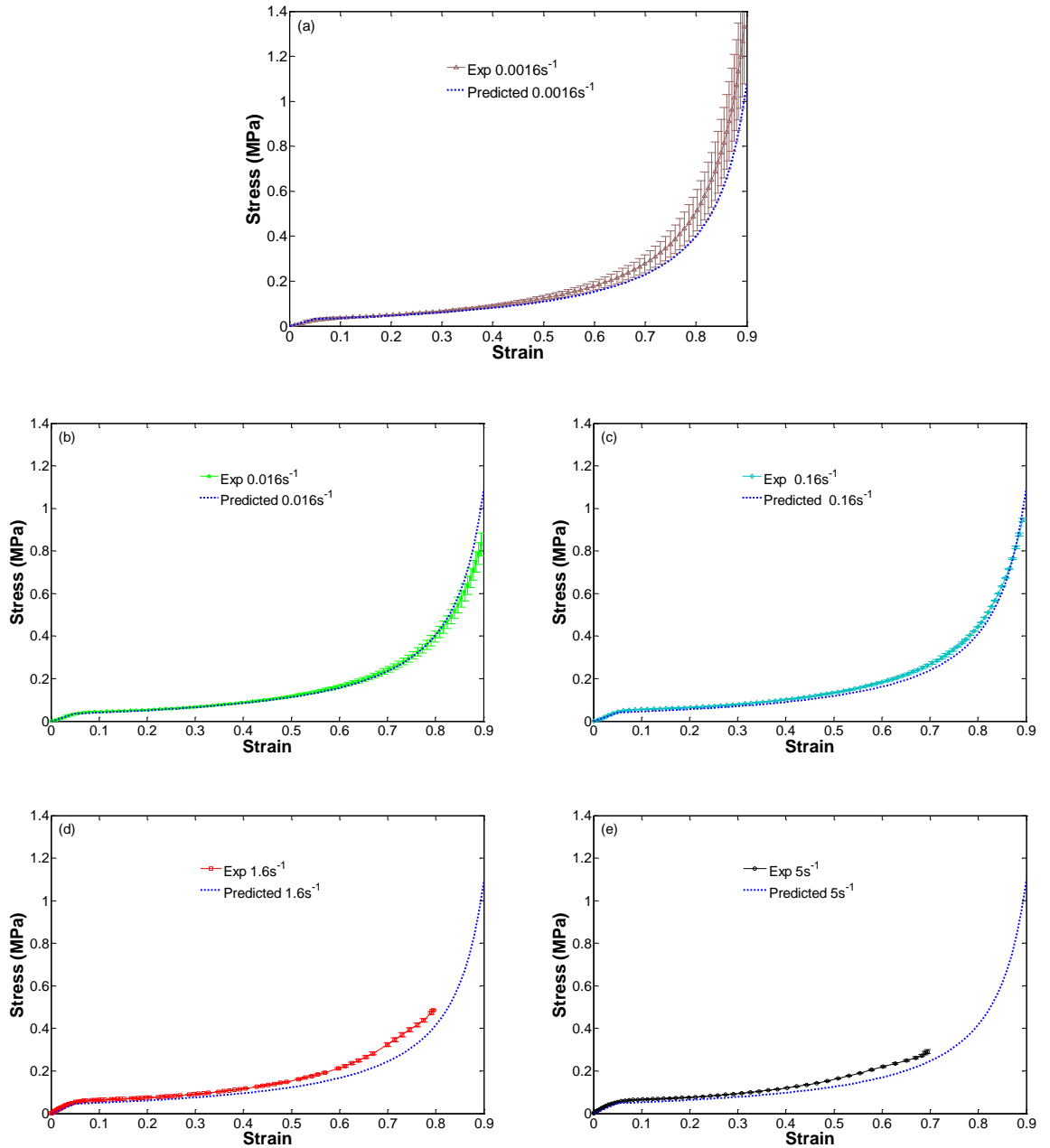


Figure 4-9. (a), (b), (c), (d), and (e) Experimental uniaxial compression curves (continuous lines) with different strain rates in the transverse direction, together with predicted uniaxial compression curves (dotted lines) using Equation (4-8).

Figure 4-10 show a comparison between uniaxial compressions for various specimen sizes in transverse direction and those predicted by two: a factor of  $1/cr^2$  in the principal

direction, gas model, see Equation (4-8) a reasonable agreement in the results is can be observed.

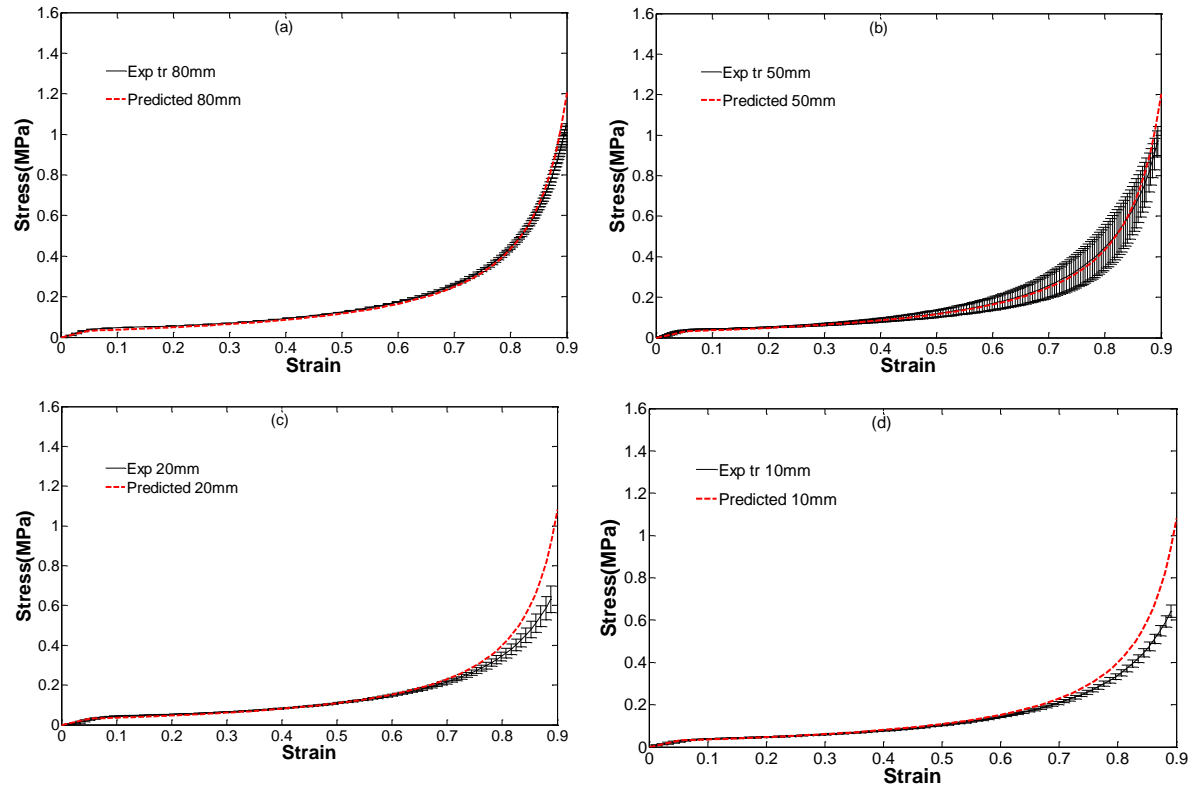


Figure 4-10. Experimental uniaxial compression curves in the transverse (continuous lines) with predicted (dotted lines) uniaxial compression curves using Equation (4-8) for specimen sizes (a)  $80 \times 80 \times 80 \text{ mm}^3$ , (b)  $50 \times 50 \times 50 \text{ mm}^3$ , (c)  $20 \times 20 \times 20 \text{ mm}^3$  and (d)  $10 \times 10 \times 10 \text{ mm}^3$ .

#### 4.4. Prediction of Size Effect on Mechanical Properties

One aspect of the experimental characterisation of the LDPE foam focused on the effect of specimen size on the mechanical response. This section examines the compression loading under large strain and assumes the specimen size dependence is related to gas diffusion out of the foam. The stress-strain response is analysed by assuming isothermal compression of the gas. A method is suggested to predict the uniaxial compression response of the foam at various specimen sizes using factors related to the rate of change of pressure with respect to volumetric strain, inside the foam specimens.

When closed-cell foams are compressed under large strain i.e. beyond the elastic region, assuming isothermal compression of the gas (see Section 2.2.2.1) and zero Poisson's ratio, the uniaxial compression stress,  $\sigma$ , can be calculated from Equation (4-9)

$$\sigma = \sigma_o + \frac{P_o \varepsilon}{1 - \varepsilon - R} \quad (4-9)$$

where the value  $\varepsilon/(1-\varepsilon-R)$  represents the gas volumetric strain. The values of the gas volumetric strain curves were determined from the experimental data for the four specimen sizes. The stress versus volumetric strain data are shown in Figure. 4-11 and Figure. 4-12 and the gradient of these curves represents the rate of change of the internal gas pressure with respect to the volumetric strain within the cells during loading.

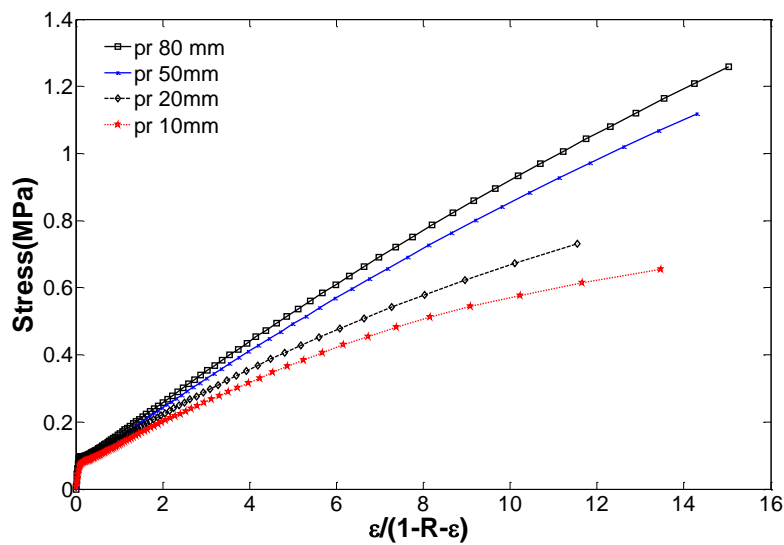


Figure. 4-11. Typical stress and gas volumetric strain curves for four cubes in the principal direction.

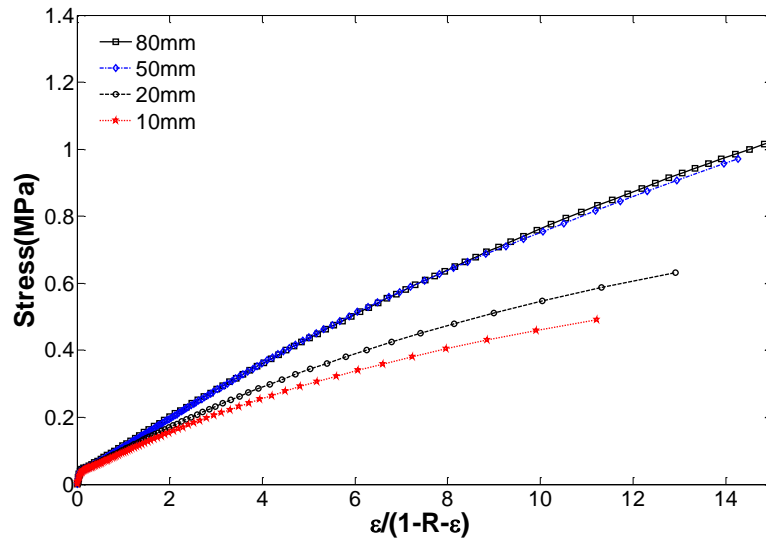


Figure. 4-12. Typical stress and gas volumetric strain curves for four cubes in the transverse direction.

As show in Figure 4-13 and Figure 4-14, the slope of the stress and the volumetric strain curves decrease with volumetric strain. This means that the rate in increase of the gas pressure inside the closed cells decreases as a function of the volumetric strain.

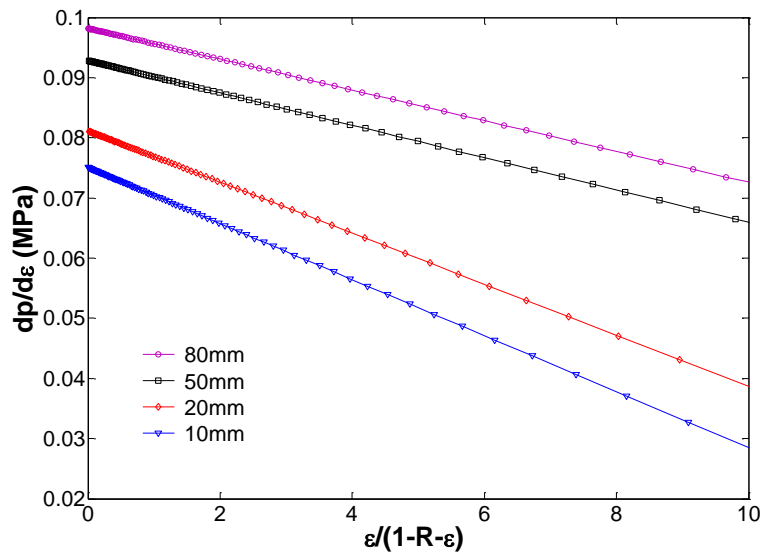


Figure 4-13. Curves for pressure decreases inside cells in the principal direction.

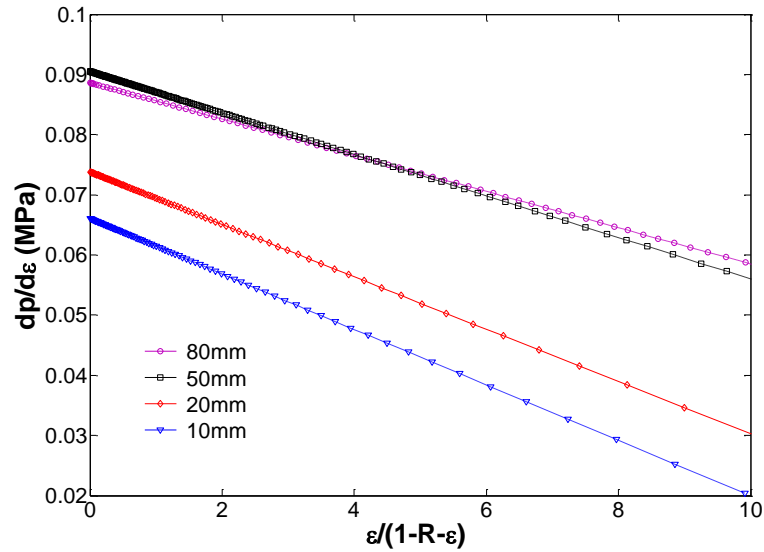


Figure 4-14. Curves for pressure decreases inside cells in the transverse direction.

In order to present the relationship between specimen sizes and, the data for  $dp/d\varepsilon$  as a function of sample size in the principal and transverse directions are fitted to polynomial Equations (4-10)

$$(dp/d\varepsilon)_{pr} = (dp/d\varepsilon)_r r^{0.5} \quad (4-10)$$

Equations (4-5) and (4-10) can be used to accurately predict the compressive stress-strain behaviours of the foam in the transverse directions when compressive loading subjected to versus specimen sizes. Figure 4-15a-c shows the experimental and predicted stress-strain behaviour under compression loading in the transverse direction, on specimen sizes  $80 \times 80 \times 80 \text{ mm}^3$ ,  $50 \times 50 \times 50 \text{ mm}^3$ ,  $20 \times 20 \times 20 \text{ mm}^3$  and  $10 \times 10 \times 10 \text{ mm}^3$ . The results show good agreement between the predicted response and experimental data.

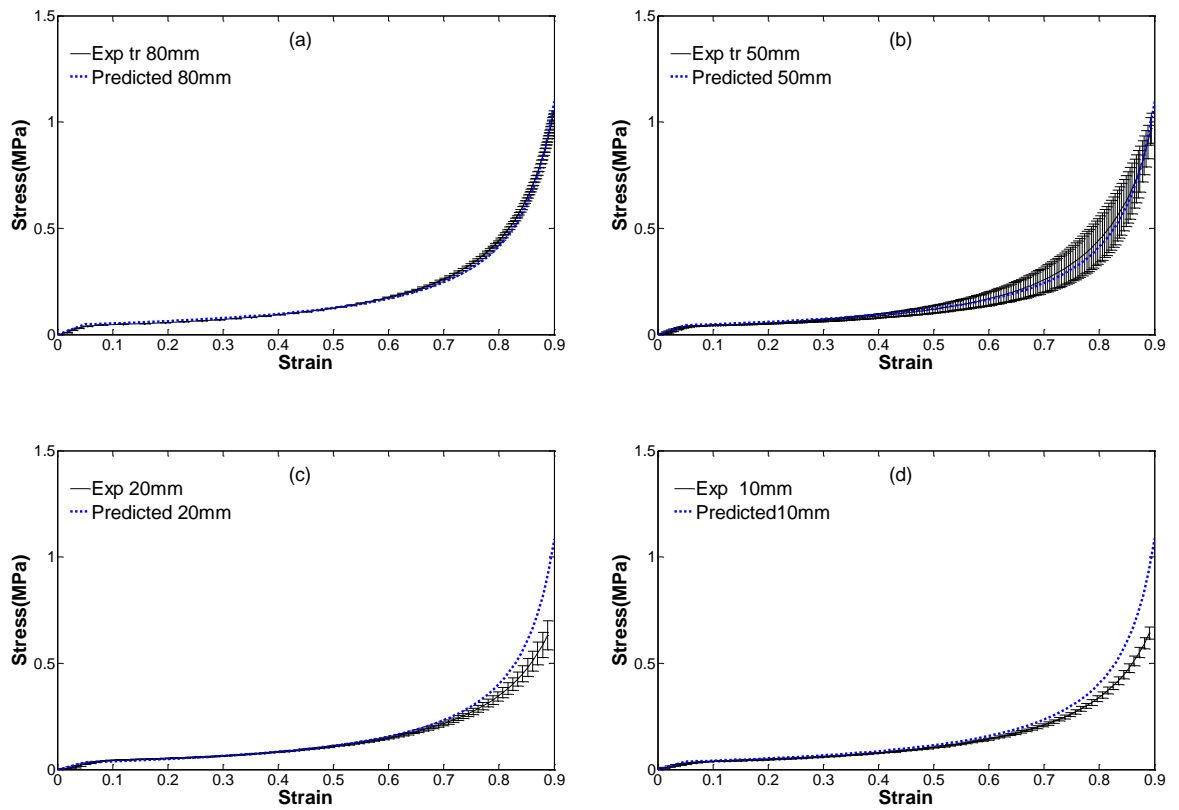


Figure 4-15. Experimental uniaxial compression curves in the transverse (continuous lines) with predicted (dotted lines) uniaxial compression curves for specimen sizes (a)  $80 \times 80 \times 80 \text{ mm}^3$ , (b)  $50 \times 50 \times 50 \text{ mm}^3$ , (c)  $20 \times 20 \times 20 \text{ mm}^3$  and (d)  $10 \times 10 \times 10 \text{ mm}^3$ .

## 4.5. Evaluation of Constitutive Models Currently Implemented in a Commercial FEA Software

In this final section, the utility of constitutive models, already implemented in a commercial FEA code (Abaqus<sup>TM</sup>), in modelling the behaviour of a non-linear transversely isotropic compressible material under large strains is examined. There are currently no models available in the commercial FEA code that can capture the full complexity of the foam's response, as measured in Chapter 3. As such, the investigation progresses by considering the use of the most suitable models currently available in the FEA code. Candidate models include:

- (i) a simple linear transversely isotropic compressible model

- (ii) a non-linear isotropic compressible hyper-elastic model
- (iii) a transversely isotropic compressible elastic plastic crushable foam model

Note that in Abaqus, each of these models can be used in conjunction with visco-elastic elements to create viscoelastic versions of these models.

When choosing a constitutive model, the first consideration is the appropriateness of the model. For example, is the desired material response linear or non-linear, elastic, plastic or rate dependent, isotropic or anisotropic, compressible or incompressible? Next, the effort and equipment required to perform the necessary characterisation tests in order to determine the constitutive parameters must be considered. Finally, once these parameters are obtained, the success of the constitutive model in producing the desired behaviour must be assessed. In order to evaluate predictions, both stress and the deformation kinematics can be used.

In this investigation the transversely isotropic compressible elastic-plastic crushable foam model was discounted due to the difficulty in performing the necessary characterisation tests. Specialised hydrostatic tests are required; due to the relatively low modulus and high compressibility of the polymer foam considered in this investigation attempts to perform these tests using equipment available in the civil engineering department, typically used in soil mechanics proved fruitless. Given this model is designed for elastic-plastic rather than elastomeric behaviour, the effort in obtaining all the necessary test data was eventually considered too great to justify the time required to perform these tests.

This left just the simple linear transversely isotropic compressible model and the non-linear isotropic compressible hyper-elastic models (or variations of these two with viscous elements added). Clearly the linear model would be limited to just small strain stress predictions while the hyperelastic model would be incapable of capturing the transverse isotropy. Still, given these were the most suitable models available, a short investigation into their ability to describe at least some of the mechanical behaviours of the bench-mark foam material was conducted and is described in Sections 3.2 and 3.3.

### 4.5.1. Influence of Material Direction on the Off Principal Axis Large Strain Kinematics

It is interesting to observe the effect of the foam's transverse isotropy on its deformation kinematics. As expected, Figure 4-16a and Figure 4-17a show that when compressed uniaxially with the direction of compression misaligned with the foam's principal directions, the foam's kinematics is not symmetric. As there are currently no suitable large-strain transversely isotropic compressible models implemented in Abaqus<sup>TM</sup> or elsewhere in the literature, accurately predicting both the stress and the kinematics for this material is not yet possible. However, Figure 4-16b and Figure 4-17b show how a linear-elastic compressible transversely isotropic model [30] can successfully approximate the observed kinematics (though not stress) under large strain uniaxial deformation. The five independent material parameters in the elastic stress-strain relation for a linear-elastic compressible transversely isotropic model [30] are listed as follows: the principal Young's modulus  $E_p = E_1 = 2.1 \text{ MPa}$ , the transverse Young's modulus  $E_t = E_2 = E_3 = 0.74 \text{ MPa}$ , the Poisson's ratios  $\nu_{tp} = \nu_{21} = \nu_{31} = 0.1$ ,  $\nu_{tt} = \nu_{23} = \nu_{12} = 0.2$ , and the principal shear modulus  $G_{12} = G_{13} = 0.7 \text{ MPa}$ , which is an average value of the tangent principal shear modulus across the low shear strain region; 0 to 5% shear strain.

The boundary conditions for uniaxial compression in the y-direction are defined in Equations from (4-11) to (4-13)

$$U_i^{TF} = U_i^1 = U_i^3 = 0 \quad (4-11)$$

$$U_i^{TF} = U_i^2 = 0.26\varepsilon \quad (4-12)$$

$$U_i^{BF} = U_i^1 = U_i^2 = U_i^3 = 0 \quad (4-13)$$

where  $U^F$  is the face displacement in the  $i$ th direction, the superscripts  $T$  and  $B$  represent the top and bottom faces. The subscript  $i$  represents the degree of freedom with  $i = 1, 2, 3$  indicating displacements in x, y, z directions respectively.

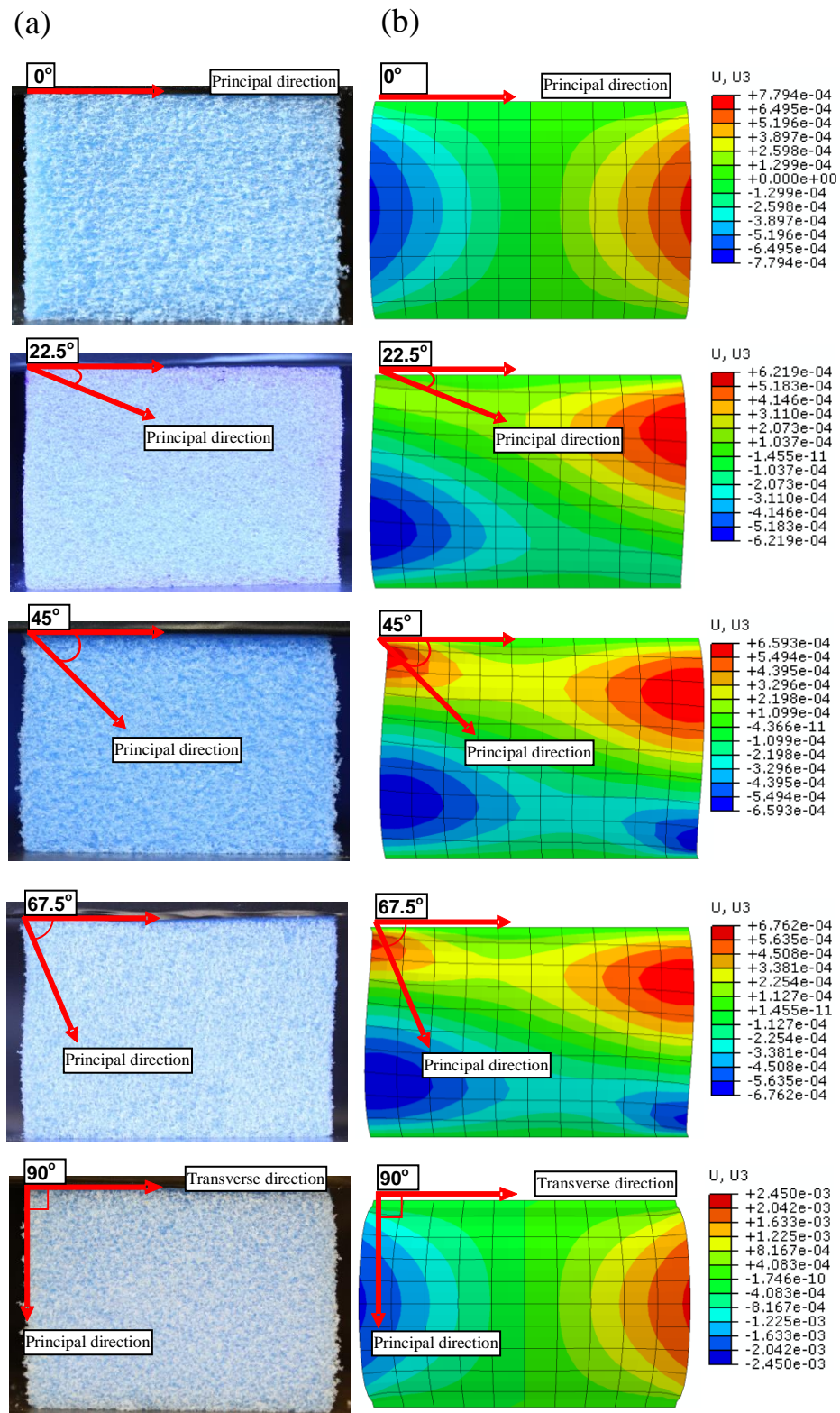
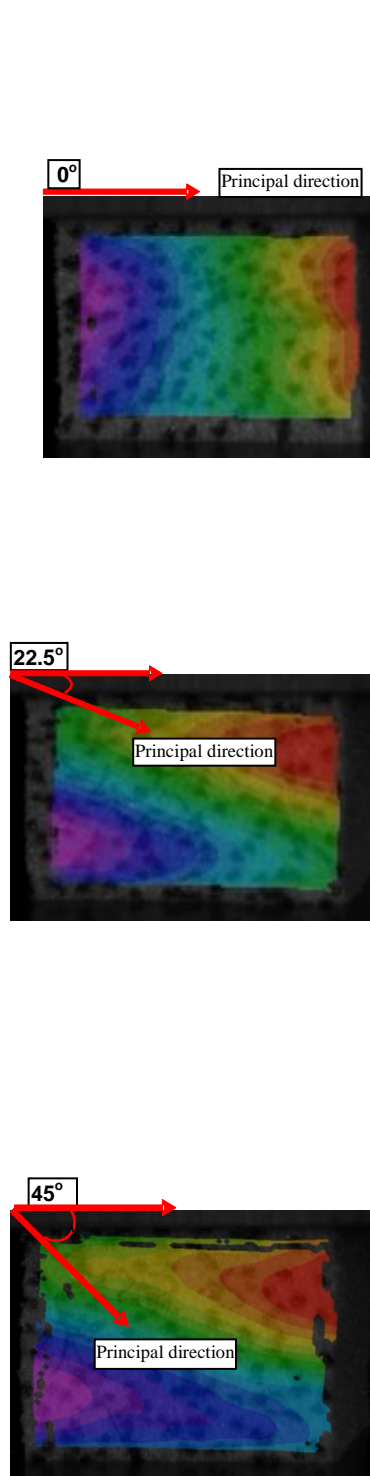
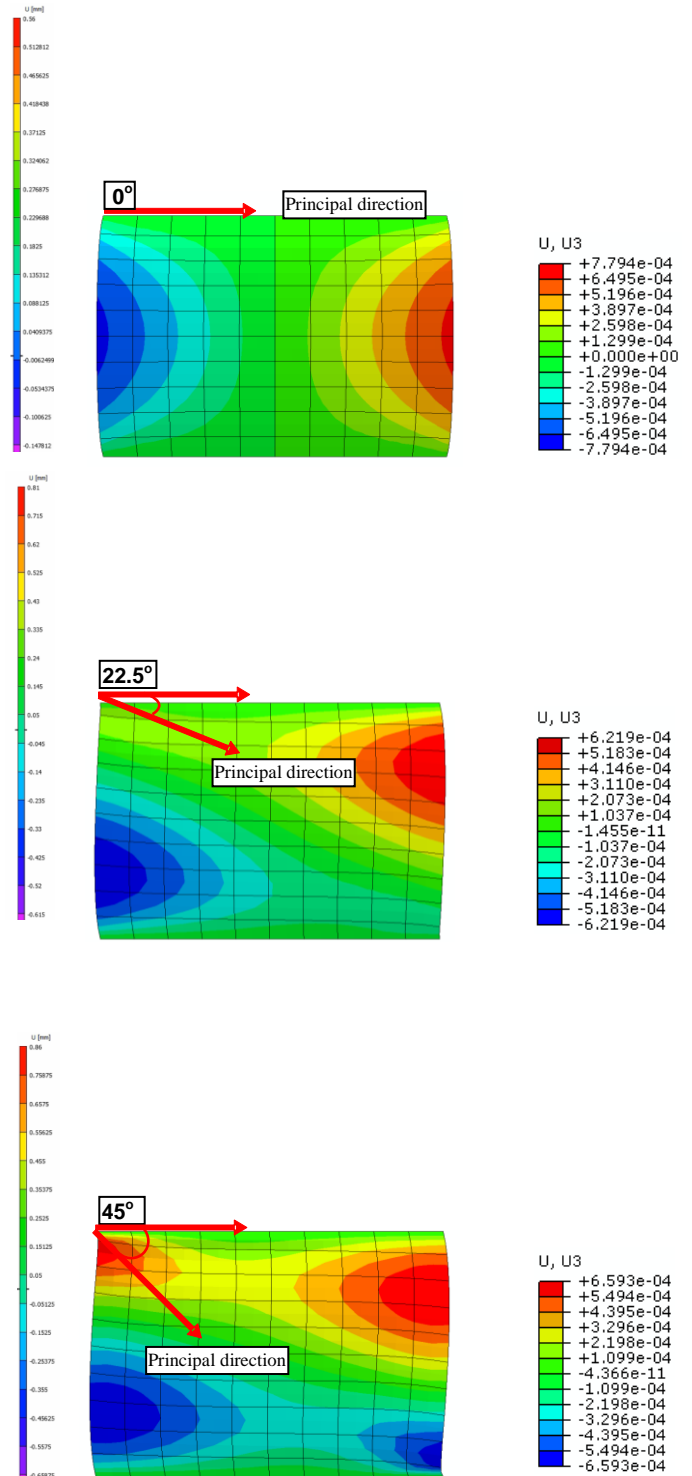


Figure 4-16. Off-axis uniaxial compression of foam to 26% engineering strain. (a): experimental observation showing principal direction. (b): Displacement predictions of linear compressible transversely isotropic model.

(a)



(b)



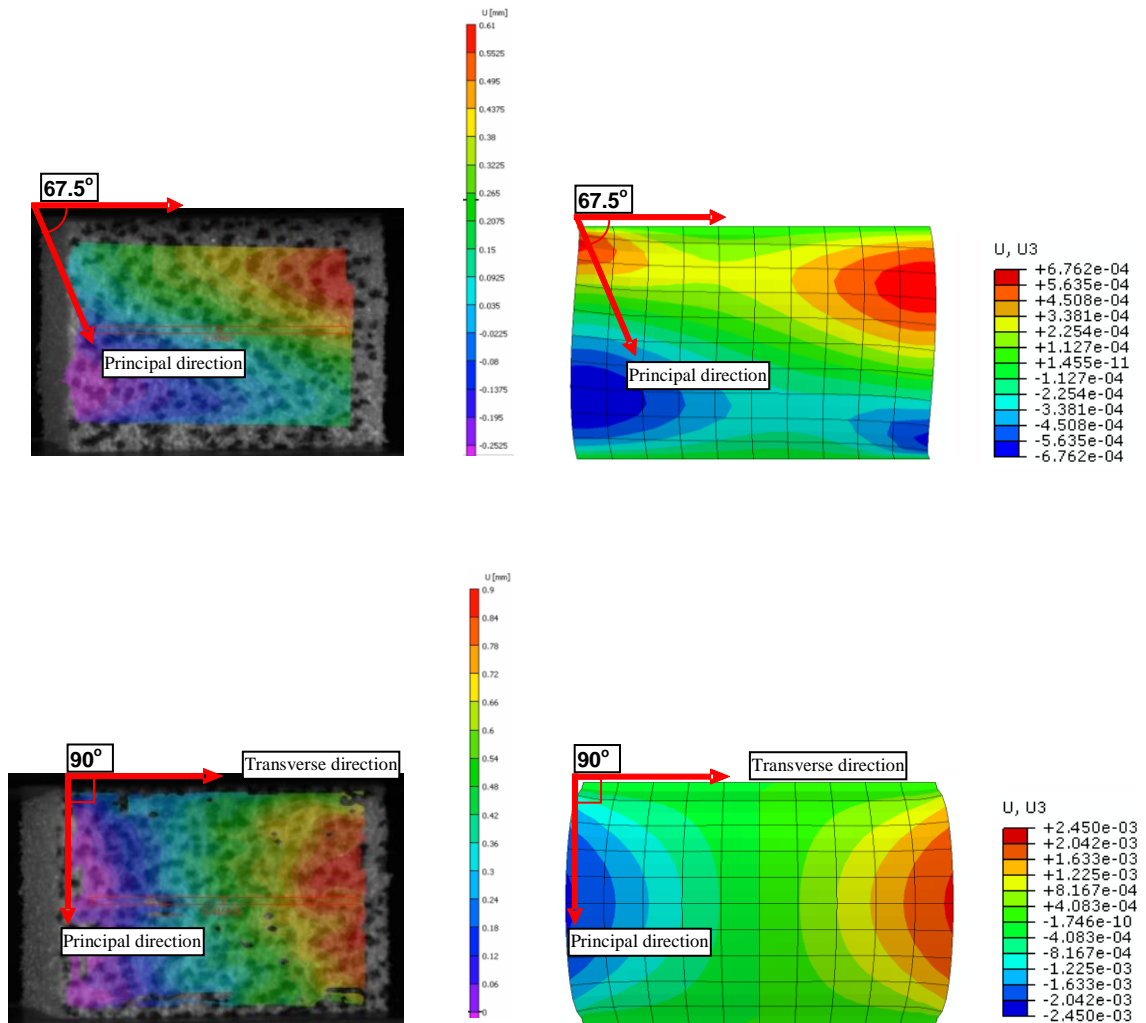


Figure 4-17. Off-axis uniaxial compression of foam to 26% engineering strain. (a): DIC observation showing principal direction. (b): Displacement predictions of linear compressible transversely isotropic model.

Thus, the linear-elastic compressible transversely isotropic model is shown to be reasonably successful in modelling the LDPE foam behaviour at low strains but, as expected is not able to model the foams behaviour at large strain.

### 4.5.1.1. Hyperfoam Evaluation

In this section a hyperelastic constitutive model currently implemented in Abaqus<sup>TM</sup> [35] based on Ogden's isotropic compressible hyperelastic model [33, 55] is used see Equation (2-11). The isotropic hyperfoam model implemented in Abaqus<sup>TM</sup> was used to fit the stress-strain data up to  $\varepsilon = 0.9$ . The strain energy function for the isotropic hyperfoam model was presented in Equation (2-11). The automated fitting algorithm implemented in Abaqus for the hyperfoam model has been used to determine the model parameters [35]. In this algorithm, the coefficient,  $\beta_i$ , is related to a nominal Poisson's ratio,  $\nu$ , (see Equation (2-14)), which implies that ABAQUS needs a single value of the Poisson's ratio to fit the stress-strain curves. However, the data in Figure 4-18a and Figure 4-18b demonstrate that for this foam the Poisson's ratios all depend on the compressive strain. Two sets of parameters are used to fit the stress-strain curves in this work. In the first attempt, the number of parameters is minimised. Only 2 terms are used (i.e.,  $N = 2$ ) and the Poisson's ratio is assumed to be zero [4]. The parameters are listed in Table 4.1 and the fitting results are shown in Figure 4-18a. The relative root mean square error, \*R, in Table 4.1 indicates the fitting is not very close, due to the limited number of terms. To achieve a better fit, more terms are used (i.e.,  $N = 5$  or 6). For the cases of  $0^\circ$  and  $90^\circ$ , the average values of  $\nu_{pt} = 0.14$  and  $\nu_{pt} = 0.068$  (across strain ranging from 0 to 0.9) are used as the values of the Poisson's ratio, respectively. For off-axial compression cases, the Poisson's ratio is determined by a "trial and error" method. The obtained parameters as well as the relative root mean square error are listed in Table 4.2. Although including more terms leads to a better fit, the improved fit comes at the cost of predicting a negative value of the small strain shear modulus, Equation (2-12), which is clearly not realistic and means that the condition  $\mu_i > 0$  given in Equation (2-12) is not strictly enforced by the fitting algorithm. This is an issue has been highlighted previously by Mills [4] who noted that that while many published papers use Ogden's model with  $N = 2$  for fitting uniaxial compression data, together with a positive shear modulus to fit the stress-strain data, curve fitting can nevertheless be improved by using  $N > 2$ . However, in this case the predicted stress-strain curve usually lies far from the actual response when extrapolating beyond the experimental data range used for the fit, especially if a negative shear modulus is used. It is noted that

the isotropic hyperfoam model used here is an elastic model and therefore it cannot predict the foam's unloading response, which is different from the loading path. Some researchers in the literature employed the crushable foam model in ABAQUS to simulate the loading/unloading cycle (e.g. [158]).

While the isotropic hyperfoam model can be used to fit individual stress-strain curves, it is clear that a single parameter set is unable fit all the experimental dataset produced at different compression rotation angles and different rates. To do this would require a visco-hyperelastic transversely isotropic constitutive model, such a model is not yet available in the commercial FEA code used in this investigation.

Table 4.1. Parameters for the hyperfoam model,  $N=2$  and zero Poisson's ratio: Uniaxial compression test.

Cube Angle	0°	22.5°	45°	67.5°	90°
Parameters					
$\mu_1$ (Pa)	711022	811243	754632	552101	470382
$\alpha_1$	18.6934	22.0534	25	25	25
$\mu_2$ (Pa)	3302.89	4046.29	8546.15	12858.7	14107.5
$\alpha_2$	-0.840163	-0.711396	-0.329322	-0.127271	-0.149412
*R	10.49%	12.83%	4.52%	5.05%	4.95%

\*R: Relative root mean square error

Table 4.2. Parameters for the hyperfoam model, N= 5 or 6: Uniaxial compression test.

Cube Angle	0°	22.5°	45°	67.5°	90°
Parameters					
$\mu_1$ (Pa)	2.089659E6	876434	908555	3.055548E6	3.753758E6
$\alpha_1$	3.91570	4.46131	5.77016	6.34324	6.19758
$\mu_2$ (Pa)	-5.623113E6	-2.657494E6	-2.752651E6	-1.473845E6	-5.29943E6
$\alpha_2$	5.64197	7.54975	9.34026	4.04149	9.55526
$\mu_3$ (Pa)	4.271477E6	2.694941E6	2.696404E6	-4.1506680E6	-1.614123E6
$\alpha_3$	7.79685	12.1958	14.6259	10.6011	4.04002
$\mu_4$ (Pa)	-128902	-131243	-204771	290180	308900
$\alpha_4$	-1.45923	-1.85798	-2.09766	1.44267	1.89405
$\mu_5$ (Pa)	4.16944	4063.21	111328	-82200.5	-50027.5
$\alpha_5$	-4.68042	-2.76254	-2.25273	-1.52676	-1.20555
$\mu_6$ (Pa)				2.986498E6	3.414045E6
$\alpha_6$				15.9782	13.5413
Poisson's ratio	0.14	0.12	0.1	0.08	0.068
*R	9.28%	9%	2.03%	1.64%	2.36%

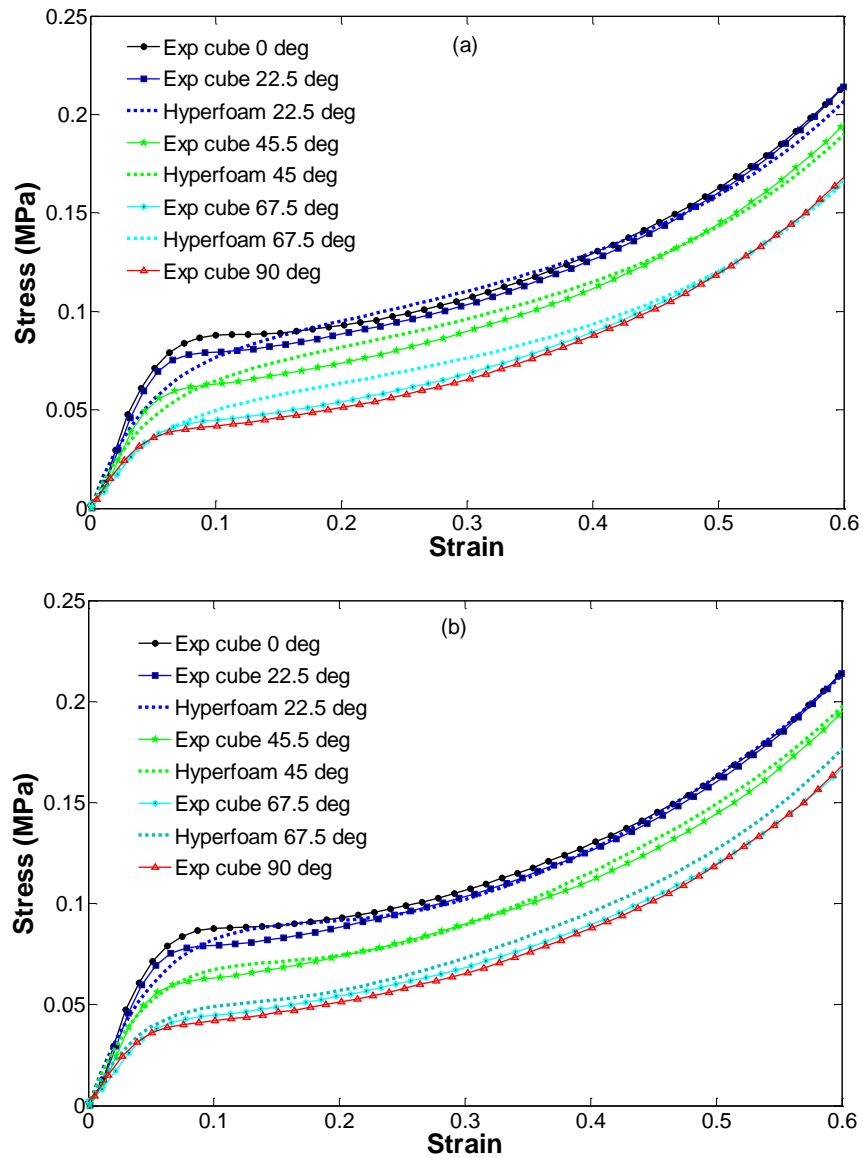


Figure 4-18. (a) Experimental uniaxial compression curves (continuous lines) predicted by compressible isotropic hyperfoam model fitted to the predicted curves with positive shear moduli ( $N = 2$ ); and (b) Experimental uniaxial compression curves (continuous lines) predicted by compressible isotropic hyperfoam model fitted to the predicted curves with negative shear moduli ( $N = 5$  or  $6$ ).

## 4.6. Summary

In this chapter attempts have been made to predict the foams response using simple interpolation methods including the use of: (i) a rotation matrix to predict the stress-strain response at defined off-axis material orientations by interpolating between the stress-strain curves measured for the principal and transverse directions, (ii) a combined phenomenological/gas model to predict the uniaxial compression stress-strain curves for strain rates  $0.016\text{s}^{-1}$ ,  $0.16\text{s}^{-1}$  and  $1.6\text{s}^{-1}$  by interpolating between curves fitted to data at  $0.0016\text{s}^{-1}$  and  $5\text{s}^{-1}$ , (iii) a microstructural anisotropy factor to predict the transverse response from the principal response, or visa versa and (iv) the rate of change of internal pressure to predict the response of different specimen sizes. The techniques provide reasonable predictions for the LDPE foam described in this research. The aim of this exercise was to help understand the mechanisms behind the transversely isotropic rate and size dependent response of the foam and also to find a convenient way to predict the behaviour of the foam under different loading conditions rather than having to measure the behaviour for each condition.

Attempts to include the non-linear transversely isotropic loading response of the foam in FEA have been made though it is clear that current models implemented in the FEA code are not yet capable of modelling this non-linear, transversely isotropic rate and size dependent response. The development of such a continuum based model is beyond the scope of this thesis, instead subsequent work will focus on relating this behaviour to the detailed foam microstructure. Eventually, once a suitable continuum-based constitutive model is developed and implemented in a FEA code, the predictions of such a micro-scale model can be fed into the continuum-based constitutive model to create a fully predictive multi-scale model for non-linear TI rate dependent flexible foams.

## **Chapter 5. Modelling of Transversely Isotropic Closed-cell Foam Using a Micro to Macromechanics Approach**

### **5.1. Introduction**

An important goal of the current work is to make macroscale large-strain viscoelastic predictions for flexible closed-cell transversely isotropic polymeric foam using micro-scale information without recourse to macro-scale testing. Ultimately, the aim is to eliminate or at least reduce the amount of mechanical testing required to characterise a given material. For the sake of simplicity, the process involves the use of pre-existing analytical models wherever possible, resorting to numerical simulations only when analytical predictions are not adequate. The process can be summarised as follows: small strain behaviour is considered first, to do this the parameters of a linear elastic transversely isotropic constitutive model are determined using a combination of existing microstructural analytical models devised by Gibson and Ashby [1] and numerical (finite element) microstructural simulations based on Kelvin-cell geometries with periodic boundary conditions. Predictions of the latter are first fitted to isotropic analytical predictions by appropriate modification of microstructural parameters (such as edge and face thickness), and then the Kelvin model is ‘stretched’ in order to predict properties in the principal and transverse directions.

Yield stresses in the principal and transverse directions are subsequently found using numerical and analytical techniques [1]. Next, the large strain response of the foam in the principal and transverse directions is determined by combining yield stress predictions with predictions of a simple gas pressure model [1, 4, 135, 159]. Finally, in order to evaluate the approach, predictions are compared against experimental results. This chapter consists of two main parts: the first focusing on small strain analysis, the second extends the predictions to large strain analysis.

### 5.1.1. Gibson and Ashby Analytical Model

The most convenient approach to investigate the mechanical properties of foams using a multi-scale modelling strategy is through analytical modelling (see Figure 5-1) [1]. Here, simple closed form equations can be quickly employed to give first order estimates of the foam's mechanical properties based on, for example, the properties of the constituent material, the gas pressure and the foam's relative density. Such models exist for both isotropic and anisotropic microstructures. Here the models developed by Gibson and Ashby [1] are employed. In general such analytical theories are restricted to predictions of the linear elastic response and yield stress at the end of the small-strain linear regime [1]. For example, using their small-strain analytical model Gibson and Ashby were able to predict the linear stiffness properties of orthotropic foams and their yield stress ratio, i.e. the yield stress in the principal direction divided by that in the transverse direction. In reality it is not possible to produce a regular Representative Unit Cell (RUC) for irregular foam structures as the latter includes a variety of cell shapes and sizes and a range of edge and face thicknesses and cross sections. However, this idealisation makes the modelling much more tractable for numerical and analytical analyses but also means that in order to provide reasonable results simple calibrate (5-1) on constants have to be included in the theory. These constants have already been determined by comparing the model prediction against experimental results for a variety of different types of foam (e.g. high or low density [1]) making the calibrated models both accurate and convenient to use.

The simplest method of representing closed-cell foam is by using cubic cell models. Typical examples of isotropic and anisotropic foam cells are given in Figure 5-1a and Figure 5-1b showing cubic and cuboid cell models for closed-cell foams [1]. The isotropic foam cell model is assumed to represent the mechanical response of the foam in the transverse direction. The cell models can be elongated in the foam-extrusion direction (see Figure 5-1b) in order to represent the mechanical behaviour in the extruded or principal direction (here corresponding to the  $y$ -direction). Using these models, Gibson and Ashby proposed a general method for understanding the foam compression mechanism [1]. Effectively, the mechanical properties of cellular solids are based on two separate factors: the first is the structure of the foam, i.e. cell shape and size, the relative density and the

solid material distributed between the cell faces and edges. The second is the property of the material in the cell edges and walls.

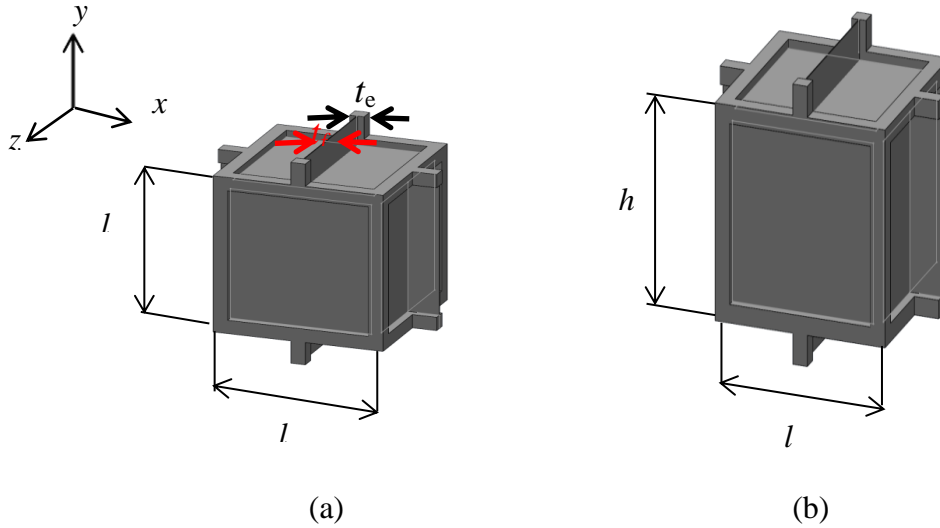


Figure 5-1. (a) A cubic representative unit-cell model for closed cell foam, showing face thickness  $t_f$ , and the cell edge thickness  $t_e$ ; (b) An elongated cuboid representative unit cell with, shape anisotropy ratio  $r = 1.5$  where  $r = h/l$  [1]

### 5.1.1.1. Determination of Small-strain Elastic Moduli for the Isotropic Case

Linear elasticity is limited to small strains, normally 5% or less, and, according to Gibson and Ashby [1], in this region the bulk engineering stress in flexible closed-cell foams is dominated by contributions from three different stress generation mechanisms, namely: the gas pressure inside the closed cells, tension of the cell walls and bending of the cell edges. This is written mathematically in Equation (5-1)

$$E = E_s(E_g + E_f + E_e) \approx E_s \left( C_1 \phi^2 R^2 + (1 - \phi)R + \frac{p_o(1 - 2\nu)}{E_s(1 - R)} \right) \quad (5-1)$$

where  $E$  and  $E_s$  represent the modulus of elasticity of the foam and the solid material respectively.  $E_g$  represents the influence of the compression of gas inside the closed cells,  $E_f$  represents the effect of tension of the cell faces and  $E_e$  represents the contribution from

bending of the cell edges. Also,  $C_1$  is a constant of proportionality (or calibration factor) of the material and equals 0.69 for relative densities less than 0.2. The constant of proportionality was determined by fitting to experimental data.  $R$  is the relative density of the foam,  $\phi$  is the volume fraction of the solid contained in the cell edges and therefore  $\phi = 1$  for open-cell foams whereas  $\phi < 1$  for closed-cell foams. For closed-cell foams,  $(1 - \phi)$  is the fraction of the solid contained in the cell faces. The instantaneous volume of the foam during compression can be predicted using Equation (5-2)

$$\frac{V}{V_o} = 1 - \varepsilon(1 - 2\nu) \quad (5-2)$$

The initial contribution due to the compression of gas,  $E_g$  in Equation (5-1) is calculated simply by assuming that the gas inside the cells is excluded from the volume occupied by the bulk of the solid cell edges and walls and so its volume decreases from  $V_o^g$  to  $V_g$  which can be calculated using Equation (5-3)

$$\frac{V_g}{V_o^g} = \frac{1 - \varepsilon(1 - 2\nu) - R}{1 - R} \quad (5-3)$$

where  $\nu \approx 0.33$ , according to experimental data presented by Gibson and Ashby [1]. The influence on the modulus of elasticity is computed from Boyle's law using Equation (5-4). Here  $p_o$  is the pressure of the gas inside the closed cell and assumed to be equal to the atmospheric pressure. Also, the pressure after strain  $\varepsilon$  is given by

$$pV_g = p_oV_o^g \quad (5-4)$$

The equation is valid only for isothermal conditions. The applied compression pressure is

$$p = p_o - p_{at} \quad (5-5)$$

The influence of the gas pressure on the modulus is found by

$$E_g = dp / d\varepsilon \quad (5-6)$$

which is typically negligible compared to the other influences for small compressions. The main influence on  $E$  results from the membrane stress in the cell faces,  $E_f$  and bending of cell edges  $E_e$  [1]. When closed-cell foams are subjected to uniaxial compression the bending deformation of the cell edges leads the cell faces to stretch normal to the compression loading. The applied force,  $F$ , causes the cell edges to bend (see Figure 5-2).

The stretching is nearly linear elastic with the applied force, therefore the work done  $\frac{1}{2} F \delta$  is equivalent to the force causing the cell edges to bend and cell faces to stretch. The bending force,  $F_b$ , is given by

$$F_b \propto \frac{1}{2} S \delta^2 \quad (5-7)$$

where the stiffness of the cell edges,  $S$ , is given by

$$S \propto E_s I / l^3 \quad (5-8)$$

here,  $l$  is the cell edge length,  $I$  is the second moment of area of the edges and

$$I \propto t_e^4 \quad (5-9)$$

Also, the force due to stretching of the faces is

$$F_s \propto \frac{1}{2} E_s \varepsilon^2 V_f \quad (5-10)$$

here  $\varepsilon$  is the strain resulting from stretching of cell faces and the volume of solid in a cell face is  $V_f$

$$V_f \propto 12 t_f [1] \quad (5-11)$$

Where

$$\varepsilon \propto \delta / l \quad (5-12)$$

and  $t_f$  is the face thickness. Thus, the modulus of elasticity of the cell faces is given by

$$E_f = E_s \beta \left( \frac{t_f}{l} \right) \quad (5-13)$$

and the modulus of elasticity of cell edges is given by

$$E_e = E_s a \left( \frac{t_e}{l} \right)^4 \quad (5-14)$$

where  $a$  and  $\beta$  are simply more empirically determined constants of proportionality proposed by Gibson and Ashby [1]. The latter are estimated by one experimental measurement, thereby ‘calibrating’ the result for all other relative densities of the same kind of foam. A similar method, again from [1], leads to an expression for the shear modulus  $G_{II}$ . Mechanical deformation under an imposed shear load is again described by the cell wall bending. The shear modulus for open-cell foam is given as:

$$G_{tt} = \frac{\tau}{\gamma} = \frac{C_3 E_s I}{l^4} \quad (5-15)$$

The experimental data suggests  $C_3$  is approximately equal to  $3/8$  and the shear modulus for closed-cell foams can be written as

$$\frac{G_{tt}}{E_s} \approx \frac{3}{8} \{ \phi^2 R^2 + (1 - \phi) R \} \quad (5-16)$$

The influence of gas pressure disappears under pure shear as the latter does not produce any change in volume. Also, the wall tension effects depend on the value of  $\phi$ , i.e. the maximum influence of wall tension occurs when  $\phi \approx 0$  closed-cell (in this case all material will be on cell walls). On the other hand the tension of cell walls can be ignored for open-cell foams when  $\phi \approx 1$ , see Equation (5-49).

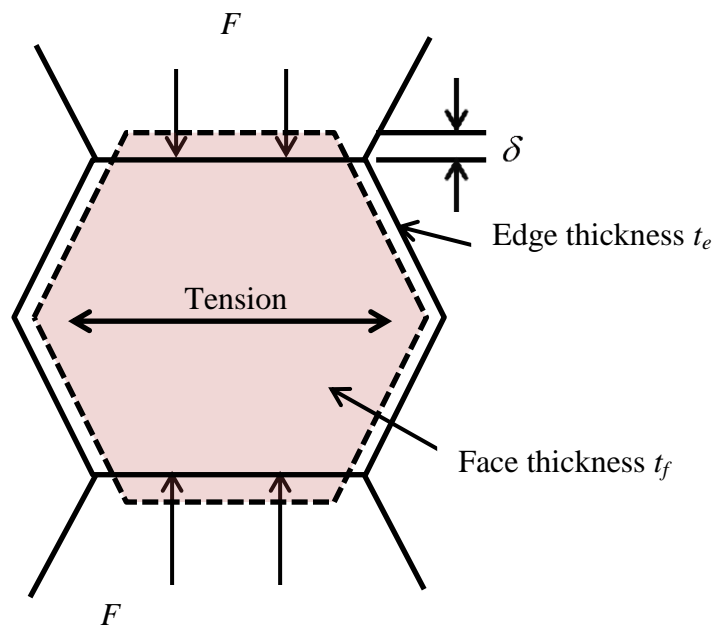


Figure 5-2. Stretching of the face of closed-cell foam during compression.

### 5.1.1.2. Determination of Yield Stress and Strain for Isotropic Case

The Gibson and Ashby model has also been used to calculate the large-deformation response for closed-cell foams. When the compression strain of foam becomes large (larger than a value of about 0.05), the cell faces and edges buckle in the loading direction, see Figure 5-3. Consequently edge buckling can be described by Euler's equation

$$F_{crit} = \frac{n^2 \pi^2 E_s I}{l^2} \quad (5-17)$$

where the parameter  $n$  characterises the degree of freedom at the end of the column. Increasing compressive deformation of the foam causes edges buckling and starts the elastic collapse of the foam. The elastic-yield stress  $\sigma_{el}$  of the foam is

$$\sigma_{el} \propto F / l^2 \quad (5-18)$$

also, from the Equations (5-17) and (5-18) the elastic-yield stress is given as

$$\sigma_{el} \propto \frac{F_{crit}}{l^2} \propto \frac{E_s I}{l^4} \quad (5-19)$$

also from the Equation (5-9)

$$R \propto t^2 / l^2 \quad (5-20)$$

The elastic-yield stress for open cell foam can be written as:

$$\sigma_{el} = E_s C_2 R^2 \quad (5-21)$$

The constant,  $C_2$  is estimated from experimental data to be approximately 0.05.

Gibson and Ashby considered the gas in the closed-cells foams subject to compressive loading. The gas in the closed-cells will be compressed and the internal pressure can affect the elastic yield stress. The initial gas pressure is  $p_o$  and the atmospheric pressure is  $p_{at}$ . In the case of  $p_o > p_{at}$ , the pressure difference  $p_o - p_{at}$  causes tension between cell faces and cells edges. They cannot buckle until the applied loading has exceeded both the buckling load

and the tension load of the cell edges is described by Equation (5-22) (here face effects are ignored). So the elastic-yield stress for closed-cell foams can be calculated using

$$\sigma_{el} = E_s \left( 0.05R^2 + \frac{p_o - p_{at}}{E_s} \right) \quad (5-22)$$

In man-made foams,  $p_o$  is normally approximately equal to  $p_{at}$  and the gas has an insignificant effect on the yield stress [1]. Thus, at this point all the parameters for isotropic foam can be related back to the properties of the constituent material and the foam microstructure.

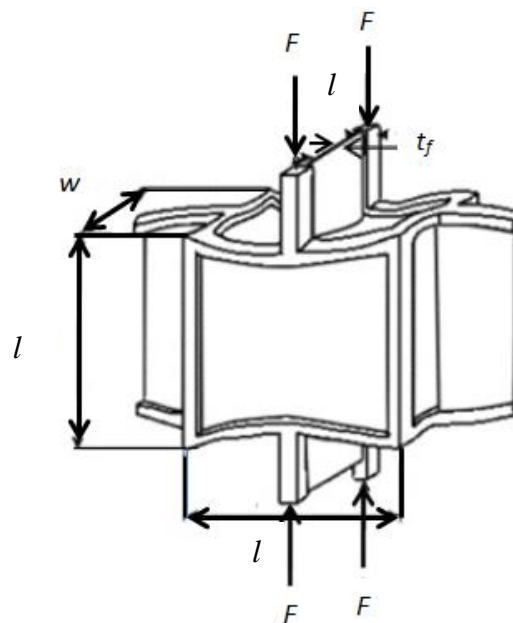


Figure 5-3. Elastic buckling in the cell walls of a closed cell.

### 5.1.1.3. Determination of Small-strain Elastic Moduli for the Transversely Isotropic case

In order to calculate the modulus of elasticity in the principal direction, statistical measurements should be used to determine the anisotropy ratio  $r$ , where  $r = h/l$  and  $h$  and  $l$  are the average values of the principal cell dimensions, see Figure 5-1b, which illustrates an idealised unit closed-cell. The principal direction is parallel to the  $y$  direction. Let the modulus of elasticity of foam in the principal direction be  $E_p$ , and that in the transverse direction is  $E_t$ . To compute the ratio  $E_p/E_t$ , the anisotropy ratio,  $r$ , can be employed. Figure 5-1b illustrates how the unit cell is stretched. The technique of calculating the modulus, described in the previous section can be slightly changed to analyse the transversely isotropic case [1]. Compression loading in the  $y$  direction is supported by four beams of length,  $h$ . The compression force,  $F$  on a single beam is proportional to  $\sigma_p h^2$ , where  $\sigma_p$  is the stress in the principal direction. The deflection,  $\delta_p$ , for a single beam is

$$\delta_p \propto Fh^3 / E_s I \quad (5-23)$$

The compression strain  $\varepsilon_p$  is calculated from the deformation  $\delta_p$  using

$$\varepsilon_p = \delta_p / h \quad (5-24)$$

so from these the  $E_p$  can be found from

$$E_p = \frac{\sigma_p}{\varepsilon_p} = \frac{C_1 E_s h}{l^5} = C_1 E_s \frac{t^4 h}{l^4 l} \quad (5-25)$$

Compressive loading in the transverse direction is supported by two beams of length  $h$  and two beams of length  $l$ , see Figure 5-1b. The displacement,  $\delta_t$ , of both groups must be the same; consequently, the compression loading supported by the longer beams is less than that supported by the shorter beams. The force in the longer beam is proportional to

$$F_p \propto E_s I / h^3 \quad (5-26)$$

and that in the shorter beam is proportional to

$$F_t \propto E_s I / l^3 \quad (5-27)$$

The whole applied force in the transverse direction  $F_t$  can be obtain from

$$F_t = \sigma_t h l \quad (5-28)$$

and the strain  $\varepsilon_t$  by

$$\varepsilon_t = \delta_t / l \quad (5-29)$$

Rewriting the equations (5-14), (5-25) to (5-27) the elastic modulus in transverse direction  $E_t$  can be calculated from the expression

$$E_t = \frac{\sigma_t}{\varepsilon_t} = \frac{C_1 E_s I}{2h} \left( \frac{1}{l^3} + \frac{1}{h^3} \right) = \frac{C_1 E_s t_e^4 l}{2 l^4 h} \left( 1 + \frac{l^3}{h^3} \right) \quad (5-30)$$

where  $\sigma_t = \sigma_{el}$

Results of the analysis for the transverse direction, the isotropic analysis of the previous

$$v_{pt} = E_{pt} (v_{tp} / E_t) \quad (5-31)$$

section, are reused in this case. Rewriting both equations (5-25) and (5-30) with  $r = h/l$ , the Young's modulus is now calculated as a function of the anisotropy ratio:

$$\frac{E_p}{E_t} = \frac{2r^2}{1+1/r^3} \quad (5-32)$$

Clearly the Young's modulus ratio is significantly influenced by the shape anisotropy ratio,  $r$ . In the case of closed-cell foam, the face tension stresses are important, and contribute an

additional contribution given as;  $(1-\phi) \frac{2r}{1+(1/r)}$ . The modulus of elasticity in the

principal direction can be calculated from the modified expression

$$\frac{E_p}{E_t} = \frac{2r^2}{1+(1/r)^3} + (1-\phi) \frac{2r}{1+(1/r)} \quad (5-33)$$

The Poisson's ratio of the foam is calculated as follows

$$v_{tp} = \frac{E_t}{2G_{tt}} - 1 \quad (5-34)$$

A similar analysis for calculating the shear modulus,  $G_{pt}$ , results in the expression

$$\frac{G_{pt}}{G_{tt}} = \frac{2}{1+r} \quad (5-35)$$

The analytical model of Gibson and Ashby [1] is used to predict  $E_t$  and  $G_{tt}$  in Equations (5-1) and (5-16), i.e. the properties in the plane of isotropy, using a first estimate of  $\nu_{tt}$ . The predicted values of  $E_t$  and  $G_{tt}$  are then used to obtain a revised estimate of  $\nu_{pt}$ .

Here the influence of the initial relative density of the foam,  $R$  on the mechanical properties of the regular foam model was studied. In Figure 5-4 the predicted modulus of elasticity for the transverse and principal directions are displayed as function of the relative densities. Both curves show a similar general path, with increasing relative density. This is due to the fact that by increasing relative density, the edge diameters and cell face thickness increases. As expected, the curve for modulus of elasticity in the principal direction lies higher than the curve for the transverse direction. Also, it is clear that as the relative density increases, the difference between  $E_t$  and  $E_p$  also increases.

The second set of calculations carried out from the Gibson and Ashby models are the shear moduli in the principal and transverse directions. Figure 5-5 shows the influence of relative density ranging from 0.01 to 0.4 for both directions. The variation of the shear modulus with relative density shows a similar general path with increasing relative density as the compressive modulus. It is interesting to note that the curve for shear modulus in the principal direction lies lower than the corresponding curve for the transverse direction.

Comparison between the experimental uniaxial compressions tests (see Table 5.1), shear tests and results predicted by the Gibson and Ashby analytical model gives poor agreement. The result suggests that, despite providing reasonable success in predicting the transverse properties of the foam, the analytical model cannot accurately predict either  $E_p$  or  $G_{pt}$ , see Equations (5-25) and (5-35). In order to obtain these elastic parameters alternative methods must be used. In this investigation, finite element modelling is employed.

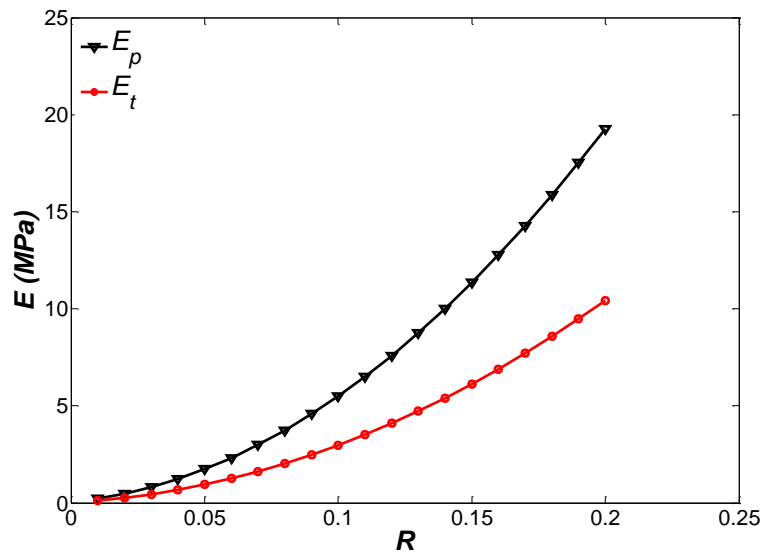


Figure 5-4. Variation of modulus of elasticity with relative density for a cubic and an elongated cuboid unit cell (curves predicted with  $r=1.2$ ).

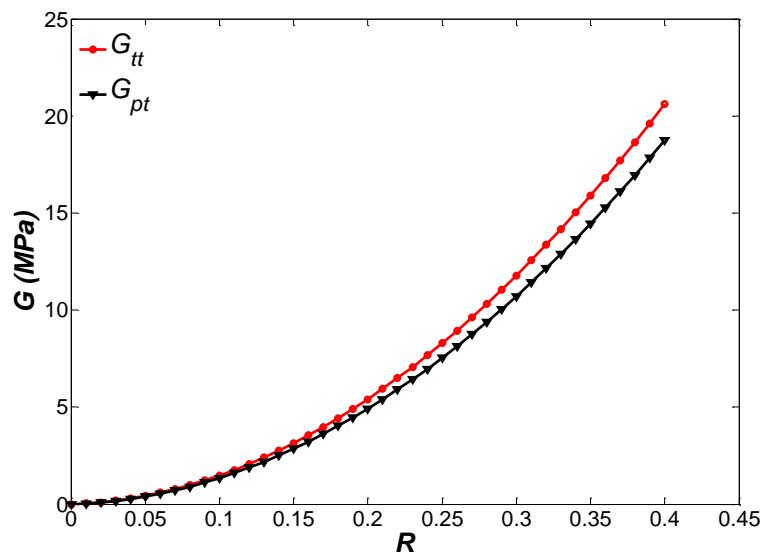


Figure 5-5. Variation of shear modulus with relative density for a cubic and an elongated cuboid unit cell (curves predicted with  $r=1.2$ ).

Table 5.1. Experimental and predicted results obtained using G&A model for the properties of LDPE foam

Parameters	$E_p$	$E_t$	$G_{pt}$	$G_{tt}$
Experimental (MPa)	$2.039 \pm 0.363$	$0.741 \pm 0.157$	0.7	0.34
Prediction G&A model (MPa)	1.38 see Eq (5-33)	0.749 see Eq (5-1)	0.301 see Eq (5-35)	0.33 see Eq (5-16)

### 5.1.1.4. Determination of Yield Stress for Transversely Isotropic Case

The ratio of the elastic-buckling stress,  $\sigma_p / \sigma_t$ , can be calculated by extending the techniques of Section 5.1.1.2. For loading in the principal direction, see Figure 5-3, cell edges buckle when the compression loading on the walls grows larger than the value of Euler buckling load, given by:

$$F_{crp} = \frac{n_p^2 \pi^2 E_s I}{h^2} \quad (5-36)$$

Also, Gibson and Ashby showed that the compression load can be written as

$$F_p \propto \sigma_p l^2 \quad (5-37)$$

and the elastic-yield stress in the principal direction can be given as

$$\sigma_p = \frac{C_1 n_p^2 \pi^2 E_s I}{h^2 l^2} \quad (5-38)$$

Gibson and Ashby proposed the rotation stiffness  $n$  for elastomeric honeycombs. They explained that  $n$  is related to the degree of freedom and cell shape anisotropy, the value of  $n = 0.5$  indicates rotation is freely allowed and  $n = 2$  indicate no rotation. Here, a rotational stiffness  $n_t = 0.686$  was assumed for regular cells and  $n_p = 0.718$  for elongated cells, as suggested by Gibson and Ashby [1] where  $n_p$  characterises the rotational stiffness for the principal direction of compression loading, and  $C_1$  is again a constant of proportionality of the material, which is estimated by fitting Equation (5-38) to the experimental data. For compression loading in the transverse direction, the buckling load is given by

$$F_{crit} = \frac{n_i^2 \pi^2 E_s I}{l^2} \tag{5-39}$$

and

$$F_i \propto \sigma_i l h \tag{5-40}$$

Consequently, from above Equations (5-36) to (5-40) the ratio of yield stress can be defined as a function of the anisotropy ratio by

$$\frac{\sigma_p}{\sigma_t} = \frac{n_p^2}{n_t^2} \frac{1}{r} \tag{5-41}$$

Again, the influence of  $R$  on the elastic yield stress in transverse and principal directions is investigated. Figure 5-6 shows how the elastic yield stress of the foam model under compression loading varies with the relative density. The relative foam densities used ranges between 0.01 and 0.4. A first indication from this figure is that increasing the relative densities causes an increase in the elastic yield stress in both directions. Moreover, this causes the difference between  $\sigma_t$  and  $\sigma_p$  to increase. The curve for the principal direction lies lower than the curve for the transverse direction.

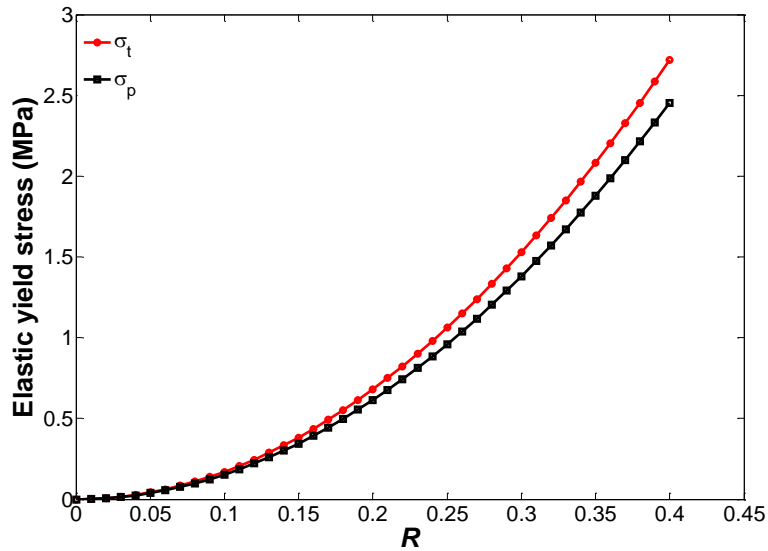


Figure 5-6. Variation of yield stress with relative density for a cubic and an elongated cuboid unit cell (curves predicted with  $r=1.2$ ).

Figure 5-7 shows the stress-strain curves for the load in the principal and transverse directions. The diagram shows both curves in the principal and transverse direction are

predicted using Gibson and Ashby’s model (see Equations (5-22) and (5-41)). The results show that the predicted curve in the transverse direction is very close to the experimental data, while it is not in principal direction. Also, the yield point is fitted to occur at a strain 0.042.

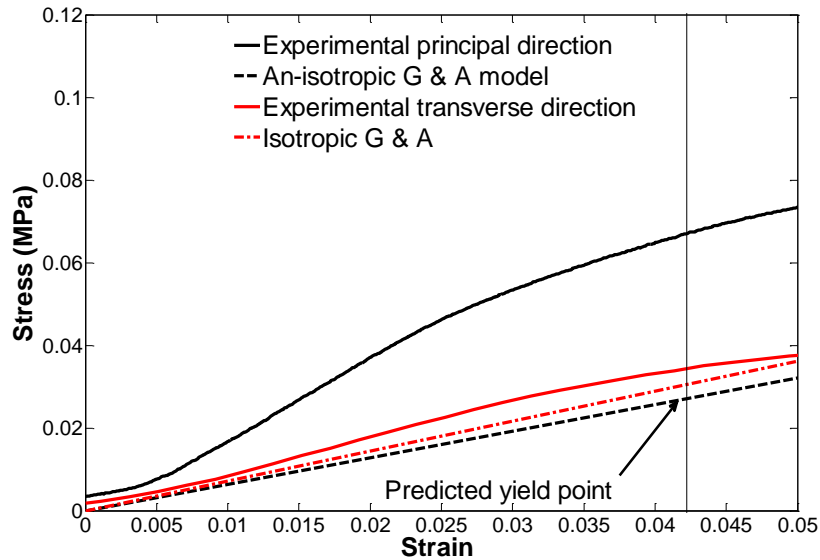


Figure 5-7. Stress-strain curves show the predicted yield strain in the principal and transverse directions using Gibson and Ashby model.

Table 5.2. Experimental and predicted yield stress and elastic yield strain obtained using G&A model for LDPE foam

Parameters	$\sigma_t$ (MPa)	$\sigma_p$ (MPa)	$\epsilon_t$	$\epsilon_p$
Experimental	$0.026 \pm 0.016$	$0.061 \pm 0.014$	$0.032 \pm 0.007$	$0.031 \pm 0.012$
Prediction	0.032	0.029	0.042	0.042
G&A model	see Eq (5-22)	see Eq (5-41)	see Figure 5-7	see Figure 5-7

### 5.1.2. Kevin Numerical Model

As discussed in Section 5.1.1 the Gibson and Ashby’s calibrated analytical model can predict the elastic and shear moduli, Poisson’s ratio and yield stress in the transverse direction for transversely isotropic foams with reasonable accuracy. Also, this model can give good estimates for the Poisson’s ratio,  $\nu_{pt}$ , in the principal direction. Furthermore, the previous investigations [1, 4, 76, 135] have shown that the model is reasonably accurate for predicting elastic mechanical properties (see Figure 2-7). However, in this work it has

been found to be much less accurate when predicting the elastic modulus  $E_p$ , the shear modulus  $G_{pt}$  and the yield stress in the principal direction  $\sigma_p$ . For this reason, in this investigation Gibson and Ashby's model has been augmented using a Finite Element (FE) model [160]. Numerical computation, using the FE method allows an alternative, more detailed strategy to investigate the relationship between microstructure and macro-scale response. Clearly the effort in generating and running a numerical simulation is greater than the use of the simple equations resulting from analytical models, though potentially results are more accurate and a greater range of parameters can be explored. One of the simplest but most useful numerical approaches to analyse the small strain response of foams has been to use the so-called, 'Kelvin cell' with Periodic Boundary Conditions (PBC) as a Representative unit cell (RUC) [4, 75, 89]. The three-dimensional Kelvin RUC has been used by several researchers to simulate the microstructure of foams [1, 4, 75, 76, 86]. The structure for an isotropic Kelvin model consists of fourteen faces, where each unit cell has six square and eight hexagonal flat faces of equivalent edge lengths and cross sections, see Figure 5-8a. The advantage of this approach is that relatively few elements are required to make a RUC model using three-dimensional structural elements compared to a Representative Volume Element (RVE) approach, e.g. [86, 96-98, 135, 161]. Its disadvantage is that, like the analytical model, it is a major simplification of an actual random foam microstructure and has been found to over-predict the moduli of real foams [4, 72, 75, 84, 95].

In this investigation, the aim is to calibrate the Kelvin-cell numerical simulation predictions to the predictions of the Gibson and Ashby analytical model. The latter produces reasonably accurate predictions in the transverse direction but not the principal direction. Once calibrated the Kelvin-cell model is extended by the microstructural anisotropy ratio,  $r$ . The elongated Kelvin model is then use to predict the foam response in the principal direction.

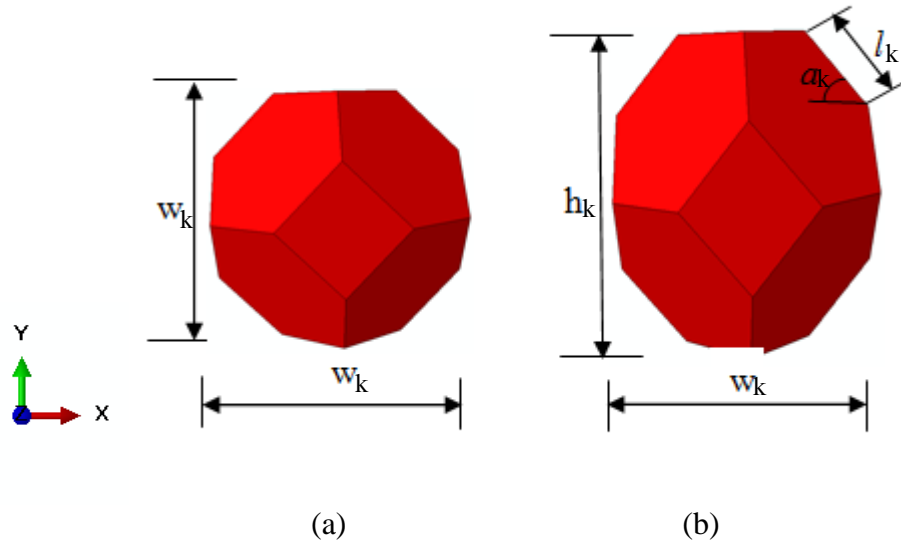


Figure 5-8. (a) Isotropic closed-cell Kelvin model (b) Anisotropic closed-cell Kelvin model.

### 5.1.2.1. Analysis Procedure

In order to determine the elastic modulus, in the principal direction,  $E_p$ , for the transversely isotropic case a simple procedure is proposed. This involves first generating a FE model (see Section 5.1.2.2) of a closed-cell isotropic and elongated Kelvin RUC, see Figure 5-9a and Figure 5-9b with a PBC imposed (see Section 5.1.2.3). The RUC dimensions are initially determined from the foam's relative density (see Section 5.1.2.4 and 5.1.2.5). Mesh refinement is conducted in Section 5.1.2.6 to ensure convergence of the results. As already mentioned, if the relative density is used to determine theoretical values for the dimensions of the Kelvin model, then the simulations tend to over-predict the moduli of random foams [1]. The size of this over-prediction depends on the detailed microstructure of the Kelvin cell (e.g. edge cross-section shape – see Section 5.1.2.7). Therefore, some means of calibration have to be used to ‘soften’ the Kelvin RUC if it to be used to predict the behaviour of real random foams. In order to maintain a fully predictive micro to macro modelling strategy, the calibrated analytical model (see Sections 5.1 and 5.1.1.1) is used to calibrate the Kelvin RUC predictions. This leads to questions regarding the best method to artificially soften the Kelvin RUC, an issue addressed in Section 5.1.2.8. The details of fitting the Kelvin cell model geometry (e.g. edge cross-section area and cells face thickness) are shown in Section 5.1.2.9. The calibrated Kelvin

RUC is then elongated by extending the geometry in the principal direction, as shown in Figure 5-8b, to give the same anisotropy ratio,  $r$ , as measured from the image analysis of actual polymer foam (see Sections 5.1.2.10 and 5.1.2.11). The elongated (anisotropic closed-cell) Kelvin model is then used to calculate the elastic modulus,  $E_p$  and to calculate the shear modulus,  $G_{pt}$  in the principal direction.

### 5.1.2.2. Finite Element Model

The commercial FE software Abaqus Standard<sup>TM</sup> was used. Figure 5-9a and Figure 5-9b show FE models for the closed cell isotropic and elongated Kelvin RUC models using the same mesh density. Type S3R elements which model homogeneous thin shell structures were used for the faces of the RUC in which one dimension (the thickness) is significantly less than the other dimensions, and the stresses in the thickness direction are negligible. Also, type B31 Timoshenko beam elements of circular and rectangular cross sections were used to model the edges. This type of beam element is axial and shear deformable; thus, B31 element is suitable for modelling relatively strut members, in which both axial and shear deformations are important. In order to fix the two sets of elements together, tie constraints were applied to distinct nodes occupying the same co-ordinates, and the tie joint was implemented as a linear tie joint, which is a multipoint constraint accessed using the option 'constraint-tie' in Abaqus<sup>TM</sup>. When a contact pair uses the constraint-tie formulation, Abaqus<sup>TM</sup> uses the undeformed shape of the model to determine which slave nodes are within the adjustment zone. Abaqus<sup>TM</sup> then adjusts these slave nodes' positions into a zero-penetration state and forms constraints between these slave nodes and the surrounding nodes on the master surface. The tie constraints are formed with a surface-to-surface. One important advantage of a constraint-tie formulation is the easy for changing in mesh density within the model, see [162].

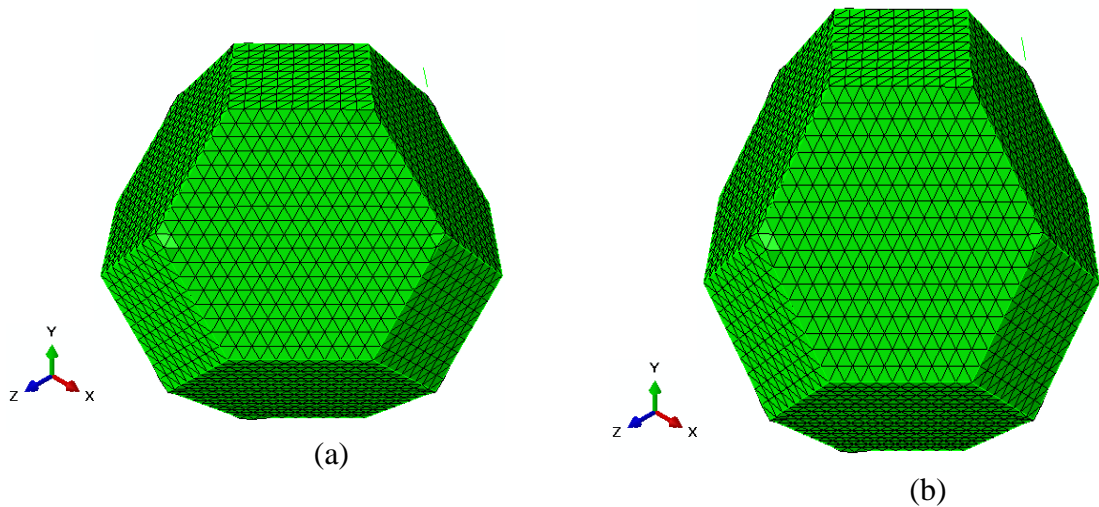


Figure 5-9. FEM models of (a) Isotropic and (b) Anisotropic Kelvin closed-cell foam.

### 5.1.2.3. Periodic Boundary Conditions

The concept of a 3D periodic boundary condition (PBC) suggested by Thiyagasundaram et al. [89] is used in this work to simulate both isotropic and transversely isotropic foams. Generally speaking, in order to apply a PBC on a three dimensional structure, it is necessary that the unit cell structure is totally under a periodic mechanism, which means that the node on one boundary must have a counterpart at the same vertical (on top and bottom) or horizontal location along the opposite displacement and rotation (see Figure 5-10, where the sides: 1-2, 3-4 and 5-6 refer to right-left, top-bottom and front-back faces respectively). In this work, the procedure for implementing a 3D periodic boundary condition on the RUC model is described in below Section:

#### 5.1.2.3.1. Boundary Conditions during Compression and Simple Shear Simulations

Periodic boundary conditions, as defined by Thiyagasundaram et al. [89], are applied on the six side edges of the Kelvin foam model. The periodic boundary conditions for uniaxial compression (in the y-direction) and shear test (in x-y plane) are defined in Equations (5-42) to (5-48)

$$U_i^T = U_i^B + U_i^{d1} \quad (\text{Uniaxial compression test}) \quad (5-42)$$

$$U_i^L = U_i^R + U_i^{d2} \quad (\text{Shear test}) \quad (5-43)$$

$$U_i^I = U_i^O + U_i^{d3} \quad (\text{Shear test}) \quad (5-44)$$

$$U_j^T = U_j^B \quad (\text{Uniaxial compression test}) \quad (5-45)$$

$$U_j^L = U_j^R \quad (\text{Shear test}) \quad (5-46)$$

$$U_j^I = U_j^O \quad (\text{Shear test}) \quad (5-47)$$

$$\begin{aligned} d_1 &= X_1, Y_1, Z_1 \\ d_2 &= X_2, Y_2, Z_2 \\ d_3 &= X_3, Y_3, Z_3 \end{aligned} \quad (5-48)$$

where  $U$  is the nodal displacement in the  $i$ th direction, the subscript  $i$  represents the degree of freedom with  $i = 1, 2, 3$  indicating displacements in  $x, y, z$  respectively and  $j = 4, 5, 6$  indicating the rotation about  $x, y, z$  directions respectively. Also, faces of model are described as:  $T$ = Top,  $B$ =bottom,  $L$ =left,  $R$ = right,  $I$ =inside and  $O$ =outside of Kelvin model (See Figure 5-10). In order to implement the PBC, a Matlab code was used to generate the PBC equations for all beams elements, and then, the PBC equations were incorporate in an input file in the commercial FE software Abaqus Standard™.

The superscript indicates side number, and the points  $d_1, d_2$  and  $d_3$  represent the three dummy nodes as shown in Equation (5-48). The displacement of dummy nodes as calculated by the FE model was used to compute the boundary conditions as presented in Equations (5-42) to (5-48)

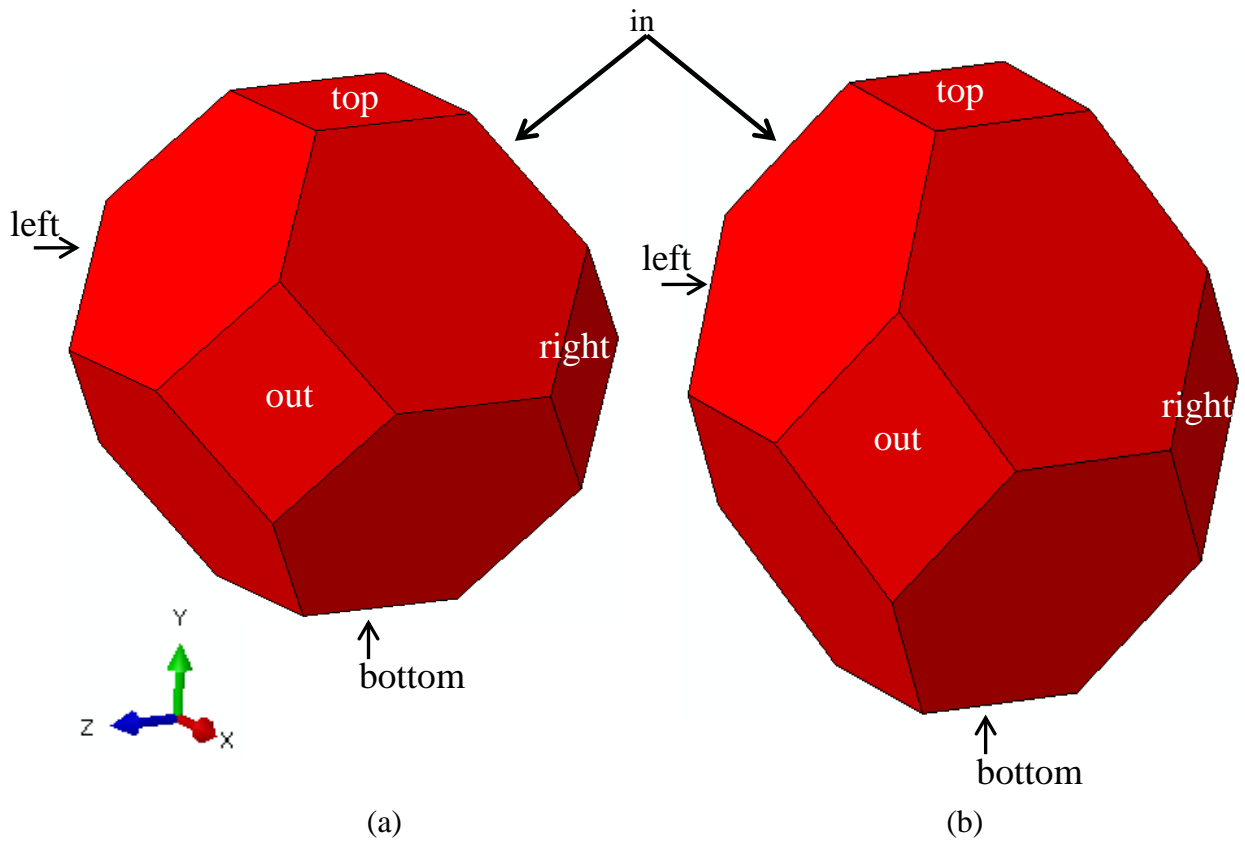


Figure 5-10. Side numbering of (a) Isotropic and (b) Anisotropic closed-cell Kelvin model.

### 5.1.2.4. Dimensions of Isotropic Kelvin Representative Unit Cell

The mechanical response of foam depends very strongly on its relative density; thus, it is useful to define a relationship between the RUC dimensions and relative density, a task already accomplished by Gibson and Ashby [1]. The precise equation depends on the microstructure and the nature of the foam, including the dimensions of the structure and whether it is either closed- or open-cell. The equations used for calculating cell edge length,  $l_k$ , are different for closed- and open-cell foams. The equations below, from [1], are used to calculate cell dimensions [1]

$$\phi = \frac{\text{edge volume}}{\text{material volume}} = \frac{\bar{n}t_{ek}^2}{\bar{n}t_{ek}^2 + Z_f t_{fk} l_k} \quad (5-49)$$

$$R = 1.2 \left( \frac{t_{ek}^2}{l_k^2} + 0.7 \frac{t_{fk}}{l_k} \right) \quad (5-50)$$

$$\frac{t_{fk}}{l_k} = 1.4(1 - \phi)R \quad (5-51)$$

$$\frac{t_{ek}}{l_k} = 0.93\phi^{1/2}R^{1/2} \quad (5-52)$$

The subscript,  $k$ , refers to the Kelvin foam model. The cell face thickness is  $t_{fk}$ , the cell-edge thickness is  $t_{ek}$ ,  $\bar{n}$  is the average number of edges of each face in a unit cell,  $Z_f$  is the number of faces joined per edge and  $f$  is the number of faces on a unit cell. These parameters are used to design a unit cell Kelvin foam model. For most true foams [1], microscopic measurements showed that  $Z_f = 3$ ,  $Z_e = 4$ ,  $\bar{n} \approx 5$  and  $f \approx 14$ . The values of the model parameters calculated from Equations (5-49) to (5-52) are presented in Table 5.3. Note that the predicted dimensions, based on relative density  $R$ , are not expected to be the same as those measured using an optical microscope because the shape and distribution of the cells in the actual foam are very different to those in the Kelvin RUC. Details of the experimental method used to measure these quantities are described in Sections 5.1.2.7 and 5.1.2.8.

Table 5.3. Dimensions of Kelvin model closed-cell RUC predicted by G&A model [1] and measured using microscopy.

Parameter	predicted dimensions in (mm)	measured dimensions in (mm)
$t_{ek}$ (edge thickness)	0.18	$0.055 \pm 0.011$
$t_{fk}$ (face thickness)	0.001	$0.003 \pm 0.001$
$l_k$ (cell edge length)	0.94	$0.43 \pm 0.15$

### 5.1.2.5. Dimensions of Elongated Kelvin Repeat Unit Cell Model

When the cell is stretched in the  $Y$ -direction to represent anisotropy, the angle defined by  $a_k$  in Figure 5-8b is changed. In this case the height of the cell in the stretched direction is

$$h_k = 2\sqrt{2}l_k \tan a \quad (5-53)$$

while the width in the principal and transverse directions remains as

$$w_k = 2\sqrt{2}l_k \quad (5-54)$$

Thus, the measured anisotropy ratio,  $r$ , can be related to  $a_k$  by the expression

$$r = \frac{h_k}{w_k} = \tan a_k \quad (5-55)$$

According to Lu et al [159] the relative density,  $R$ , of the elongated Kelvin model is related to the edge length  $l_k$  and the edge thickness  $t_{ek}$  by

$$R = \frac{\sqrt{2}\sqrt{(1+r^2)}+1}{2\sqrt{2}rl_k^2}(\pi t_{ek}^2 / 4) \quad (5-56)$$

The lengths of beam elements in this elongated Kelvin RUC are longer than those placed along the edges of the isotropic RUC. The change the edge length influences the thickness of the edges and faces if the relative density is held constant.

### 5.1.2.6. Mesh Convergence of RUC

In order to use the FE simulations to calculate reliable and accurate data the mesh should be sufficiently refined. The optimum mesh density is usually a compromise between accuracy and computational cost. In order to investigate mesh convergence, uniaxial compression simulations have been conducted using progressively finer meshes for an isotropic Kelvin RUC. The predicted elastic modulus versus number of elements used to model the RUC is shown in Figure 5-11. It can be seen that as the mesh density increases from 906, 1326, 1866, 2526, 5226, 6366 to 7626 elements, the shear modulus quickly converges to a unique value. In this work the optimum mesh density of 5226 elements is used to reduce the computational time while permitting validation of the 3D element RUC model with analytical and experimental tests.

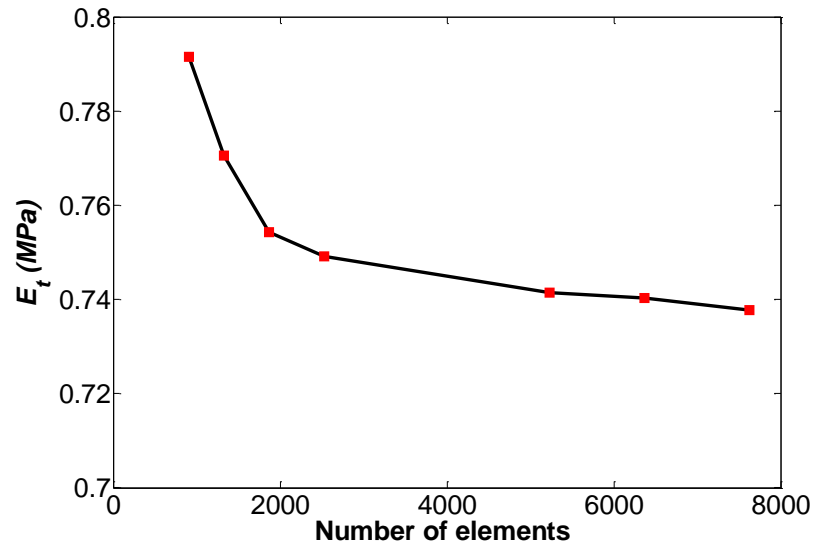


Figure 5-11. Number of elements to achieve convergence of response of isotropic unit cell model.

### 5.1.2.7. Influence of Detailed RUC Microstructure and Boundary Condition

It is known that the Kelvin model over-predicts the stiffness of real random foams [160], the degree to which the RUC over-predicts the moduli depends in the details of the Kelvin foam microstructure. For example, the edge cross section can be changed from circular to rectangular; the influence of this change on both compression and shear moduli is shown in Figure 5-12 and Figure 5-13. Note these changes maintain the relative density of the foam. The Kelvin RUC has also been analysed analytically [86] using a circular cross-section assumption and assuming the periodic boundary condition is performed according to Equation (2-29). Also, the coefficients of Equation (2-29),  $m$  and  $\beta_m$ , are both taken to be 3. Predictions from this theory are compared against numerical predictions in Figure 5-12. The results show that the relative density has significant influence on the elastic modulus with different edge cross sectional geometry. Similarly, the shear modulus can be calculated using edges of either circular or rectangular cross section. The results shown in Figure 5-13 indicate that both the relative density and the edge geometry have a significant influence on the shear modulus, which is higher for the circular cross section than for the

rectangular cross-section of the same relative density. The circular cross sections have a higher second moment of inertia than the rectangular edge cross sections. Also, the effects of the moment of inertia appear more clearly in the shear test due to the strong bending loading which is more dominant than for the compression test (axial loading).

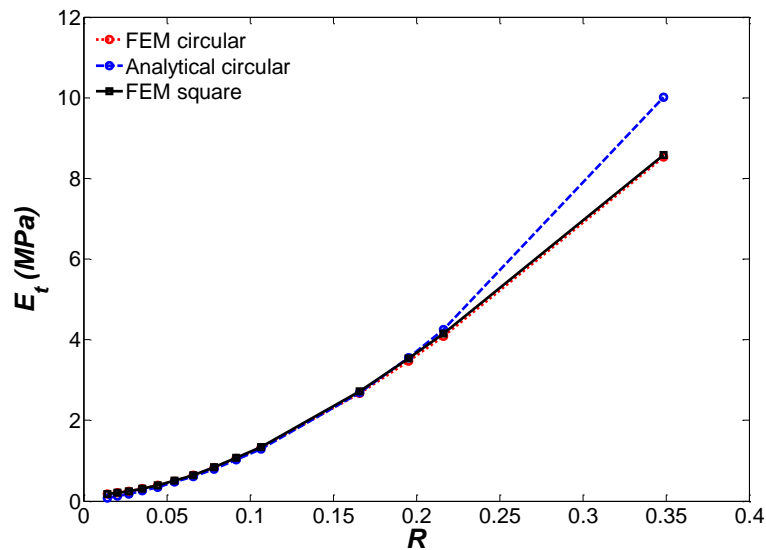


Figure 5-12. The Young's modulus-relative density with different edges cross sections.

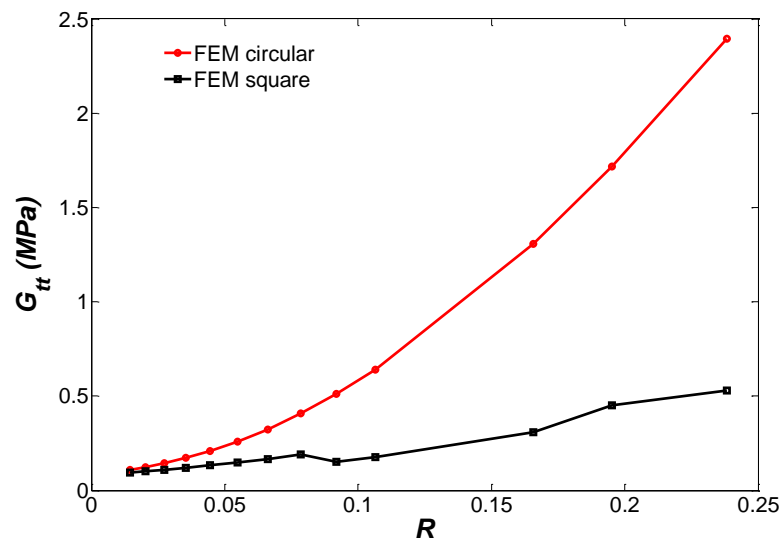


Figure 5-13. The shear modulus-relative density with different edge cross sections.

### 5.1.2.8. Methods to Artificially Soften the Kelvin RUC Response

Due to its regular microstructure, the Kelvin model is known to over-predict the mechanical properties of random foams at small strains, see Section 5.1.2.7. Several methods to purposely soften the elastic response of the Kelvin RUC can be used. Some methods are demonstrated in this section and can be classed into material changes and geometric changes. Possible changes to material behaviour include decreasing the elastic modulus of the constituent material (see Figure 5-14), or changing the geometry by, for example, decreasing the thickness of the edges and/or faces of the RUC (see Figure 5-15 and Figure 5-16). Ideally, the method of softening the RUC should be simple to implement and allow for a continuous decrease in the RUC stiffness, as opposed to a discrete change. Computational cost is not a particularly important issue here as the simulations are fast, usually completing in a matter of minutes. Nevertheless, improving the computational speed is a minor positive point. In this section three methods are used to fit the Kelvin RUC stiffness to predictions of the calibrated analytical model, see Section 5.1.1.1. Each method is evaluated in turn. The best two of these methods are then employed in predicting the elastic modulus, shear modulus and yield stress of a transversely isotropic Kelvin RUC.

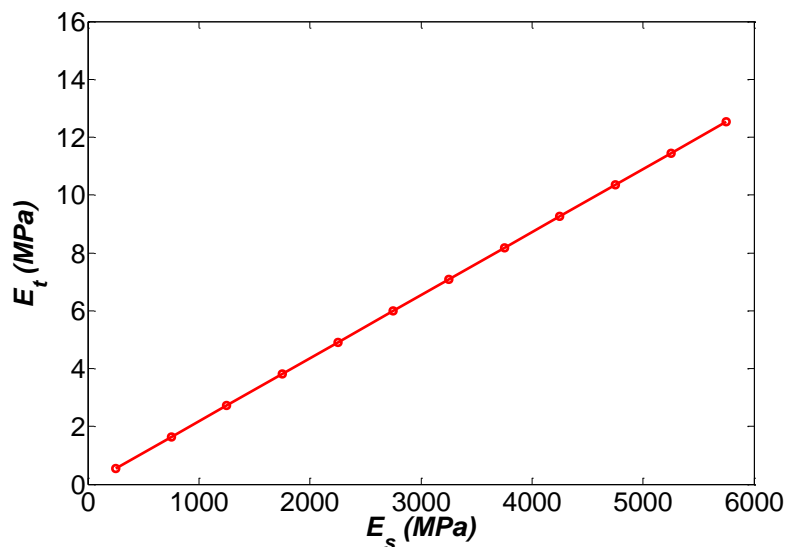


Figure 5-14. The  $E_t$  elastic modulus of LDPE foam in transverse direction versus  $E_s$  the elastic modulus of polyethylene at a constant relative density 0.043 of Polyethylene foam (for edges of Circular cross-section).

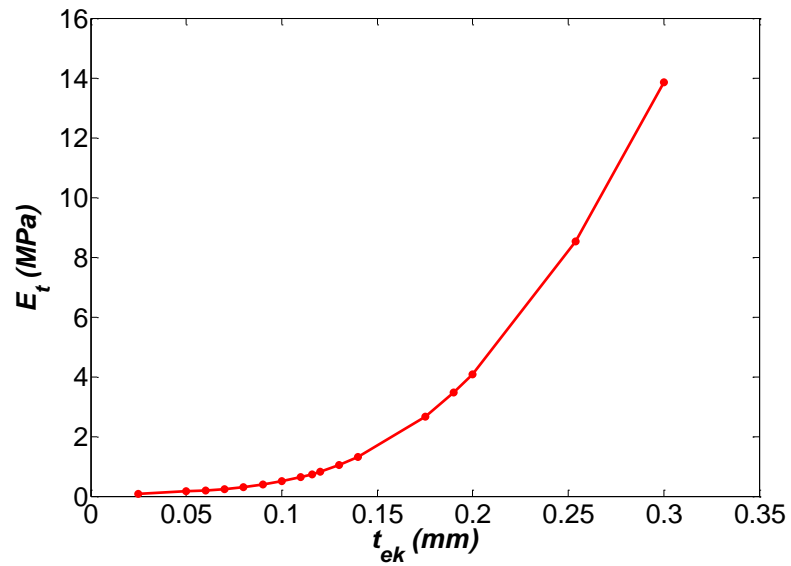


Figure 5-15. The  $E_t$  elastic modulus of foam in transverse direction-  $t_{ek}$  edge thickness (for edges of circular cross-section).

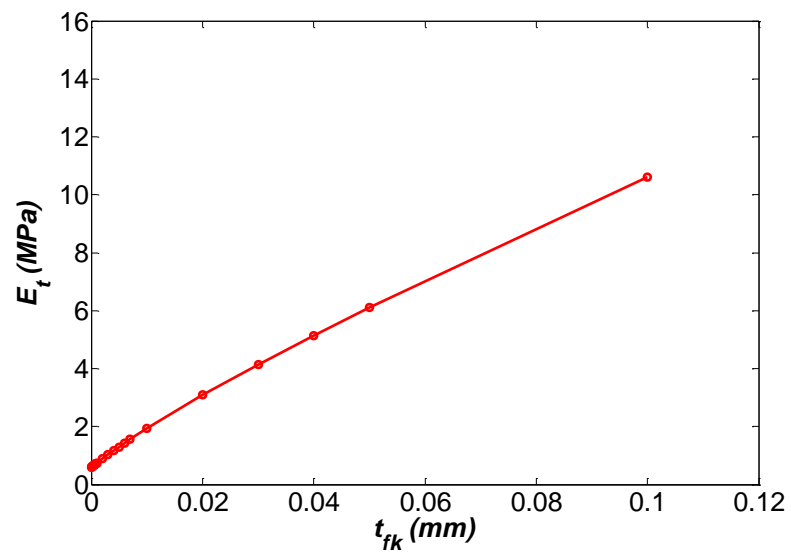


Figure 5-16. The  $E_t$  elastic modulus of transverse direction versus  $t_{fk}$  face thickness (for edges of circular cross-section).

### 5.1.2.9. Fitting the Edge and Face Thicknesses Using Uniaxial Compression Tests

In order to determine the compressive modulus in the principal direction,  $E_p$ , of the transversely isotropic Kelvin RUC with a shape anisotropy ratio of  $r$ , the following procedure was adopted and shows the method of calculating the compressive modulus values in the transverse and principal directions for a foam. The value of the fitted modulus in the Kelvin cell simulation  $E_t$  is 0.74MPa, and the value of  $E_t$  can be calculated using Equation (5-1) is 0.749MPa; the predicted value of  $E_p$  from the Kelvin cell simulation is 1.92 MPa, while the experimental value is  $2.039 \pm 0.363$  MPa. Finite element simulations are used to calculate the effects of cell wall thickness on  $E_p$  and  $E_t$ . A unit cell with beam elements (type B31) representing its edges and elements (type S3R) representing its faces was modelled to determine the compressive modulus in the transverse and principal directions. The dimensions of the cell in the transverse plane were 2.67 mm x 2.67 mm, while the dimensions in the principal plane were 2.67 mm x 3.2 mm. The total number of elements was 183 beam elements and 5043 shell elements.

The cross-section of the beam is modified and used as a uniform circular cross-section with a radius of 0.116mm in isotropic model, a radius of 0.1495 mm in the anisotropic model and cell face thickness of  $1 \times 10^{-3}$  mm in both planes. A linear elastic-isotropic material model was used for the cell edges and faces. Two mechanical properties (compress modulus and shear modulus) were used to characterise the solid material in the cell edges and faces. Figure 5-17 shows the uniaxial compression test for a typical isotropic and anisotropic Kelvin unit cell

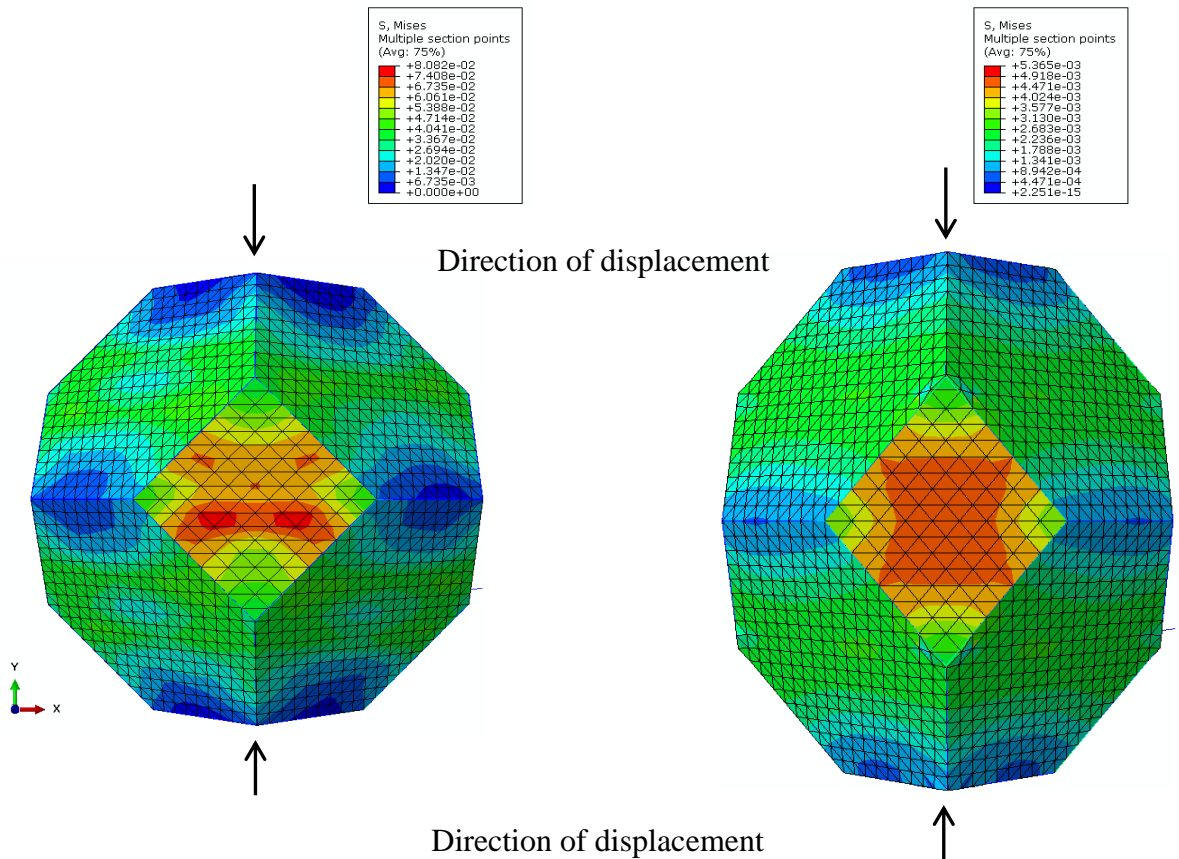


Figure 5-17. Uniaxial compression tests for (a) isotropic and (b) anisotropic Kelvin model.

### 5.1.2.10. Simulations of Uniaxial Compression Test

In this section the effect of relative density on the foam’s modulus of elasticity is studied in detail. Figure 5-18 shows the effect of relative density on the modulus of elasticity in the principal and transverse directions. The modulus of elasticity in both directions for with relative densities ranging from 0.014 to 0.35, follow different general curves. The increase of modulus of elasticity in the principal direction is larger than in the transverse direction. This indicates that the mechanical response in the principal direction is more sensitive to

relative density than in the transverse direction. Note that the thickness of the cell faces is kept constant in all the tests.

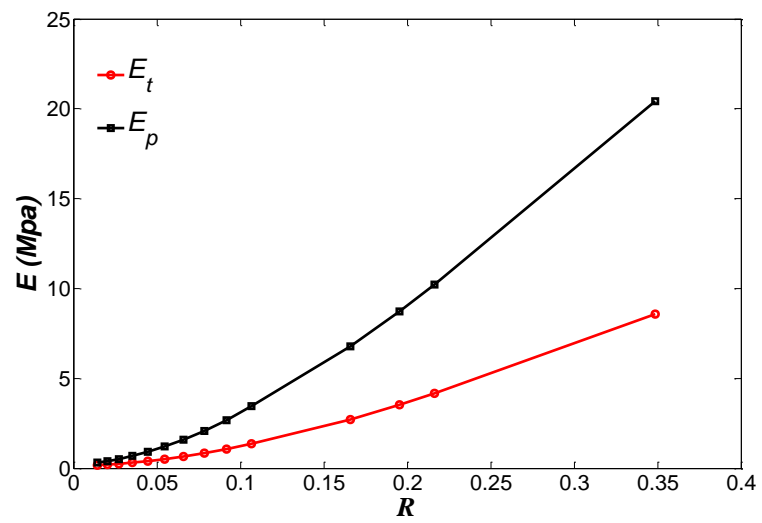


Figure 5-18. Young's modulus concentration versus relative density.

### 5.1.2.11. Shear Test Results

The second series of numerical simulations is based on the proposed models (Figure 5-19) showing the method of calculating the shear modulus in the transverse and principal directions for a foam of relative density of 0.0734. Here the edge and face thicknesses, the number and type of elements used are the same as in the previous section.

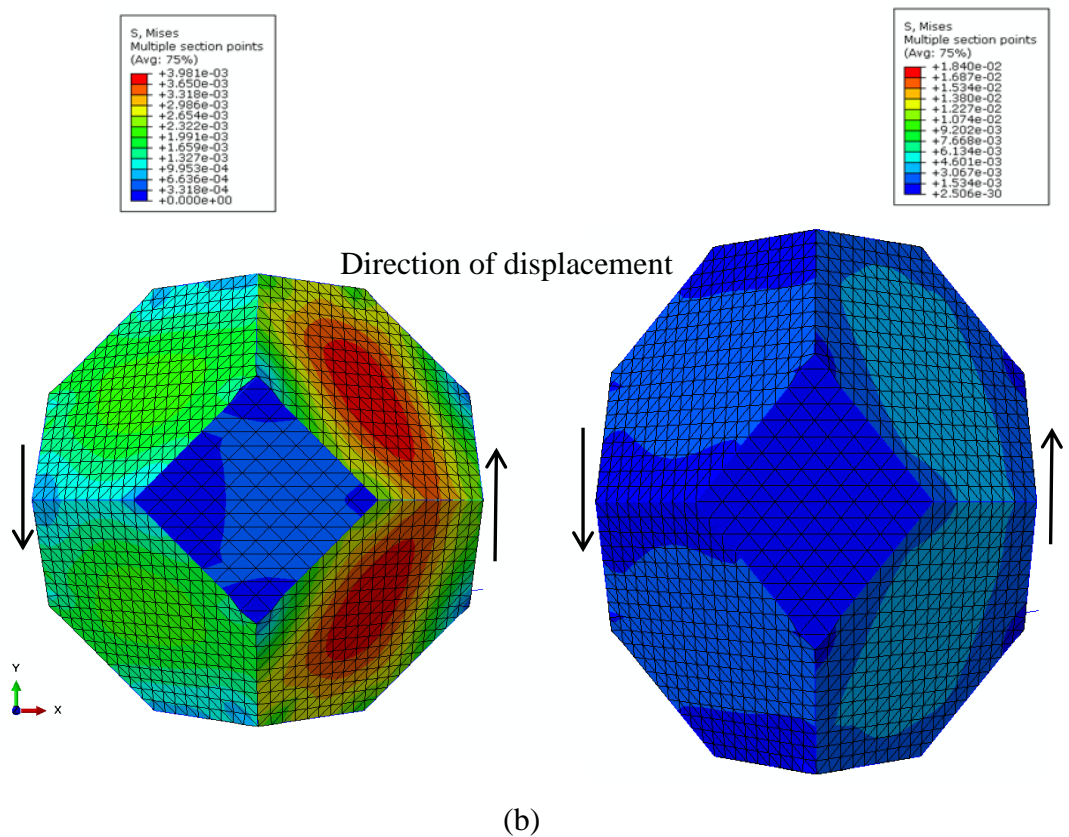


Figure 5-19. Shear test for (a) isotropic and (b) anisotropic Kelvin model unit cell.

Figure 5-20 shows the effect of relative density ranging, from 0.0144 to 0.0785, on the shear modulus for both directions. The curves follow a similar general trend, with both increasing with increasing relative density. This shows that the relative density has a significant effect on the shear modulus. As expected, the curve for the shear modulus in the transverse direction lies lower than the one for the principal direction.

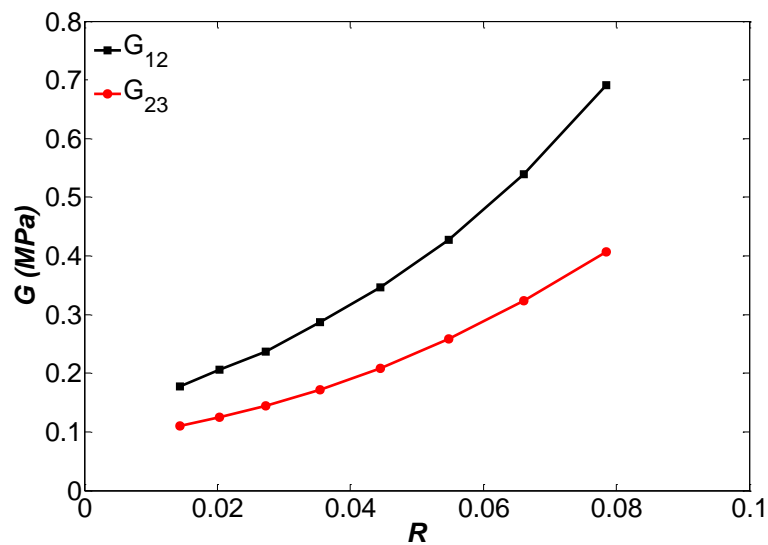


Figure 5-20. Shear modulus with versus relative density for principal  $G_{12}$  transverse  $G_{23}$  Directions.

The experimental and predicted values of the elastic constants are presented in Table 5.4.

Table 5.4. Experimental and predicted results obtained for the properties of extruded LDPE foams.

Parameters	Experimental (MPa)	G&A model	Error	Kelvin model	Error
$E_p$	$2.039 \pm 0.363$	1.38(MPa)	32%	1.92(MPa)	5.84%
$E_t$	$0.741 \pm 0.157$	0.749(MPa)	1%	-----	-----
$\sigma_p$	$0.061 \pm 0.014$	0.029(MPa)	45.2830%	0.08(MPa)	31%
$\sigma_t$	$0.026 \pm 0.016$	0.032(MPa)	23%	-----	-----
$G_{12}$	0.7	0.3017(MPa)	56.90%	0.64(MPa)	8.57%
$G_{23}$	0.34	0.33(MPa)	2.94%	-----	-----
$\nu_{12} = \nu_{23}$	0.227	0.19	16.3%	-----	-----
$\nu_{21}$	0.124	0.106	14.52%	-----	-----

\*Note error = (Experimental value- calculated value)/ Experimental value\*100%

## 5.2. Large strain Modelling

### 5.2.1. Predicting the Off-axis Stress-strain Curves

Finally, the stress-strain curves for specified off-axis sample orientations are calculated. The calculated stresses in the principal and transverse directions are used to make the off-axis predictions. The same procedure as that performed in Section 4.2 is employed. The rotational transformation used in Section 4.2 is used to calculate the yield stress of a linear compressible transversely isotropic material when loaded off-axis, see Equation (4-1) [36] where

$$E_p = \sigma_p / \varepsilon_p, E_t = \sigma_t / \varepsilon_t \quad (5-57)$$

and the yield stress at any difiend angle is given by the expression

$$\sigma_{(\theta)} = E_{(\theta)} * \varepsilon_{el} \quad (5-58)$$

$$\sigma = \sigma_{(\theta)} - P_a \left( \frac{1 - R}{(1 - \varepsilon)(1 + \nu\varepsilon)^2 - R} - 1 \right) \text{ for unloading stress} \quad (5-59)$$

Here the gas model was modified for predicting unloading behaviour of material (see Equation (5-59). The unloading stress-strain was predicted using a yield stress of the opposite sign. The values of the yield stress in the Equation (5-58), gas model Equations (2-33), (5-59) are then used to predict the stress-strain curves for loading -unloading in the principal direction and at any specified angle, as shown in Figure 5-21.

### 5.2.2. Comparison between Model and Actual Foam

Figure 5-21 shows a comparison between the experimental uniaxial compression test results and those predicted by the combined models (analytical, numerical and gas models); reasonable agreement in the results is observed. The predicted compression stress-strain curves are similar to experimental results until the strain is approximately equal to 0.5, (see Figure 5-21a-e). The reason for this is that the actual material has a variable Poisson's ratio, while in this prediction the Poisson's ratio value was constant value. Poisson's ratio has a more significant effect for unloading curves than for loading.

High Poisson's ratio used for unloading caused a significant reduction in the predicted strength of the material. No constitutive equation can be used for predicting Poisson's ratio for large strain; currently we only have an equation to calculate Poisson's ratio for small strain, which can be created using the shear modulus and modulus of elasticity.

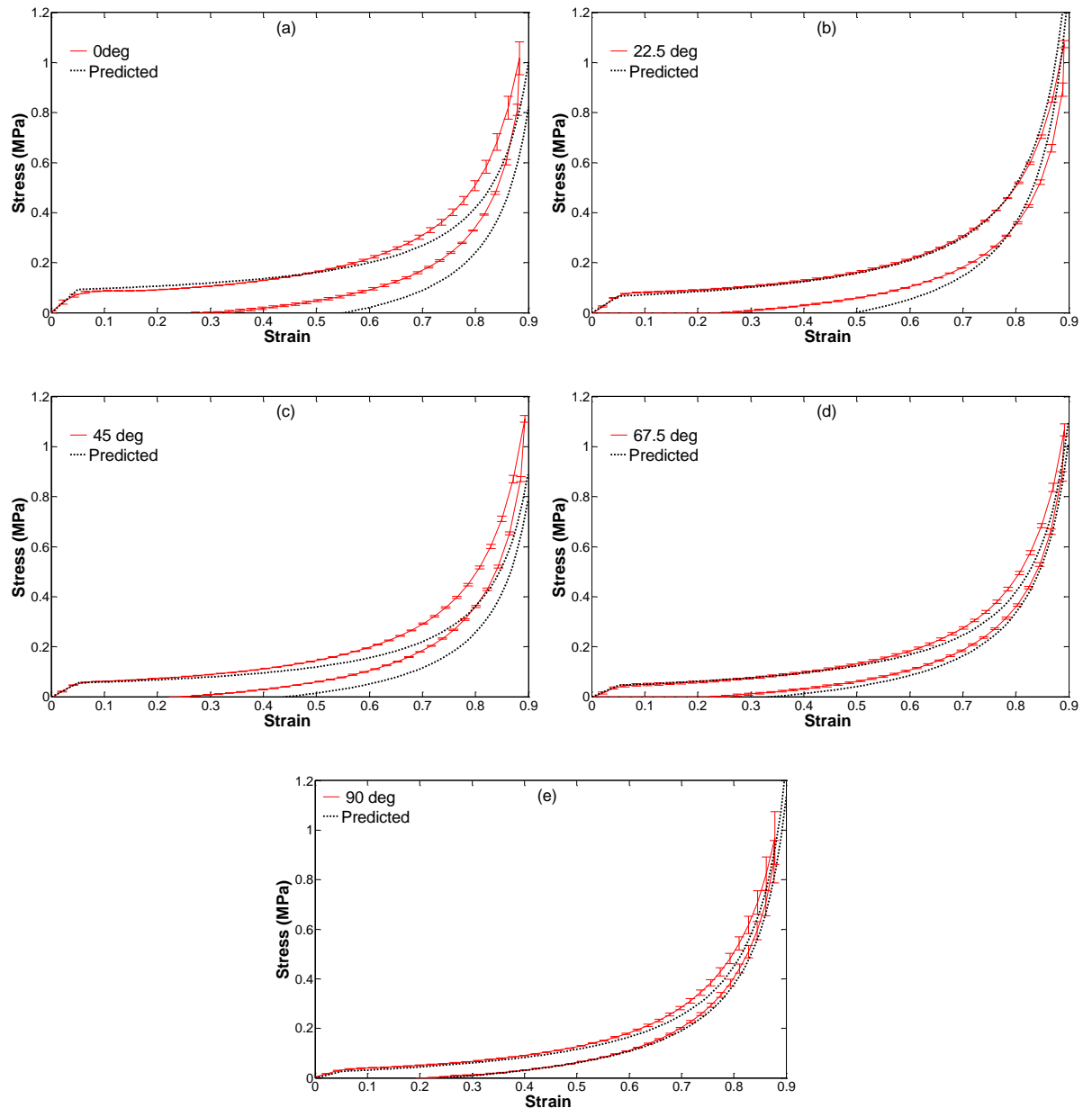


Figure 5-21. Experimental uniaxial compression curves (continuous lines) with different degree of rotation of principal axis together with predicted uniaxial compression curves (dashed lines) using equations (5-58), (2-33) and (5-59), (a) for  $\theta = 0^\circ$ , (b) for  $\theta = 22.5^\circ$ , (c) for  $\theta = 45^\circ$ , (d) for  $\theta = 67.5^\circ$  and (e) for  $\theta = 90^\circ$ .

Figure 5-22 shows a comparison between Young’s modulus values at any specified orientation from the analytical and numerical models with experimental data for transversely isotropic foam. There is good agreement observed between experimental and predicted values.

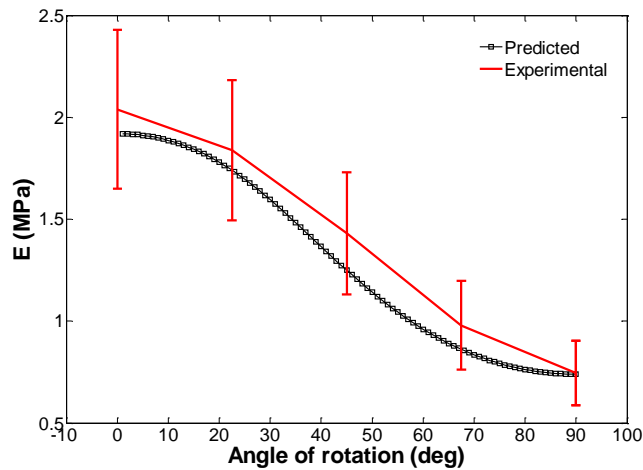


Figure 5-22. Comparison between modulus of elasticity predicted by analytical and numerical with experimental data.

Figure 5-23 shows a comparison between Poisson’s ratios from experimental results with values predicted at any specified orientation using the combined analytical and numerical models. There is reasonable agreement noted between the predicted and experimental values.

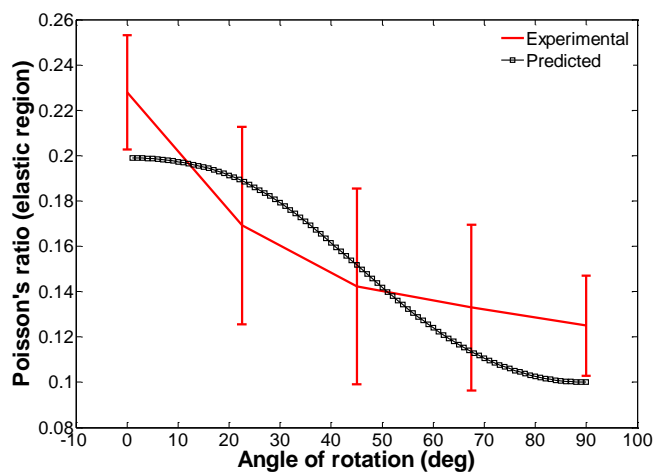


Figure 5-23. Comparison between Poisson’s ratio predicted by analytical model and experimental data.

### 5.3. Summary

A micro to macro mechanics model technique for the stress analysis of transversely isotropic foam has been described, and a new method for adapting a micro to macro mechanical model has been proposed. Analytical models based on Gibson and Ashby's closed-cell cube model were used to predict the linear-elastic parameters of foams for comparison with data from experimental tests. The modelling of closed-cell foam is based on a cubic closed-cell model and anisotropic closed-cell RUC, with  $r=1.2$  from microscopic measurements, see Section 3.3.3.1. The isotropic model was used to predict the elastic parameter in the transverse direction, while the anisotropic numerical model was used to predict the elastic parameters in the principal direction. The analytical model does not well predict  $E_p$ ,  $\sigma_p$  or  $G_{12}$  thus, a numerical Kelvin cell RUC model was used to predict linear-elastic parameters in the principal direction. FE simulations of transversely isotropic foam based on the isotropic Kelvin closed-cell model were used in fitting results with analytical values in the transverse direction. Predictions were then made in the principal direction after stretching the cell using an anisotropy ratio of  $r=1.2$ . The isotropic Kelvin model was subjected to uniaxial compression and shear loading, as was the anisotropic model. Both models were employed using the same periodic boundary conditions.

An examination of the effects of relative density on shear modulus shows there is some relation between relative density and the shear modulus in both directions, while the tests do not exhibit this for a change in relative density with modulus of elasticity, i.e. the anisotropic model is more sensitive to increasing the relative density than the isotropic model. Foam elastic constants predicted by the models shows generally reasonable agreement with experimental tests. The previous techniques are suitable for predicting elastic-linear parameters. To examine stress-strain curves for large strain the gas model initially introduced in Section 4.3 was employed. The latter is suitable for isotropic and anisotropic closed-cell foam thus, in order to obtain stress-strain curves at any defined orientation, the rotation transformation equation was used to calculate linear-elastic parameters at off-axis orientations, the gas model was then used to extend the stress-strain curves to large strain and predict the stress-strain data at specified angles. The predicted

stress-strain curves in the principal and transverse directions and at a defined angles exhibit good agreement with experimental data. The micro to macro mechanics model looks to be a reasonably accurate and reliable method. Analytical analyses and numerical simulations are applicable to predicting the mechanical behaviour of transversely isotropic compressible materials undergoing large deformations.

## **Chapter 6. Conclusions and Recommendations for Future Work**

Chapter 1 provided an introduction to the use of foams in modern day engineering and explained why foams have unique properties and how these unique properties are manifest in terms of their mechanical response. A brief overview of how foams are manufactured was given and the relationship between manufacture process, microstructure and the foam's bulk mechanical properties were highlighted.

In Chapter 2, a literature review of relevant test methods used to characterise the mechanical behaviour of engineering foams was provided, along with explanations of how previous researchers have used the resulting test data to quantify, analyse and interpret foam behaviour. The response of real foams subject to various different loading conditions, as determined in previous work, was reviewed. Commonly observed behaviours include viscoelasticity and anisotropy; the latter is often associated with anisotropy at the microstructural level due to the influence of the manufacture process. An overview of the body of previously published work on both macro and micro-scale modelling of foams was presented. Attention was paid to work focusing on modelling both viscoelasticity and material anisotropy.

In order to examine the ability and accuracy of existing models to capture the behaviour of transversely isotropic compressible viscoelastic foams, a melt-extruded LDPE closed cell foam was chosen as a representative benchmark material for subsequent characterisation and macro-scale modelling. In Chapter 3 the foam's mechanical response was characterised using uniaxial compression and simple shear tests and as expected, was found to be highly transversely isotropic, compressible and rate dependent. The foam's compressive modulus and yield strengths were found to be almost three times as high in the principal direction when compared to that in the transverse direction. The material response also showed a strong dependence on the size of the test specimen, with the largest specimens (80x80x80 mm<sup>3</sup>) stiffer and stronger than the smallest (10x10x10 mm<sup>3</sup>) by a factor of more than two times, presumably due to weakening of the foam structure near cut

surfaces but also due to the effect of gas diffusion through the closed-cell foam. Measurements of the foam's Poisson's ratio using two different methods revealed a non-linear relationship, with the property initially decreasing sharply with strain before steadying to an approximately constant value at large strain. Elastic and yield properties showed strong strain-rate dependence, increasing approximately linearly with the natural log of the strain-rate. The energy absorption efficiency of the foam also increased with strain-rate though the onset strain of densification was found to be relatively insensitive to changes in the strain rate. The foam also showed almost full strain recovery after unloading indicating an underlying elastomeric response, though the recovery was rate dependent and some degree of permanent damage remained even after long recovery times. Shear tests revealed strong dependence of the shear modulus with strain, with the latter rapidly decreasing with strain. Investigations into the foam microstructure using micro-CT and optical microscopy revealed significant anisotropy in the average cell geometry; as might be expected the cells were elongated in a preferred direction, corresponding to the flow and draw direction used in the foam's manufacture. The anisotropy ratio of the cells was found to be around 1.2.

In Chapter 4, attempts to predict experimental test data from a reduced data set were made using simple interpolation methods and empirical models. The aim here was to examine if the information gathered on rate dependence and anisotropy measured in Chapter 3 could be condensed into simple relationships. The first interpolation demonstrated how off-axis stress-strain data could be predicted from shear properties together with uniaxial data collected in the principal and transverse directions, using a simple matrix rotation. The method provided reasonably accurate predictions suggesting that a linear elastic transversely isotropic compressible model should be capable of providing accurate stress and strain predictions under small strains. A combined empirical / gas model was used to capture the rate dependence of the foam at high strains and again provided reasonable predictions when interpolating between curves produced at the highest and lowest strain rates. The success of this method showed that the foam's strain-rate dependence followed a relatively simple semi-natural logarithmic relationship that could be easily fitted using an empirical model. The success of the gas model in predicting the stress-strain curve over large strains provided strong evidence to suggest that the stress at large strain is

predominantly due to the compression of gas trapped inside the foam. Perhaps surprisingly, it was found that the stress-strain curves in the transverse and principal directions could be predicted from one another by using a simple multiplication factor corresponding to the value of  $r^2$ . The importance of the internal gas pressure on the foam's stress-strain response suggested that the rate of change of internal pressure with volumetric strain could be used to shift stress-strain data to take specimen size dependency into account. Finally, a short investigation into the use of constitutive models available in the commercial FEA code, Abaqus<sup>TM</sup>, in representing the foam's behaviour, was conducted. Comparisons showed that a linear elastic transversely isotropic compressible model could predict qualitatively similar kinematics when compressed under off-axis uniaxial compression, though as expected was unable to reproduce the non-linear stress strain response of the real foam. Use of an isotropic compressible hyperelastic model could reproduce the non-linear stress-strain response of the foam under uniaxial compression for any given strain-rate or material orientation, though a new fitting process had to be used for each scenario, severely limiting the use of the model for most practical purposes.

In Chapter 5 an established micromechanical analytical model formulated by Gibson and Ashby [1] was used to investigate the foam's small strain mechanical behaviour by incorporating microstructural information gathered in Chapter 3. The isotropic version of their model was found to give reasonably good predictions for the response of the LDPE foam at small strain in the transverse direction, but the anisotropic version of their model was less successful in predicting the response in the principal direction. In order to reproduce the transversely isotropic response of the foam the analytical model was augmented by a numerical FEA approach based on a Kelvin Repeat Unit Cell (RUC) with periodic boundary conditions. Once again, only the small strain response was examined. The method involved first calibrating the predictions of the isotropic Kelvin RUC to the predictions of the isotropic Gibson and Ashby model using a 'softened' Kelvin RUC model. In this way, the numerical predictions were still derived from microstructural information rather than being fitted to experimental data. The Kelvin RUC was then elongated by the anisotropy ratio,  $r$ , to produce predictions in the principal direction. The resulting combined analytical/numerical predictions, which were effectively based entirely on microstructural information, produced good agreement with the experimental data for the foam's small strain response. The same gas model employed in Chapter 4 was then

used to extend the stress-strain predictions into the large strain region and once again produced good agreement across a wide range of strains.

## 6.1. Future Work

The mechanical behaviour of transversely isotropic compressible viscoelastic polymer foams is clearly very complex and there are currently no constitutive models available in the commercial FEA code used in this study that are capable of accurately describing the full complexity of the foam's response. However, in Chapter 4, it was shown that much of the complexity can be captured by combining a few, relatively simple models. One exciting avenue for future work could be to use these combined simple models to interpolate the measured foam response from just a few measured experimental data to create a database of foam behaviour across a wide range of strain and strain-rates. A hypo-elastic constitutive model, based on the linear elastic transversely isotropic compressible foam model could then be implemented in an Abaqus user subroutine (Umat or Vumat) and provide a vehicle by which the database of foam behaviours could be implemented in the FE code, i.e. the linear elastic parameters produced by the combined model could be fed into the code during the numerical simulation, according to state dependent variables such as strain and strain rate. In this way the parameters of the hypo-elastic constitutive model, which are constant in any given time step, would become both strain and strain rate dependent over the course of the simulation and could also be selected according to whether the foam was under the conditions of either loading or unloading. A similar approach was demonstrated recently by Harrison et al. [163] when modelling the large deformation mechanics of advanced composite materials during forming. More ambitiously, rather than interpolating the database of material behaviour from a reduced number of limited experimental test data, as in Chapter 4, the database could instead be predicted from microstructural models, as in Chapter 5.

## Appendix I: Publications

### Journal papers

1- **Jebur, Q.H.**, Harrison, P., Guo, Z., Schubert, G., Ju, X., and Navez, V. (2012) *Characterisation and modelling of a transversely isotropic melt-extruded LDPE closed cell foam under uniaxial compression*. Proceedings of the Institution of Mechanical Engineers, Part C: Journal of Mechanical Engineering Science, 226 (9). pp. 2168-2177. ISSN 0954-4062 (doi:10.1177/0954406211431528).

### Conference papers

1- **Jebur, Q.H.**, Harrison, P., and Guo, Z. (2012) *Predicting the transversely isotropic behaviour of closed-cell foam subjected to compressive loading*. In: 8th European Solid Mechanics Conference (ESCM2012), 9-13 July 2012, Graz, Austria.

2- **Jebur, Q.H.**, Harrison, P., Guo, Z., Schubert, G., and Navez, V. (2011) *Characterisation and Modelling of a Melt-Extruded LDPE Closed Cell Foam*. In: International Conference on Advances in Experimental Mechanics: Integrating Simulation and Experimentation for Validation, 7 - 9 September 2011, Edinburgh, UK.

3- Keisuke Sasagawa , S.C., Magnus Gislason, **Qusai Hatem**, K. Elizabeth Tanner , David B. Allan and Yuji Tanabe, *A finite element modelling for the tibia of a spinal cord injured patient* European Society of Biomechanics (ESB) in Portugal on 1st to 4th July 2012.

## Appendix II: References

1. Gibson, L.J., and Ashby, M.F., *Cellular solids structure and properties*. Cambridge University press, UK. 1997.
2. Moreu, Y.M., and Mills, N. J., *Rapid hydrostatic compression of low-density polymeric foams*. Polymer Testing, 2004. **23**(3): p. 313-322.
3. Huber, A.T., and Gibson, L. J., *Anisotropy of foams*. Journal of Materials Science, 1988. **23**(8): p. 3031-3040.
4. Mills, N.J., *Engineering and biomechanics applications and design guide*. Butterworth-Heinemann. UK. 2007.
5. <http://www.storopack.com/en/products-solutions/flexible-protective-packaging/foam-pad-foam-packaging.html>.
6. <http://www.bloomberg.com/news/2010-12-09/gladiator-helmet-seeks-to-eliminate-concussion-pain-from-football-players.html>.
7. <http://www.insulationpipe.net/foam-pipe-insulation.html>.
8. <http://www.swimminglessons.com.sg/the-difference-a-life-jacket-makes/>.
9. <http://www.istaproducts.com/details+Rectangle+Bio+Foam+%28Large%29/products/237>.
10. <http://www.globalmarket.com/product-info/pvc-foam-anti-slip-mat-roll-with-paper-bannerol-493421.html>.
11. Banhart, J., *Manufacture, characterisation and application of cellular metals and metal foams*. Progress in Materials Science, 2001. **46**(6): p. 559-632.
12. Ramamurthy, K., E.K. Kunhanandan Nambiar, and G. Indu Siva Ranjani, *A classification of studies on properties of foam concrete*. Cement and Concrete Composites, 2009. **31**(6): p. 388-396.
13. Duarte, I. and M. Oliveira, *Aluminium Alloy Foams: Production and Properties*, in *Centro de Tecnologia Mecânica e Automação 2012*: Departamento de Engenharia Mecânica, Universidade de Aveiro.
14. Antunes, M., Arencon, D., Realinho, V., and Velasco, J. I., *Microstructure anisotropy in polyolefin flexible foams*, in *5th International Eeigm-Amase-Forgemat Conference on Advanced Materials Research*, D. Horwat, et al., Editors. 2009.

15. Jebur, Q.H., Harrison, Philip., Guo, Zaoyang., Schubert, Gerlind., Ju, Xiangyang., and Navez, Vincent, *Characterisation and modelling of a transversely isotropic melt-extruded low-density polyethylene closed cell foam under uniaxial compression*. Proceedings of the Institution of Mechanical Engineers Part C- Journal of Mechanical Engineering Science, 2012. **226**(C9): p. 2168-2177.
16. Jebur, Q.H., Harrison, P., and Guo, Z. Y. *Characterisation and Modelling of a Melt-Extruded LDPE Closed Cell Foam*. in *Advances in Experimental Mechanics Viii*. 2011. Edinburgh, UK: Trans Tech Publications Ltd.
17. Montminy, M.D., Tannenbaum, A. R., and Macosko, C. W, *The 3D structure of real polymer foams*. Journal of Colloid and Interface Science, 2004. **280**(1): p. 202-211.
18. Mu, Y., and Yao, Guangchun., *Anisotropic compressive behavior of closed-cell Al-Si alloy foams*. Materials Science and Engineering A-Structural Materials Properties Microstructure and Processing, 2010. **527**(4-5): p. 1117-1119.
19. Mu, Y.L., and Yao, G.C., *The influence of cell shape anisotropy on the compressive property of closed-cell Al-Si alloy foams*. Tms 2010 139th Annual Meeting & Exhibition - Supplemental Proceedings, Vol 2: Materials Characterization, Computation and Modeling and Energy. 2010. 253-258.
20. Mu, Y.L., Yao, G. C., and Luo, H. J., *Anisotropic damping behavior of closed-cell aluminum foam*. Materials & Design, 2010. **31**(1): p. 610-612.
21. Verpoest, I., and Rodriguez,Perez, *Complexly shaped anisotropic foam manufacturing*. Katholiek University Levuen, Belgiun., 2011.
22. Harold F. Giles., John R. Wagner., and Eldridge M. Mount, *Extrusion: The Definitive Processing Guide And Handbook*. William Andrew Publishing (12 Dec 2005).
23. Michael, A., Hugh, Shercliff., and David Cebon, *Materials engineering, science, processing and design*. University of Cambridge, UK, 2007.
24. Park, C., and Nutt, S. R., *Anisotropy and strain localization in steel foam*. Materials Science and Engineering A-Structural Materials Properties Microstructure and Processing, 2001. **299**(1-2): p. 68-74.

25. Youngliang, M., Guangchun, Yao., and Honjie, Luo, *Effect of cell shape on the compressive behaviour of closed cell aluminium foams*. *Materials & Design*, 2009. **31**(2010): p. 1567-1569.
26. Morgan, J.S., Wood, J. L., and Bradt, R. C., *Cell size effects on the strength of foamed glass*. *Materials Science and Engineering*, 1981. **47**(1): p. 37-42.
27. Cao, X.Q., Wang, Zhi.Hua., Ma, Hong.Wei., Zhao, Long.Mao., and Yang, Gui.Tong, *Effects of cell size on compressive properties of aluminum foam*. *Transactions of Nonferrous Metals Society of China*, 2006. **16**(2): p. 351-356.
28. Hagiwara, H., and Green, David J., *Elastic Behavior of Open-Cell Alumina*. *Journal of the American Ceramic Society*, 1987. **70**(11): p. 811-815.
29. Mills, N.J., and Gilcrist, A., *Creep and recovery of polyolefin foams - Deformation mechanisms*. *Journal of Cellular Plastics*, 1997. **33**(3): p. 264-&.
30. ABAQUS User manual version 6.8, *Linear elastic behaviour*, in *Section 18.2.1* 2008.
31. Timoshenko, S., and Goodier, J. N, *Theory of elasticity*. 2nd ed. / by S. P. Timoshenko and J. N. Goodier. ed. 1951, New York, etc.: McGraw Hill. xviii, 506p.
32. Ogden, R.W., *Large deformation isotropic elasticity correlation of theory and experiment for incompressible rubber like solids*. *Proceedings of the Royal Society of London Series A-Mathematical and Physical Sciences*, 1972. **326**(1567): p. 565-584.
33. Ogden, R.W., Saccomandi, G., and Sgura, I., *Fitting hyperelastic models to experimental data*. *Computational Mechanics*, 2004. **34**(6): p. 484-502.
34. Widdle, R.D., *Measurement and modeling of the mechanical properties of flexible polyurethane foam*. Ph.D thesis Purdue University, August 2005.
35. ABAQUS User manual version 6.8, *Fitting of elastomeric foam test data*, in *Section 3.1.5* 2008.
36. Isaac, M.D., and Ori, I., *Engineering mechanics of composite materials*. 2005 Oxford University press, UK.
37. Tagarielli, V.L., Deshpande, V. S., Fleck, N. A., and Chen, C., *A constitutive model for transversely isotropic foams, and its application to the indentation of balsa wood*. *International Journal of Mechanical Sciences*, 2005. **47**(4-5): p. 666-686.

38. Weiss, J.A., B.N. Maker, and S. Govindjee, *Finite element implementation of incompressible, transversely isotropic hyperelasticity*. Computer Methods in Applied Mechanics and Engineering, 1996. **135**(1-2): p. 107-128.
39. Iliev, R.V., *Elastic-plastic response of structural foams subjected to localized static loads*. Materials & Design, 2006. **27**(10): p. 947-954.
40. Jeon, I., Asahina, Tadashi., Kang, Ki-Ju., Im, Seyoung., and Lu, Tian Jian, *Finite element simulation of the plastic collapse of closed-cell aluminum foams with X-ray computed tomography*. Mechanics of Materials, 2010. **42**(3): p. 227-236.
41. Rusch, K.C., *Load-compression behaviour of brittle foams*. Journal of Applied Polymer Science, 1970. **14**(5): p. 1263-&.
42. Brinson., H.F. and L.C. Brinson, *Polymer engineering science and viscoelasticity: An Introduction* Springer. 2010.
43. Song, B., Chen, W. N. W., Dou, S. B., Winfree, N. A., and Kang, J. H., *Strain-rate effects on elastic and early cell-collapse responses of a polystyrene foam*. International Journal of Impact Engineering, 2005. **31**(5): p. 509-521.
44. Houlsby, G.T., and Puzrin, A. M., *Principles of Hyperplasticity*, ed. Springer. 2006.
45. Haojiang, Ding., W.C., and Ling, Zhang., *Elasticity of transversely isotropic materials*. Springer 2006.
46. Sabah, K.H., *Linear and non-linear behaviour of viscoelastic materials for thin plates subjected to generl loading* Ph.D. thesis University of Almustansyria 2006.
47. Johnson, A.R., Quigley, C. J., and Freese, C. E., *A viscohyperelastic finite element model for rubber*. Computer Methods in Applied Mechanics and Engineering, 1995. **127**(1-4): p. 163-180.
48. Kim, Y.I., *Advanced numirical and experimental transiet modelling of water and gas pipline flows incoporating distributed and local effects*, in *School of Civil, Environmental and Mining Engineering*, University of Adelaide 2008.
49. Mills, N.J., *Finite Element models for the viscoelasticity of open-cell polyurethane foam*. Cellular Polymers, 2006. **25**(5): p. 293-316.
50. Hernandez, Z.J.E., Figueroa, J. D. C., Rayas-Duarte, P., Martinez-Flores, H. E., Arambula, G. V., Luna, G. B., and Pena, R. J., *Influence of high and low molecular weight glutenins on stress relaxation of wheat kernels and the relation to*

- sedimentation and rheological properties*. Journal of Cereal Science, 2012. **55**(3): p. 344-350.
51. Holzapfel, G.A., *Nonlinear solid Mechanics*. John Wiley and Sons (2000).
52. Mooney, M., *A theory of large elastic deformation*. Journal of Applied Physics, 1940. **11**(9): p. 582-592.
53. Rivlin, R.S., *Large elastic deformation of isotropic materials.4.further developments of the general theory*. Philosophical Transactions of the Royal Society of London Series A-Mathematical and Physical Sciences, 1948. **241**(835): p. 379-397.
54. Bardenhagen, S.G., Brydon, A. D., and Guilkey, J. E., *Insight into the physics of foam densification via numerical simulation*. Journal of the Mechanics and Physics of Solids, 2005. **53**(3): p. 597-617.
55. Ogden, R.W., *Non-linear elastic deformations*. 1997, : Dover, New York, USA.
56. Widdle, R.D., Bajaj, A. K., and Davies, P., *Measurement of the Poisson's ratio of flexible polyurethane foam and its influence on a uniaxial compression model*. International Journal of Engineering Science, 2008. **46**(1): p. 31-49.
57. Zhou, X., Sha, D., and Tamma, K. K., *A novel non-linearly explicit second-order accurate L-stable methodology for finite deformation: hypoelastic/hypoelasto-plastic structural dynamics problems*. International Journal for Numerical Methods in Engineering, 2004. **59**(6): p. 795-823.
58. Xiao, H., O.T. Bruhns, and A. Meyers, *Hypo-elasticity model based upon the logarithmic stress rate*. Journal of Elasticity, 1997. **47**(1): p. 51-68.
59. Weiss, J.A. and J.C. Gardiner, *Computational modeling of ligament mechanics*. Critical Reviews in Biomedical Engineering, 2001. **29**(3): p. 303-371.
60. Peng, X.Q., Z.Y. Guo, and B. Moran, *An anisotropic hyperelastic constitutive model with fiber-matrix shear interaction for the human annulus fibrosus*. Journal of Applied Mechanics-Transactions of the ASME, 2006. **73**(5): p. 815-824.
61. Guo, Z.Y., Caner, F., Peng, X. Q., and Moran, B., *On constitutive modelling of porous neo-Hookean composites*. Journal of the Mechanics and Physics of Solids, 2008. **56**(6): p. 2338-2357.

62. Jemiolo, S. and J.J. Telega, *Transversely isotropic materials undergoing large deformations and application to modelling of soft tissues*. Mechanics Research Communications, 2001. **28**(4): p. 397-404.
63. Zhurov, A.I., Evans, Sam L., Holt, Catherine A., and Middleton, John, *A nonlinear compressible transversely-Isotropic viscohyperelastic constitutive model of the periodontal ligament*. ASME Conference Proceedings, 2008. **2008**(48630): p. 707-719.
64. Zhurov, A.I., Limbert, Georges, Aeschlimann, Daniel P., and Middleton, John, *A constitutive model for the periodontal ligament as a compressible transversely isotropic visco-hyperelastic tissue*. Computer Methods in Biomechanics and Biomedical Engineering, 2007. **10**(3): p. 223-235.
65. Deshpande, V.S., and Fleck, N. A., *High strain rate compressive behaviour of aluminium alloy foams*. International Journal of Impact Engineering, 2000. **24**(3): p. 277-298.
66. Deshpande, V.S. and N.A. Fleck, *Multi-axial yield behaviour of polymer foams*. Acta Materialia, 2001. **49**(10): p. 1859-1866.
67. Mills, N.J., *Improving the crushable foam model for low density polystyren foam*. University of Birmingham, 2003.
68. Gilchrist, A., and Mills, N. J., *Impact deformation of rigid polymeric foams: experiments and FEA modelling*. International Journal of Impact Engineering, 2001. **25**(8): p. 767-786.
69. Lubliner, J., *A model of rubber viscoelasticity*. Mechanics Research Communications, 1985. **12**(2): p. 93-99.
70. Li, B., Gu, Y. D., English, R., Rothwell, G., and Ren, X. J., *Characterisation of nonlinear material parameters of foams based on indentation tests*. Materials & Design, 2009. **30**(7): p. 2708-2714.
71. Mills, N.J., Fitzgerald, C., Gilchrist, A., and Verdejo, R., *Polymer foams for personal protection: cushions, shoes and helmets*. Composites Science and Technology, 2003. **63**(16): p. 2389-2400.
72. Andrew M. Kraynik. and William E. Warren, *The elastic behaviour of low density cellular plastics*. Chapter 7 Low Density Cellular Plastics Eds. Hilyard N.C. & Cunningham A., Chapman and Hall, London., 1994.

73. Zhu, H.X., Knott, J. F., and Mills, N. J., *Analysis of the elastic properties of open-cell foams with tetrakaidecahedral cells*. Journal of the Mechanics and Physics of Solids, 1997. **45**(3): p. 319-343.
74. Gibson, L.J., Ashby, M. F., Zhang, J., and Triantafillou, T. C., *Failure surfaces for cellular materials under multiaxial loads.1. modeling* International Journal of Mechanical Sciences, 1989. **31**(9): p. 635-663.
75. Warren, W.E., and Kraynik, A. M., *Linear elastic behavior of a low-density Kelvin foam with open cells*. Journal of Applied Mechanics-Transactions of the Asme, 1997. **64**(4): p. 787-794.
76. Mills, N.J., *The high strain mechanical response of the wet Kelvin model for open-cell foams*. International Journal of Solids and Structures, 2007. **44**(1): p. 51-65.
77. Gong, L., Kyriakides, S., and Jang, W. Y., *Compressive response of open-cell foams. Part I: Morphology and elastic properties*. International Journal of Solids and Structures, 2005. **42**(5-6): p. 1355-1379.
78. Zhu, H.X., Hobdell, J. R., and Windle, A. H., *Effects of cell irregularity on the elastic properties of open-cell foams*. Acta Materialia, 2000. **48**(20): p. 4893-4900.
79. Dement'ev. A.G and Tarakanov. Q.G, *Effect of cellular structure on the mechanical properties of plastic foams*. Journal Polymer Mechanics., 1970. **6**(4): p. 519-525.
80. Zhu, H.X., Mills, N. J., and Knott, J. F., *Analysis of the high strain compression of open-cell foams*. Journal of the Mechanics and Physics of Solids, 1997. **45**(11-12): p. 1875-1904.
81. Triantafillou, T.C., Zhang, J., Shercliff, T. L., Gibson, L. J., and Ashby, M. F., *Failure surfaces for cellular materials under multiaxial loads.2. compression of models with experimental*. International Journal of Mechanical Sciences, 1989. **31**(9): p. 665-678.
82. Maiti, S.K., Gibson, L. J., and Ashby, M. F., *Deformation and energy-absorption diagrams for cellular solids*. Acta Metallurgica, 1984. **32**(11): p. 1963-1975.
83. Gergely, V., and Clyne, T. W., *Drainage in standing liquid metal foams: modelling and experimental observations*. Acta Materialia, 2004. **52**(10): p. 3047-3058.
84. Mills, N.J., and Zhu, H. X., *The high strain compression of closed-cell polymer foams*. Journal of the Mechanics and Physics of Solids, 1999. **47**(3): p. 669-695.

85. Dement'ev. A.G and Tarakanov. Q.G, *Model analysis of the cellular structure of plastic foams of the polyurethane type*. Vladimir Scientific Research Institute of Synthetic Resins. Translated from Mekhanika Polimerov, 1970. **6**(5): p. 744–749.
86. Vladimir, S., *Modelling of the mechanical properties of low-density foams*. Ph.D thesis Delft University, 1998.
87. Sullivan, R.M., and Ghosn, Louis J., *Shear moduli for non-isotropic, open cell foams using a general elongated Kelvin foam model*. International Journal of Engineering Science, 2009. **47**(10): p. 990-1001.
88. Gong, L., and Kyriakides, S., *Compressive response of open cell foams - Part II: Initiation and evolution of crushing*. International Journal of Solids and Structures, 2005. **42**(5-6): p. 1381-1399.
89. Thiyyagasundaram, P., Sankar, Bhavani V., and Arakere, Nagaraj K., *Elastic Properties of Open-Cell Foams with Tetrakaidecahedral Cells Using Finite Element Analysis*. AIAA Journal, 2010. **48**(4): p. 818-828.
90. Roberts, A.P., and Garboczi, E. J., *Elastic moduli of model random three-dimensional closed-cell cellular solids*. Acta Materialia, 2001. **49**(2): p. 189-197.
91. Clutton, E.Q., and Rice, G. N., *Structure property relationships in thermoplastic foams*. Cellular Polymers, 1992. **11**(6): p. 429-449.
92. Ostrogorsky, A.G., Glicksman, L. R., and Reitz, D. W., *Aging of polyurethane foams*. International Journal of Heat and Mass Transfer, 1986. **29**(8): p. 1169-1176.
93. Pilon, L., Fedorov, A. G., and Viskanta, R., *Gas diffusion in closed-cell foams*. Journal of Cellular Plastics, 2000. **36**(6): p. 451-474.
94. McKown, S.T., *The progressive collapse of novel aluminium foam structures*, Ph.D. thesis. University of Liverpool.2005.
95. Mills, N.J., Stampfli, R., Marone, F., and Bruhwiler, P. A., *Finite element micromechanics model of impact compression of closed-cell polymer foams*. International Journal of Solids and Structures, 2009. **46**(3-4): p. 677-697.
96. Zhu, H.X., and Windle, A. H., *Effects of cell irregularity on the high strain compression of open-cell foams*. Acta Materialia, 2002. **50**(5): p. 1041-1052.
97. Zhang, J.-l. and Z.-x. Lu, *Numerical Modeling of the Compression Process of Elastic Open-cell Foams*. Chinese Journal of Aeronautics, 2007. **20**(3): p. 215-222.

98. Song, Y.Z., Wang, Z. H., Zhao, L. M., and Luo, J. A., *Dynamic crushing behavior of 3D closed-cell foams based on Voronoi random model*. Materials & Design, 2010. **31**(9): p. 4281-4289.
99. Daoud, A., *Compressive response and energy absorption of foamed A359-Al<sub>2</sub>O<sub>3</sub> particle composites*. Journal of Alloys and Compounds, 2009. **486**(1-2): p. 597-605.
100. An, Y.G., H. Vegter, and J. Heijne, *Development of simple shear test for the measurement of work hardening*. Journal of Materials Processing Technology, 2009. **209**(9): p. 4248-4254.
101. Lin, J.Y., and Huang, J. S., *Stress relaxation of cellular materials*. Journal of Composite Materials, 2005. **39**(3): p. 233-245.
102. Andrews, E.W., J.S. Huang, and L.J. Gibson, *Creep behavior of a closed-cell aluminum foam*. Acta Materialia, 1999. **47**(10): p. 2927-2935.
103. Ozturk, U.E. and G. Anlas, *Hydrostatic compression of anisotropic low density polymeric foams under multiple loadings and unloadings*. Polymer Testing, 2011. **30**(7): p. 737-742.
104. Briody Conor, D., Barry, Jerrams, Steve, and Ronan, Stephen, *Prediction of compressive creep behaviour in flexible polyurethane foam over long time scales and at elevated temperatures*. Polymer Testing, 2012. **31**(8): p. 1019-1025.
105. Sutton, M.A., Wolters, W. J., Peters, W. H., Ranson, W. F., and McNeill, S. R., *Determination of displacements using an improved digital correlation method*. Image and Vision Computing, 1983. **1**(3): p. 133-139.
106. Bruck, H.A., McNeill, S. R., Sutton, M. A., and Peters, W. H., *Digital image correlation using Newton-Raphson method of partial-differential correction*. Experimental Mechanics, 1989. **29**(3): p. 261-267.
107. Wang, Y., and Cuitiño, and Alberto M., *Full-field measurements of heterogeneous deformation patterns on polymeric foams using digital image correlation*. International Journal of Solids and Structures, 2002. **39**(13-14): p. 3777-3796.
108. Jin, H., Lu, Wei-Yang., Scheffel, Simon., Hinnerichs, Terry D., and Neilsen, Michael K., *Full-field characterization of mechanical behavior of polyurethane foams*. International Journal of Solids and Structures, 2007. **44**(21): p. 6930-6944.

109. Vesenjak, M., Veyhl, C., and Fiedler, T., *Analysis of anisotropy and strain rate sensitivity of open-cell metal foam*. Materials Science and Engineering A-Structural Materials Properties Microstructure and Processing, 2012. **541**: p. 105-109.
110. Zaretsky, E., Asaf, Z., Ran, E., and Aizik, F., *Impact response of high density flexible polyurethane foam*. International Journal of Impact Engineering, 2012. **39**(1): p. 1-7.
111. Tekog̃lu, C., Gibson, L. J., Pardoen, T., and Onck, P. R., *Size effects in foams: Experiments and modeling*. Progress in Materials Science, 2011. **56**(2): p. 109-138.
112. Andrews, E., W. Sanders, and L.J. Gibson, *Compressive and tensile behaviour of aluminum foams*. Materials Science and Engineering: A, 1999. **270**(2): p. 113-124.
113. Rehorek, L., I. Dlouhy, and Z. Chlup, *Tensile behaviour of open cell ceramic foams*. Ceramics-Silikaty, 2009. **53**(4): p. 237-241.
114. Aly, M.S., *Effect of pore size on the tensile behavior of open-cell Ti foams: Experimental results*. Materials Letters, 2010. **64**(8): p. 935-937.
115. Kabir, M.E., M.C. Saha, and S. Jeelani, *Tensile and fracture behavior of polymer foams*. Materials Science and Engineering: A, 2006. **429**(1–2): p. 225-235.
116. <http://info.admet.com/specifications/bid/38926/How-to-perform-a-foam-tensile-strength-test-ASTM-D3574>.
117. Viot, P., *Hydrostatic compression on polypropylene foam*. International Journal of Impact Engineering, 2009. **36**(7): p. 975-989.
118. Kim, Y. and S. Kang, *Development of experimental method to characterize pressure-dependent yield criteria for polymeric foams*. Polymer Testing, 2003. **22**(2): p. 197-202.
119. Bozorg-Haddad, A., Iskander, Maged., and Chen, Yufan, *Compressive strength and creep of recycled HDPE used to manufacture polymeric piling*. Construction and Building Materials, 2012. **26**(1): p. 505-515.
120. Ronan, S., Alshuth, T., Jerrams, S., Murphy, N., *Long-term stress relaxation prediction for elastomers using the time–temperature superposition method*. Materials & Design, 2007. **28**(5): p. 1513-1523.
121. Yeo, S.S., and Hsuan, Y. G., *Evaluation of creep behavior of high density polyethylene and polyethylene-terephthalate geogrids*. Geotextiles and Geomembranes, 2010. **28**(5): p. 409-421.

122. Lankford, J. and K.A. Dannemann, *Strain rate effects in porous materials*. Porous and Cellular Materials for Structure Applications, 1998. **521**: p. 103-108.
123. Davies, O.L. and M.J. Mills, *The rate dependence of confer polyurethane foams*. Cellular Polymers, 1999. **18**(2): p. 117-136.
124. Paul, A., and Ramamurty, U., *Strain rate sensitivity of a closed-cell aluminum foam*. Materials Science and Engineering A-Structural Materials Properties Microstructure and Processing, 2000. **281**(1-2): p. 1-7.
125. Sarva, S.S., Deschanel, S., Boyce, M. C., and Chen, W. N., *Stress-strain behavior of a polyurea and a polyurethane from low to high strain rates*. Polymer, 2007. **48**(8): p. 2208-2213.
126. Holmquist, T.J., Templeton, D. W., and Bishnoi, K. D., *Constitutive modeling of aluminum nitride for large strain, high-strain rate, and high-pressure applications*. International Journal of Impact Engineering, 2001. **25**(3): p. 211-231.
127. Luong, D.D., Pinisetty, Dinesh., and Gupta, Nikhil, *Compressive properties of closed-cell polyvinyl chloride foams at low and high strain rates: Experimental investigation and critical review of state of the art*. Composites Part B: Engineering, 2013. **44**(1): p. 403-416.
128. Yu, J.L., Wang, E. H., and Li, J. R., *An experimental study on the quasi-static and dynamic behavior of aluminum foams under multi-axial compression*. Advances in Heterogeneous Material Mechanics 2008, ed. J.H. Fan and H.B. Chen. 2008, Lancaster: Destech Publications, Inc. 879-882.
129. Pastorino, P., Scarpa, F., Patsias, S., Yates, J. R., Haake, S. J., and Ruzzene, M., *Strain rate dependence of stiffness and Poisson's ratio of auxetic open cell PU foams*. Physica Status Solidi B-Basic Solid State Physics, 2007. **244**(3): p. 955-965.
130. Wang, C.F., Zheng, Z. J., and Yu, J. L., *Micro-inertia effect and dynamic Poisson's ratio of closed-cell metallic foams under compression*. Advances in Heterogeneous Material Mechanics 2011, ed. J.H. Fan, et al. 2011, Lancaster: Destech Publications, Inc. 266-269.
131. Yi, F., Zhu, Zhengang., Zu, Fangqiou., and Hu, Shisheng, *Strain rate effects on the compressive property and the energy-absorbing capacity of aluminum alloy foams*. Materials Characterization, 2001. **47**(5): p. 417-422.

132. Wang, Z., Shen, Jianhu., Lu, Guoxing., and Zhao, Longmao, *Compressive behavior of closed-cell aluminum alloy foams at medium strain rates*. Materials Science and Engineering: A, 2011. **528**(6): p. 2326-2330.
133. Andrews, E.G., G. Onck., P. and Gibson, L. J, *Size effects in ductile cellular solids. Part II: experimental results*. International Journal of Mechanical Sciences, 2001. **43**(3): p. 701-713.
134. Ruiz-Herrero, J.L., Rodriguez-Perez, M. A., and de Saja, J. A., *Sample size effect on the effective diffusion coefficients for the gas contained in closed-cell polyethylene-based foam subjected to compressive creep tests*. Journal of Applied Polymer Science, 2006. **99**(5): p. 2204-2210.
135. Sue, J.W., *Effect of microstructure of closed cell foam on strength and effective stiffness*. Ph.D thesis Texas A&M University, 2006.
136. Malekjafarian, M. and S.K. Sadrnezhaad, *Closed-cell Al alloy composite foams: Production and characterization*. Materials & Design, 2012. **42**: p. 8-12.
137. Avalor, M., Belingardi, G., and Montanini, R., *Characterization of polymeric structural foams under compressive impact loading by means of energy-absorption diagram*. International Journal of Impact Engineering, 2001. **25**(5): p. 455-472.
138. Chan, K.C., and Xie, L. S., *Dependency of densification properties on cell topology of metal foams*. Scripta Materialia, 2003. **48**(8): p. 1147-1152.
139. Nieh, T.G., Higashi, K., and Wadsworth, J., *Effect of cell morphology on the compressive properties of open-cell aluminum foams*. Materials Science and Engineering A-Structural Materials Properties Microstructure and Processing, 2000. **283**(1-2): p. 105-110.
140. Vural, M. and G. Ravichandran, *Microstructural aspects and modeling of failure in naturally occurring porous composites*. Mechanics of Materials, 2003. **35**(3-6): p. 523-536.
141. Li, Q.M., Magkiriadis, I., and Harrigan, J. J., *Compressive strain at the onset of densification of cellular solids*. Journal of Cellular Plastics, 2006. **42**(5): p. 371-392.
142. Tuncer, N. and G. Arslan, *Designing compressive properties of titanium foams*. Journal of Materials Science, 2009. **44**(6): p. 1477-1484.

143. Miltz, J., and Ramon, O., *Energy-Absorption characteristics of polymeric foams used as cushioning materials* Polymer Engineering and Science, 1990. **30**(2): p. 129-133.
144. Brezny, R., and Green, D. J., *Characterization of edge effects in cellular materials* Journal of Materials Science, 1990. **25**(11): p. 4571-4578.
145. Rhodes, M.B., *Applicable Techniques of Optical Microscopy for Polyurethane Investigations*. Journal of Elastomers and Plastics 1980 **12** (4): p. 201-218
146. Cho, K.Y., and Rizvi, S. S. H., *3D Microstructure of supercritical fluid extrudates. II: Cell anisotropy and the mechanical properties*. Food Research International, 2009. **42**(5-6): p. 603-611.
147. Maire, E., Fazekas, A., Salvo, L., Dendievel, R., Youssef, S., Cloetens, P., and Letang, J. M., *X-ray tomography applied to the characterization of cellular materials. Related finite element modeling problems*. Composites Science and Technology, 2003. **63**(16): p. 2431-2443.
148. Knackstedt, M.A., Arns, C. H., Saadatfar, M., Senden, T. J., Limaye, A., Sakellariou, A., Sheppard, A. P., Sok, R. M., Schrof, W., and Steininger, H., *Elastic and transport properties of cellular solids derived from three-dimensional tomographic images*. Proceedings of the Royal Society A-Mathematical Physical and Engineering Sciences, 2006. **462**(2073): p. 2833-2862.
149. Youssef, S., Maire, E., and Gaertner, R., *Finite element modelling of the actual structure of cellular materials determined by X-ray tomography*. Acta Materialia, 2005. **53**(3): p. 719-730.
150. Tokmakova, S.P., *Anisotropy of Poisson's ratio in transversely isotropic rocks*. Nonlinear Acoustics Fundamentals and Applications, 2008. **1022**: p. 413-416.
151. ASTM., *Standard test method for compressive properties of rigid cellular plastics*, in *D1621 – 04a* 2004.
152. Surhone, L.M., M.T. Tennoe, and S.F. Henssonow, *Imagej*. (VDM Verlag Dr. Mueller AG & Co. Kg), , 2010.
153. *Vic-3D, Testing Guide, correlated solutions*. 2010 Germany.
154. <http://www.watermark-software.com>, 2010.

155. British Standard, *Rubber, vulcanized or thermoplastic-Determination of stress relaxation in compression at ambient and at elevated temperatures*. BS ISO 3384-2005.
156. British Standard, *Rigid cellular plastics — Determination of shear strength*. BS ISO 1922-2001.
157. [www.365astronomy.com/bresser-biolux-al-microscope-kit-p-1731.html](http://www.365astronomy.com/bresser-biolux-al-microscope-kit-p-1731.html).
158. Mills, N.J. and Y. Masso-Moreu, *Finite element analysis (FEA) applied to polyethylene foam cushions in package drop tests*. Packaging Technology and Science, 2005. **18**(1): p. 29-38.
159. Lu, Z.X., J.X. Huang, and X. Chen, *Analysis and simulation of high strain compression of anisotropic open-cell elastic foams*. Science China-Technological Sciences, 2010. **53**(3): p. 863-869.
160. Gong, L., Kyriakides, S., Jang, W. Y., and Triantafyllidis, N., *On the stability of Kelvin cell foams under compressive loads*. Journal of the Mechanics and Physics of Solids, 2005. **53**(4): p. 771-794.
161. Alsayednoor, J., Harrison, P. and Guo, Z., *Large Strain Compressive Response of 2-D Periodic Representative Volume Element for Random Foam Microstructures*. Mechanics of Materials (in press). 2012.
162. ABAQUS User manual version 6.11, *Defining tied contact in Abaqus/Standard*, 2011.
163. Harrison, P., W.R. Yu, and A.C. Long, *Rate dependent modelling of the forming behaviour of viscous textile composites*. Composites Part A-Applied Science and Manufacturing, 2011. **42**(11): p. 1719-1726.